Technische Universität München

Fakultät für Medizin

Context-specific characterization of the stromal tumor microenvironment in Pancreatic Ductal Adenocarcinoma

Tatiana Isabel Rodrigues Martins

Vollständiger Abdruck der von der Fakultät für Medizin der Technischen Universität München zur Erlangung des akademischen Grades eines

Doctor of Philosophy (Ph.D.)

genehmigten Dissertation.

Vorsitz: Prof. Dr. Agnes Görlach

Betreuer*in: Prof. Dr. Dieter Saur

Prüfer*innen der Dissertation:

1. Priv.doz. Dr. Jan Böttcher

2. Prof. Dr. Maximilian Reichert

Die Dissertation wurde am 27.02.2023 bei der Fakultät für Medizin der Technischen Universität München eingereicht und durch die Fakultät für Medizin am 03.04.2023 angenommen.

b

Ao Danilo

"You feel like the ocean being warmed by the sun."
Simple song, The Shins

Index

List of Figures

List of Tables

List of Abbreviations

2D	Two-dimensions
3D	Three-dimensions
ACTA2	Alpha smooth muscle actin gene
ADAM	Metalloendopeptidase
ADEX	Aberrantly differentiated endocrine exocrine
AKT	Protein kinase B
ALK	Anaplastic lymphoma kinase
ANOVA	Analysis of variance
apCAFs	Antigen-presenting cancer-associated fibroblasts
ARID1	AT-rich interactive domain-containing protein 1A
BAPN	β-Aminopropionitrile
BMP1	Bone morphogenetic protein 1
BRAF	Proto-oncogene B-raf
BRCA2	Breast cancer type 2 susceptibility protein
CAFs	Cancer-associated Fibroblasts
CCL	Chemokine (C-C motif) ligand
CD	Cluster of differentiation
cDC	Conventional dendritic cells
CDKN2a	Cyclin Dependent Kinase Inhibitor 2A
CN	Cellular neighborhood
CODEX	Co-dectection by indexing
COL1A1	Type I collagen alpha-1
COL3A1	Collagen type III alpha 1 chain
COL4A1	Type IV collagen alpha protein
COL4A2	Collagen type IV alpha 2 chain
COL6A1	Collagen type VI alpha 1 chain
CSF1	Colony Stimulating Factor 1
CSFR	Colony stimulating factor 1 receptor
CSPG4	Chondroitin sulfate proteoglycan 4
CTGF	Connective tissue growth factor
CTL4	Cytotoxic T-lymphocyte-associated protein 4
CXCL	Chemokine (C-X-C motif) ligand
DAPI	4′,6-diamidino-2-phenylindole
DDR2	Discoidin domain-containing receptor 2
DEG	Differential expressed genes
DES	Desmin
DNA	Deoxyribonucleic acid
DPT	Dermatopontin
DRS	Dual recombinase system
DSB	Double-strand breaks
Early myCAFs	Early myofibroblasts
ECM	Extracellular matrix
EMT	Epithelial-to-mesenchymal transition
EpCAM	Epithelial cell adhesion molecule
ER	Estrogen receptor
ERK	Extracellular signal-regulated kinase
ES	Enrichment score
F480	EGF-like module-containing mucin-like hormone receptor-like 1
FABP4	Fatty Acid-Binding Protein 4
FAK	Focal adhesion kinase
FBLN4	EGF-containing fibulin extracellular matrix protein 2
FDR	False discovery rate

FFPE	Formalin-fixed paraffin-embedded
FGFR2	Fibroblast growth factor receptor 2
FN	Fibronectin
FOLFORINOX	Chemotherapy regimen containing leucovorin calcium (folinic acid), fluorouracil, irinotecan hydrochloride, and oxaliplatin
FoxP3	Forkhead box P3
FSP1	Fibroblast-specific protein 1
G1	Grade 1
G2	Grade 2
G3	Grade 3
G4	Grade 4
GAPDH	Glyceraldehyde-3-phosphate dehydrogenase
GEMM	Genetically Engineered Mouse Model
GFAP	Glial fibrillary acidic protein
GFP	Green fluorescence protein
H&E	Hematoxylin and eosin staining
HGF	Hepatocyte growth factor
iCAFs	Inflammatory cancer-associated fibroblasts
ICB	Immune checkpoint blockade
IF	Immunofluorescence
IFNγ	Interferon-gamma
iGD	Increased gene dosage
IHC	Immunohistochemistry
IL1	Interleukin 1
IL6	Interleukin 6
IL6 iCAFs	Interleukin 6 expressing iCAFs
IL6 myCAFs	Interleukin 6 expressing-myCAFs
iNOS	Inducible nitric oxide synthase
ITGB	Integrin beta chain
JAK	Janus kinase
KC	GEMM containing the constructs Pdx1-cre and LSL-KrasG12D
KEGG	Kyoto encyclopedia of genes and genomes
KPC	GEMM containing the constructs Pdx1-cre, LSL-KrasG12D, and LSL-Trp53R172H
KRAS	Kirsten rat sarcoma virus
KRT18	Cytokeratin 18
LAMA2	Laminin Subunit Alpha 2
LIF	Leukemia inhibitory factor
LOH	Loss of heterozygosity
LOX	Lysyl-oxidase
LOXi	LOX inhibitor
LOXL2	Lysyl oxidase-like 2
LRRC15	Leucine-rich repeat-containing protein 15
LY6C	Lymphocyte antigen 6 complex, locus C1
MDSC	Myeloid-derived suppressor cell
MEK	Mitogen-activated protein kinase kinase
MHCII	Major histocompatibility complex class II
MMP	Matrix metalloproteinase
MRC1	Mannose receptor c-type 1
mRNA	Messenger RNA
MSI	Microsatellite instability
mTOR	Mammalian target of rapamycin
MYC	Proto-oncogene MYC
myCAFs	Myofibroblasts
MYH11	Myosin heavy chain 11
NES	Normalized enrichment score
NES	Nestin

NFκB	Nuclear factor kappa-light-chain-enhancer of activated B-cells
NT	Non-treated
OVA	Ovalbumin
PALB2	Partner and localizer of BRCA2
PanIN	Pancreatic intraepithelial neoplasia
PARP	Poly (ADP-ribose) polymerase
PC1	Principal component 1
PC2	Principal component 2
PCA	Principal component analysis
PCR	Polymerase chain reaction
PCR	Polymerase chain reaction
PD1	Programmed cell death protein 1
PDAC	Pancreatic Adenocarcinoma
PDGFRα	Platelet-derived growth factor receptor alpha
PDK1	Phosphoinositide-dependent kinase-1
PD-L1	Programmed death-ligand 1
PDPN	Podoplanin
PI3K	Phosphatidylinositol 3-kinase
Pi3kca	Phosphatidylinositol 3-kinase gene
PSCs	Pancreatic stellate cells
qPCR	Quantitative PCR
RET	Proto-oncogene Ret
RNA	Ribonucleic acid
RNAseq	RNA sequencing
RNF43	Ring finger protein 4
RTK	Receptor tyrosine kinase
SM22	Smooth muscle protein 22-alpha
SMAD	SMAD family
SMAD4	SMAD family Member 4
SPARC	Secreted protein acidic and rich in cysteine
SPINK4	Serine protease inhibitor Kazal-type 4
STAT	Signal transducer and activator of transcription
TCR	T cell receptor
TGFB2	Transforming Growth Factor Beta 2
TGFBR2	Transforming growth factor beta receptor 2
TGFβ1	Transforming growth factor-beta 1
TIMP	Metallopeptidase inhibitor
TME	Tumor Microenvironment
TRP53	Transformation-related protein 53
WHO	World Health Organization
WNT	WNT family member
WT	Wild-type
YAP	Yes-associated protein
ZEB1	Zinc-finger E-box-binding homeobox 1
αSMA	Alpha smooth muscle actin

Note: This thesis follows the HUGO Gene Nomenclature Committee (HGNC) guidelines.

Abstract

Pancreatic adenocarcinoma (PDAC) presents an extensive desmoplastic reaction. Cancer-associated fibroblasts (CAFs) are the most abundant population, outnumbering tumor cells and other populations in the TME. However, the role of CAFs in PDAC desmoplasia remains poorly elucidated despite their contribution to tumor progression and therapy resistance.

Therefore, to determine the role of CAFs in PDAC, a murine PDAC cohort was analyzed using CAFs-targeted multiplex immunofluorescence panels, phenotyping CAFs populations within the tumor microenvironment (TME), and characterizing the stromal PDAC architecture. The further stratification of the cohort according to oncogenic-driver, differentiation, and *Trp53* status uncovered context-specific activation patterns and different stromal organizations. The data suggests stromal regulation via PI3K-driven non-autonomous mechanisms in the context of differentiated tumors. Moreover, shallow stromal responses in poorly-differentiated tumors translated into tumor cell-centric neighborhoods, in which CAFs may act as bystanders. Additionally, the stratification according to *Trp53* status showed a preferential activation from iCAFs (inflammatory CAFs) toward myCAFs (myofibroblasts) with *Trp53* loss of heterozygosity (LOH). *Trp53* LOH induced transcriptional changes in tumor cells leading to the upregulation of MYC and EMT (epithelial-to-mesenchymal) programs, associated with the expression of *Zeb1*, *Col4a1,* and *Loxl2*. Indeed, inhibiting ECM (extracellular matrix) accumulation using a LOX inhibitor in a tumor organoid-fibroblasts co-culture setting reversed myCAFs-associated phenotype activation towards iCAFs only in the context of *Trp53* deficiency. Further analysis of myCAFs-rich TME revealed an increased tumoral and stromal deposition of Collagen IV and LOX, suggesting an exacerbation of ECM remodeling. In contexts of higher stromal abundance, myCAFs were associated with increased metastatic potential, suggesting cooperation between tumor cells and myCAFs in metastasis formation.

These data offer new insights into the context-specific role of the stromal TME and the use of myCAFs as a potential biomarker of metastasis in well-differentiated tumors with a highly-developed stromal response.

Zusammenfassung

Das duktale Adenokarzinom des Pankreas (PDAC) weist eine ausgedehnte desmoplastische Reaktion auf. Krebs-assoziierte Fibroblasten (CAF, cancer-associated fibroblasts) sind die am häufigsten vorkommende Population und übertreffen Tumorzellen und andere Populationen in der Tumormikroumgebung (TMU). Die Rolle von CAF bei der PDAC-Desmoplasie ist jedoch noch weitestgehend ungeklärt.

Um die Rolle von CAFs in PDAC zu bestimmen, wurde eine murine PDAC-Kohorte anhand von Multiplex Immunhistochemie analysiert. Das diente zur Phänotypisierung von CAF-Populationen innerhalb der TMU und zur Charakterisierung der stromalen PDAC-Architektur. Die weitere Stratifizierung der Kohorte nach onkogenem Treiber, Differenzierung und *Trp53*-Status deckte kontextspezifische Aktivierungsmuster und unterschiedliche stromale Organisationen auf. Die präsentierten Daten unterstützen die Hypothese der Stromaregulation über PI3K-gesteuerte nicht-autonome Mechanismen im Zusammenhang mit differenzierten Tumoren. Außerdem wurden flache Stromareaktionen in schlecht differenzierten Tumoren in tumorzellzentrische Nachbarschaften übersetzt, in denen CAF Bystander-Effekte hervorrufen könnten. Zusätzlich zeigte die Stratifizierung nach *Trp53*-Status eine bevorzugte Aktivierung von iCAF zu myCAF mit *Trp53*-Heterozygotieverlust. *Trp53*-Heterozygotieverlust induzierte transkriptionelle Veränderungen in Tumorzellen, die zur Hochregulierung von MYC- und EMT-Programmen führten. Diese Programmen waren mit der Expression von *Zeb1*, *Col4a1* und *Loxl2* assoziiert. In einem Tumor Organoid-Fibroblasten Ko-Kultur-Modell kehrte die Hemmung der extrazellulären Matrix (EZM)-Akkumulation durch Lysyl-Oxidase-Inhibitor die myCAFs-assoziierte CAF-Aktivierung in Richtung eines iCAF-Phänotyps nur im Zusammenhang mit Trp53-Mangel um. Eine weitere Analyse von myCAF-reichem TMU ergab eine erhöhte tumorale und stromale Ablagerung von Kollagen IV und LOX, was auf einen erhörhten Umbau der EZM hindeutet. Im Zusammenhang mit einer höheren Stroma-Häufigkeit waren myCAF mit einem erhöhten Metastasierungspotenzial verbunden, was auf eine Zusammenarbeit zwischen Tumorzellen und myCAF bei der Metastasenbildung hindeutet.

Diese Daten bieten neue Einblicke in die kontextspezifische Rolle der stromalen TMU und die Verwendung von myCAF als potenzieller Biomarker der Metastasen.

1 Introduction

Pancreatic Cancer ranks 12th in the list of cancers with the most incidence in the world and 4th with the highest mortality, accounting only in 2020 with 495773 new cases and 466003 deaths (Ferlay J, 2020a). The International Agency for Research on Cancer from the World Health Organization (WHO) estimates that the incidence and mortality of Pancreatic Cancer will increase by approximately 60% by 2040 (Ferlay J, 2020b; Rahib *et al.*, 2021). Although the increase in the incidence may be attributed to the increasing life expectancy in developed countries, environmental, lifestyle, and hereditary factors also play an essential role (Klein, 2021; Park *et al.*, 2021). Inherited genetic susceptibilities explain approximately 23% of pancreatic cancer cases, with the remaining associated with the prevalence of smoking, diabetes, alcohol, and exposure to toxic substances (Klein, 2021; Park *et al.*, 2021).

The prognosis for Pancreatic Cancer patients is one of the most dismal among all cancer entities. Even though significant efforts have been made to decrease cancer-related death, the 5-year survival rate stands at 10%, increasing by 5% since the beginning of the millennium (Park *et al.*, 2021).

1.1 Pancreatic Adenocarcinoma

Pancreatic Ductal Adenocarcinoma (PDAC) is an exocrine form of Pancreatic Cancer and represents approximately 90% of all Pancreatic Cancers (American Cancer Society, 2022).

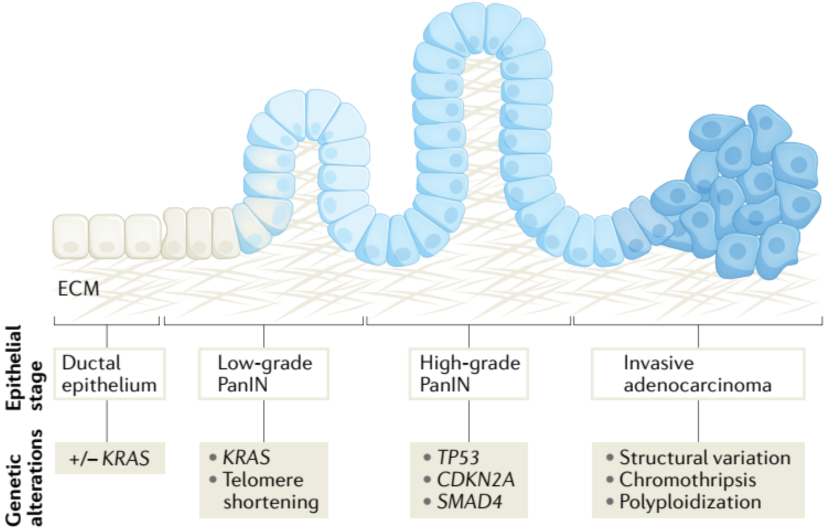

Figure 1 – Histological alterations in PDAC during tumor progression.

PDAC tumorigenesis comprises a series of histological alterations associated with molecular alterations. The process starts with the accumulation of KRAS mutations and telomere shortening. High-grade PanINs present mutations in tumor suppressor genes, leading to increased genomic instability characteristic of invasive tumors. (Connor and Gallinger, 2022) Used with permission.

PDAC tumorigenesis is a multi-step process that comprises molecular and histological alterations. The tumorigenesis process is thought to start in the normal ductal epithelium that undergoes neoplasia (Connor and Gallinger, 2022). The ductal and acinar cells undergo a gradual dysplastic process that originates from a spectrum of precursor lesions with specific genetic alterations (Connor and Gallinger, 2022; Storz, 2017; Ying *et al.*, 2016). The most common precursor lesions are PanINs (Pancreatic intraepithelial neoplasia) that can present visible low-grade alterations (PanIN1) to high-grade alterations (PanIN3) (Connor and Gallinger, 2022; Notta *et al.*, 2017; Ying *et al.*, 2016). The PanINs' progression toward adenocarcinoma is concomitant with the accumulation of several genetic alterations. The increasing PanIN dysplasia is generally characterized by the accumulation of other genetic alterations besides *KRAS*, such as the loss of tumor suppressor genes such as *TRP53*, *SMAD4*, and *CDKN2A*, contributing to a higher genomic instability, resulting in divergent tumor mutational landscapes (Notta *et al.*, 2017; Raphael *et al.*, 2017; Waddell *et al.*, 2015).

Even though the PDAC mutational landscape is diverse, no targeted therapy is available, with PDAC stratification being done based on the tumor stage for clinical purposes (Ducreux *et al.*, 2015; Neoptolemos *et al.*, 2018; van Roessel *et al.*, 2018). PDAC staging criteria were drawn by the American Joint Committee on Cancer, stratifying patients based on variables of tumor progression such as tumor size and blood vessel invasion, amount of lymph node metastasis, and presence of distant metastasis (van Roessel *et al.*, 2018). The PDAC standard of care is based on the resectability of the tumor, the only curative therapeutic option (Ducreux *et al.*, 2015). However, resectable disease diagnosis is rare, with less than 20% of the patients eligible for surgery (Ducreux *et al.*, 2015). Patients with resectable disease follow up on surgery with adjuvant chemotherapy, whereas patients with borderline-resectable and unresectable diseases undergo only chemotherapy (Ducreux *et al.*, 2015; Neoptolemos *et al.*, 2018). Chemotherapy regimens are based on DNA-interfering agents and are defined based on performance status, with FOLFORINOX offering prolonged overall survival compared with nab-paclitaxel, 5-fluorouracil, and platin-based agents (Ducreux *et al.*, 2015; Neoptolemos *et al.*, 2018).

The current classification based on tumor stage does not offer an efficient stratification of PDAC patients, in which histological variables, such as tumor grade, were not considered, despite their potential prognostic value (Hartwig *et al.*, 2011; Kalimuthu *et al.*, 2020; Yin *et al.*, 2020). Tumor grade is a three-tiered system classification defined by the WHO based on the gradual loss of differentiation features (Haeberle and Esposito, 2019; Kalimuthu *et al.*, 2020). Tumors presenting a differentiated morphology exhibit glandular structures with slight-to-moderate polymorphic nuclei and lower mitotic index, whereas poorly-differentiated PDAC present loss of the glandular compartment, generally associated with tumor cell budding, polymorphic nuclei, and a high degree of mitoses (Haeberle and Esposito, 2019). The differentiation status of the tumor is indicative of patient survival, with patients harboring well-differentiated (G1) and moderately-differentiated tumors (G2) exhibiting a longer overall survival rate than poorly-differentiated tumors (G3) (Hartwig *et al.*, 2011; Kalimuthu *et al.*, 2020; Yin *et al.*, 2020). Nonetheless, differentiated and poorly-differentiated tumors present a continuum of tumor cell states that originate a heterogenous response to therapy (Aung *et al.*, 2018; Bailey *et al.*, 2016; Kalimuthu *et al.*, 2020; Moffitt *et al.*, 2015; Puleo *et al.*, 2018).

Therefore, new stratification systems composed of clinical, histological, and mutational variables should be developed to stratify patients with PDAC more efficiently.

1.1.1 Molecular landscape

PDAC harbors a complex mutational landscape. Several genomic studies have identified multiple somatic and germline alterations, contributing to intra- and inter-tumoral disease heterogeneity (Raphael *et al.*, 2017; Waddell *et al.*, 2015; Witkiewicz *et al.*, 2015).

KRAS is the most mutated gene in PDAC, where approximately 90% of the tumors present gain-of-function mutations (Philip *et al.*, 2022; Raphael *et al.*, 2017; Waddell *et al.*, 2015; Witkiewicz *et al.*, 2015). Most *KRAS* mutations are in codon 12, where the substitution of glycine by aspartic acid (G12D) represents 43% of all *KRAS* mutations, followed by, in 30.8% of cases, the replacement of glycine by valine (G12V) and 14.2% the substitution of glycine by arginine (G12R) (Philip *et al.*, 2022). In PDAC, mutations in G12C (glycine to cystine) affect only 1.9% of patients (Philip *et al.*, 2022; Raphael *et al.*, 2017; Witkiewicz *et al.*, 2015). Novel KRAS inhibitors have been developed in the past decade (Hallin *et al.*, 2022; Kwan *et al.*, 2022). Sotorasib and adagrasib are small molecules that bind to the P2 catalytic pocket when KRAS is in its GDP-bound state, locking it in that conformation and blocking further downstream signaling (Ostrem *et al.*, 2013). However, these inhibitors are G12C-specific, targeting only a small cohort of PDAC patients (Ostrem *et al.*, 2013). Although $\text{KRAS}^{\text{G12C}}$ inhibitors controlled disease and increased overall survival, patients treated with $\text{KRAS}^{\text{G12C}}$ inhibitor alone developed resistance to this treatment (Awad *et al.*, 2021; Hong *et al.*, 2020). The emergence of resistance was due to newly acquired *KRAS* mutations and other genetic alterations that activate RTK-RAS signaling independently of KRAS (Awad *et al.*, 2021). Novel selective $\text{KRAS}^{\text{G12D}}$ inhibitors are being developed with similar mechanisms of action to $\text{KRAS}^{\text{G12C}}$, demonstrating exciting therapeutic potential in PDAC (Hallin *et al.*, 2022).

Most *KRAS* mutant tumors present further deletions or inactivating mutations in *TRP53,* followed by at least a frequency of 30% in mutations or deletions of *CDKN2A* and *SMAD4 (Raphael et al., 2017; Waddell et al., 2015).* Alterations in several other genes are also present at a frequency inferior to 10% (Raphael *et al.*, 2017; Waddell *et al.*, 2015; Witkiewicz *et al.*, 2015). Alterations in TGFβ signaling occur with the deletion of *TGFBR2* in 5-7% of patients (Raphael *et al.*, 2017; Witkiewicz *et al.*, 2015). DNA repair pathways can also be affected, presenting inactivations in *BRCA1* (1%), *BRCA2* (4%), and *PALB2* (1%), potentially sensitizing tumors to platinum-based therapies and PARP inhibitors (Raphael *et al.*, 2017; Waddell *et al.*, 2015). Moreover, about 7% of patients presented inactivation of the tumor suppressor *RNF43,* which may confer sensitivity to WNT inhibitors (Jiang *et al.*, 2013; Raphael *et al.*, 2017; Waddell *et al.*, 2015; Witkiewicz *et al.*, 2015). Recurrent genomic alterations in chromatin remodeling genes such as *ARID1A* and *KDM6A* were present at a frequency of 6-15% and 3-18% of patients, suggesting that this group may have more sensitivity to epigenetic-based therapies (Raphael *et al.*, 2017; Waddell *et al.*, 2015; Witkiewicz *et al.*, 2015).

KRAS wild-type tumors represent approximately 10% of all PDAC cases (Philip *et al.*, 2022; Raphael *et al.*, 2017; Witkiewicz *et al.*, 2015). Genetic alterations in *TRP53* occurred in 41% of *KRAS* wild-type tumors, followed generally by gain-of-function mutations in *BRAF*, representing approximately 4-13% of the alterations (Philip *et al.*, 2022; Witkiewicz *et al.*, 2015). *BRAF* mutations were mutually exclusive with *KRAS* mutations, contrary to *PIK3CA* mutations, which often occurred concomitantly (Aung *et al.*, 2018; Witkiewicz *et al.*, 2015). In addition, mutations in DNA-repair pathways (5.2% in *BRCA2* and 2.1% in *PALB2*), chromatin remodeling (11.6% in *ARID1A*), and cell cycle (10.3% in *CDKN2A*) were also present at a frequency of approximately 10% or less in *KRAS* wild-type tumors (Philip *et al.*, 2022). KRAS wild-type tumors also presented a higher frequency in gene fusion events, more prevalent in *BRAF*, *FGFR2*, *ALK,* and *RET (Philip et al., 2022)*. KRAS wild-type tumors were likelier to be MSI-high tumors when compared to KRAS-mutated PDAC, indicating that this cohort might be more sensitive to immune checkpoint therapies (Colle *et al.*, 2021; Luchini *et al.*, 2021; Philip *et al.*, 2022).

The molecular landscape of PDAC has been well characterized, where tumors follow the same mutational path in most cases, with alterations in four genes making up for the bulk of the genomic changes (Raphael *et al.*, 2017; Waddell *et al.*, 2015; Witkiewicz *et al.*, 2015). Nevertheless, the alterations in these four genes do not seem to explain good clinical response and extended overall survival (Dal Molin *et al.*, 2015). Since additional mutations are present at a low frequency, adequate enrollment of patients in clinical trials complicates the evaluation of clinical responses for targeted drugs (Chang *et al.*, 2014). It is also likely that other factors, such as epigenetic changes and the nature of stroma and immune compartment, may impact gene expression and contribute to the heterogenous responses to therapy (Connor and Gallinger, 2022)

1.1.2 Transcriptional subtypes

The characterization of PDAC based on histological features has been described but does not yet offer prognostic information that could be valuable for treatment selection (Ducreux *et al.*, 2015; Kalimuthu *et al.*, 2020; Puleo *et al.*, 2018). Therefore, in the past decade, several studies stratified PDAC on a transcriptional basis to complement histopathological classifiers to provide help in treatment decisions (Bailey *et al.*, 2016; Chan-Seng-Yue *et al.*, 2020; Collisson *et al.*, 2011; Kalimuthu *et al.*, 2020; Moffitt *et al.*, 2015; Puleo *et al.*, 2018).

The transcriptomic stratification of PDAC resulted in different definitions, albeit some subtypes overlap between classifications (Bailey *et al.*, 2016; Chan-Seng-Yue *et al.*, 2020; Collisson *et al.*, 2019; Kalimuthu *et al.*, 2020; Moffitt *et al.*, 2015; Puleo *et al.*, 2018). Those differences likely arose from experimental design choices and patient material availability. Nevertheless, two main subtypes were identified across all studies: classical and basal.

In the Collison *et al.* classification, non-treated resected human PDAC were microdissected, and mRNA expression was analyzed using hybridization arrays, leading to the identification of three subtypes: Classical, Quasi-mesenchymal and Exocrine-like (Collisson *et al.*, 2011). The Classical subtype was enriched in adhesion and epithelial genes, the Quasi-mesenchymal subtype presented high expression of mesenchymal genes, and the Exocrine-like subtype exhibited high expression of digestive enzyme genes (Collisson *et al.*, 2011). This classification also revealed that patients with tumors belonging to the Classical subtype presented an overall better prognosis and extended survival than the Quasi-mesenchymal subtype (Collisson *et al.*, 2011).

The analysis performed by Moffitt and colleagues deepened the Collisson classification, identifying tumor-specific and stroma-specific subtypes. In this study, the authors analyzed primary and metastatic

PDAC using a combination of microarrays and RNAseq (Moffitt *et al.*, 2015). The samples were then deconvoluted, and confounding gene signatures from normal tissue and stroma were removed, identifying four subtypes in PDAC: two tumor-specific and two stroma-specific (Moffitt *et al.*, 2015). Similarly to the Collison classification, tumor-specific subtypes were divided into Classical and Basal-like. The Collison-classical gene signature corresponded to most Moffitt-classical tumors, while the Quasi-mesenchymal gene signature matched both the Basal-like subtype and the stromal subtypes (Moffitt *et al.*, 2015). Alongside those differences, resectable Classical tumors presented a better overall survival than resectable Basal-like tumors, with the latter responding better to adjuvant chemotherapy (Moffitt *et al.*, 2015). Nevertheless, Stage III/IV Classical tumors responded better to first-line chemotherapy than the Basal-like subtype (Aung *et al.*, 2018). Finally, the stromal subtypes were classified into Normal and Activated, occurring in both Classical and Basal-like subtypes. The Normal subtype was enriched in stellate cell-related genes and *ACTA2*, while the Activated subtype enriched ECM-related, macrophage-related, and cytokine genes, dichotomizing the stromal TME into "good" and "bad" (Moffitt *et al.*, 2015). Patients harboring tumors with Normal stroma presented an increased survival over patients harboring an Activated one (Moffitt *et al.*, 2015). Nonetheless, these differences appeared less evident when Basal-like tumors showcased either a Normal or an Activated phenotype than in the Classical phenotype, presenting the idea that stroma may be, depending on the context, tumor-promoting or tumor-retraining (Moffitt *et al.*, 2015).

Bailey and colleagues introduced the immunogenic PDAC subtype. The deconvolution of untreated primary human PDAC led to the definition of four subtypes: the Squamous, the Pancreatic progenitor, the ADEX, and the Immunogenic (Bailey *et al.*, 2016). When benchmarked to the Collisson definition, the Squamous subtype mostly overlapped with the Quasi-mesenchymal subtype, the Pancreatic progenitor overlapped with the Classical subtype, and the ADEX overlapped with the Exocrine-like subtype (Bailey *et al.*, 2016). The Immunogenic subtype was correlated with a higher immune cell infiltrate and was defined by enriched gene expression profiles related to T cell infiltration, concomitant with an upregulation of *CTL4* and *PD1*, suggesting an immunosuppressive environment (Bailey *et al.*, 2016).

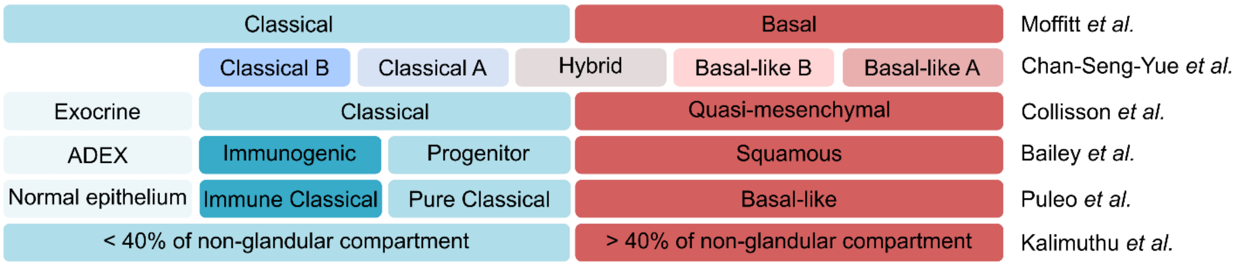

Figure 2 – Summary of the transcriptional phenotypes in PDAC.

The various transcriptional phenotypes defining the tumor compartment are depicted in each line, showing the overlap between the phenotypes. Adapted from: Connor and Gallinger, 2022.

Other characterizations supported the subtypes previously described. Using a cohort of purified tumor cells by laser microdissection, Chan-Seng-Yue and colleagues expanded the Classical and

Basal-like subtypes classification (Chan-Seng-Yue *et al.*, 2020). This new nomenclature added more transcriptional groups, defining more granularly tumor-specific subtypes. Classical-A and Classical B define mainly the Classical subtype, and the Basal-like subtype, characterized by KRAS imbalances, was further divided into Basal-A and Basal-B (Chan-Seng-Yue *et al.*, 2020). Some tumors presented multiple gene expression signatures and did not match either classical or basal-like subtypes defined in previous stratification efforts, being classified by Chan-Seng-Yue *et al.* as a hybrid subtype (Chan-Seng-Yue *et al.*, 2020). These data suggest that cancer cell states occur in a continuum defined by the extreme Classical-B and Basal-A states. This study also corroborated that classical subtypes have a better prognosis and are present in the early stages of PDAC than basal-like subtypes (Chan-Seng-Yue *et al.*, 2020). Nonetheless, in advanced disease, there is different sensitivity between basal-like subtypes in response to chemotherapy (Chan-Seng-Yue *et al.*, 2020). Another study phenotyping PDAC tumor cell lines also defined the spectrum of cell states that may constitute the TME. Müller and colleagues defined three cell states composing an epithelial phenotype, C2a, C2b, and C2c, and a mesenchymal cluster C1 (Mueller *et al.*, 2018). On the edge of the phenotypes were the C2a and C1 clusters, associated with histologically differentiated phenotypes and *Kras*$^{G12D/WT}$ and an undifferentiated phenotype with the loss of wild-type *Kras* and increased *Kras* gene dosage (Mueller *et al.*, 2018).

Puleo and colleagues' characterization aligned with previous Moffitt *et al.* and Bailey *et al.* classifications. This stratification used bulk PDAC tumor tissue to measure mRNA expression and, through deconvolution of tumor, stromal and immune signatures defined five PDAC subtypes (Puleo *et al.*, 2018). This classification integrated tumor with stromal characteristics, establishing subtypes with tumor-intrinsic classical or Basal-like features and different levels and stroma nature (Puleo *et al.*, 2018). Additionally, these subtypes presented different clinical outcomes, suggesting that stroma may play a role in retraining or promoting tumor growth and metastasis (Puleo *et al.*, 2018).

Further work identified the TME as a central regulator of tumor cell states, plasticity, and therapy response. Tumor microenvironment-derived cues can shape tumor transcriptional subtypes from classical to basal and mediate the sensitivity to chemotherapy (Raghavan *et al.*, 2021).

Therefore, integrating TME states with cancer cell states is crucial to provide a better prognosis of therapy response.

1.1.3 Tumor microenvironment

The PDAC TME is threefold, comprising an extensive stromal reaction, microbiome, and a dysfunctional immune response (Bailey *et al.*, 2016; Clark *et al.*, 2007; Geller *et al.*, 2017; Grunwald *et al.*, 2021; Knudsen *et al.*, 2017; Riquelme *et al.*, 2019; Whatcott *et al.*, 2015). Therefore, cell types, such as CAFs, immune cells, endothelial cells, and bacteria, cohabitate with tumor cells in an ECM-rich microenvironment, contributing in a context-specific manner to tumor progression and metastasis (Geller *et al.*, 2017; Riquelme *et al.*, 2019; Whatcott *et al.*, 2015).

The microbiome diversity influences PDAC progression (Riquelme *et al.*, 2019). The presence of an intratumoral PDAC microbiome has, in its essence, a detrimental effect on PDAC progression

(Pushalkar *et al.*, 2018). Nevertheless, its composition can exhibit tumor-supporting or tumor-restraining effects (Geller *et al.*, 2017; Pushalkar *et al.*, 2018; Riquelme *et al.*, 2019). Patients harboring tumors with high content of intratumoral bacterial diversity exhibited better overall survival than tumors with more homogeneous bacterial profiles (Riquelme *et al.*, 2019). These differences likely arise with the migration of the microbes from the gut toward the pancreas, contributing to cancer cell growth, immunosuppression, and therapy resistance (Geller *et al.*, 2017; Riquelme *et al.*, 2019).

Pancreatic adenocarcinoma is, in most cases, an immunological “cold” tumor, with only a subset of cases being immunologically active - “hot” tumors (Bailey *et al.*, 2016; Danilova *et al.*, 2019; Knudsen *et al.*, 2017). From a clinical point of view, patients harboring “hot” tumors present a better prognosis than patients with a dysfunctional immune response (Danilova *et al.*, 2019; Knudsen *et al.*, 2017). Immunologic active tumors are characterized by functional innate and adaptive responses, correlating with extended overall survival (Knudsen *et al.*, 2017). The anti-tumor immune response is likely driven by the presence of neoantigens and a higher tumor mutational burden (Connor *et al.*, 2017; Knudsen *et al.*, 2017). The PDAC immunosuppressive microenvironment contains several immune cell types linked with immune evasion and tumor progression, such as T regulatory cells, myeloid-derived suppressor cells (MDSC), neutrophils, and tumor-associated macrophages (Clark *et al.*, 2007; Ino *et al.*, 2013). During tumor progression, tumor cells upregulate mechanisms, producing cytokines that sustain immunosuppression (Siolas *et al.*, 2021). For example, tumor-associated neutrophils are recruited to the TME via CCR2 in response to $TRP53^{R172H}$-induced NFκB signaling, mediating T cell inactivation (Chao *et al.*, 2016; Nielsen *et al.*, 2021; Siolas *et al.*, 2021). Other immunosuppressive populations, such as tumor-associated macrophages and MDSCs also affect T cell function (Candido *et al.*, 2018; Zhao *et al.*, 2009). The stimulation of $CSFR^{+}$ macrophages by CSF1 leads to an immunosuppressive TME with dense stroma, exhausted T cells, and increased tumor growth (Candido *et al.*, 2018). Moreover, GM-CSF-mediated MDSC recruitment inhibits T cell response through T regulatory cell induction (Pylayeva-Gupta *et al.*, 2012; Siret *et al.*, 2019). In fact, T regulatory cells have immunosuppressive functions by inhibiting antigen-presenting cell (APC) function via CTL4, blocking T cell priming and activation (Togashi *et al.*, 2019). However, in PDAC, T regulatory cells are not indicative of a worse prognosis (Knudsen *et al.*, 2017). The PDAC immunosuppressive TME can result from decreased antigenicity, diminished T cell function, and exclusion of T cells from the TME (Hegde *et al.*, 2020; Nicolas-Boluda *et al.*, 2021; Salmon *et al.*, 2012; Yamamoto *et al.*, 2020). The decreased T cell function in the PDAC TME is not only caused by T cell inactivation by immunosuppressive populations but also by inefficient $CD8^{+}$ priming due to very low levels of functional conventional dendritic cells (cDC) and high Th17 responses (Hegde *et al.*, 2020). Additionally, MHC-I impaired expression in tumor cells due to autophagy upregulation leads to dysfunctional presentation of tumor neoantigens, perpetuating immune evasion (Yamamoto *et al.*, 2020). Finally, the accumulation of ECM can shield tumor cells from anti-tumorigenic populations, mediating an immune exclusion response (Akhurst and Hata, 2012; Nicolas-Boluda *et al.*, 2021; Salmon *et al.*, 2012). Tumors with a loose ECM present an increasing migration of T cells toward the core of the tumor, facilitating tumor cell-T cell interactions (Akhurst and Hata, 2012; Nicolas-Boluda *et al.*, 2021; Salmon *et al.*, 2012).

The desmoplastic reaction in PDAC is associated with a high number of cancer-associated fibroblasts and extensive extracellular matrix deposition (Whatcott *et al.*, 2015). The stromal TME can assume two main phenotypes - reactive and deserted, dependent on fibroblast plasticity (Grunwald *et al.*, 2021). The reactive stromal TME presented a higher content of αSMA^{+} cells, $IL6^{+}$ cells, and lower ECM deposition, associated with poorly-differentiated phenotypes, while deserted stromal TME presented an enhanced ECM response and a lower content of αSMA^{+} cells (Grunwald *et al.*, 2021). These histological stromal phenotypes created sub-TMEs within the tumor ecosystem, impacting survival (Grunwald *et al.*, 2021). Even though the co-existence of the sub-TMEs was associated with a worse prognosis, the analysis was performed using a single marker analysis. To better understand these stromal phenotypes, a CAFs subpopulation analysis using high-content imaging should be conducted to dissect CAFs activation profiles populating these stromal subtypes.

1.1.3.1 Cancer-associated fibroblasts

Cancer-associated fibroblasts (CAFs) are cells with mesenchymal morphology, negative for epithelial, endothelial, and immune cell markers, lacking any mutations found in tumor cells (Sahai *et al.*, 2020). In the PDAC TME, CAFs differentiate from normal tissue-resident fibroblasts, such as stellate cells and mesothelial cells, comprising most of the tumor area (Apte *et al.*, 2004; Dominguez *et al.*, 2020; Elyada *et al.*, 2019; Huang *et al.*, 2022; Whatcott *et al.*, 2015).

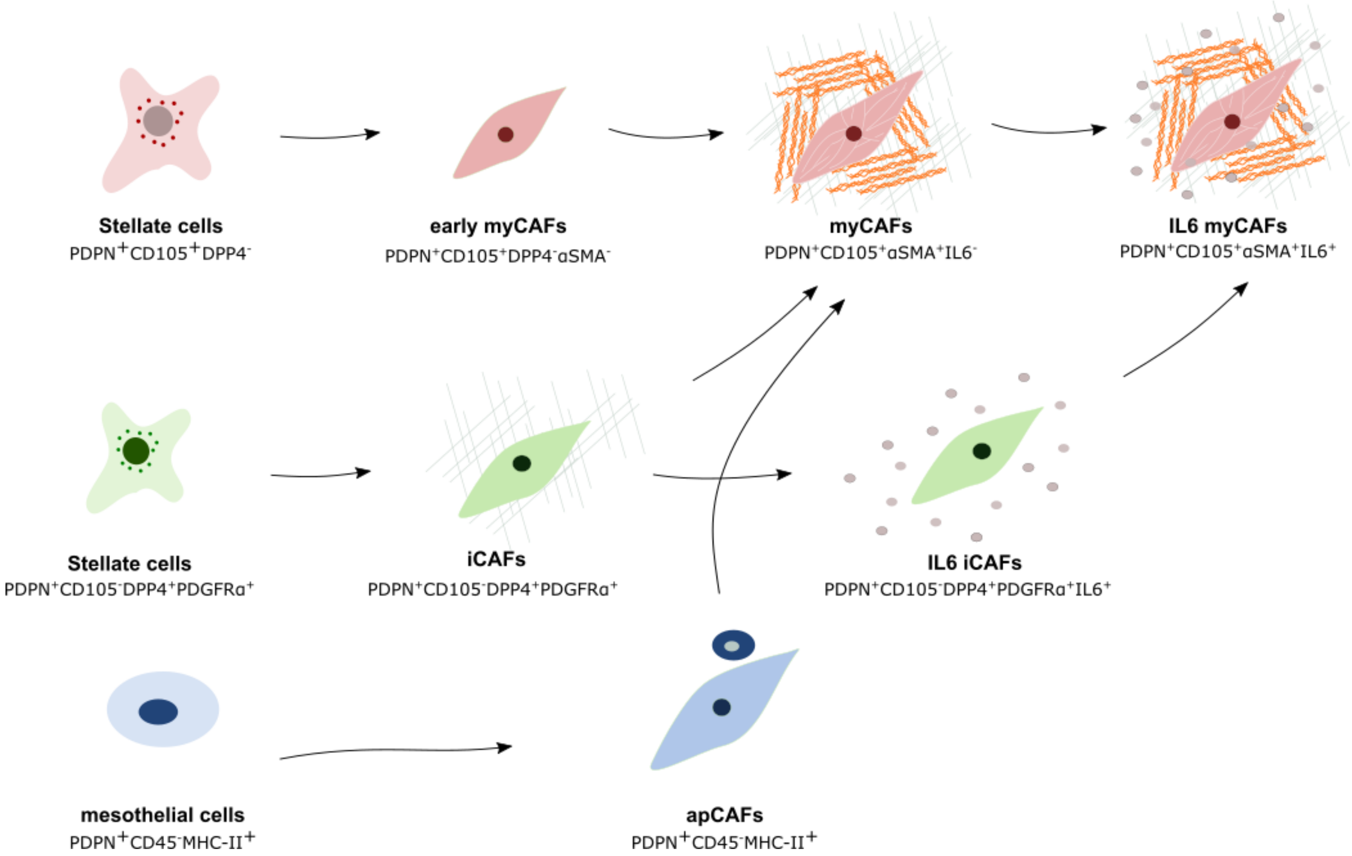

Figure 3 – Model of the phenotypic diversification of CAFs phenotypes.

CAFs arise from pancreatic mesenchymal populations, such as stellate cells and mesothelial cells, and upon stimuli, differentiate into a plethora of phenotypes. These phenotypes are dynamic and compose a continuum of activation states. $CD105^{+}$ stellate cells give rise to an intermediate myCAF phenotype, early myCAFs, negative for αSMA expression. With further stimuli, myCAFs present full activation markers (αSMA expression) and may express IL6 – IL6 myCAFs. On the other hand, CD105$^-$ stellate cells differentiate into CAFs with inflammatory features, iCAFs. It is still unclear the activation path of iCAFs and if populations expressing different iCAFs activation markers harbor the same functions. There is strong evidence that IL6 expressing iCAFs present a cytokine-secreting phenotype. Mesothelial cells are the mesenchymal population in the pancreas that differentiate in MHCII$^+$ CAFs, interfering with antigen presentation. Antigen-presenting CAFs inhibit CD4$^+$ T cells via the TCR receptor, activating them in T regulatory cells.

CAFs showcase a continuum of phenotypes rather than discrete cell states (Dominguez *et al.*, 2020; Friedman *et al.*, 2020; Hutton *et al.*, 2021). Besides the intermediary states, three main types of CAFs have been identified in PDAC and other cancer entities: inflammatory CAFs (iCAFs), myofibroblasts (myCAFs), and antigen-presenting CAFs (apCAFs) (Dominguez *et al.*, 2020; Elyada *et al.*, 2019; Foster *et al.*, 2022; Friedman *et al.*, 2020; Huang *et al.*, 2022; Hutton *et al.*, 2021). These CAFs display different transcriptional programs, where iCAFs present a NFκB signaling program associated with cytokine-rich secretome, myCAFs present an ECM remodeling and TGFβ signaling program, and apCAFs exhibit an IFNγ signaling program. The intermediate states can assume a mix of the transcriptional programs described (Dominguez *et al.*, 2020; Foster *et al.*, 2022; Friedman *et al.*, 2020; Kieffer *et al.*, 2020). However, it is unknown whether the intermediate states retain the functions of the main subtypes.

The phenotypic diversification intrinsic to CAFs complicates the establishment of correlations that allow the extrapolation of CAFs' functional roles. PDPN, a universal fibroblast marker, exhibits an expression pattern mostly restricted to CAFs, whereas other subtype markers, such as αSMA, IL6, LY6C, and PDGFRα, are present in other cell types (Dominguez *et al.*, 2020; Elyada *et al.*, 2019; Hutton *et al.*, 2021). The stratification of tumors according to the stroma amount showed that patients harboring tumors with a dense stromal response have a better prognosis (Jiang *et al.*, 2020; Torphy *et al.*, 2018). Nevertheless, CAFs subtypes and their roles within TME appear to contribute differently to patient prognosis (Heger *et al.*, 2022; Hu *et al.*, 2022; Peng *et al.*, 2022).

1.1.3.1.1 Inflammatory cancer-associated fibroblasts

Inflammatory cancer-associated fibroblasts (iCAFs) were described in 2017 by Öhlund and colleagues as a cytokine-secreting type of fibroblasts in PDAC, defined by a high expression of PDGFRα, negative-to-low expression of αSMA, and alternatively LY6C and IL6 (Dominguez *et al.*, 2020; Elyada *et al.*, 2019; Friedman *et al.*, 2020; Ohlund *et al.*, 2017).

DPP4$^+$ stellate cells are thought to be the cell of origin of iCAFs (Dominguez *et al.*, 2020). Tumor-derived IL1α binds to the IL1R receptor in stellate cells and activates the NFκB signaling (Biffi *et al.*, 2019; Dominguez *et al.*, 2020). IL1-induced LIF secretion activates the JAK-STAT signaling axis in an autocrine fashion, defining the iCAFs phenotype (Biffi *et al.*, 2019). Although TNFα contributes to the differentiation of stellate cells into iCAFs, it is not essential to maintain the phenotype (Biffi *et al.*, 2019). However, upregulation of TGFβ1 signaling inhibits iCAFs phenotype, circumventing IL1-Induced JAK/STAT signaling (Biffi *et al.*, 2019). Moreover, stiffness likely modulates the iCAFs phenotype (Biffi *et al.*, 2019; Discher *et al.*, 2005; Elyada *et al.*, 2019; Foster *et al.*, 2022; Huang *et al.*, 2012). The modulation of the iCAFs phenotype was performed using a soft substrate as matrigel, and 2D culturing conditions provoked the loss of iCAFs markers expression and upregulation of myCAFs markers (Biffi *et al.*, 2019; Elyada *et al.*, 2019). Additionally, iCAFs can differentiate into myCAFs depending on other stimuli (Biffi *et al.*, 2019; Hutton *et al.*, 2021).

Inflammatory CAFs expand during tumor progression, comprising up to 45% of CAFs in PDAC TME (Elyada *et al.*, 2019; Huang *et al.*, 2022). iCAFs can present different activation states depending on the expression of LY6C or IL6 (Friedman *et al.*, 2020), but until now, there is no consensus if this population exerts both tumor-promoting and tumor-restraining effects (Biffi *et al.*, 2019; Hu *et al.*, 2022; Nicolas *et al.*, 2022; Peng *et al.*, 2022; Zhang *et al.*, 2018). On the one hand, the upregulation of NFκB signaling leads to the secretion of a plethora of cytokines involved in tumor progression and immunosuppression (Biffi *et al.*, 2019; Dominguez *et al.*, 2020; Friedman *et al.*, 2020; Peng *et al.*, 2022; Zhang *et al.*, 2018). Inflammatory Ly6C$^+$ iCAFs content lead to a decrease in CD8$^+$ T cell proliferation and an increase in T regulatory cell markers, whereas LY6C$^-$ iCAFs are linked to a higher role in wound healing (Friedman *et al.*, 2020; Steele *et al.*, 2021). On the other hand, iCAFs are enriched in metabolic transcriptional programs correlated with an inflammatory state abundant in T cells, natural killer cells, and interferon activity, suggesting that these tumors may respond better to immune checkpoint blockade (ICB) (Hu *et al.*, 2022). Additionally, iCAFs have been linked to epithelial-to-mesenchymal transition (EMT) and therapy resistance (Feldmann *et al.*, 2021; Hu *et al.*, 2022; Mosa *et al.*, 2020; Peng *et al.*, 2022; Su *et al.*, 2018). Nicolas and colleagues recently described the role of iCAFs in therapy resistance in colorectal cancer models. The mechanism relies on IL1-derived iCAFs' production of nitrate oxide via iNOS, leading to DNA damage (Nicolas *et al.*, 2022). Exposure to radio- or chemotherapy provokes further DNA damage, activating a Trp53-dependent senescence program (Nicolas *et al.*, 2022). The senescent-associated iCAFs phenotype secretes additional cytokines and ECM, supporting tumor invasion and metastasis (Nicolas *et al.*, 2022). Combinatorial treatments using chemotherapy and IL1 inhibitors are being considered to bypass iCAFs-driven therapy resistance (ClinicalTrials.gov, NCT04942626).

1.1.3.1.2 Antigen-presenting cancer-associated fibroblasts

Antigen-presenting cancer-associated fibroblasts (apCAFs) were recently identified by Elyada and colleagues in PDAC and are defined by MHCII and CD74 expression (Elyada *et al.*, 2019). This CAFs subtype arises from mesothelial cells and has a role in tumor immunity (Elyada *et al.*, 2019; Huang *et al.*, 2022). MHCII expression in apCAFs suggested that this CAF subtype interacts with CD4$^+$ T cells. Indeed, functional assays showed that apCAFs induced the early activation of CD4$^+$ T cells, whereas other CAFs subtypes did not play a role (Elyada *et al.*, 2019; Huang *et al.*, 2022). When apCAFs were co-cultured with CD4$^+$T cells after the stimulation with the OVA peptide, early markers of TCR ligation, such as CD25 and CD69, were detected in CD4$^+$ T cells (Elyada *et al.*, 2019). Nevertheless, apCAFs failed to fully activate co-stimulatory molecules (CD40, CD80, CD86) and clonal expansion of CD4$^+$ T cells (Elyada *et al.*, 2019). When the CD4$^+$ T cells co-cultured with apCAFs were phenotyped, they expressed classical markers of T regulatory cells, such as CD25 and FoxP3 (Huang *et al.*, 2022). Therefore, apCAFs seem to have an immunosuppressive role in PDAC by inducing T regulatory cells and inhibiting the proliferation of CD8$^+$ T cells (Huang *et al.*, 2022).

Antigen-presenting CAFs are a plastic cell type, and the maintenance of the phenotype depends on external cues (Elyada *et al.*, 2019; Huang *et al.*, 2022). Elyada and colleagues reported that apCAFs isolated from tumors and culture in 2D conditions differentiated into myCAFs-like populations (Elyada *et al.*, 2019). Additionally, Huang and colleagues showed that in *in vivo* models, mesothelial cells could express αSMA, a marker of myCAF activation (Huang *et al.*, 2022). However, whether these cells retained antigen-presenting capacity was not stated. The strategy stated in the literature is the activation of naïve fibroblasts into apCAFs-like populations. TGFβ1 was described, combined with IL1α, to induce pan-mesothelial cells' differentiation into functional apCAFs *in vitro* (Huang *et al.*, 2022). Other reports also showed that stimulation of normal pancreatic fibroblasts with IFNγ led to the upregulation of MHC-II and CD74 (Hutton *et al.*, 2021).

Antigen-presenting CAFs expand during tumor progression and may contribute significantly to stromal TME. Studies measuring the abundance of CAFs in the PDAC reported that apCAFs represent 0%-35% of the stromal TME (Elyada *et al.*, 2019; Huang *et al.*, 2022). Despite this heterogeneity, apCAFs were correlated with T regulatory cells in PDAC (Huang *et al.*, 2022). Until now, the extension of apCAFs contribution to immunosuppression was not addressed, and whether apCAFs-targeted therapies can impact overall survival.

1.1.3.1.3 Myofibroblasts

Myofibroblasts (myCAFs) were first described in 1971 as ECM-producing cells with contractile properties participating in the wound-healing process (Gabbiani *et al.*, 1972; Majno and Gabbiani, 1971). Nevertheless, only in the last decades, myCAFs started to be acknowledged for their role in PDAC (Dominguez *et al.*, 2020; Krishnamurty *et al.*, 2022; Ozdemir *et al.*, 2014; Peng *et al.*, 2022; Rhim *et al.*, 2014).

MyCAFs initially differentiate from CD105$^+$ stellate cells and are classically defined by αSMA expression and alternatively by LRRC15 expression (Desmoulière *et al.*, 1993; Dominguez *et al.*, 2020; Hutton *et al.*, 2021; Krishnamurty *et al.*, 2022). Other mesenchymal cell lineages, such as CD105$^-$ stellate cells and mesothelial cells, can adopt a myCAFs phenotype upon exposure to specific stimuli (Biffi *et al.*, 2019; Dominguez *et al.*, 2020; Elyada *et al.*, 2019; Huang *et al.*, 2022; Hutton *et al.*, 2021).

TGFβ signaling is the main culprit of myCAF activation (Biffi *et al.*, 2019; Desmoulière *et al.*, 1993; Dominguez *et al.*, 2020; Krishnamurty *et al.*, 2022). Inhibition of TGFβ signaling via TGFβ1 neutralization or TGFBR2 disruption showed an abrogation of the myCAFs phenotype and a shift towards an iCAFs phenotype (Biffi *et al.*, 2019; Krishnamurty *et al.*, 2022). The upregulation of cell adhesion and ECM production are also fundamental for the myCAFs phenotype (Dominguez *et al.*, 2020). The secretion of TGFβ1 activates TGFBR2, followed by the activation of SMAD family proteins, leading to the upregulation of ECM proteins (Akhurst and Hata, 2012; Huang *et al.*, 2012; Verrecchia *et al.*, 2001). The accumulation of ECM induces matrix stiffness that activates mechano-transducing mechanisms, leading to myCAF activation (Discher *et al.*, 2005; Huang *et al.*, 2012). Additional axes, such as WNT and Hedgehog signaling, can potentiate TGFβ1-driven myCAFs activation (Avgustinova *et al.*, 2016; Mosa *et al.*, 2020; Rhim *et al.*, 2014; Steele *et al.*, 2021).

MyCAFs populations comprise a continuum of activation states, starting with CD105$^+$ stellate cells activation into early myCAFs that finally originate myCAFs (Dominguez *et al.*, 2020; Hutton *et al.*, 2021; Krishnamurty *et al.*, 2022). During the activation process, myofibroblasts exhibited a downregulation in basement membrane genes and increased the expression of fibrillar collagen genes (Dominguez *et al.*, 2020). Early myCAFs and myCAFs comprised up to 65% of all CAFs in the tumor (Dominguez *et al.*, 2020; Krishnamurty *et al.*, 2022). Stratification of patients revealed an impact of myCAFs content on overall survival, with patients harboring myCAF-high tumors presenting worse overall survival than those with low content in myCAFs (Hu *et al.*, 2022). However, myCAFs may confer an overall survival advantage after the treatment with neoadjuvant therapy (Heger *et al.*, 2022).

Therefore, the role of myCAFs in PDAC appears to be context-dependent, presenting both tumor-promoting and tumor-suppressor functions. Myofibroblasts' tumor-promoting role is based on tumor growth stimulation and immunosuppression (Hutton *et al.*, 2021; Krishnamurty *et al.*, 2022; Mosa *et al.*, 2020; Steele *et al.*, 2021). The abundance of WNT ligands involved in myCAFs phenotype activation can act in an autocrine manner, stimulating tumor cell growth (Arensman *et al.*, 2014; Mosa *et al.*, 2020; Steele *et al.*, 2021). Additionally, myCAFs-derived immunosuppressive TME blocks T cell function due to T cell exhaustion and increases checkpoint proteins in T regulatory cells surface (Chakravarthy *et al.*, 2018; Dominguez *et al.*, 2020; Kieffer *et al.*, 2020; Krishnamurty *et al.*, 2022). Patients resistant to immunotherapies showcase a high content of myCAFs, particularly in immune-excluded tumors (Chakravarthy *et al.*, 2018; Dominguez *et al.*, 2020; Kieffer *et al.*, 2020; Krishnamurty *et al.*, 2022). MyCAFs are a potential biomarker of ICB responsiveness and therapies regiments, where the combination of myCAFs depletion or transdifferentiation to iCAFs with ICB rendered PDAC to immunotherapy (Grauel *et al.*, 2020; Krishnamurty *et al.*, 2022). On the other hand, myCAFs may act as tumor-suppressing agents. Although the mechanisms by which this effect could be exerted are unclear, there is evidence that ECM may play a role (Chen *et al.*, 2021; Laklai *et al.*, 2016; Tian *et al.*, 2019). MyCAFs present an ECM remodeling transcriptional program upon activation by TGFβ1, being responsible for part of collagen I deposition in the TME (Chen *et al.*, 2021; Dominguez *et al.*, 2020; Friedman *et al.*, 2020; Kieffer *et al.*, 2020). Myofibroblasts-derived collagen I modulates cancer cells' secretome and the creation of an immunosuppressive environment, decreasing the content of CD206$^+$F4/80$^+$arginase-1$^+$ MDSCs, increasing T and B cells, and restraining tumor progression (Chen *et al.*, 2021).

Several clinical studies evaluating the potential to inhibit TGFb signaling are being undertaken as a proxy for myCAFs depletion or myCAF effect management. In these studies, small molecules or immunotherapy targeting TGFβ1 (ClinicalTrials.gov, NCT03834662*,* NCT04390763, NCT02937272, NCT04624217), CTGF (ClinicalTrials.gov, NCT03941093), and Angiotensins (ClinicalTrials.gov, NCT03563248, NCT05077800) combined with adjuvant therapy, and ICB are currently being investigated for different stages of PDAC, but the results have not yet been announced.

2 Aims

Immune populations have been extensively characterized in the tumor microenvironment, but little is known about CAFs. In recent years, efforts have been made to discover CAFs subpopulations, and although these studies unraveled the diversity of CAFs populations in PDAC, many questions about their impact on the TME composition, architecture, and interactions within the TME remain open.

The characterization of CAFs populations is complex and comes with additional challenges. CAFs are very sensitive to digestion-based protocols, resulting in an underrepresentation of the subpopulations in digestion-based single-cell studies. Furthermore, strategies to model these populations *in vitro* and *in vivo* are poorly developed.

This thesis offers a systematic analysis of the stromal TME in PDAC with the preservation of the tissue architecture. Murine PDAC was characterized in a context-specific manner to reveal context-specific cues that may lead to preferential CAFs activation, using a combination of multiplex immunofluorescence, transcriptomics, and organoid-CAFs co-culture. This characterization addressed questions not yet answered:

i) Do tumor cell driver mutations activate mechanisms that influence CAFs activation?

ii) Does the differentiation of the tumor affect stromal compartment activation and CAFs-tumor cell interplay? How do Kras iGD-induced mechanisms direct CAFs to a preferential activation state?

iii) Does Trp53 status influence CAFs activation profile? Which Trp53-related mechanisms may be involved in CAF activation?

In addition, this work also provides new insights into *in vitro* and *in vivo* models to study CAF subpopulation's role in PDAC. Stellate cells have been used as a primary *in vitro* model of CAF activation. Nonetheless, they become activated in traditional 2D culture after some days, blocking the differentiation into different CAFs subtypes. Indeed, CAFs subpopulations isolated from tumors lost their phenotype when cultured in 2D without the addition of external differentiation cues. Until today, there is no record of a locked CAF activation model that could reproduce the specific activation features. This thesis addresses this question and provides preliminary insights into CAF phenotype-locking strategies.

The analysis of CAF subpopulations' role *in vitro* only offers a glimpse of the full effect. Many studies have been attempting CAF genetic manipulation *in vivo* models. Although this allows a complete understanding of CAFs' effect in PDAC, specific targeting was hard to achieve. Experts view the DRS system as an elegant strategy for studying CAFs. The expression of the Cre recombinase using stromal promotors may allow for spatially confined manipulation of CAFs. Nevertheless, no record of systematic characterization of DRS models to study CAFs was found. Therefore, this thesis provides a systematic characterization of stromal cre-driver mouse lines to understand to which extent these populations can be targeted *in vivo*.

3 Materials and Methods

3.1 Materials

The materials used in this thesis comprised technical equipment, consumables, reagents, buffers and solutions, commercial kits, antibodies and dies, primers, cell and organoid lines, mice strains, and software described below.

3.1.1 Technical equipment

The technical equipment used in this thesis is described in Table 1.

Table 1 – List of the technical equipment used

Technical equipment	Company, headquarter location
Analytical balance ABJ-NM/ABS-N	Kern & Sohn GmbH, Balingen, DE
Aperio Versa 8 digital scanner	Leica Microsystems GmbH, Wetzlar, DE
Autoclave VX-150	Systec GmbH, Linden, DE
AxioCam MRc	Carl Zeiss AG, Oberkochen, DE
Bag sealer Folio FS 3602	Severin Elektrogeräte GmbH, Sundern, DE
Centrifuge 5415 D	Eppendorf AG, Hamburg, DE
Centrifuge 5427 R	Eppendorf AG, Hamburg, DE
Centrifuge Heraeus™ Multifuge™ X3 FR	Thermo Fisher Scientific Inc., Waltham, MA, USA
CO2 incubator HERAcell™ VIOS 250i	Heraeus Holding GmbH, Hanau, DE
Confocal microscope TCS SP8	Leica Microsystems GmbH, Wetzlar, DE
Cryogenic sample storage	Worthington Industries, Inc., Columbus, OH, USA
Cryostat CM3050 S	Leica Microsystems GmbH, Wetzlar, DE
Digital orbital shaker	Heathrow Scientific, Vernon Hills, IL, USA
Electrophoresis power supply Consort EV243	AlphaMetrix Biotech GmbH, Rödermark, DE
Electrophoresis power supply EPS 601	Amersham Biosciences Corp., Little Chalfont, GB
Electrophoresis power supply PowerPac 1000	Bio-Rad Laboratories Inc., Hercules, CA, USA
Electrophoresis power supply PowerPac™ HC	Bio-Rad Laboratories Inc., Hercules, CA, USA
Freezer	Liebherr, Bulle, DE
Fridge	Siemens AG, Munich, DE
Gel documentation system UVP UVsolo touch	Analytik Jena GmbH, Jena, DE
Gel Electrophoresis System Biometra Compact L/XL	Analytik Jena GmbH, Jena, DE
Heated paraffin embedding module HistoCore Arcadia H	Leica Microsystems GmbH, Wetzlar, DE
HERA freeze™ HFU T Series	Thermo Fisher Scientific Inc., Waltham, MA, USA
Homogenizer SilentCrusher M with tool 6F	Heidolph Instruments GmbH & Co. KG, Schwabach, DE
Incubator 206	MELAG oHG, Berlin, DE
Incubator U26	Memmert, GmbH + Co.KG, Büchenbach, DE
Laminar flow	ARGE Labor- und Objekteinrichtungen GmbH, Wathlingen, DE
Leica M205 FCA stereocospe	Leica Microsystems GmbH, Wetzlar, DE
Magnetic stirrer, Ikamag® RCT	IKA® Werke GmbH & Co. KG, Staufen, DE

Table 1 – List of the technical equipment used (continued)

Technical equipment	Company, headquarter location
Microcentrifuge LLG-uniCFUGE 2	Faust Laborbedarf AG, Schaffhausen, CH
Microscope Axio Vert.A1	Carl Zeiss AG, Oberkochen, DE
Microscope DM IL LED	Leica Microsystems GmbH, Wetzlar, DE
Microscope ICC50 W	Leica Microsystems GmbH, Wetzlar, DE
Microtome Microm HM355S	Thermo Fisher Scientific Inc., Waltham, MA, USA
Microwave MAX	Whirlpool, Benton Harbor, MI, USA
Mini-PROTEAN® Tetra Cell	Bio-Rad Laboratories Inc., Hercules, CA, USA
Mixer RT-3D	Fröbel Labortechnik GmbH, Lindau, DE
Multimode microplate reader CLARIOstar	BMG Labtech, Ortenberg, DE
NanoPhotometer® N60	Implen GmbH, Munich, DE
Odyssey® Fc imaging system	Li-Cor Biosciences, Lincoln, NE, USA
Orbital shaker Rotamax 120	Heidolph, Instruments GmbH & Co. KG, Schwabach, DE
Paraffin tissue floating bath SB80	Microm, Walldorf, DE
pH meter pH 50+ DHS	XS Instruments, Carpi, IT
Precision balance PCB	Kern & Sohn GmbH, Balingen, DE
Roller mixer RM5	Ingenierbüro CAT M. Zipperer GmbH, Ballrechten Dottingen, DE
Stemi SV 11 stereomicroscope	Carl Zeiss AG, Oberkochen, DE
Thermal Cycler Biometra TOne	Analytik Jena GmbH, Jena, DE
Thermomixer comfort	Eppendorf AG, Hamburg, DE
Tissue processor ASP300S	Leica Microsystems GmbH, Wetzlar, DE
Vertical laminar flow cabinet ENVAIReco® Safe Comfort	ENVAIR Ltd., Haslingden, GB
Vortex-Genie™ 2	Scientific Industries Inc., Bohemia, NY, USA
Water bath 1083	GFL Gesellschaft für Labortechnik mbH, Burgwedel, DE

3.1.2 Consumables

The consumables used in this thesis are described in Table 2.

Table 2 – List of consumables used

Consumables	Company, headquarter location
µ-Slide 8 Well, ibiTreat	Ibidi GmbH, Gräfelfing, DE
25 mL pipetting reservoir	Argos Technologies, Vernon Hills, IL, USA
25 mm syringe filter 0.2 µm	Sigma-Aldrich, St. Louis, MO, USA
Aluminum foil	Carl Roth GmbH & Co. KG, Karlsruhe, DE
Black nail polish	dm-drogerie markt GmbH + Co. KG, Karlsruhe, DE
Blood glucose test strips	Abbott GmbH & Co. KG, Ludwigshafen, DE
Cell scrapers	Sarstedt Inc, Nümbrecht, DE
Combitips® advanced 0.2, 1 and 2.5 mL	Eppendorf AG, Hamburg, DE
Conical tubes 15 and 50 mL	Greiner Bio-One, Kremsmünster, AT
Cotton-tipped applicators	Lohmann & Rauscher GmbH & Co. KG, Neuwied, DE
Cover slips 18 x 18 mm	Paul Marienfield GmbH & Co. KG, Lauda Köningshofen, DE
Cover slips 24 x 50 mm	Thermo Fisher Scientific Inc., Waltham, MA, USA
CryoPure tubes	Sarstedt AG & Co., Nümbrecht, DE
Dewar carrying flask, type B	KGW-Isotherm, Karlsruhe, DE
Disposable scalpels	Feather Safety Razor Co. Ltd., Osaka, JP
Dry ice	Linde plc, Dublin, IE

Table 2 – List of consumables used (continued)

Consumables	Company, headquarter location
Falcon® 6-, 24- and 96-well clear flat bottom cell culture microplates	Corning Inc., Corning, NY, USA
Glass staining dish and 20-slide unit	VWR International Ltd., Radnor, PA, USA
Hand Tally Counter	neoLab Migge GmbH, Heidelberg, DE
Ice block COOL PACK	Coolike Regnery GmbH, Bensheim, DE
ImmEdge™ hydrophobic barrier pen	Vector Laboratories Inc., Burlingame, CA, USA
Immersion oil Type F	Leica Microsystems GmbH, Wetzlar, DE
Lab glassware	Schott AG, Mainz, DE
Microscope slides Superfrost®	Thermo Fisher Scientific Inc., Waltham, MA, USA
Microtome blades S35 and C35	Feather Safety Razor Co. Ltd., Osaka, JP
Multilpy®-µStrip PCR reaction tubes	Sarstedt AG & Co., Nümbrecht, DE
Multipette® stream	Eppendorf AG, Hamburg, DE
Neubauer hemocytometer 0.100 mm Depth	Assistent, Sondheim vor der Rhön, DE
Nitrocellulose blotting membrane Amersham™ Protran™ 0.2 µm NC	GE Healthcare, Chicago, IL, USA
Paper role	Mobiloclean Handelsgruppe GmbH & Co. KG, Munich, DE
Parafilm™ M Laboratory Wrapping Film	Bemis Company Inc., Neenah, WI, USA
Pasteur pipettes	Hirschmann Laborgeräte GmbH & Co. KG, Eberstadt, DE
Petri dishes 10 and 15 cm	Sarstedt AG & Co., Nümbrecht, DE
Pipette tips 10, 100, 200 and 1000 µL	Sarstedt AG & Co., Nümbrecht, DE
Pipettes Reference®, Research®	Eppendorf AG, Hamburg, DE
Plastic ruler 30 cm	Möbius & Ruppert GmbH & Co. KG, Erlangen, DE
Plastic staining dish	Carl Roth GmbH & Co. KG, Karlsruhe, DE
Precision wipes	Kimberly-Clark Worldwide Inc., Irving, TX, USA
Reaction tubes 0.5, 1.5, and 2 mL	Sarstedt AG & Co., Nümbrecht, DE
Rotilabo®-folded filters type 113P	Carl Roth GmbH & Co. KG, Karlsruhe, DE
Rotilabo®-stirring magnets set I	Carl Roth GmbH & Co. KG, Karlsruhe, DE
Safe-lock tubes BioPur® 1.5 and 2 mL	Eppendorf AG, Hamburg, DE
Serological pipettes 5, 10, 25, and 50 mL	Greiner Bio-One, Kremsmünster, AT
Shrink wrap film	VEMATEC GmbH, Berlin, DE
Single use syringes Omnifix® 1 mL and 30 mL	B. Braun Melsungen AG, Melsungen, DE
Single-use needles Sterican® 20G and 25G	B. Braun Melsungen AG, Melsungen, DE
Slide Staining and Storage System	VWR International Ltd., Radnor, PA, USA
Slide storage box 25 and 100 slides	Sigma-Aldrich, St. Louis, MO, USA
Stripettor™ Ultra Pipet controller	Corning Inc., Corning, NY, USA
Surgical instruments	Thermo Fisher Scientific Inc., Waltham, MA, USA
Tissue culture flasks 25, 75, and 175 cm2	Greiner Bio-One, Kremsmünster, AT
Tissue embedding cassettes Q Path® MacroStar VI and VIII	VWR International Ltd., Radnor, PA, USA
Tissue paper strong 100V	Lucart Professional, Villa Basilica, IT
Tubes 15 mL and 50 mL	Sarstedt AG & Co., Nümbrecht, DE
Vertical staining jar with glass lid	VWR International Ltd., Radnor, PA, USA
Whatman™ cellulose Western blotting paper	GE Healthcare, Chicago, IL, USA

3.1.3 Reagents

The reagents used in this thesis are described in Table 3.

Table 3 – List of reagents used

Reagents	Company, headquarter location
1,4-Dithiothreitol (DTT)	Carl Roth GmbH & Co. KG, Karlsruhe, DE
100%, 96%, 80%, and 70% Ethanol (EtOH)	Otto Fischar GmbH & Co. KG, Saarbrücken, DE
2-Mercaptoethanol, 98%	Sigma-Aldrich, St. Louis, MO, USA
2-Propanol (isopropanol)	Carl Roth GmbH & Co. KG, Karlsruhe, DE
3,3,5-Triiodo-L-thyronine, powder	Sigma-Aldrich, St. Louis, MO, USA
4-Hydroxytamoxifen (4-OHT)	Sigma-Aldrich, St. Louis, MO, USA
Acetic acid glacial	Carl Roth GmbH & Co. KG, Karlsruhe, DE
Aceton	Otto Fischar GmbH & Co. KG, Saarbrücken, DE
Acrylamide Rotiphorese® gel 30	Carl Roth GmbH & Co. KG, Karlsruhe, DE
Advanced Dulbecco's Modified Eagle Medium/Ham's F-12	Gibco, Grand Island, NY, USA
Agarose, powder	Sigma-Aldrich, St. Louis, MO, USA
Ammonium persulfate, powder	Sigma-Aldrich, St. Louis, MO, USA
Ammonium sulfate, powder	Sigma-Aldrich, St. Louis, MO, USA
Antigen unmasking solution, citric acid based	Vector Laboratories Inc., Burlingame, CA, USA
Aqua sterile water	B. Braun Melsungen AG, Melsungen, DE
Avidin/Biotin blocking kit	Vector Laboratories Inc., Burlingame, CA, USA
Bovine Pituitary extract, powder	Corning, New York, NY, USA
Bovine serum albumin (BSA) fraction V	SERVA Electrophoresis GmbH, Heidelberg, DE
Bradford reagent	SERVA Electrophoresis GmbH, Heidelberg, DE
Bromophenol blue	Sigma-Aldrich, St. Louis, MO, USA
Calcium chloride dihydrate, powder	Sigma-Aldrich, St. Louis, MO, USA
Cell recovery solution	Corning, New York, NY, USA
Cholera toxin from *Vibrio cholerae*, powder	Sigma-Aldrich, St. Louis, MO, USA
Collagenase P, powder	Roche Deutschland Holding GmbH, Grenzach Wyhlen, DE
Collagenase type 2, powder	Worthington Biochemical Corp., Lakewood, NJ, USA
Collagenase type I, powder	Worthington Biochemical Corp., Lakewood, NJ, USA
Complete EDTA-free protease inhibitor cocktail tablets	Roche Deutschland Holding GmbH, Grenzach Wyhlen, DE
Cresol red	AppliChem GmbH, Darmstadt, DE
D(+)-saccharose	Carl Roth GmbH & Co. KG, Karlsruhe, DE
Dexamethasone, powder	Sigma-Aldrich, St. Louis, MO, USA
D-Glucose, powder	Gibco, Grand Island, NY, USA
Dimethyl sulfoxide (DMSO)	Carl Roth GmbH & Co. KG, Karlsruhe, DE
Disodium hydrogen phosphite, powder	Carl Roth GmbH & Co. KG, Karlsruhe, DE
DMSO	AppliChem GmbH, Darmstadt, DE
dNTP mix, 10 mM each	Fermentas GmbH, St. Leon-Rot, DE
Dodecylsulfate Na-salt in pellets (SDS)	SERVA Electrophoresis GmbH, Heidelberg, DE
Donkey, Goat and Rat, Rabbit serums	LINARIS Biologische Produkte GmbH, Dossenheim, DE
Dulbecco's phosphate-buffered saline (PBS)	Sigma-Aldrich, St. Louis, MO, USA
Dulbecco′s Modified Eagle′s Medium/Nutrient Mixture F-12 Ham	Sigma-Aldrich, St. Louis, MO, USA
Eosin 2% w/v	HiMedia Laboratories Pvt. Ltd., Mumbai, IN
Ethanol absolute ≥ 99.8%	Sigma-Aldrich, St. Louis, MO, USA
Ethidium bromide	Sigma-Aldrich, St. Louis, MO, USA
Ethylenediaminetetraacetic acid (EDTA)	Sigma-Aldrich, St. Louis, MO, USA
Fetal bovine serum (FBS) Superior	Sigma-Aldrich, St. Louis, MO, USA
Forene® isoflurane	Abbott GmbH & Co. KG, Ludwigshafen, DE
Frozen section medium Richard-Allan Scientific NEG-50	Thermo Fisher Scientific Inc., Waltham, MA, USA
GeneRuler™ 100 bp DNA ladder	Fermentas GmbH, St. Leon-Rot, DE
Glycerol	Merck, Darmstadt, DE

Table 3 – List of reagents used (continued)

Reagents	Company, headquarter location
Glycine, powder	Sigma-Aldrich, St. Louis, MO, USA
Hematoxylin solution Gill no. 3	Sigma-Aldrich, St. Louis, MO, USA
HEPES, powder	Carl Roth GmbH & Co. KG, Karlsruhe, DE
High glucose Dulbecco's Modified Eagle's Medium	Sigma-Aldrich, St. Louis, MO, USA
Histodenz, powder	Sigma-Aldrich, St. Louis, MO, USA
Hydrochloric acid (HCl), 37%	Sigma-Aldrich, St. Louis, MO, USA
Hydrogen peroxide (H2O2) 30%	Merck, Darmstadt, DE
ITS+ Premix Universal Culture Supplement	Corning, New York, NY, USA
Luminol	Sigma-Aldrich, St. Louis, MO, USA
Magnesium chloride hexahydrate, powder	Carl Roth GmbH & Co. KG, Karlsruhe, DE
Magnesium chloride, powder	Carl Roth GmbH & Co. KG, Karlsruhe, DE
Magnesium sulfate heptahydrate, powder	Carl Roth GmbH & Co. KG, Karlsruhe, DE
Matrigel® Basement Membrane Matrix, Phenol Red-Free, *LDEV-Free	Corning, New York, NY, USA
Methanol	Carl Roth GmbH & Co. KG, Karlsruhe, DE
Mounting medium Cytoseal™ XYL	Thermo Fisher Scientific Inc., Waltham, MA, USA
Multiscribe Reverse Transcriptase	Thermo Fisher Scientific Inc., Waltham, MA, USA
N, N, N', N'-Tetramethylethylenediamine	Sigma-Aldrich, St. Louis, MO, USA
N, N-dimethylformamide	Sigma-Aldrich, St. Louis, MO, USA
Nicotinamid, powder	Sigma-Aldrich, St. Louis, MO, USA
Nonidet P40	Roche Deutschland Holding GmbG, Grenzach Wyhlen, DE
Nu-Serum™ IV Growth Medium Supplement	Corning, New York, NY, USA
PageRuler™ Plus prestained protein ladder	Thermo Fisher Scientific Inc., Waltham, MA, USA
Paraformaldehyde, powder	Sigma-Aldrich, St. Louis, MO, USA
PBS powder	Sigma-Aldrich, St. Louis, MO, USA
p-Coumaric acid	Sigma-Aldrich, St. Louis, MO, USA
Peanut oil	Sigma-Aldrich, St. Louis, MO, USA
Penicillin-Streptomycin	Sigma-Aldrich, St. Louis, MO, USA
Phosphatase inhibitor mix I, powder	SERVA Electrophoresis GmbH, Heidelberg, DE
Picric acid, powder	Sigma-Aldrich, St. Louis, MO, USA
Potassium chloride, powder	Carl Roth GmbH & Co. KG, Karlsruhe, DE
Potassium dihydrogen phosphate, powder	Carl Roth GmbH & Co. KG, Karlsruhe, DE
Powdered milk blotting grade, powder	Carl Roth GmbH & Co. KG, Karlsruhe, DE
PowerUp™ SYBR™ Green Master Mix	Thermo Fisher Scientific Inc., Waltham, MA, USA
Proteinase K	AppliChem GmbH, Darmstadt, DE
Random hexamers	Roche Deutschland Holding GmbG, Grenzach Wyhlen, DE
Reaction buffer S	Peqlab Biotechnologie GmbH, Erlangen, DE
Recombinant Murine EGF, powder	Peprotech, Rocky Hill, NJ, USA
Recombinant Murine IL1α, powder	Peprotech, Rocky Hill, NJ, USA
Reverse Transcription buffer 10x	Thermo Fisher Scientific Inc., Waltham, MA, USA
RNAse inhibitor	Thermo Fisher Scientific Inc., Waltham, MA, USA
RNase-dree DNase set	Qiagen GmbH, Hilden, DE
ROTI®Histofix 4%	Carl Roth GmbH & Co. KG, Karlsruhe, DE
ROTI®Histol	Carl Roth GmbH & Co. KG, Karlsruhe, DE
Sodium bicarbonate, powder	Carl Roth GmbH & Co. KG, Karlsruhe, DE
Sodium chloride, powder	Merck, Darmstadt, DE
Sodium hydroxide 1M solution (NaOH)	AppliChem GmbH, Darmstadt, DE
Sucrose, powder	Sigma-Aldrich, St. Louis, MO, USA
Tamoxifen, powder	Sigma-Aldrich, St. Louis, MO, USA
Taq DNA polymerase	Qiagen GmbH, Hilden, DE
Tris hydrochloride, powder	J.T.Baker® Chemicals, Phillipsburg, NJ, USA
TRIS Pufferan®, powder	Carl Roth GmbH & Co. KG, Karlsruhe, DE

Table 3 – List of reagents used (continued)

Reagents	Company, headquarter location
Tris-Acetate-EDTA buffer 50x	Klinikum rechts der Isar der TUM Krankenhausapotheke, Munich, DE
Triton™ X-100	Sigma-Aldrich, St. Louis, MO, USA
Trypan blue solution	Sigma-Aldrich, St. Louis, MO, USA
TrypLE™ Express Enzyme	Thermo Fisher Scientific Inc., Waltham, MA, USA
TrypZean® solution 1×	Sigma-Aldrich, St. Louis, MO, USA
Tween® 20	Sigma-Aldrich, St. Louis, MO, USA
Vectashield® mounting medium for fluorescence	Vector Laboratories Inc., Burlingame, CA, USA
Y-27632 -dihydrochlorid, powder	Sigma-Aldrich, St. Louis, MO, USA
β-Aminopropionitrile monofumarate	Sigma-Aldrich, St. Louis, MO, USA

3.1.4 Buffers, solutions, and culture media

The buffers, solutions, and culture media used in this thesis are described in Table 4.

Table 4 – List of the buffer and solution used and their composition

Buffer/ Solution	Composition
Antigen retrieval Tris-EDTA pH9	10 mM Tris-base 1 mM EDTA Diluted in distilled water
Cell culture freezing medium	20% FCS 10% DMSO 70% High-glucose DMEM
Cell culture medium	10% FCS 1% Penicillin-Streptomycin In High-glucose DMEM
Collagenase I	200U/mL Collagenase I Diluted in PBS
Collagenase II	2 mg/mL collagenase II Diluted in culture medium
Collagenase P	0.75 U/mL Collagenase P Diluted with GBSS
GBSS pH 7.6	1.5 mM Calcium chloride dihydrate 5 mM Potassium chloride 0.22 mM Potassium Phosphate Monobasic 1.0 mM Magnesium Chloride Hexahydrate 0.3 mM Magnesium Sulfate Heptahydrate 137 mM Sodium chloride 2.7 mM Sodium bicarbonate 0.85 mM Sodium Phosphate Dibasic 5.55 mM D-glucose Diluted ddH$_2$O pH Adjustment with HCl
GBSS without NaCl pH 7.6	1.5 mM Calcium chloride dihydrate 5 mM Potassium chloride 0.22 mM Potassium Phosphate Monobasic 1.0 mM Magnesium Chloride Hexahydrate 0.3 mM Magnesium Sulfate Heptahydrate 2.7 mM Sodium bicarbonate 0.85 mM Sodium Phosphate Dibasic 5.55 mM D-glucose Diluted ddH$_2$O

Table 4 – List of the buffer and solution used and their composition (continued)

Buffer/ Solution	Composition
Gitschier’s buffer	67 mM Tris, pH 8.8 16.6 mM Ammonium sulfate 6.7 mM Magnesium chloride Diluted in ddH_2O
Histodenz	28.75% of Histodenz Diluted in GBSS without NaCl
IP buffer, pH 7.9	50 mM HEPES 150 mM NaCl 1 mM EDTA 0.5% Nonidet P40 10% Glycerol Diluted in ddH_2O pH adjustment with NaOH 4% Phosphatase inhibitor 1% Protease inhibitor
Laemmli, pH 6.8	2% SDS 10% Glycerol 45.6 mM Tris hydrochloride 0.15 mM Bromophenol blue 1% 2-Mercaptoethanol Diluted in ddH_2O
Organoid culture medium	200 mg/mL D-Glucose 0.5% ITS + premix 5 nM 3,3,5-Triiodo-L-thyronine 1 µM Dexamethasone 100 ng/mL Cholera toxin 1% Penicillin-Streptomycin 5% Nu-Serum IV 20 ng/mL EGF 25 µg/mL Bovine Pituitary extract 10 mM Nicotinamide Advanced DMEM/F12 10 µM Y27632
Organoid freezing medium	20% FCS 10% DMSO 70% Advanced DMEM/F12
Pan-fibroblasts culture medium	10% FCS 1% Penicillin-Streptomycin In DMEM/F12
Pan-fibroblasts freezing medium	10% DMSO 90% FCS
PBS-T	0.1% Tween® 20 Diluted in PBS
Running buffer	25 mM Tris 192 mM Glycine 0.1% SDS Diluted in ddH_2O
Resolving gel buffer, pH 8.8	1.5 M Tris-Base Diluted in ddH_2O pH adjustment with HCl
Soriano lysis buffer	0.5% Triton™ X-100 10% 10x Gitschier’s buffer 1% 2-Mercaptoethanol Diluted in ddH_2O 400 µg/mL Proteinase K

Table 4 – List of the buffer and solution used and their composition (continued)

Buffer/ Solution	Composition
Stacking gel buffer, pH 6.8	0.5 M Tris-Base Diluted in ddH_2O pH adjustment with HCl
SucRot solution	1.5 mg/mL Cresol red 100 mM Tris (pH 9.0) 30% D-saccharose
Transfer buffer	25 mM Tris 192 mM Glycine 2% Methanol Diluted in ddH_2O
Resolving gel	x% polyacrylamide 0.1% SDS 0.05% APS 0.03% TEMED 25% resolving gel buffer
Stacking gel	4% polyacrylamide 0.1% SDS 0.05% APS 0.2% TEMED 25% stacking gel buffer

3.1.5 Kits

The commercial kits used in this thesis are described in Table 5.

Table 5 – Commercial kits used

Kit	Company, headquarter location
3,3'-Diaminobenzidine (DAB) peroxidase substrate kit	Vector Laboratories Inc., Burlingame, CA, USA
Avidin/ biotin blocking kit	Vector Laboratories Inc., Burlingame, CA, USA
QIAshredder	Qiagen GmbH, Hilden, DE
RNeasy® Mini kit	Qiagen GmbH, Hilden, DE
Vectastain® elite ABC kit	Vector Laboratories Inc., Burlingame, CA, USA

3.1.6 Antibodies and Dies

The primary and secondary antibodies and dies used in this thesis are described in Table 6.

Table 6 – Antibodies and dies used

Antibody/ Die	Category	RRID	Company, headquarter location
CD45	MCA1031G	AB_321730	Bio-Rad Laboratories Inc., Hercules, CA, USA
KRT18	SAB4501665	AB_10746153	Sigma-Aldrich, St. Louis, MO, USA
COL1A1	72026	AB_2904565	Cell Signaling Technology Inc., Danvers, MA, USA
Collagen IV	ab6586	AB_305584	Abcam, Cambridge, UK
DAPI	40011	NA	Biotium Inc., Hayward, CA, USA
Donkey anti-goat 594	A-11058	AB_2534105	Thermo Fisher Scientific Inc., Waltham, MA, USA
Donkey anti-rabbit 405	A-48258	AB_2890547	Thermo Fisher Scientific Inc., Waltham, MA, USA
Donkey anti-rabbit 680	A-32802	AB_2762836	Thermo Fisher Scientific Inc., Waltham, MA, USA

Table 6 – Antibodies and dies used (continued)

Antibody/ Die	Category	RRID	Company, headquarter location
Donkey anti-rat 488	A-21208	AB_2535794	Thermo Fisher Scientific Inc., Waltham, MA, USA
Eosin	S007	NA	HiMedia Laboratories Pvt. Ltd., Mumbai, IN
EpCAM	PA5-19832	AB_10984102	Thermo Fisher Scientific Inc., Waltham, MA, USA
FABP4	AF1443	AB_2102444	R&D Systems, Minneapolis, MN, USA
Fibronectin	ab2413	AB_2262874	Abcam, Cambridge, UK
GAPDH	2118	AB_561053	Cell Signaling Technology Inc., Danvers, MA, USA
Goat anti-arm. hamster 647	A-21451	AB_1500615	Thermo Fisher Scientific Inc., Waltham, MA, USA
Goat anti-rabbit Cy3	111-166-045	AB_2338008	Dianova Gesellschaft für biochemische, immunologische und mikrobiologische Diagnostik mbH, Hamburg, DE
Goat anti-rabbit DyLight800	SA535571	AB_2556775	Thermo Fisher Scientific Inc., Waltham, MA, USA
Goat anti-rat AF555	A-21434	AB_2535855	Thermo Fisher Scientific Inc., Waltham, MA, USA
Hematoxylin	GHS332	NA	Sigma-Aldrich, St. Louis, MO, USA
IL6	AF-406-NA	AB_354478	R&D Systems, Minneapolis, MN, USA
Lysyl Oxidase	MA5-32817	AB_2810093	Thermo Fisher Scientific Inc., Waltham, MA, USA
MHCII	107605	AB_313320	Biolegend, San Diego, CA, USA
MYH11	HPA015310	AB_1854261	Sigma-Aldrich, St. Louis, MO, USA
Nestin	AF2736	AB_416673	R&D Systems, Minneapolis, MN, USA
PDGFRα	14-1401-82	AB_467491	Thermo Fisher Scientific Inc., Waltham, MA, USA
PDPN	14-5381-82	AB_1210505	Thermo Fisher Scientific Inc., Waltham, MA, USA
Phospho-SMAD2 S645/467	3108	AB_490941	Cell Signaling Technology Inc., Danvers, MA, USA
S100A4	HPA007973	AB_1079858	Sigma-Aldrich, St. Louis, MO, USA
Sirius Red F3B	365548	NA	Sigma-Aldrich, St. Louis, MO, USA
SMAD2/3	8685	AB_10889933	Cell Signaling Technology Inc., Danvers, MA, USA
SMAD4	46535	AB_2736998	Cell Signaling Technology Inc., Danvers, MA, USA
Vimentin	5741	AB_10695459	Cell Signaling Technology Inc., Danvers, MA, USA
αSMA	ab5694	AB_2223021	Abcam, Cambridge, UK
Biotinylated anti-rabbit	BA-1000	AB_2313606	Vector Laboratories Inc., Burlingame, CA, USA

3.1.7 Primers

The primers listed in Table 7 were synthesized by Eurofins Genomics GmbH and diluted in di-distilled water to a concentration of 10 µM.

Table 7 – Primers used in this thesis

Primer name	Sequence (5'-3')
Acta2 fw	ACTCTCTTCCAGCCATCTTTCA
Acta2 rv	GCTCCCCTTGAGCTGTGTAATAG
CAG-sc-LP	GTACTTGGCATATGATACACTTGATGTAC

Table 7 – Primers used in this thesis (continued)

Primer name	Sequence (5'-3')
Col1a1 fw	GAGAGGTGAACAAGGTCCCG
Col1a1 rv	AAACCTCTCTCGCCTCTTGC
Col6a1B-UP3	ACACACCGTAGCAACAGGAAGTC
Cre-mB-LP2	TAGCTGGCCCAAATGTTGCT
Cre-neu-LP	CAGGGTGTTATAAGCAATCCC
Cre-neu-UP	CCTGGAAAATGCTTCTGTCCG
Ctgf fw	CCCAGACCCAACTATGATGC
Ctgf rv	GATGCACTTTTTGCCCTTCTTA
Flpopt-scLP	CGTTGTAAGGGATGATGGTGAACT
Gabra-LP	CAATGGTAGGCTCACTCTGGGAGATGATA
Gabra-UP	AACACACACTGGAGGACTGGCTAGG
Gapdh fw	CCTGCCAAGTATGATGAC
Gapdh rv	GGAGTTGCTGTTGAAGTC
Il6 fw	GACAAAGCCAGAGTCCTTCAGAGAG
Il6 rv	CTAGGTTTGCCGAGTAGATCTC
KrasG12Dmut-UP	CCATGGCTTGAGTAAGTCTGC
Kras-URP-LP1	AGCTAATGGCTCTCAAAGGAATGTA
Kras-WT-UP1	CACCAGCTTCGGCTTCCTATT
mTgfb1_LP	GCTGATCCCGTTGATTTCC
Mycoplasma fw1	CGCCTGAGTAGTACGTTCGC
Mycoplasma fw2	CGCCTGAGTAGTACGTACGC
Mycoplasma fw3	TGCCTGGGTAGTACATTCGC
Mycoplasma fw4	TGCCTGAGTAGTACATTCGC
Mycoplasma fw5	CGCCTGAGTAGTATGCTCGC
Mycoplasma fw6	CACCTGAGTAGTATGCTCGC
Mycoplasma fw7	CGCCTGGGTAGTACATTCGC
Mycoplasma rv1	GCGGTGTGTACAAGACCCGA
Mycoplasma rv2	GCGGTGTGTACAAAACCCGA
Mycoplasma rv3	GCGGTGTGTACAAACCCCGA
Nestin-Cre-UP2	CACCCGGATGAAGCAGGAAC
oIMR1900	ACTCCTTCATAAAGCCCT
oIMR1901	ATCACTCGTTGCATCGACCG
p48-Cre-GT-LP-URP	CCTCGAAGGCGTCGTTGATGGACTGCA
p48-Cre-GT-mut-UP-neu	GCCACCAGCCAGCTATCAA
p48-Cre-GT-wt-UP	CCACGGATCACTCACAAAGCGT
p53 berns LP-F	GCACCTTTGATCCCAGCACATA
p53 berns Up-E	CACAAAAACAGGTTAAACCCAGC
p53-frt2	CTTTCTAACAGCAAAGGCAAGC
p53-ftr1	CAAGAGAACTGTGCCTAAGAG
Pdgfra fw	CTTTCTGGTCCTCAGCTGTCTC
Pdgfra rv	GGGTCGTCTTCTTCAGACATGG
PDGFRa-CTM-LP	ATGTTTAGCTGGCCCAAATG
PDGFRa-CTM-UP	TCAGCCTTAAGCTGGGACAT
PdgfraEGFP_MT-rv	ACGAAGTTATTAGGTCCCTCGAC
PdgfraEGFP_WT-fw	CCCTTGTGGTCATGCCAAAC
PdgfraEGFP_WT-rv	GCTTTTGCCTCCATTACACTGG
pdx5ut-scUP	AGAGAGAAAATTGAAACAAGTGCAGGT
PdxKON-LP1	CACGTGGTTTACCCTGGAGC
Pdx-Prom-UP2	GCTCATTGGGAGCGGTTTTG
pGL3-pA-pause UP	TGAATAGTTAATTGGAGCGGCCGCAATA
pGL3-pA-pause4645-UP	GATCAGTTATCTAGAGAAATGTTCTGGCACCTGCA
PI3K-genotyp-RevPr	AAATAGCCGCAGGTCACAAAGTCTCCG
R26-td-E-mutLP	TCAATGGGCGGGGGTCGTT
R26-Tva-GT-UP	AAAGTCGCTCTGAGTTGTTAT
R26-Tva-GT-WT-LP	GGAGCGGGAGAAATGGATATG
R26-Tva-SA-mut	GCGAAGAGTTTGTCCTCAACC

Table 7 – Primers used in this thesis (continued)

Primer name	Sequence (5’-3’)
Tgfb1 fw	CGAAGCGGACTACTATGCTAAA
Tgfb1 rv	GGGTCGTCTTCTTCAGACATGG
Trp53R172H-mut-UP4	GCCACCATGGCTTGAGTAA
Trp53R172H-URP-LP	CTTGGAGACATAGCCACACTG
Trp53R172H-WT-UP2	AGCCTTAGACATAACACACGAACT
V-Cre-LP2	ACATCTTCAGGTTCTGCGGG
KrasG12D_human_fw	AAAGGTACTGGTGGAGTATTTGATAGTG
KrasG12D_human_rv	GGTCCTGCACCAGTAATATGCA

3.1.8 Cell lines and organoid lines

The organoid lines and the cell lines used in this thesis are described in Table 8.

Table 8 – Organoid and cell lines used

Cell line/organoid line	Source
TRM-695 PPT organoid	Prof.Dr. med Dieter Saur laboratory
TRM-676 PPT organoid	Prof.Dr. med Dieter Saur laboratory
20738 PPT organoid	Prof.Dr. med Dieter Saur laboratory
P4989 PPT organoid	Prof.Dr. med Dieter Saur laboratory
CR16031 PPT organoid	Prof.Dr. med Dieter Saur laboratory
63577 PPT organoid	Prof.Dr. med Dieter Saur laboratory
V5128 PPT organoid	Prof.Dr. med Dieter Saur laboratory
PdkCPB11171 PPT organoid	Prof.Dr. med Dieter Saur laboratory
V5130 PPT organoid	Prof.Dr. med Dieter Saur laboratory
5671 PPT cell line	Prof.Dr. med Dieter Saur laboratory
16990 PPT cell line	Prof.Dr. med Dieter Saur laboratory
53578 PPT cell line	Prof.Dr. med Dieter Saur laboratory
5748 PPT cell line	Prof.Dr. med Dieter Saur laboratory
8182 PPT cell line	Prof.Dr. med Dieter Saur laboratory
8349 PPT cell line	Prof.Dr. med Dieter Saur laboratory
8028 PPT cell line	Prof.Dr. med Dieter Saur laboratory
S134 PPT cell line	Prof.Dr. med Dieter Saur laboratory
S559 PPT cell line	Prof.Dr. med Dieter Saur laboratory
8570 PPT cell line	Prof.Dr. med Dieter Saur laboratory
5123 PPT cell line	Prof.Dr. med Dieter Saur laboratory
16992 PPT cell line	Prof.Dr. med Dieter Saur laboratory
9091 PPT cell line	Prof.Dr. med Dieter Saur laboratory
8248 PPT cell line	Prof.Dr. med Dieter Saur laboratory
5320 PPT cell line	Prof.Dr. med Dieter Saur laboratory
8513 PPT cell line	Prof.Dr. med Dieter Saur laboratory
3202 PPT cell line	Prof.Dr. med Dieter Saur laboratory

3.1.9 Mice strains

The animal models used in this thesis resulted from the breeding combinations of mice strains described in Table 9.

Table 9 – Mouse strain used

Mouse strain	Lab nomenclature	MGI	RRID
Gt(ROSA)26Sor$^{tm2(Pik3ca*)Dsa}$	LSL-Pi3kcaH1047R	MGI:5510667	NA
Gt(ROSA)26Sor$^{tm3(CAG-Cre/ERT2)Dsa/J}$	R26-CAG-CreER	MGI:5616874	NA
Gt(ROSA)26Sor$^{tm3(TGFb1)/J}$	LSL-Tgfb1	NA	NA

Table 9 – Mouse strain used (continued)

Mouse strain	Lab nomenclature	MGI	RRID
Gt(ROSA)26Sor$^{tm4(ACTB\text{-}tdTomato,\text{-}EGFP)Luo}$	R26-mTmG	MGI:3716464	IMSR_APB:7404
Kras^{tm1Dsa}	FSF-Kras	MGI:5616879	NA
Kras^{tm4Tyj}	LSL-KrasG12D	MGI:2429948	IMSR_JAX:008179
Pdgfra$^{tm11(EGFP)Sor}$	PDGFRa-H2b-EGFP	MGI:2663656	IMSR_JAX:007669
Ptf1a$^{tm1(cre)Hnak}$	p48-Cre	MGI:3701996	IMSR_JAX:023329
Tagln$^{tm2(cre)Yec}$	Sm22-Cre	MGI:3706313	IMSR_JAX:006878
Tg(Col6a1-cre)1Gkl	Col6a1-Cre	MGI:3775430	IMSR_EM:05102
Tg(Cspg4-cre/Esr1*)BAkik	Cspg4-CreER	MGI:4819178	IMSR_JAX:008538
Tg(Gfap-cre)73.12Mvs	Gfap1-Cre	MGI:3522215	IMSR_JAX:012886
Tg(Gfap-cre)77.6Mvs	Gfap2-Cre	MGI:3838840	IMSR_JAX:024098
Tg(GFAP-cre/ERT2)505Fmv	Gfap-CreER	MGI:3774167	IMSR_JAX:012849
Tg(Myh11-cre/ERT2)1Soff	Myh11-CreER	MGI:3819270	IMSR_JAX:019079
Tg(Nes-cre/ERT2)KEisc	Nest-CreER	MGI:3767432	IMSR_JAX:016261
Tg(Pdgfra-cre)1Clc	Pdgfra-Cre	MGI:4837746	IMSR_JAX:013148
Tg(Pdgfra-cre/ERT)467Dbe	Pdgfra-CreER	MGI:5056164	IMSR_JAX:018280
Tg(Pdx1-cre)6Tuv	Pdx1-Cre	MGI:3032531	IMSR_JAX:014647
Tg(Pdx1-flp)1Dsa/J	Pdx1-Flp	MGI:5616872	NA
Tg(S100a4-cre)1Egn	Fsp1-Cre	MGI:3712292	IMSR_JAX:030644
Trp53$^{tm1.1Dgk}$	p53-frt	MGI:5306612	IMSR_JAX:017767
Trp53^{tm1Brn}	p53 lox	MGI:1931011	IMSR_JAX:032435
Trp53$^{tm2.1Tyj}$	LSL-p53 R172H	MGI:3039264	IMSR_JAX:008183

3.1.10 Software and databases

The software and databases used in this thesis are described in Table 10.

Table 10 – Software and databases used

Software	RRID	Source
Aperio ImageScope v12.4.3.7001	SCR_020993	Leica Microsystems CMS GmbH, DE
Aperio VERSA v1.04.125	SCR_021016	Leica Microsystems CMS GmbH, DE
AxioVision v4.8	SCR_002677	Carl Zeiss AG, Oberkochen, DE
Fiji v2.3.0/1.53q	SCR_002285	Max Planck Institute of Molecular Cell Biology and Genetics, Dresden, DE
FlowJo v10.6.1	SCR_008520	Becton, Dickinson, and Company (BD), Franklin Lakes, NJ, USA
GraphPad Prism 5.0 and 8.0	SCR_002798	GraphPad Software, San Diego, CA, USA
GSEA	SCR_003199	Broad Institute Inc., Boston, MA, USA
Image Studio Software v5.2.5	SCR_015795	Li-Cor Biosciences, Lincoln, NE, USA
Imaris 9.6	SCR_007370	Bitplane AG, Zurich, CH
Leica Application Suite X v3.6.1	SCR_013673	Leica Microsystems CMS GmbH, DE
MARS® Data Analysis Software Version 3.20R2	SCR_021015	BMG Labtech, Ortenberg, DE
Microsoft Excel	SCR_016137	Microsoft Corp., Redmont, WA, USA
Pubmed	SCR_004846	National Library of Medicine, Bethesda, MD, USA

Table 10 – Software and databases used (continued)

Software	RRID	Source
PyRAT software v4.2-552	NA	Scionics Computer Innovation GmbH, Dresden, DE
QuPath v0.3.2	SCR_018257	Queens University Belfast, Ireland, UK
R v3.6.2	SCR_001905	The R Foundation, Indianapolis, IN, USA
SnapGene Viewer	SCR_015052	GSL Biotech LLC, Chicago, IL, USA
ZEISS ZEN v2.3	SCR_013672	Carl Zeiss AG, Oberkochen, DE

3.2 Methods

3.2.1 *In vivo* experiments

All mouse experiments were compliant with European guidelines and approved by the Institutional Animal Care and Use Committees (IACUC) of the local authorities of the Technical University of Munich and the Regional Government of Bavaria (Regierung von Oberbayern).

3.2.1.1 Breeding strategies

The mouse strains were intercrossed to obtain the desired genotypes. The intercross of the mice strains originated several mouse lines described in Table 11.

Table 11 - Breeding strategy used to obtain the tumor animals analyzed in this thesis

Mouse line	Strains
FKCol6a1	Tg(Pdx1-flp)1Dsa/J; Kras^{tm1Dsa}; Tg(Col6a1-cre)1Gkl; Gt(ROSA)26Sor$^{tm4(ACTB-tdTomato,-EGFP)Luo}$ Or Tg(Pdx1-flp)1Dsa/J; Kras^{tm1Dsa}; Trp53$^{tm1.1Dgk}$; Tg(Col6a1-cre)1Gkl; Gt(ROSA)26Sor$^{tm4(ACTB-tdTomato,-EGFP)Luo}$
FKCspg4	Tg(Pdx1-flp)1Dsa/J; Kras^{tm1Dsa}; Tg(Cspg4-cre/Esr1*)BAkik; Gt(ROSA)26Sor$^{tm4(ACTB-tdTomato,-EGFP)Luo}$ Or Tg(Pdx1-flp)1Dsa/J; Kras^{tm1Dsa}; Trp53$^{tm1.1Dgk}$; Tg(Cspg4-cre/Esr1*)Bakik; Gt(ROSA)26Sor$^{tm4(ACTB-tdTomato,-EGFP)Luo}$
FKGfap1	Tg(Pdx1-flp)1Dsa/J; Kras^{tm1Dsa}; Tg(Gfap-cre)73.12Mvs; Gt(ROSA)26Sor$^{tm4(ACTB-tdTomato,-EGFP)Luo}$ Or Tg(Pdx1-flp)1Dsa/J; Kras^{tm1Dsa}; Trp53$^{tm1.1Dgk}$; Tg(Gfap-cre)73.12Mvs; Gt(ROSA)26Sor$^{tm4(ACTB-tdTomato,-EGFP)Luo}$
FKGfap2	Tg(Pdx1-flp)1Dsa/J; Kras^{tm1Dsa}; Tg(Gfap-cre)77.6Mvs; Gt(ROSA)26Sor$^{tm4(ACTB-tdTomato,-EGFP)Luo}$ Or Tg(Pdx1-flp)1Dsa/J; Kras^{tm1Dsa}; Trp53$^{tm1.1Dgk}$; Tg(Gfap-cre)77.6Mvs; Gt(ROSA)26Sor$^{tm4(ACTB-tdTomato,-EGFP)Luo}$
FKGfapER	Tg(Pdx1-flp)1Dsa/J; Kras^{tm1Dsa}; Tg(GFAP-cre/ERT2)505Fmv; Gt(ROSA)26Sor$^{tm4(ACTB-tdTomato,-EGFP)Luo}$ Or Tg(Pdx1-flp)1Dsa/J; Kras^{tm1Dsa}; Trp53$^{tm1.1Dgk}$; Tg(Pdx1-flp)1Dsa/J; Kras^{tm1Dsa}; Trp53$^{tm1.1Dgk}$; Tg(GFAP-cre/ERT2)505Fmv; Gt(ROSA)26Sor$^{tm4(ACTB-tdTomato,-EGFP)Luo}$

Table 11 - Breeding strategy used to obtain the tumor animals analyzed in this thesis (continued)

Mouse line	Strains
FKMyh11	Tg(Pdx1-flp)1Dsa/J; Kras$^{\text{tm1Dsa}}$; Tg(Myh11-cre/ERT2)1Soff; Gt(ROSA)26Sor$^{\text{tm4(ACTB-tdTomato,-EGFP)Luo}}$ Or Tg(Pdx1-flp)1Dsa/J; Kras$^{\text{tm1Dsa}}$; Trp53$^{\text{tm1.1Dgk}}$; Tg(Myh11-cre/ERT2)1Soff; Gt(ROSA)26Sor$^{\text{tm4(ACTB-tdTomato,-EGFP)Luo}}$
FKNest	Tg(Pdx1-flp)1Dsa/J; Kras$^{\text{tm1Dsa}}$; Tg(Nes-cre/ERT2)Keisc; Gt(ROSA)26Sor$^{\text{tm4(ACTB-tdTomato,-EGFP)Luo}}$ Or Tg(Pdx1-flp)1Dsa/J; Kras$^{\text{tm1Dsa}}$; Trp53$^{\text{tm1.1Dgk}}$; Tg(Nes-cre/ERT2)Keisc; Gt(ROSA)26Sor$^{\text{tm4(ACTB-tdTomato,-EGFP)Luo}}$
FKPdgfra	Tg(Pdx1-flp)1Dsa/J; Kras$^{\text{tm1Dsa}}$; Tg(Pdgfra-cre)1Clc; Gt(ROSA)26Sor$^{\text{tm4(ACTB-tdTomato,-EGFP)Luo}}$ Or Tg(Pdx1-flp)1Dsa/J; Kras$^{\text{tm1Dsa}}$; Trp53$^{\text{tm1.1Dgk}}$; Tg(Pdgfra-cre)1Clc; Gt(ROSA)26Sor$^{\text{tm4(ACTB-tdTomato,-EGFP)Luo}}$
FKPdgfraER	Tg(Pdx1-flp)1Dsa/J; Kras$^{\text{tm1Dsa}}$; Tg(Pdgfra-cre/ERT)467Dbe; Gt(ROSA)26Sor$^{\text{tm4(ACTB-tdTomato,-EGFP)Luo}}$ Or Tg(Pdx1-flp)1Dsa/J; Kras$^{\text{tm1Dsa}}$; Trp53$^{\text{tm1.1Dgk}}$; Tg(Pdgfra-cre/ERT)467Dbe; Gt(ROSA)26Sor$^{\text{tm4(ACTB-tdTomato,-EGFP)Luo}}$
FKSm22	Tg(Pdx1-flp)1Dsa/J; Kras$^{\text{tm1Dsa}}$; Tagln$^{\text{tm2(cre)Yec}}$; Gt(ROSA)26Sor$^{\text{tm4(ACTB-tdTomato,-EGFP)Luo}}$ Or Tg(Pdx1-flp)1Dsa/J; Kras$^{\text{tm1Dsa}}$; Trp53$^{\text{tm1.1Dgk}}$; Tagln$^{\text{tm2(cre)Yec}}$; Gt(ROSA)26Sor$^{\text{tm4(ACTB-tdTomato,-EGFP)Luo}}$
KC	Tg(Pdx1-cre)6Tuv; Kras$^{\text{tm4Tyj}}$ Or Ptf1a$^{\text{tm1(cre)Hnak}}$; Kras$^{\text{tm4Tyj}}$
KPC	Tg(Pdx1-cre)6Tuv; Kras$^{\text{tm4Tyj}}$; Trp53$^{\text{tm2.1Tyj}}$ Or Tg(Pdx1-cre)6Tuv; Kras$^{\text{tm4Tyj}}$; Trp53$^{\text{tm1Brn}}$
PC	Tg(Pdx1-cre)6Tuv; Gt(ROSA)26Sor$^{\text{tm2(Pik3ca*)Dsa}}$ Or Ptf1a$^{\text{tm1(cre)Hnak}}$; Gt(ROSA)26Sor$^{\text{tm2(Pik3ca*)Dsa}}$
R26-TGFbi	Gt(ROSA)26Sor$^{\text{tm3(CAG-Cre/ERT2)Dsa/J}}$; Gt(ROSA)26Sor$^{\text{tm3(TGFb1)/J}}$

3.2.1.2 Genotyping

Mice were genotyped at the age of 2 - 3 weeks. First, each mouse got a code mark in the ear corresponding to a numerical number. Then, the earpiece was collected for genotyping, and the genomic DNA was extracted using the Soriano lysis buffer. The genotype of each mouse line was determined using a combination of PCRs (Table 12). The amplified products were run in a 1.5 to 2% agarose gel in TE buffer containing Ethidium bromide. The bands were detected by exposing the gels to UV light in an UVP UVsolo touch imaging device.

Table 12 - PCRs used to genotype the mouse lines

Mice strain	Primers composing the PCR
Gt(ROSA)26Sor$^{\text{tm2(Pik3ca*)Dsa}}$	pGL3-pA-pause4645-UP PI3K-genotyp-RevPr

Table 12 - PCRs used to genotype the mouse lines (continued)

Mice strain	Primers composing the PCR
Gt(ROSA)26Sor$^{\text{tm3(CAG-Cre/ERT2)Dsa/J}}$	R26-td-E-mutLP R26-Tva-GT-UP R26-Tva-GT-WT-LP pGL3-pA-pause-4645-UP Cre-neu-LP CreERTM-UP CreER-sc-LP1
Gt(ROSA)26Sor$^{\text{tm3(TGFb1)/J}}$	R26-Tva-GT-UP mTgfb1_LP pGL3-pA-pause UP R26-Tva-GT-UP R26-Tva-GT-wt_LP FsaSFneosa_LP2
Gt(ROSA)26Sor$^{\text{tm4(ACTB-tdTomato,-EGFP)Luo}}$	CAG-sc-LP R26-Tva-GT-UP R26-Tva-GT-WT-LP
Kras$^{\text{tm1Dsa}}$	Kras-WT-UP1 Kras-URP-LP1 R26-Tva-SA-mut
Kras$^{\text{tm4Tyj}}$	Kras-WT-UP1 Kras-URP-LP1 KrasG12Dmut-UP
Pdgfra$^{\text{tm11(EGFP)Sor}}$	PdgfraEGFP_WT-fw PdgfraEGFP_WT-rv PdgfraEGFP_MT-rv
Ptf1a$^{\text{tm1(cre)Hnak}}$	p48-Cre-GT-LP-URP p48-Cre-GT-wt-UP p48-Cre-GT-mut-UP-neu
Tagln$^{\text{tm2(cre)Yec}}$	oIMR7055 oIMR7056 oIMR7057
Tg(Col6a1-cre)1Gkl	Col6a1B-UP3 Cre-mB-UP2
Tg(Cspg4-cre/Esr1*)BAkik	Cre-neu-UP Cre-neu-LP Gabra1-UP Gabra1-LP
Tg(Gfap-cre)73.12Mvs	oIMR1900 oIMR1901
Tg(Gfap-cre)77.6Mvs	oIMR1900 oIMR1901
Tg(GFAP-cre/ERT2)505Fmv	CreERTM-UP CreER-sc-LP1
Tg(Myh11-cre/ERT2)1Soff	CreERTM-UP CreER-sc-LP1
Tg(Nes-cre/ERT2)KEisc	Nestin-Cre-UP2 Nestin-Cre-LP Gabra1-UP Gabra1-LP
Tg(Pdgfra-cre)1Clc	PDGFRa-CTM-UP PDGFRa-CTM-LP Gabra-UP Gabra-LP

Table 12 - PCRs used to genotype the mouse lines (continued)

Mice strain	Primers composing the PCR
Tg(Pdgfra-cre/ERT)467Dbe	PDGFRa-CTM-UP PDGFRa-CTM-LP Gabra-UP Gabra-LP
Tg(Pdx1-cre)6Tuv	Pdx-Prom-UP2 V-Cre-LP2 PdxKON-LP1
Tg(Pdx1-flp)1Dsa/J	pdx5ut-scUP Flpopt-scLP Gabra-UP Gabra-LP
Tg(S100a4-cre)1Egn	Cre-neu-UP Cre-neu-LP Gabra1-UP Gabra1-LP
$Trp53^{tm1.1Dgk}$	p53-ftr1 p53-frt2
$Trp53^{tm1Brn}$	p53 berns Up-E p53 berns LP-F
$Trp53^{tm2.1Tyj}$	Trp53R172H-WT-UP2 Trp53R172H-URP-LP Trp53R172H-mut-UP4

3.2.1.3 Tamoxifen treatment

At 2-3 months, mice were fed chow containing 400 mg tamoxifen citrate per kilogram (CreActive TAM400) for 2 - 4 weeks. Control animals were fed Pancrex-Vet food, respectively.

3.2.1.4 Euthanization and dissection

Mice were euthanized with Forene® isoflurane, fixed, and disinfected with 70 % ethanol. Pancreatic tissue was isolated, and tissue pieces were collected for cryopreservation, cell line isolation, organoid isolation, and the organs necessary for consequent analysis were fixed in 4% Roti-Histofix. Cryopreserved samples were kept at -80°C until further use.

3.2.2 *In vitro* experiments

The *in vitro* experiments were performed under sterile conditions. Cells were kept in incubators at 37 °C with 5% CO_2 in a humidified atmosphere.

3.2.2.1 Cell line isolation and culture

During mouse necropsy, a tumor piece was collected, minced, and incubated for 24 hours with 2 mg/mL of Collagenase II. The day after, the suspension was centrifuged at 350 g and cultured in cell culture medium. When the culture reached 80% of confluence was split, and the line was expanded. Culture preservation was achieved by freezing the lines in cell culture freezing solution, and the frozen lines were stored in a liquid nitrogen vapor phase.

3.2.2.2 Organoid isolation and culture

During mouse necropsy, a tumor piece was collected, minced, and incubated for 20 minutes with 200U/mL Collagenase I. After the digestion, the suspension was centrifuged at 350 g, embedded in matrigel, and cultured in organoid medium. Media was changed every 3-4 days. The cultures were split every 7 days or when cells shed into the organoid core. During splitting, organoids were kept in cold solutions to dissolve matrigel and incubated with Cell recovery solution for 15 minutes and TrypLE for 5 minutes before being re-embedded in matrigel. Culture preservation was achieved by freezing the lines in an organoid medium freezing solution, and the frozen lines were stored in a liquid nitrogen vapor phase.

3.2.2.3 Pancreatic fibroblast isolation and culture

During mouse necropsy, at least two whole pancreases were collected, minced, and incubated for 20 minutes with a collagenase P solution. After the digestion, the suspension was centrifuged at 350 g, resuspended in GBSS with NaCl, and a solution of Histodenz was layered on top. Next, the setup was centrifuged at 1400 g for 20 minutes without a break, originating a fuzzy layer containing the fibroblasts. Next, the fibroblasts were collected, washed in GBSS with NaCl, centrifuged, and resuspended in fibroblast media for culture. Finally, cells were expanded, preserved in fibroblast freezing medium, and stored in liquid nitrogen vapor phase.

3.2.2.4 Cell lines quality controls

Regenotyping, mycoplasm analysis, and the presence of human oncogenic KRAS were used as quality controls of cell lines, organoid lines, and fibroblasts.

3.2.2.4.1 Mycoplasm analysis

The lines were cultured in medium without antibiotics until the medium turned yellow, and approximately 2 mL of medium was collected and centrifuged at 350 g to remove dead cells. Then, the supernatant was centrifuged for 10 min at 16,000 g. The pellet was resuspended in water, and a PCR with the primers mycoplasma fw1, mycoplasma fw2, mycoplasma fw3, mycoplasma fw4, mycoplasma fw5, mycoplasma fw6, mycoplasma fw7, mycoplasma rv1, mycoplasma rv2, and mycoplasma rv3 was performed. The binary PCR was analyzed in an agarose gel.

3.2.2.4.2 Human contamination analysis

The lines were cultured in the correspondent medium, and the cells were collected and pelleted when confluency was reached. The pellet was resuspended in Soriano buffer to isolate genomic DNA, and PCR was performed with the primers KrasG12D_human_fw and KrasG12D_human_rv. The binary PCR was analyzed in an agarose gel.

3.2.2.5 Organoid-fibroblasts co-culture

The organoids and fibroblasts were cultured according to 3.2.2.2. The 12500 organoid cells and 50000 PDGFRa-H2b-EGFP fibroblasts were seeded in 25 µL matrigel. The cultures were incubated with organoid media without Y27632 and cultures for 7 days. In the LOX inhibitor treatments, the cultures were treated on day 1 with 500 µM of β-Aminopropionitrile (BAPN). Media were changed every 3 days.

3.2.2.6 Fibroblasts tamoxifen treatment

The R26 $^{CreER/Stop\text{-}Tgfb1}$ fibroblasts were incubated for 14 days with 1µM of 4-hydroxy-tamoxifen or ethanol to activate Cre. The paired lines were used for 2D and 3D assays.

3.2.2.7 Wound-healing assay

Paired pan-fibroblast lines with basal and overexpression of *Tgfb1* were seeded in 6 well plates. When the lines reached confluency, a scratch was made with a 100 µL tip, and fibroblast migration was monitored for 10 hours using a Leica brightfield microscope. The wound-gap closure was measured using the FIJI extension - wound healing size tool (Suarez-Arnedo *et al.*, 2020).

3.2.2.8 Fibroblasts 2D assays

Paired pan-fibroblast lines with basal and overexpression of *Tgfb1* were seeded at a density of 2000 cells/cm^2 and cultured in fibroblast media. On day 5, the cells were collected for quantitive mRNA analysis. In the LOX inhibitor treatments, the *Tgfb1* overexpression fibroblast line was treated on day 1 with 100, 250, and 500 µM of β-Aminopropionitrile (BAPN), and cells were collected for protein analysis.

3.2.2.9 Fibroblasts 3D assays

Paired pan-fibroblasts were seeded at a concentration of 75000 cells/ 50 µL matrigel and cultured in organoid media without Y27632. On day 1, the culture was supplemented with 1 ng/mL of IL1α. On day 5, the cells were collected for quantitive mRNA analysis.

3.2.3 Histological-based experiments

Histological experiments were performed in cryopreserved tissue and FFPE. First, cryopreserved tissue was washed in PBS and immediately fixed with 4% formaldehyde for 2 hours at 4°C. Next, it was washed in PBS 3 times and dehydrated in high-concentrated sucrose solutions overnight. Then, tissues were embedded in Richard-Allan Scientific NEG-50, frozen in an Ethanol-dry ice bath, and at -80 °C. Tissues were serially cut into 5 µm-thick sections using the Leica CM3050 S cryostat. Slides were kept at -80 °C until the experiment was performed.

Mouse organs collected during the necropsy and fixed for 24h in 4% Roti-Histofix were washed and kept in PBS at 4 °C until further processing. For long-term storage, the organs were placed into histo-cassettes and dehydrated, cleared, and embedded in paraffin using the tissue processor ASP300S and the heated paraffin embedding module HistoCore Arcadia H. The paraffin blocks were stored at room temperature. Serial cuts 1.5 µm-thick were obtained using the microtome Microm HM355S.

3.2.3.1 Hematoxylin and eosin staining

Hematoxylin and eosin (H&E) staining were performed in cryopreserved and FFPE samples to perform the histopathological evaluation of the tumor. For FFPE samples, the initial step was the deparaffinization of the specimen using ROTI®Histol, followed by hydration of the samples using decreasing concentrations of Ethanol and distilled water. Next, the nuclei were stained with eosin for 30 seconds, followed by extensive washes with tap water. The specimen was then stained for 20 seconds with eosin, extensively washed with tap water, and dehydrated using increasing concentrations of Ethanol. Finally, the sample was incubated with ROTI®Histol and mounted in a sealing mounting media. Cryosections were hydrated in water and stained for 3 seconds with hematoxylin and 3 seconds with eosin. Then, the samples suffered the same processing workflow as FFPE samples. The tissues were scanned using the Aperio Versa 8 Digital Scanner.

The pathological grading was performed in collaboration with Dr. med. vet. Katja Steiger and Nils Wirges from the core Facility Comparative Experimental Pathology at the Institute of Pathology, Technical University of Munich.

3.2.3.2 Sirius Red staining

FFPE tissue sections were deparaffinized using ROTI®Histol and hydrated using decreasing concentrations of Ethanol and distilled water. The specimens were stained for one hour in Sirius red staining solution, followed by at least three times in 0.5 % acetic acid. After dehydration, the tissue samples were incubated in Roti® Histol and subsequently mounted with a sealing medium. The tissues were scanned using the Aperio Versa 8 Digital Scanner. The stained tumor area was quantified using QuPath v.0.3.0 (Bankhead *et al.*, 2017).

3.2.3.3 Immunohistochemistry

FFPE tumor sections were deparaffinized and hydrated. Heat-mediated antigen retrieval was performed by boiling the sections for 20 minutes in a citric acid-based antigen unmasking solution pH 6.0 or Tris-EDTA solution pH 9.0. The slides were cooled down, washed in PBS, and incubated with 3% H_2O_2 solution for 20 min at room temperature to block endogenous peroxidase activity. Next, the samples were blocked with 5% goat serum/avidin in PBS for 1 hour at room temperature. The primary antibodies COL1A1 (1:100), Collagen IV (1:100), Fibronectin (1:100), LOX (1:100), and αSMA (1:200) were incubated overnight at 4 ºC. Following washing thrice in PBS, the tissues were incubated with the biotinylated anti-rabbit secondary for 1 hour at RT. The detection was performed using the Vectastain® elite ABC and the DAB peroxidase substrate kit according to manufacturer protocol. The samples were counterstained with hematoxylin, dehydrated, incubated in Roti®Histol, and mounted. The tissues were scanned using the Aperio Versa 8 Digital Scanner. The quantification of the stained cells in the whole tumor was performed using QuPath v.0.3.0 (Bankhead *et al.*, 2017).

3.2.3.4 Immunofluorescence

3.2.3.4.1 Standard immunofluorescence

Cryopreserved tumor sections were hydrated and fixed with 4% formaldehyde for 1 minute. Next, the samples were blocked with 3% BSA, 0.1% Triton™ X-100 for 1 hour at room temperature. The primary antibodies Nestin (1:100), PDGFRα (1:50), FSP1 (1:100), Vimentin (1:100), GFAP (1:100), PDPN (1:100), KRT18 (1:200), Myh11 (1:100), EpCAM (1:50), Desmin (1:50), CD45 (1:100) and αSMA (1:100) were incubated overnight at 4 ºC. Then, the samples were washed thrice in 0.1% Triton™ and incubated with the correspondent secondary (1:500) for 1 hour at RT, washed, and mounted. The acquisition was performed in the SP8 Leica confocal system.

3.2.3.4.2 Multiplex immunofluorescence

Cryopreserved tumor sections were hydrated and fixed with 4% formaldehyde for 1 minute. Then, the samples were blocked with 3% BSA, 0.1% Triton™ X-100 in PBS with 10% donkey serum for 1 hour at room temperature.

For panel 1, the primary antibodies αSMA (1:100) and PDPN (1:100) were incubated overnight at 4ºC in 10% donkey serum, 3% BSA, 0.1% Triton™ X-100. The next day, the samples were washed three times with 0.1% Triton™ and incubated with PDGFRα (1:50) and IL6 (1:50) for 3 hours at room temperature. After washing thrice in 0.1% Triton™, the tissues were incubated with the donkey anti-goat 594 (1:200) and donkey anti-rat 488 (1:200) in 10% donkey serum, 3% BSA, 0.1% Triton™ X-100 in PBS for 1 hour at RT. Samples were washed with 0.1% Triton™ X-100 in PBS, blocked with 10% goat serum, 3% BSA, 0.1% Triton™ X-100 for 1 hour. Next, the samples were washed and incubated with goat anti-rabbit Cy3 (1:200) and goat anti-Armenian hamster 647 (1:200) in 10% goat serum, 3% BSA, 0.1% Triton™ X-100 in PBS for 1 hour at room temperature. Next, the samples were washed three times 0.1% Triton™ X-100 in PBS and blocked with 10% rabbit serum, 3% BSA, 0.1% Triton™ X-100 in PBS. The KRT18-AF680 was incubated for 3 hours at room temperature, followed by three washes with 0.1% Triton™ X-100 in PBS.

For panel 2, the primary antibodies FABP4 (1:400), PDPN (1:100), and CD45 (1:400) were incubated overnight at 4 ºC in 10% donkey serum, 3% BSA, 0.1% Triton™ X-100. The next day, the samples were washed three times with 0.1% Triton™ and incubated with the donkey anti-goat 594 (1:200) in 10% donkey serum, 3% BSA, 0.1% Triton™ X-100 in PBS for 1 hour at RT. Next, samples were washed with 0.1% Triton™ X-100 in PBS, blocked with 10% goat serum, 3% BSA, 0.1% Triton™ X-100 for 1 hour. Then, the samples were washed and incubated with goat anti-rat 555 (1:200) and goat anti-Armenian hamster 647 (1:200) in 10% goat serum, 3% BSA, 0.1% Triton™ X-100 in PBS for 1 hour at room temperature. Next, the samples were washed three times with 0.1% Triton™ X-100 in PBS and blocked with 10% rabbit/rat serum, 3% BSA, 0.1% Triton™ X-100 in PBS. Next, the KRT18-AF680 and the MHCII-488 antibodies were incubated for 3 hours at room temperature, followed by three washes with 0.1% Triton™ X-100 in PBS.

Finally, the samples were stained with DAPI (1:1000) and mounted in vectashield. The acquisition was performed in the SP8 Leica confocal system.

3.2.3.4.3 Whole-mount immunofluorescence

The domes were washed with PBS and fixed for 1 hour with 2% formaldehyde. Then, the cultures were blocked with 3% BSA, 0.1% Triton™ X-100 in PBS with 10% goat serum for 1 hour at room temperature. Next, the cultures were incubated with αSMA (1:200) and PDPN (1:200) antibodies in 10% goat serum, 3% BSA, 0.1% Triton™ X-100 in PBS overnight with orbital agitation. The next day, the samples were washed for one day every 30 minutes with 0.1% Triton™ X-100 in PBS with orbital agitation. Then, the cultures were incubated with goat anti-rabbit Cy3 (1:200) and goat anti-Armenian hamster 647 (1:200) in 10% goat serum, 3% BSA, 0.1% Triton™ X-100 in PBS for 1 hour at room temperature with orbital agitation. Finally, the samples were washed for 2 hours and mounted in PBS. The acquisition was performed in the SP8 Leica confocal system.

3.2.3.4.4 Immunofluorescence analysis

Standard immunofluorescence was analyzed through the manual count of positive cells using the FIJI plugin Cell counter. The number of fields per animal analyzed was dependent on the experiment: 20 fields of view were counted in the quantification of the mesenchymal αSMA expression, 5 fields of view were counted in the quantification of CAFs populations in the co-culture setting, and 3 fields of view were quantified in the stromal cre driver lines.

The multiplex immunofluorescence was analyzed in Imaris and Cytomap. The images were loaded into Imaris, and each cell type was segmented using the Cells module according to pre-defined marker criteria. The segmentation data was exported, and the absolute number of each population in tumor samples was retrieved. The relative abundance was calculated. To calculate the correlation between cell populations, the relative abundance was input in GraphPad, and a Spearman correlation was computed. The neighborhood analysis was performed in Cytomap (Stoltzfus *et al.*, 2020). CSV files compiling each sample phenotypic and spatial information of each cell were input into Cytomap. The Euclidean distance between groups of cells was calculated, and cellular neighborhoods within the tissue were determined. To calculate the cellular neighborhoods, a raster scan neighborhood with a 20 µm radius was performed with the cellular types, except pericytes, in panel 1. The raster scan generated local neighborhoods evenly distributed throughout the tissue in a grid pattern. The local neighborhoods were clustered according to local composition and density using a NN self-organizing map algorithm with the number of regions determined by the Davies-Bouldin criterion, generating regional cellular neighborhoods (CNs) with similar composition.

3.2.4 DNA experiments

3.2.4.1 End-point PCR

The PCRs were performed using genomic DNA as the template for the reaction. The 1 µL of the template was added to 12.5 µL of S-mix, the optimized primer concentration and double-distilled water generating a 25 µL reaction. The desired amplicon was obtained by 40 cycles of denaturation (95°C for 45 seconds), annealing (55°-65°C for 30-60 seconds), and elongation (72°C for 60-90 seconds).

3.2.5 RNA experiments

3.2.5.1 RNA extraction

The RNA extraction was performed using a Rneasy kit according to the instructions provided by the manufacturer. Prior to the RNA extraction, the lysates were passed through QIAshredder spin columns to further homogenize the lysates and reduce viscosity. Then, RNA concentration was determined, and the isolated RNA was stored at -80 °C. Bulk samples were previously homogenized in RLT buffer supplemented with 1% 2-mercaptoethanol using SilentCrusher M, whereas pellets containing the cell lines, organoids, or fibroblasts were solely resuspended in RLT buffer supplemented with 1% 2-mercaptoethanol.

3.2.5.2 Quantitative PCR

Complementary DNA was used as a template for the qPCR reaction. One microgram of RNA was added to the reverse transcriptase, random primers, and a reaction mix to produce cDNA, which was diluted 5 times in water before further use.

To quantify mRNA transcripts, a 20 µL reaction containing 10 µL of SYBR green Master mix, 1 µL diluted cDNA, and 100 nM of forward and reverse primers were used. The samples were tested in triplicates in a 96-well plate using a StepOnePlus real-time PCR system. The pair of primers used to amplify a transcript were: *Acta2* (acta2 fw and acta2 rv), *Pdgfra* (pdgfra fw and pdgfra rv), *Ctgf* (ctgf fw and ctgf rv), *Tgfb1* (tgfb1 fw and tgfb1 rv), *Il6* (il6 fw and il6 rv) and *Col1a1* (col1a1 fw and col1a1 rv). *Gapdh* (gapdh fw, gapdh rv) was used as a housekeeping gene.

Relative mRNA expression was quantified using the $2^{-\Delta\Delta CT}$ method (Livak and Schmittgen, 2001). Primer efficiency was calculated with serial cDNA dilutions, and primers with an efficiency between 1.9 and 2.1 were selected for further analysis.

3.2.5.3 RNA sequencing

Bulk 3' transcript end RNA-seq (SCRB-seq) RNA sequencing of bulk tumor samples, cell lines, and organoid lines was performed in collaboration with the laboratory of Professor Dr. Roland Rad (TranslaTUM, Technical University Munich). From each sample, 2 µg were further processed for sequencing, and cDNA was synthesized containing sample barcodes. The cDNA libraries were prepared using the Nextera kit, and the cDNA fragments were sequenced.

3.2.6 Protein analysis

For protein analysis, the cell pellets were resuspended in ice-cold IP buffer, originating a whole cell lysate. The cell lysate was quantified using the Bradford method (Bradford, 1976). A standard curve and each sample were incubated with Bradford buffer, and the absorbance was measured at 595 nm. The mean absorbance of each sample was interpolated in the standard curve of known concentrations. Each sample was measured in triplicates.

3.2.6.1 Western-blot

Proteins were separated using a polyacrylamide gel electrophoresis in denaturing conditions (SDS-PAGE). Resolving gels with different polyacrylamide content were made depending on the best condition to separate the proteins of interest. The samples were diluted in Laemmlli buffer to the desired concentration and were denatured at 95°C for 5 minutes before being loaded in the gel (Laemmli, 1970). The electrophoresis was carried out with running buffer at a maximum voltage of 120 V for the time necessary to obtain clear band separation.

After protein separation with SDS-PAGE, the proteins were blotted onto a nitrocellulose blotting membrane Amersham™ Protran™ 0.2 µm NC. The immunoblotting was carried out at 4°C for 2 hours at 100V in transfer buffer. First, the membranes were blocked using 5% milk in PBS for 1 hour at room temperature with agitation. Then, the membranes were incubated with Fibronectin (1:1000), COL1A1 (1:1000), LOX (1:1000), pSMAD2 (1:1000), SMAD2/3 (1:1000), SMAD4 (1:1000), and GAPDH (1:1000) in 5% milk in PBS-T overnight at 4°C with agitation. Next, the membranes were washed three times with PBS-T and incubated with Goat anti-rabbit DyLight800 (1:10000) for 1 hour at room temperature under agitation. Finally, the membranes were washed extensively and scanned at 800 nm using the Odyssey® Fc imaging system.

3.2.7 RNA-sequencing analysis

3.2.7.1 Bulk analysis

Bioinformatical analysis of RNA-seq data was performed using R version 3.6.2. The sequenced data were aligned to the reference genome (GRCm38) and processed to generate sample- and gene-wise unique molecular identifier tables. Further analyses were performed using DEseq2 (Love *et al.*, 2014). Genes with a fold-change equal to or superior to 2 and an adjusted p-value inferior to 0.05 were considered significant. Gene set enrichment analysis was performed with gProfiler or the GSEA software (Mootha *et al.*, 2003; Reimand *et al.*, 2007; Subramanian *et al.*, 2005). After data normalization, immune and myCAF deconvolution was performed with mMCPcounter (Petitprez *et al.*, 2020). The additional signatures of myCAFs (*Mmp11*, *Col11a1*, *C1qtnf3*, *Cthrc1*, *Col12a1*, *Col10a1*, *Lrrc15*, and *Itga11*) and dendritic cells (*Lyz1*, *Cd300e*, *Mafb*, *Krt79*, *Batf3*, *Msr1*) were added to the already defined and were based on Dominguez et al. and Zillionis et al., respectively (Dominguez *et al.*, 2020; Zilionis *et al.*, 2019).

3.2.7.2 Single-cell RNA sequencing analysis

The scRNA-seq data analyzed were performed by Dominguez et al. and retrieved from the ArrayExpress database with the accession number E-MTAB-8483. The analysis was performed in python using SCANPY, where doublets, cells expressing less than 1500 counts, more than 15000 counts, or showing 15% mitochondrial gene counts were excluded from the analysis (Wolf *et al.*, 2018). In addition, genes occurring in less than 5 cells were filtered out. Counts were normalized and displayed as a log10 transformation (Lun *et al.*, 2016). Dimensionality reduction was performed with Uniform

Manifold Approximation and Projection (UMAP), and the Leiden algorithm accomplished cell clustering. The markers used to annotate the clusters were defined by recent CAFs literature.

3.2.8 Statistical analysis

All statistical analyses were performed using GraphPad Prism and R studio. Experimental data are reported as mean±standard deviation, except in the tumor cell-CAFs communication plots, where distances to tumor cells are depicted as the median. Statistical comparisons were performed using a two-tailed t-test with a welch correction, except for the analysis of *Tgfb1* basal expression and T*gfb1* overexpression pan-fibroblasts lines treated with IL1α, where a one-way ANOVA with Tukey *post hoc* correction for multiple comparisons was performed. Additionally, the statistical analysis of the wound gap closure between *Tgfb1* basal expression and T*gfb1* overexpression pan-fibroblast lines was conducted using a two-way ANOVA. Survival analyses were performed using a log-rank (Mantel-Cox) test, and statistical analyses of metastasis formation were performed using a two-sided Fisher's exact test. In all tests, a p-value or an adjusted p-value inferior to 0.05 was considered significant. The exact p-values resultant from the statistical test are depicted in the figures.

4 Results

Contributions to this thesis besides the author are acknowledged in figure legends and the methods section. Unless otherwise stated, all analyses were performed by the author.

4.1 Characterization of the stromal tumor-microenvironment in context-specif Pancreatic Adenocarcinoma

Pancreatic adenocarcinoma presents an extensive desmoplastic reaction where CAFs can outnumber tumor cells and other populations in the TME (Whatcott *et al.*, 2015). Despite making up most of the tumor area, little is still known about the role of CAFs subpopulations in the TME. Recent studies shed light on PDAC TME and described several CAFs subpopulations. However, this description was mainly done using dissociative single-cell techniques, losing spatial information and the tumor architecture. Even though CAFs' cellular ratios were described, one has to stress that these values do not reflect an accurate measure of CAFs in PDAC. CAFs are very sensitive to digestion-based protocols, making up less than 15% of the total cell content in some characterizations (Dominguez *et al.*, 2020; Elyada *et al.*, 2019; Hutton *et al.*, 2021). Additionally, it is unknown whether different susceptibilities to tissue digestion within the CAFs subpopulations could affect the representativity within the overall CAF group.

Multiplex IF is a single-cell method that allows the preservation of tissue architecture and the accurate representation of all cell types. It is a versatile technique that combines information about single-cell protein expression, cell-cell interactions, and cellular context at a regional level. Therefore, to systematically characterize the stromal TME in PDAC, two multiplex IF panels containing markers that defined the CAFs phenotypes described to this date were implemented. These panels were applied to multiple samples of murine PDAC, the obtained images were processed, and the fluorescent signal was segmented using Imaris. For every cell, an object was created containing intensity data for every channel, coordinates, and volumetric data. This information allowed the determination of PDAC stromal cell composition, tumor cell neighborhoods, and regional cellular neighborhoods (Figure 4). The cellular neighborhoods provide a functional understanding of cell populations. When coupled with transcriptomics and clinical features, this spatial data integration may help understand how tissue architecture and composition influence mechanisms driving the disease outcome.

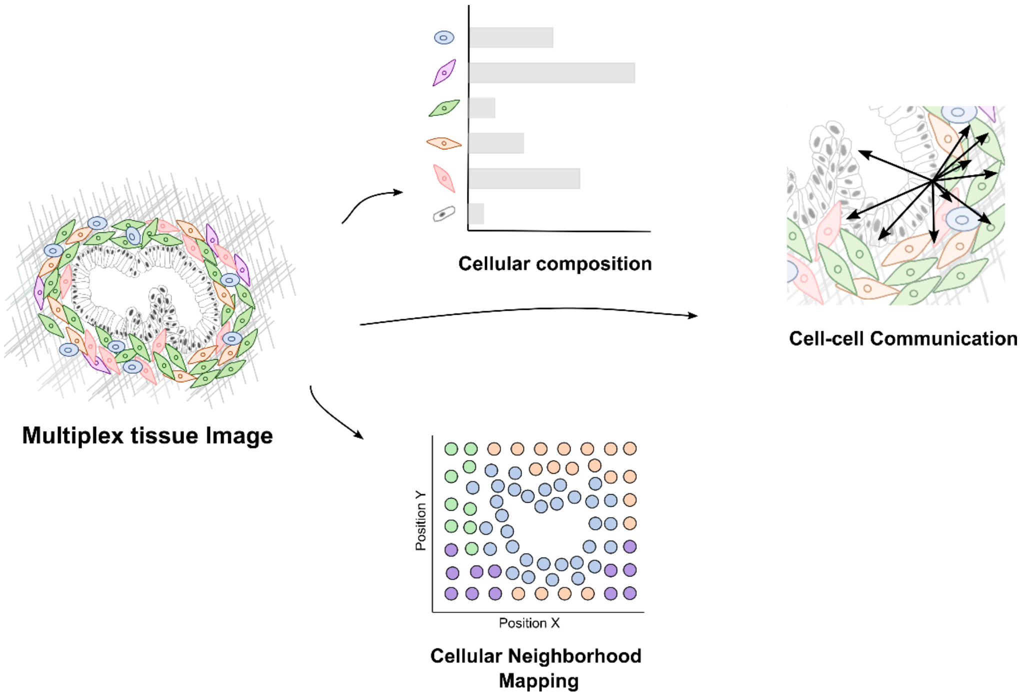

Figure 4 – Conceptual Framework for PDAC characterization using Multiplex histocytometry.

The mouse samples were stained with the CAFs Panels, and the multiplexed images were acquired. Next, the TME populations in the images were segmented using the Cell-based algorithm in Imaris, originating spatial information about each cell. This information allowed the determination of the spatial composition of the tumors and the calculation of the shortest distance between groups of populations to determine tumor cell-CAFs neighborhood profiles and cellular neighborhood maps.

4.1.1 Implementation of multiplex immunofluorescence workflow to profile cancer-associated fibroblasts in PDAC

4.1.1.1 Marker selection was performed using available CAFs scRNAseq datasets and literature mining

The implementation of a multiplex immunofluorescence workflow involves several steps. The initial step is to understand the relevant cell types for the question to be addressed.

This work aims to determine stromal cell composition and stromal architecture in PDAC. Therefore CAFs subpopulations needed to be included. Figure 2 shows the scRNAseq analysis of the Dominguez *et al.* dataset. This dataset comprises 12514 cells, the vast majority being CAFs. The cell annotation of the scRNAseq cell clusters is depicted in Figure 5-A. The dataset presented eight cell populations, six of which were fibroblasts and two were tumor cells.

The identification of CAFs is complex. As a mesenchymal cell type, CAFs express various markers and can overlap with mesenchymal tumor cells. Pdpn has been reported as a specific CAF marker. Nonetheless, with the upregulation of the EMT program, tumor cells may also express *Pdpn*. Cytokeratins, however, seem to be specific to the tumor cells compartment. Therefore, a combination of the markers *Krt18* and *Pdpn* was used to identify tumor cells and CAFs. Immune cells were not present in this dataset, and *Cd45* gene expression was not detected. The bubble plot in Figure 5-B shows the mean expression of selected markers that allowed the phenotyping of tumor cells and different CAFs populations.

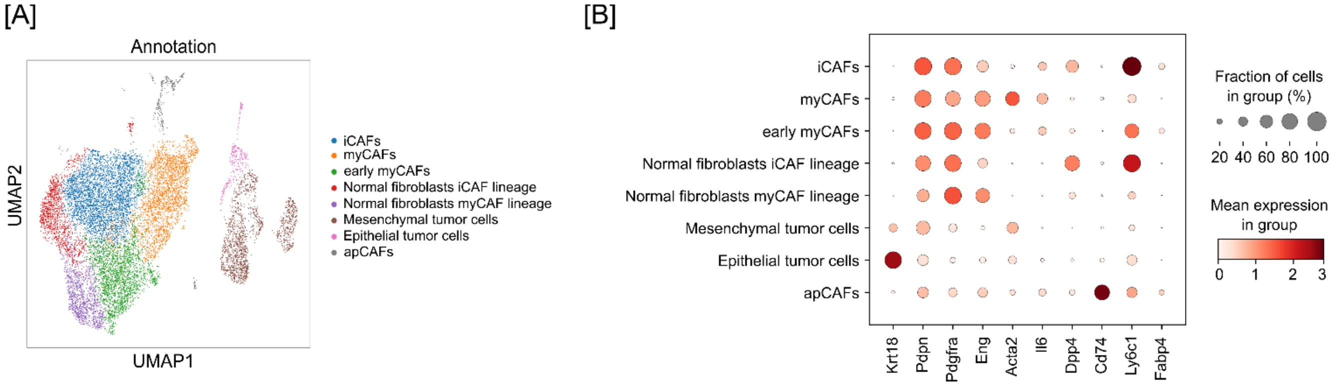

Figure 5 – Analysis of the Dominguez *et al.* scRNA seq data reveals markers to phenotype the three main types of CAFs and their transitory populations.

[A] Unsupervised clustering of viable 12514 mesenchymal cells in PDAC is depicted in the UMAP plot. The different cell type clusters are color coded.

[B] Mean expression of selected CAFs' subpopulations markers. The dot size represents the fraction of cells expressing the marker in the cluster, and the intensity of the color represents the expression levels.

Acknowledgments: Daniele Lucareli performed the scRNAseq analysis. The annotation process was done together with the author of this thesis.

The CAFs populations in this dataset comprised normal fibroblasts, transitory activation CAFs states, and end-point activated CAFs. Several papers have already described the three final CAFs phenotypes in PDAC: iCAFs, myCAFs, and apCAFs (Dominguez *et al.*, 2020; Elyada *et al.*, 2019; Foster *et al.*, 2022; Huang *et al.*, 2022).

Even though iCAFs appeared to differentiate from normal fibroblasts that might express *Eng* or not, most iCAFs presented a strong expression of *Pdgfra* and *Ly6c*. Additionally, *Il6* was described as a marker of iCAFs. However, the Dominguez et al. scRNAseq shows that *Il6* expression was not restricted to iCAFs.

Myofibroblasts arise mainly from normal fibroblasts expressing *Eng*. These fibroblasts get activated – early myCAFs – and, depending on the paracrine stimuli, can originate *Acta2* expressing myCAFs with additional expression of *Il6*.

Antigen-presenting CAFs originate from a different cell type – mesothelial cells. ApCAFs can express *Pdpn*, *Cd74*, and *H2-ab* but are negative for *Cd45*. Table 13 summarizes the protein markers that can be used to phenotype CAFs.

Table 13 – CAFs subpopulations phenotypic protein markers.

Population	**Gene markers**	**Protein markers**
iCAFs	*Pdpn*, *Pdgfra*, *Dpp4*, *Ly6c1*	PDPN, PDGFRα, DPP4, LY6C1
myCAFs	*Pdpn*, *Eng*, *Acta2*	PDPN, CD105, αSMA
apCAFs	*Pdpn*, *Cd74*, *Cd45*, *H2-ab*	PDPN, MHCII, CD74, CD45
Early myCAFs	*Pdpn*, *Eng*	PDPN, CD105
IL6 myCAFs	*Pdpn*, *Eng, Acta2, Il6*	PDPN, CD105, αSMA, IL6
IL6-iCAFs	*Pdpn*, *Pdgfra, Il6*	PDPN, PDGFRα, IL6

Stellate cell proper lineage identification requires many markers. According to the latest literature, the normal fibroblasts that give rise to CAFs can be followed by a combination of PDPN, DPP4, CD105, and WT1 (Dominguez *et al.*, 2020; Foster *et al.*, 2022; Huang *et al.*, 2022). However, some markers, like FABP4, allow a pervasive quantification of stellate cell abundance. This marker appears to identify normal fibroblasts associated with a stellate cell phenotype, although the gene expression was considerably low in normal fibroblast populations in the Dominguez *et al.* scRNAseq dataset.

Since the relevant cell types and the questions to be addressed are laid out, it is essential to understand which imaging technology could be used. Imaging methods with high multiplex capacities, such as Co-detection by Indexing (CODEX) and Mass-cytometry imaging, have been described with fantastic results. Nonetheless, these methods require an investment in expensive new hardware and reagents, with the availability of antibodies compatible with those techniques still being limited. On the other hand, other imaging methods, such as confocal microscopy, can still offer multiplex capacity, although to a lower extent. Confocal microscopy can offer, in addition, many other advantages. Traditional imaging protocols used in confocal microscopy are reasonably easy to establish and allow the user a wide selection of antibodies. Due to the availability of an in-house confocal microscope and already available expertise implemented by Tânia Santos, this equipment was chosen to integrate the CAFs multiplex IF workflow.

4.1.1.2 Panel design for stroma profiling included validation of primary and secondary antibodies

The panel design is the second step in implementing a multiplex immunofluorescence workflow based on the marker selection and the available technology.

The ideal panel to characterize the stromal TME would have all populations. There are six CAFs populations, final and transitory states, defined by a total of ten markers. The addition of a tumor cell marker – KRT18 – is paramount to studying tumor-stromal interactions. Finally, a counter staining must be present to determine the cell number. Therefore, a total amount of 12 markers had to be considered. However, there is a limitation with confocal microscopy to 6-7 simultaneous colors to minimize spillover and spectral overlap between fluorescent channels. One possible approach to solve this problem is to eliminate redundant markers. When analyzed closer, it is still possible to phenotype CAFs if CD105, LY6C, and CD74 are dropped. Still, there is a total of nine markers. With the inability to accommodate all nine markers within the color spectrum, the best way to overcome this limitation was to perform the CAFs characterization using two multiplex IF panels.

The rationale for dividing the populations between the panels was solely marker dependency. Therefore, populations that shared markers were allocated to the same panel. The marker distribution between the panels is depicted in Table 14. Panel 1 would then phenotype myCAFs, early myCAFs, IL6 myCAFs, iCAFs, and IL6 iCAFs, and Panel 2 would phenotype apCAFs and stellate cells.

A key aspect of panel design is to validate the antibodies to be used across negative and positive tissue controls. The antibody staining validation was performed in tissues with low protein abundance - negative controls - or high protein abundance - positive controls, which were selected following literature research and analyzed according to the pathological annotation of these markers in the selected organs. Figure 6 showcases the expression of the antibodies used in this workflow across negative controls, positive controls, normal pancreas, and pancreatic tumors.

Table 14 – CAFs markers distribution along two multiplex immunofluorescence panels.

Panel 1	Panel 2
PDPN	PDPN
KRT18	KRT18
αSMA	FABP4
IL6	CD45
PDGFRα	MHCII
Counterstaining	Counterstaining

PDPN is expressed in mesenchymal populations and has been described as a general marker for CAFs. Therefore it would be expected that a remodeled pancreas would present high expression. The PDPN expression pattern observed in pancreatic fibrotic areas resembled spindle-like shaped cells encircling cell nests. This antibody clone did not present significant expression in the skeletal muscle cells, appearing specific.

KRT18 is a low-specificity keratin present in most epithelial cells. In this setting, it was highly present in the liver and the pancreas' endocrine and exocrine compartments. Although the specificity of this clone to detect other keratins was not assessed, it allowed the correct labeling of tumor cells.

CD45 is a general immune cell marker. This antibody clone appeared specific according to stainings performed in the skeletal muscle – negative control - and the spleen – positive control. The staining in the spleen was mainly present at the membrane level, revealing an omnipresence along all cell types, as expected. In addition, the stained cells presented a round shape at the morphology level, as also expected. CD45 abundance was also evaluated in the normal and neoplastic pancreas. CD45 expression in these tissues was low-to-moderate, respectively, where it labeled resident immune cells and increased immune infiltration.

Alpha-SMA is a type of actin present in microfilaments and is generally recognized as a hallmark of myofibroblast activation. The expression of this marker is generally inexistent in the normal pancreas and presents a patterned expression profile in the tumor, depending on the activation of myCAFs and pericytes. As demonstrated in the stainings, this antibody clone staining pattern replicated the main morphologic features of myCAFs. The stained cells in the pancreatic tumor and the intestine presented a cytoplasmatic expression associated with spindle-like shaped morphology. When this antibody was evaluated in the intestine, a compartmentalized expression was appreciated, mostly accumulating in the lumen of intestinal villi.

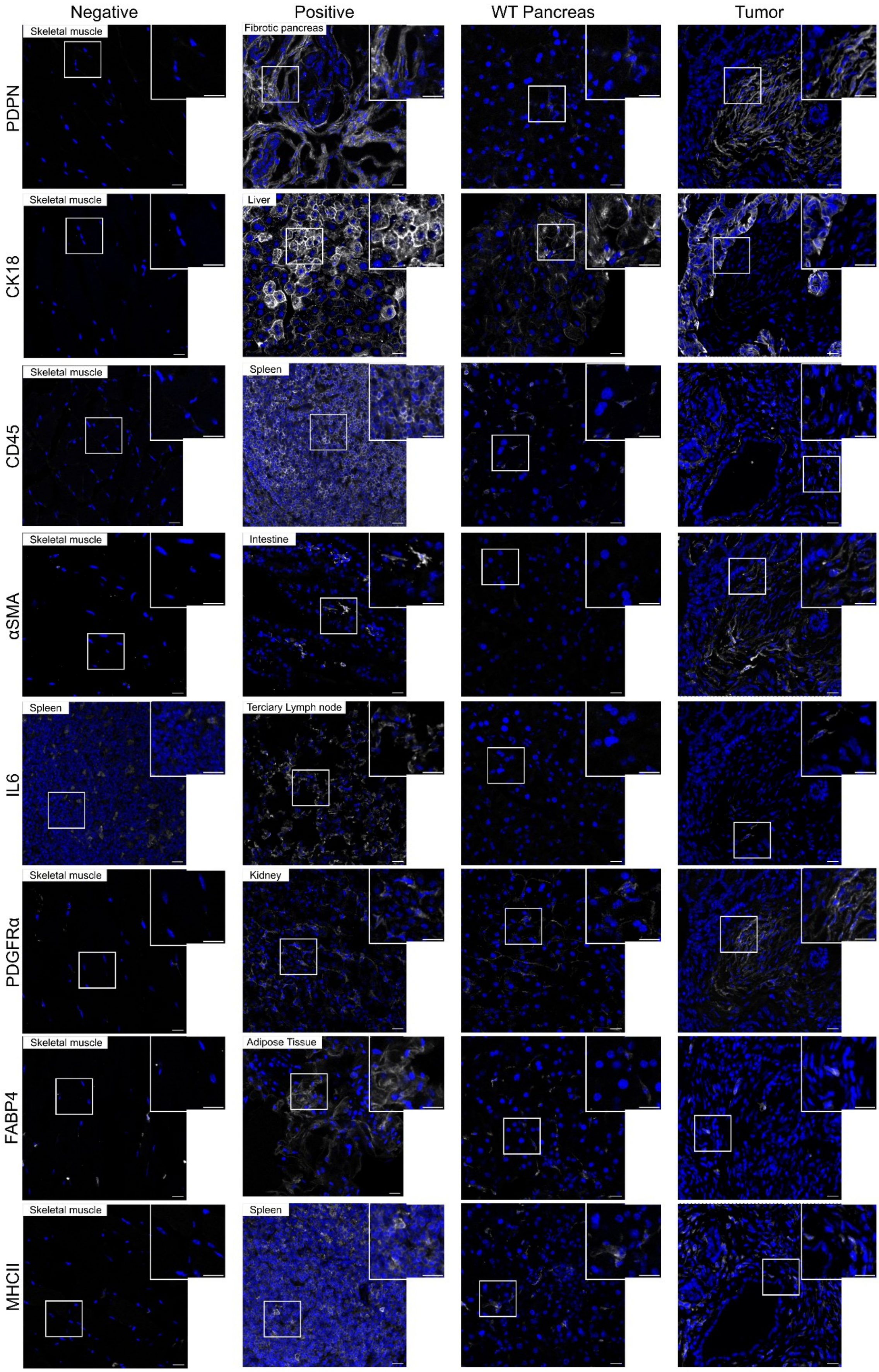

Figure 6 – Validation of primary antibodies against the protein of interest used in the panels.

The antibodies used in the CAFs panels were validated in positive and negative controls. Tissues with high protein abundance were used to confirm expression, while tissues with low protein abundance were used to confirm antibody specificity. The abundance of the protein of interest was also analyzed in the baseline conditions – normal pancreas – and within the disease state – primary pancreatic tumor. Scale bar corresponds to 20 μm.

The expression of IL6 is generally low in healthy tissues and increases with inflammation. Therefore, to validate the IL6 antibody, its expression pattern was assessed in the normal spleen and a tertiary lymph node isolated from a tumor. This IL6 antibody labeled very few cells in the spleen, and its expression increased dramatically in the lymph node. In addition, normal pancreas and tumor samples showed no-to-little IL6 expression, as expected.

PDGFRα is a known CAF marker. The controls selected to validate this antibody were skeletal muscle, as negative, and kidney, as positive control. As expected, the PDGFRα expression in the kidney was restricted to the fibroblasts in the interstitial space, and no staining was detected in the skeletal muscle. When PDGFRα abundance was evaluated in the normal and neoplastic pancreas, it was evident that the expression of this antibody clone was restricted to spindle-like shaped cells.

FABP4 is a protein involved in fatty acid metabolism, expressed in adipocytes, stellate cells, and macrophages. Therefore, skeletal muscle and adipose tissue were selected to validate the expression of this antibody. In this experiment, FABP4 was expressed in the cytoplasm across all cells in the adipose tissue, as expected. In addition, when determining the expression of FABP4 in normal and pancreatic tumor samples, it was possible to visualize the mesenchymal morphology of the positive-expressing cells in the normal pancreas, while in the tumor sample, the FABP4$^+$ cells were less branched. Although the antibody staining appeared specific, the expression of FABP4 in these tissues was low.

MHCII is a membrane marker of antigen-presenting cells. Therefore, it would be highly expressed in the spleen, where the staining pattern was mostly present around the germinal centers. In addition, the negative control – skeletal muscle – presented no-to-little staining. As expected, the normal pancreas showed a very low abundance of MHCII-positive cells with an increased amount in the tumor samples.

Table 15 summarizes the antibodies used in this workflow and the host species where the antibodies were produced.

Table 15 – Overview of the antibodies used in the workflow

Marker	Category	Host
KRT18	SAB4501665	Rabbit
PDPN	14-5381-82	Armenian hamster
CD45	MCA1031G	Rat
PDGFRα	14-1401-82	Rat
αSMA	Ab5694	Rabbit
IL6	AF406-NA	Goat
FABP4	AF1443	Goat
MHC-II	107605	Rat

The last step in the panel design is the attribution of the fluorophores to detect the protein of interest. Therefore, the spectral working range and the available fluorophores must be considered together with each selected marker's expression levels to assign a fluorophore successfully.

As previously stated, the confocal microscope selected for this workflow has advantages and limitations. The availability of an in-house microscope brings increased flexibility in the instrument usage, although the panel design must be limited to 6 colors to minimize spectral overlap and spillover between fluorescent channels. The confocal microscope offered two lasers for fluorophore excitation: an UV laser and a white light laser, with a range of excitation from 470 nm to 670 nm. The allocation of the fluorophores was done based on spectral overlap analysis using online tools, such as the Thermofisher spectraviewer. To sparse the markers as much as possible, the excitation with the UV laser would require a fluorophore with a maximum excitation value of 405 nm, and the white light laser would excite fluorophores that presented maximum excitation values around 488, 555, 594, 647, and 680 nm. Since the KRT18 showed very bright staining, it was consequently assigned to the infrared region and the fluorophore Alexa-fluor 680. PDPN showed a dimmer expression, and the best results surged when combined with the fluorophore Alexa-fluor 647. Therefore, since the infrared region would be allocated to the proteins of interest as PDPN and to keep the bright green-orange region available to other markers, the counterstaining chosen was DAPI. These markers would be part of both panels and were kept under the same fluorophores.

Table 16 – Fluorophore allocation in Panel 1

Marker	Secondary Antibody	Fluorophore
KRT18	-	Alexa-fluor 680
PDPN	Goat anti-armenian hamster	Alexa-fluor 647
PDGFRα	Donkey anti-rat	Alexa-fluor 488
αSMA	Goat anti-rabbit	Cy3
IL6	Donkey anti-goat	Alexa-fluor 594
Nuclei	-	DAPI

The allocation of IL6, αSMA, CD45, FABP4, MHCII, and PDGFRα would fall on the green and orange regions of the spectrum. For Panel 1, since IL6 expression was low in the pancreas, it was allocated to Alexa-Fluor 594. The remaining PDGFRα and αSMA were assigned to Alexa-fluor 488 and Cy3, respectively. Table 16 summarizes the allocation of the fluorophores in Panel 1.

Table 17 – Fluorophore allocation in Panel 2

Marker	Secondary Antibody	Fluorophore
KRT18	-	Alexa-fluor 680
PDPN	Goat anti-armenian hamster	Alexa-fluor 647
MHC-II	-	Alexa-fluor 488
CD45	Goat anti-rat	Alexa-fluor 555
FABP4	Donkey anti-rat	Alexa-fluor 594
Nuclei	-	DAPI

In Panel 2, since two markers were produced in rats, MHCII was selected conjugated with the Alexa fluor 488 fluorophore. Therefore, CD45 and FABP4 were assigned to Alexa-fluor 555 and 594, respectively. Table 17 summarizes the fluorophore allocation in Panel 2.

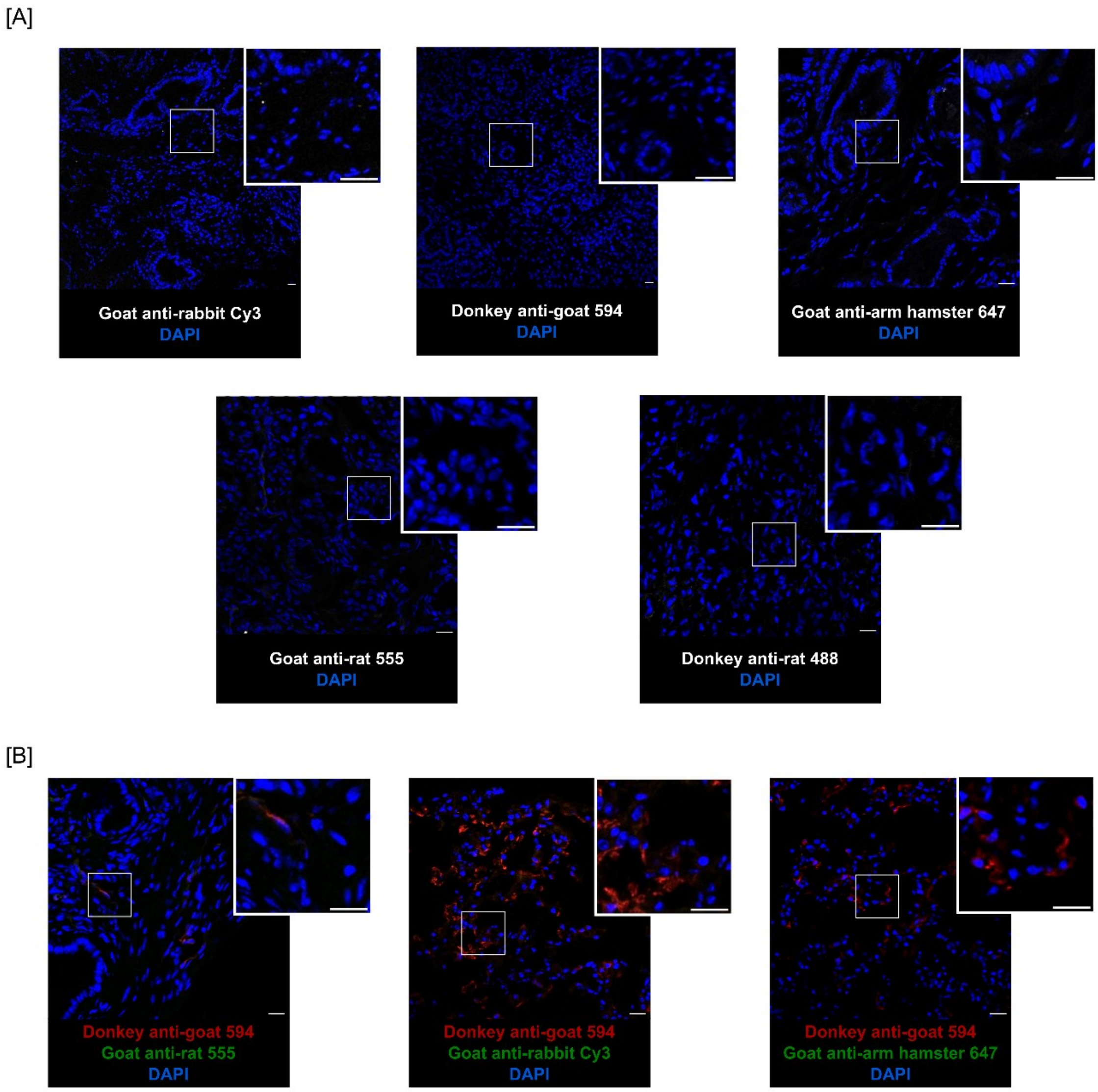

Figure 7 – Secondary Antibody and cross-reaction controls.

[A] Secondary antibody controls. Tumor samples were incubated with the secondary antibodies used in this workflow without a primary antibody to analyze unspecific binding. Scale bar corresponds to 20 µm.

[B] Cross-reaction controls corresponding to both panels. The samples were incubated with the primary antibody produced in goat and consequent Donkey anti-goat 594. Following blocking with goat serum, the samples were incubated with either goat ant-rat 55, goat-rabbit Cy3, or the goat anti-armenian hamster 647 to evaluate cross-binding between the antibodies. Scale bar corresponds to 20 µm.

Cross-reactions between primary and secondary antibodies might occur and generate false positive results. Therefore, strategies can be deployed to block unspecific binding and cross-binding between antibodies. Different cross-reactions might occur. On the one hand, the secondary antibody might react with other immunoglobulins in the tissue and bind unspecifically. The secondary antibodies used in this workflow were incubated with the tissue without a primary target to evaluate the presence of a fluorescent signal. In Figure 7-A, it can be appreciated that the secondary antibodies did not bind unspecifically to the sample, being therefore suitable to use in this protocol.

On the other hand, cross-reactions might occur from the cross-biding of secondary antibodies. If two primary antibodies are derived from the same animal, they will exhibit the same fluorophore pattern when targeted with a secondary antibody. Therefore, selecting primarily conjugated antibodies avoids the problem of secondarily targeting primary antibodies derived from the same host. In Panel 1, KRT18 was conjugated with the Alexa-fluor 680 to avoid cross-reactivity with αSMA, also produced in rabbits. In Panel 2, MHCII was purchased conjugated, and the CD45 primary antibody could be targeted with a secondary antibody. In addition, primary and secondary antibodies derived from the same host may react with each other originating a false-positive signal. On that account, the order of the incubations can be optimized to exclude those effects. For example, in Panel 1, the secondaries goat anti-rabbit Cy3 and goat anti-armenian hamster 647 could bind to the goat IL6 primary antibody available free binding spots, even after targeting that antibody by the donkey anti-goat 594. The solution to this issue is to saturate those free binding spots on the goat IL6 antibody after incubating with the donkey anti-goat 594, using a goat serum. Then the secondary goat anti-rabbit Cy3 and goat anti-armenian hamster 647 can be used. The same rationale was used in all the other possible cross-reactions. The cross-reaction controls are depicted in Figure 7-B.

The validation of the primary and secondary antibodies and the optimization of the incubation order resulted in the implementation of reliable stromal panels to profile CAFs populations in PDAC. These panels were imaged following a strategy to minimize the spillover between fluorescent channels. In both Panel 1 and Panel 2, the fluorophores were divided into two imaging sequences, allowing a better separation between the excitation and emission window of the fluorophores. The generation of these multiplex images is the core of a workflow that allows the extraction of single-cell data, resulting in the generation of datasets that accurately capture the stromal heterogeneity and architecture in PDAC.

4.1.1.3 Analysis of multiplex imaging data using supervised Imaris cell based-segmentation

The analysis of multiplex imaging data is complex and is a current field in development. This analysis comprises the processing of raw multiplex images, single-cell segmentation, cell type annotation, and spatial analysis. Several software programs are available to process and analyze multiplex tissue imaging data, following two main approaches. One is an unsupervised approach that uses the K-nearest neighbor algorithm to estimate cell type clusters according to user-selected marker intensities (Black *et al.*, 2021; Schurch *et al.*, 2020). The other is a supervised segmentation approach where cell types were retrospectively defined by well-defined markers. Imaris is a supervised, computationally friendly platform that segments cells with well-defined markers.

Imaris presents two alternatives to segment images: the surfaces module and the cells module. The surfaces module creates an object using the threshold of the channel of interest, which can be further refined by adding other parameters. The cells module allows the detection of cells with cytoplasmatic or membrane signals based on expanding the segmentation from previously identified nuclei. Both segmentation modules were tested to understand which one would perform better. The cells module presented a more accurate segmentation of CAFs populations than the surface module, despite its good results in segmenting immune populations.

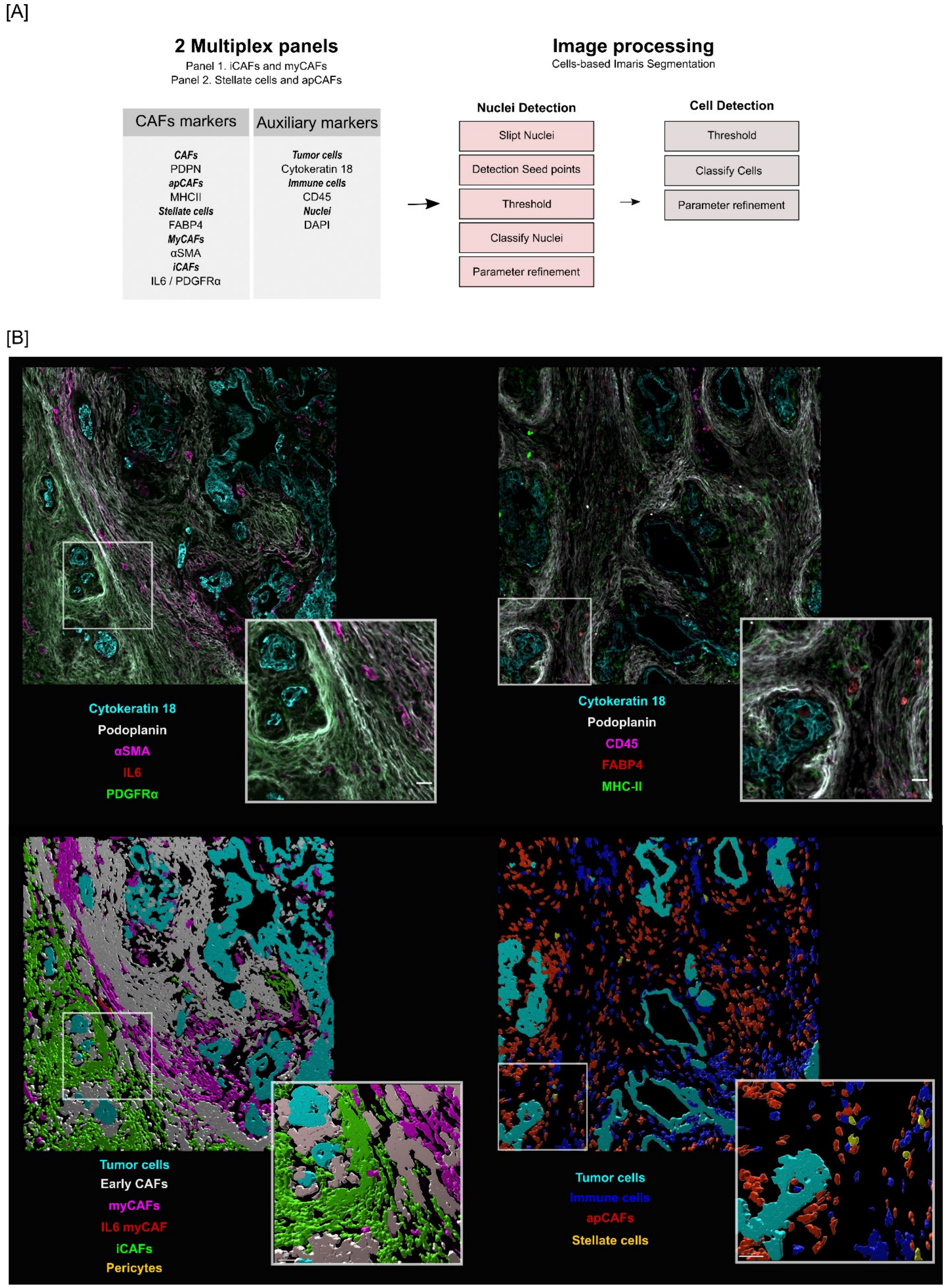

Figure 8 – Imaris Cells-based segmentation overview.

[A] Graphical scheme elucidating the Cells-based segmentation workflow. The samples were stained with CAFs markers and auxiliary markers using two panels. In each panel, two regions were imaged and segmented with the Cell-based algorithm in Imaris. The segmentation using the cell module first determined the presence of nuclei. This determination followed several consecutive steps, such as nuclei split, determination of seed points, and nuclei threshold. Then, additional parameters could be manipulated to segment the nuclei better. The final part of the segmentation is the cell body determination, which starts with the threshold of the signal of a marker of interest. Again, many parameters could be altered, such as cell area and mean intensity of other markers, to segment a cell type accurately.

[B] Representative images of each panel (top) and correspondent segmentation (bottom). On the left, Panel 1, which phenotypes myCAFs and iCAFs related populations, is depicted. On the right, Panel 2 shows the apCAFs, stellate cells, and immune populations found in the TME. The scale bars correspond to 20 µm in the top images and 50 µm in the bottom.

An overview of the Imaris cells-based segmentation is depicted in Figure 8-A. First, PDAC samples were stained and imaged. Then, the cells method was applied to the images the number of times necessary to create a segmented model of each desired cell population. This method initially detected all the nuclei and was followed by a threshold of the cytoplasmatic/ membrane channel of interest. The nuclei detection comprised several steps, such as nuclei split, DAPI signal threshold, and additional size and signal intensity adjustments. Next, cell body detection is initiated with a threshold on the signal of the marker of interest. One segmented object is created when the threshold of the marker of interest matches with one of the detected nuclei. Finally, the segmentation could be further refined by filtering the intensity levels of the other markers to represent the cell population accurately. An example of the segmentation for all the targeted cell populations is portrayed in Figure 8-B.

Since the segmentation using Imaris' cells module performed well, this program was integrated into the workflow.

4.1.2 Cohort selection was supported by histopathological analysis

The characterization of the stromal TME in PDAC was performed by deploying the multiplex immunofluorescence panels in a selection of tumor samples. The tumor samples were picked from Professor Dr. med Dieter Saur's laboratory murine biobank using histopathological analysis.

This characterization aimed to identify context-specific CAFs activation within the most relevant subtypes of PDAC. The cohort selection for analysis started from the thousands of animal samples available and is described in Figure 9-A. The initial step was the selection of the samples where a piece of tumor was cryopreserved. Next, a further filter was applied, and animals that presented *Kras*^{G12D}, *Pi3kca*^{H1047R}, and a *Braf*^{V637E} mutation were selected. Any additional deletion or mutation besides *Trp53* was excluded. Then fresh-frozen tissue samples were randomly selected, and around 90 mouse samples were analyzed histopathologically using H&E staining.

The histopathological evaluation goal was to determine which samples would be selected for further analysis. After carefully evaluating the H&E tumor samples, the ones that did not present the minimum quality parameters established were excluded. The amount of tissue available to characterize was one reason tumor samples would not be selected. Excluding tissues with extensive necrotic areas would also guarantee that this factor would not influence the characterization. In addition, an analysis to confirm that the samples were indeed a tumor was performed. Finally, this workflow would lead to a pre-selection of 24 tumor samples, where 16 were selected for further imaging and analysis.

The characteristics of the cohort analyzed in this workflow are described in Figure 9-B. Of the 16 tumors selected, 12 presented a *Kras*^{G12D} mutation, and 4 presented a *Pi3kca*^{H1047R} mutation. No *Braf*^{V637E} tumors were included in this analysis because none of the samples available was characterized as PDAC. The schemes representative of the GEMMs used in this study are depicted in Figure 9-C. The murine PDAC arose from the activation of the *Kras*^{G12D} and *Pi3kca*^{H1047R} under the *p48* or the *Pdx1* promoter after Cre-mediated stop cassette excision. In addition, those animals could bear an additional *Trp53* deletion or loss-of-function mutation (R172H).

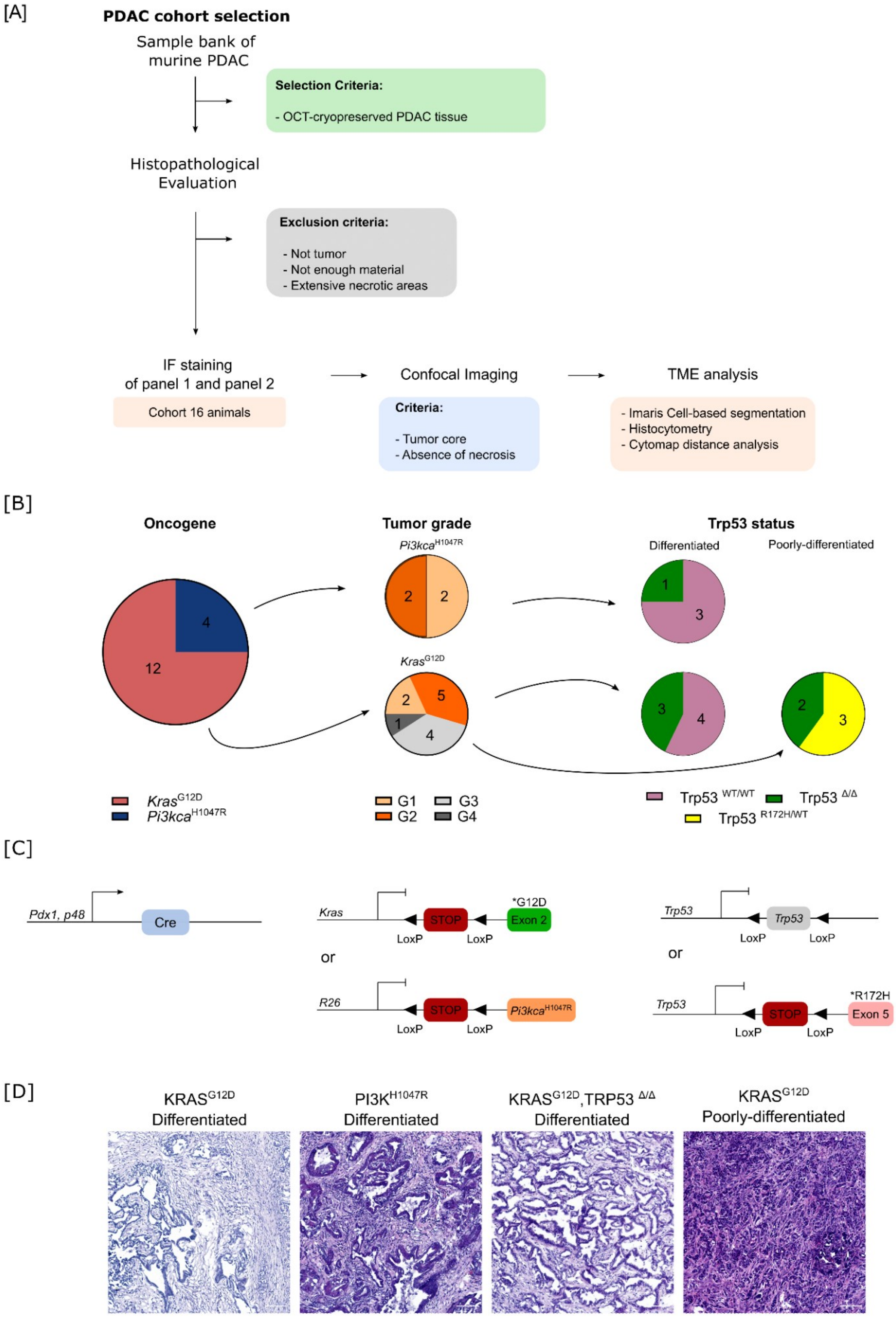

Figure 9 – PDAC study cohort design.

[A] Workflow of the study to characterize stromal TME in PDAC. The specimens selected were present in a murine sample bank. The tissues cryopreserved in OCT were selected for further pathological evaluation. The samples not histologically categorized as Adenocarcinomas were discarded, similarly to those with a high degree of necrosis or a small tissue size. The selected specimens were processed, imaged, and analyzed as previously described.
[B] Distribution of the cohort across oncogenic-driver, degree of differentiation, and initial TRP53 status
[C] PDAC GEMMs used in the stromal TME characterization. The animals that developed tumors presented the Cre recombinase expression under the p48 or the Pdx1 promoter (left panel) to activate the oncogenic driver – *Kras*^{G12D} or *Pi3kca*^{H1047R} - in pancreatic cells (middle panel). These cells could additionally harbor a deletion or a loss-of-function *Trp53* mutation (right panel).
[D] Representative H&E staining of the groups analyzed. The scale bar corresponds to 100 µm.

Acknowledgments: The animals used in this study were bred and sacrificed by all the members of AG Saur. The histopathological analysis and cohort selection were performed together with Tania Santos.

Both KRAS^{G12D} and PI3K^{H1047R} groups were classified according to grade. To simplify the analysis, tumors that exhibit well-to-moderate differentiation features formed the differentiated group, and tumors with no-to-little differentiation features were assigned to the poorly-differentiated group. Overall, in the KRAS^{G12D} group, the differentiation ratio was similar, with 7 differentiated and 5 poorly-differentiated tumors. However, the situation differed in the PI3K^{H1047R} group, which presented a higher representation of differentiated tumors. *Trp*53 is one of the most mutated genes in PDAC, where the expression of TRP53 is affected by deletions or loss-of-function mutations. The cohort in this study presented *Trp53* alterations introduced from embryogenesis. Approximately half of the tumors in the KRAS^{G12D} group presented *Trp53* alterations independently of the differentiation status, whereas, in the PI3K^{H1047R}, *Trp53* alterations were not introduced in most tumors. Representative examples of the tumor degree of differentiation in this study are shown in Figure 9-D.

4.1.3 Multiplex immunofluorescence enables the characterization of CAFs populations in PDAC

The multiplex immunofluorescence workflow optimized and described in this thesis was deployed on the 16 mouse samples to identify CAFs populations and understand how they shape the TME in PDAC (Figure 10-A).

The 8 markers used along the two panels allowed the identification of 12 groups of cells. The cell populations identified were the 6 subtypes of CAFs, stellate cells, pericytes, tumor cells and MHCII^{+} immune cells (APC immune cells), and MHCII^{-} immune cells (non-APC immune cells). Populations that could not be phenotyped by the markers used were assigned to the other cells group. The abundance of all the cell populations identified was used as variables to perform a multivariate analysis to understand how heterogenous the whole cohort was (Figure 10-B). Even though the PCA analysis showed that the samples scattered along components 1 and 2, the degree of differentiation appeared to affect the stromal TME in PDAC.

The cell populations abundance is depicted in Figure 10-C and was calculated as a percentage of the cell population within the whole TME. Tumor cell abundance was heterogeneous across the samples. Some samples presented a very high content of tumor cells (up to 70%). This was most common in poorly-differentiated samples. Furthermore, as described in Figure 10-D, tumor cell abundance negatively correlated with early myCAFs ($r = -0.78$, $p = 0.001$) and iCAFs ($r=-0.52$, $p=0.043$).

This means that in samples with a low abundance of tumor cells, there is a high content of early myCAFs and iCAFs.

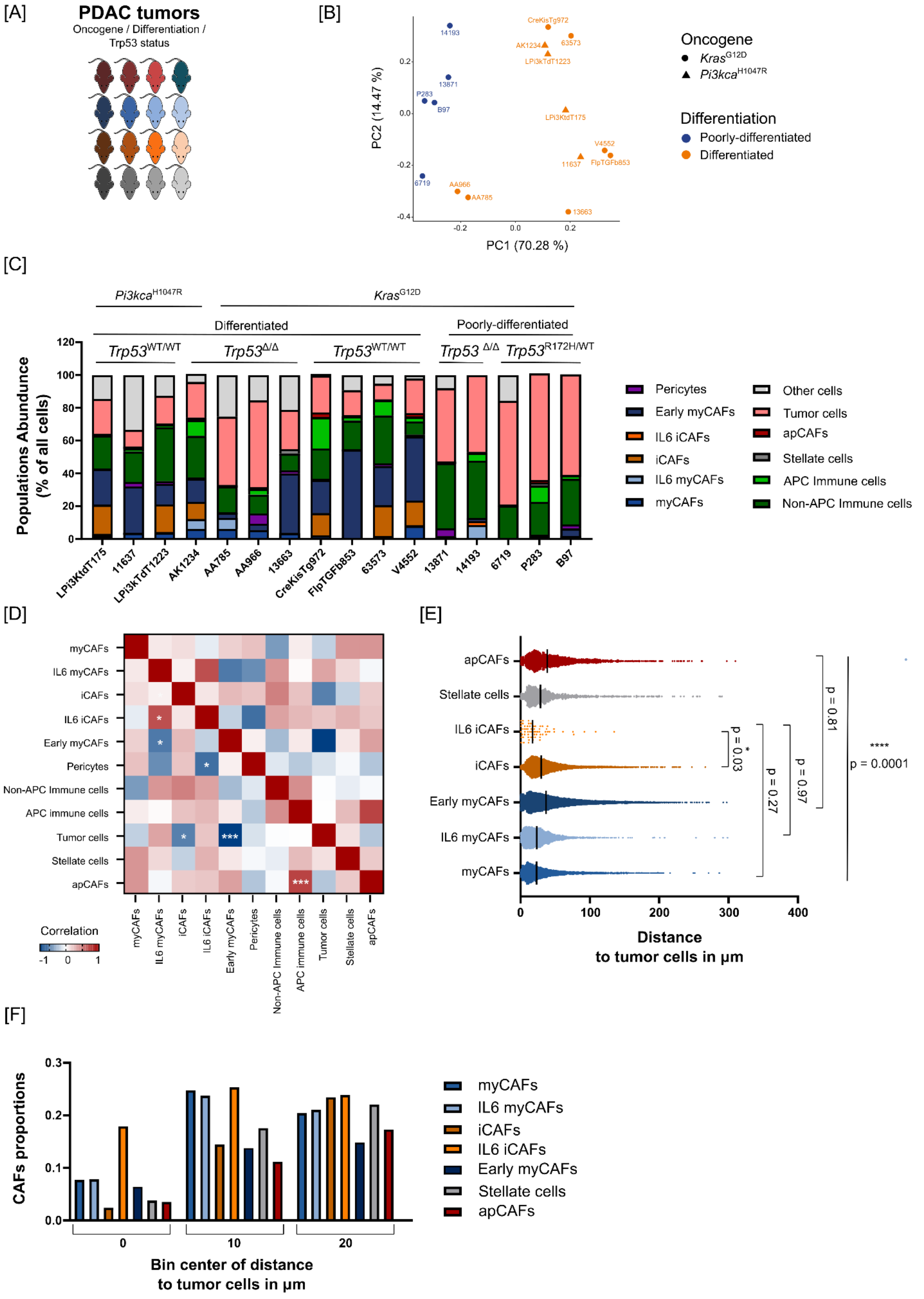

Figure 10 – Characterization of the PDAC stromal TME: composition and CAF-tumor cell interactions.

[A] Cohort for characterization of PDAC stromal TME. This cohort presents several different features and can be further grouped based on the oncogenic driver, the differentiation status of the tumor, and *Trp53* deletion (n= 16).

[B] Multivariate data analysis of the stromal TME Cohort. The PCA was performed using all cell types in the PDAC stromal TME as variables. PC1 and PC2 were plotted to depict the samples' relationships. A further layer of stratification was added to portray the tumors with different differentiation statuses and oncogenic drivers. Tumor samples were depicted with circles (*Kras*^{G12D}) or triangles (*Pi3kca*^{H1047R}) depending on the oncogene used to induce tumorigenesis. After the histopathological analysis, tumors categorized as G1 or G2 were assigned to the differentiated group (in orange), and those categorized as G3 or G4 were assigned to the poorly-differentiated group (in blue).

[C] Composition of the TME in PDAC. The multiplex images were analyzed, and the cell types were segmented and quantified. Each cell population was normalized by the total number of cells.

[D] Matrix of the Spearman correlation coefficients of the pairwise cell populations present in the PDAC TME. The significantly correlated pairs were highlighted using asterisks: * corresponds to $p < 0.05$, ** corresponds to $p < 0.01$, and *** corresponds to $p < 0.001$.

[E] Median distance of each CAF subpopulation to tumor cells. Each dot corresponds to one cell. All possible comparisons were tested using an ANOVA with a post hoc Tukey multi-comparison correction. The significant interactions were highlighted using asterisks: * corresponds to $p < 0.05$, and **** corresponds to $p < 0.0001$. The interactions between myCAFs-IL6 myCAFs, myCAFs-iCAFs, myCAFs-early myCAFs, myCAFs-Stellate cells, myCAFs-apCAFs, IL6 myCAFs-iCAFs, IL6 myCAFs-early myCAFs, IL6 myCAFs-stellate cells, IL6 myCAFs-apCAFs, iCAFs-early myCAFs, iCAFs-stellate cells, iCAFs-apCAFs, IL6 iCAFs-early myCAFs, IL6 iCAFs-stellate cells, IL6 iCAFs-apCAFs, early myCAFs-stellate cells, and stellate cells-apCAFs generated a p-value inferior to 0.0001. The interactions between apCAFs-early myCAFs, IL6 iCAFs-iCAFs, IL6 iCAFs-myCAFs, and IL6 iCAFs-IL6 myCAFs resulted in p values of respectively $p = 0.81$, $p = 0.03$, $p = 0.27$, and $p = 0.97$.

[F] Frequency distribution of CAFs subpopulations distance to tumor cells. The frequency of the distribution of all CAFs subpopulations is depicted in the bar plot with a 25 µm diameter. The bin size is 10 µm and is centered at 0, 10, and 20 µm, meaning that for each center, the CAFs are calculated using the intervals [0,5],]5,15], and]15, 25].

Acknowledgments: The animals used in this study were bred and sacrificed by all the members of AG Saur.

Cancer-associated fibroblasts content was also highly heterogeneous. In this characterization, tumors presented a CAFs abundance range from approximately 0.6% to 65%. When analyzed closely, early myCAFs were the most represented CAF population and can make up 0.1% to 55% of the tumor. However, there was no clear pattern of preferential activation of early myCAFs. In addition, early myCAFs were the population that presented one of the highest distances to tumor cells (a median of 37 µm), and only approximately 5% of them were in close contact with tumor cells, as can be appreciated in Figure 10-E and Figure 10-F.

As an “endpoint” population, myCAFs had low overall abundance in this cohort, which was unexpected. MyCAFs abundance was approximately 3%, although, in some tumors, it could make up almost 10% of all cells. Nevertheless, approximately half of myCAFs were in close contact with tumor cells, and the median distance was approximately 23 µm. In addition, IL6 myCAFs-tumor cell neighborhood profile was very similar to myCAFs with a median distance of approximately 23 µm and approximately 50% of the cells close to tumor cells. However, the IL6 myCAFs abundance mean was below 2%, presenting an expression pattern mostly in tumors with altered TRP53. Additionally, IL6 myCAFs were inversely correlated with early myCAFs ($r=-0.54$, $p=0.03$) but positively correlated with IL6 iCAFs ($r=0.689$, $p=0.002$), as shown in Figure 10-D.

The iCAFs presence in the TME was compartmentalized to the samples where *Trp53* was not deleted, and the tumor cell content was reduced. In some tumors, iCAFs content made up 20% of all cells despite a mean abundance of approximately 6% across the cohort. As expected, iCAFs were not highly present around tumor cells, where the median distance between iCAFs and tumor cells was 30 µm, and the distribution of these cells in the immediate tumor cell neighborhood is lower when compared with myCAFs-related populations. However, IL6 myCAFs mingled with tumor cells to a much greater extent. More than 50% of IL6 iCAFs were located in the immediate vicinity of tumor cells with a median distance of 17 µm. In point of fact, IL6 iCAFs were a rare population in PDAC TME with an abundance range of 0 to 2.5 %.

In this study, apCAFs were a rare population in the PDAC TME, presenting a mean abundance inferior to 1%. Although the apCAFs content peaked at 3% in some tumors, no preferential activation pattern was detected. Moreover, apCAFs positively correlated with immune cells that expressed MHCII ($r=0.73$, $p=0.002$). ApCAFs, though, were not in close contact with tumor cells. Distance analysis between apCAFs and tumor cells showed that the mean distance between these cell types was 39 µm, with only 25% of cells located within 20 µm.

As expected, the content of quiescent, lipid-retaining stellate cells was low in tumors. It appeared that most stellate cells were activated and gave rise to CAFs. Furthermore, the remaining lipid-retaining stellate cells were not located close to tumor cells. The mean distance between stellate cells and tumor cells was 29 µm, and approximately 40 % of the cells were within 20 µm of tumor cells.

Immune populations made up a significant part of the PDAC TME. In this work, immune cells were not profiled, but antigen-presenting and non-antigen-presenting immune cells were determined. Generally, the immune content in this cohort presented a variable abundance. For example, tumors with the lowest immune infiltration presented approximately 10% of $CD45^+$ cells and the highest approximately 40% of cells. In addition, it was evident that antigen-presenting immune cells were deficient in some tumors, suggesting that the activation of a functional immune response against tumor cells may be impaired.

Altogether, this workflow enabled the characterization of the stromal TME in PDAC, providing information about their content and spatial location. However, a higher multiplex capacity is needed to phenotype all cell types in the tumor, such as immune cell types and endothelial cells that could not be phenotyped and were attributed to the other cells group.

4.1.4 Characterization of oncogene-induced stromal TME activation in PDAC

A first glance at the stromal TME in PDAC showed heterogeneity. Nevertheless, the multivariate analysis suggested that tumor-intrinsic characteristics could shape the activation of CAFs. PDAC tumors are driven mainly by KRAS gain-of-function mutations which signal downstream through PI3K-PDK1 and MEK-ERK axis. Therefore, tumors with $KRAS^{G12D}$ and $PI3K^{H1047R}$ driver mutations were benchmarked to understand how the tumor cell oncogenic program may drive stromal TME activation and maintenance.

The PDAC tumor cohort analyzed was stratified into different groups, as described in Figure 11-A. First, tumors that retained differentiated features were divided according to the oncogenic driver: $Kras^{G12D}$ or $PI3K^{H1047R}$. The $Kras^{G12D}$ group was composed of 7 tumors that could harbor a *Trp53* deletion, and the $PI3K^{H1047R}$ group was composed of 4 animals, with only one sample deficient for *Trp53*.

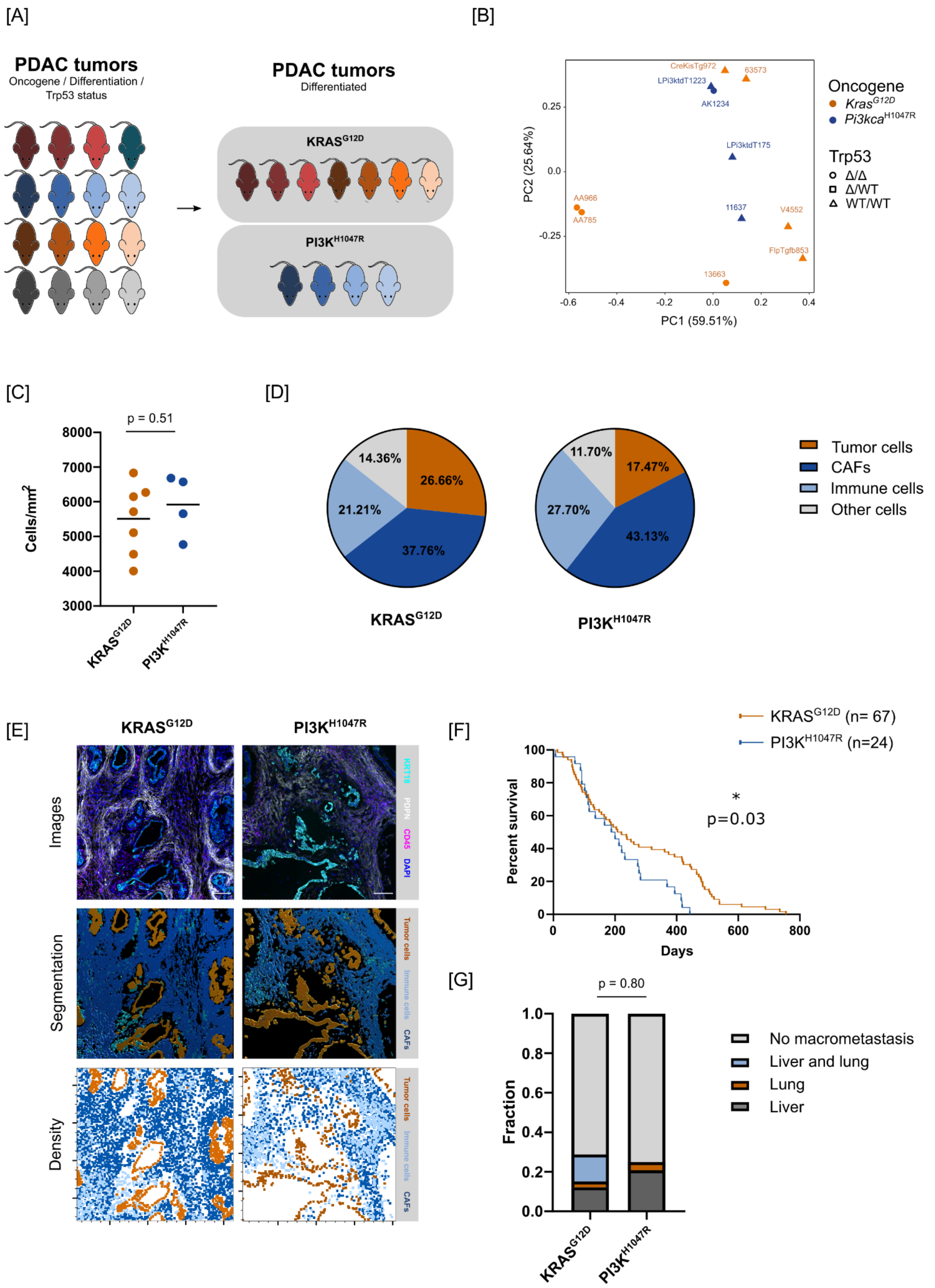

Figure 11 – The oncogene does not drive significant changes in the TME of PDAC, independently of its impact on survival.

[A] Cohort used to characterize differences in the TME driven by different oncogenes. The initial cohort presents several different features and can be further grouped based on the oncogenic driver, the differentiation status of the tumor, and Trp53 deletion. The grouping of the samples analyzed in this figure was based on the oncogene driving tumorigenesis. The animal samples categorized as differentiated were selected for this analysis and were allocated to the KRAS^{G12D} (n=7) or the PI3K^{H1047R} (n=4) group.

[B] Multivariate data analysis of the cohort. The PCA was performed using all cell types in the PDAC stromal TME as variables. PC1 and PC2 were plotted to depict the relationships between the samples. The samples were highlighted in orange (*Kras*^{G12D}) or blue (*Pi3kca*^{H1047R}) depending on the oncogene driving the tumors. A further layer of stratification was added to portray the tumors with deletion of the *Trp53* wild-type allele from tumorigenesis. Tumor samples were depicted with circles, squares, or triangles depending on if a complete loss of *Trp53* (*Trp53*$^{\Delta/\Delta}$), just one allele (*Trp53*$^{\Delta/WT}$), or if no alterations (*Trp53*$^{WT/WT}$) were introduced from tumorigenesis.

[C] Cellularity of the tumor samples per group. The cellularity represents the number of nuclei present in the whole area of the images analyzed for each tumor sample. Each dot represents the mean of the measurements made for each specimen. An unpaired t-test with Welch correction was performed to evaluate significant differences between both groups.

[D] Composition of the TME in KRAS^{G12D} and PI3K^{H1047R} tumors. The pie charts describe the composition of Tumor cells, CAFs, Immune cells, and other types of cells in the TME. Every population was subjected to an unpaired t-test with a Welch correction to test for significant differences between the groups. Post hoc correction for multiple comparisons was not performed. No statistically significant differences were observed between the groups.

[E] Representation of the immunofluorescence images, segmentation, and histocytometry analysis for the KRAS^{G12D} and PI3K^{H1047R} groups. The scale bar is 100 µm.

[F] Survival analysis comparing differentiated KRAS^{G12D} (n=67), in orange, and PI3K^{H1047R} (n=24), in blue, models using the Kaplan-Meier curve. The Log-rank test was deployed, generating a significant difference between the groups (*corresponds to p = 0.03).

[G] Metastization potential. The macrometastasis, annotated when the animal was sacrificed, are represented in the bar plot. No significant changes in metastization potential or the preferred metastization site occurred in tumors driven by KRAS^{G12D} compared to those driven by PI3K^{H1047R}. The differences were evaluated using the two-sided Fisher's exact test.

Acknowledgments: The animals used in this study were bred and sacrificed by all the members of AG Saur. The histopathological analysis of the cohort used to perform multiplex IF was done together with Tânia Santos. The histopathological analysis that allowed the identification of differentiated tumors in [F] and [G] was performed by Chen Zhao and Moritz Jesinghaus.

The general abundance of all detected populations was calculated in percentage of all cells, and a principal component analysis was performed using all populations as variables. The high variance between the samples is depicted in Figure 11-B, scattering along the PCA map, revealing no major TME changes between both groups. Indeed, when the major cell groups – Figure 11-D - were compared between KRAS^{G12D} and PI3K^{H1047R} groups, no significant changes were detected concerning tumor cells (p=0.28), immune cells (p=0.37), and CAFs (p=0.61) numbers. Tumor cell content in Kras^{G12D} was higher, representing approximately 26.60±15.29% of all cells compared with 17.45±5.43% in PI3K^{H1047R} tumors. Nonetheless, immune cell infiltration was slightly higher in PI3K-driven tumors accounting for 27.70±8.15% of the cells, wherein Kras^{G12D} tumors comprised approximately 21.21±12.01% of cells. CAFs were the most abundant population in both groups, making up 37.76±19.47% and 43.13±4.78% of cells in KRAS^{G12D} and PI3K^{H1047R} tumors, respectively.

In addition, the tumors presented similar cellularity, indicating that an equal number of cells were analyzed, and no significant necrotic and decellularized parts of the tissue were included in the analysis – Figure 11-C. As a matter of fact, this can be corroborated by the histocytometry analysis performed and showcased in Figure 11-E. With this analysis, it can be appreciated that CAFs were the most abundant populations, occupying the tumor indiscreetly. Moreover, tumor cells were located in nests surrounded by immune cells and CAFs.

Additionally, there were clinical features altered between the groups. Although differentiated KRAS-driven tumors present a significant survival advantage compared to the differentiated KRAS^{G12D} cohort, the median survival between groups was approximately 200 days (KRAS^{G12D}: 214.5 days; PI3K^{H1047R}:

194 days). Additionally, no differences in macrometastasis formation frequency (p=0.80) nor preferential metastization sites were observed.

Further differences in the stromal compartment, CAFs-tumor cell interactions, and tumor architecture were assessed to understand if KRAS^{G12D} and PI3K^{H1047R} oncogenic signaling produced differences at the cellular level.

4.1.4.1 PI3K^{H1047R} stromal compartment activation resembles KRAS^{G12D} tumors in differentiated PDAC

To understand the differences in stromal activation between KRAS and PI3K-driven tumors, CAFs population abundance within all cells and all CAFs was calculated. In most differentiated tumors, independently of the oncogenic driver, CAFs represented more than 40% of the TME – Figure 12-A. Nevertheless, the CAFs subpopulation's abundance was heterogenous, and no differential pattern emerged between the groups.

The subpopulation frequencies within the CAFs groups are shown in Figure 12-B. Early myCAFs were the most abundant population, comprising 55.93±29.21% of Kras^{G12D} CAFs populations and 50.97±24.88% of PI3K^{H1047R}. Since the variance in early myCAF content was high, no differences were observed between the groups in this population (p=0.78). Similarly, most CAFs populations' abundance remained unaltered. No statistical differences were observed between the groups in the abundance of IL6 myCAFs (p=0.93), stellate cells (p=0.39), and apCAFs (p=0.70). IL6 myCAFs made up 6.22±16.10% of CAFs in KRAS^{G12D} against 5.38±7.48% in PI3K^{H1047R}. Stellate cell abundance was very low in both groups, with a mean abundance of 2.09±2.61% in KRAS^{G12D} and 0.85±0.81% in PI3K^{H1047R} total amount of CAFs. Additionally, apCAFs mean abundance was low and variant, with a mean percentage of 2.47±2.61% and 1.78±3.14% in the overall CAF distribution of KRAS and PI3K-driven tumors, respectively.

An exception was iCAFs, where slight changes in mean abundance were observed between the groups (Kras^{G12D} - 14.91±19.36%, PI3K^{H1047R}- 29.93±21.74%). However, no statistical significance was derived (p=0.27). In addition, IL6 iCAFs were not detected in KRAS^{G12D} tumors, and in the PI3K^{H1047R} group, the abundance within CAFs was below 0.1% (p=0.16).

Myofibroblasts were also slightly altered between both groups, with a mean abundance of 18.38±21.65% in KRAS^{G12D} and 10.99±5.03% in PI3K^{H1047R}. However, the high sample variance originated non-significant results (p=0.53).

Overall, CAFs composition between KRAS and PI3K-driven tumors is very similar, and additional tumor cell characteristics may likely influence CAFs activation in PDAC.

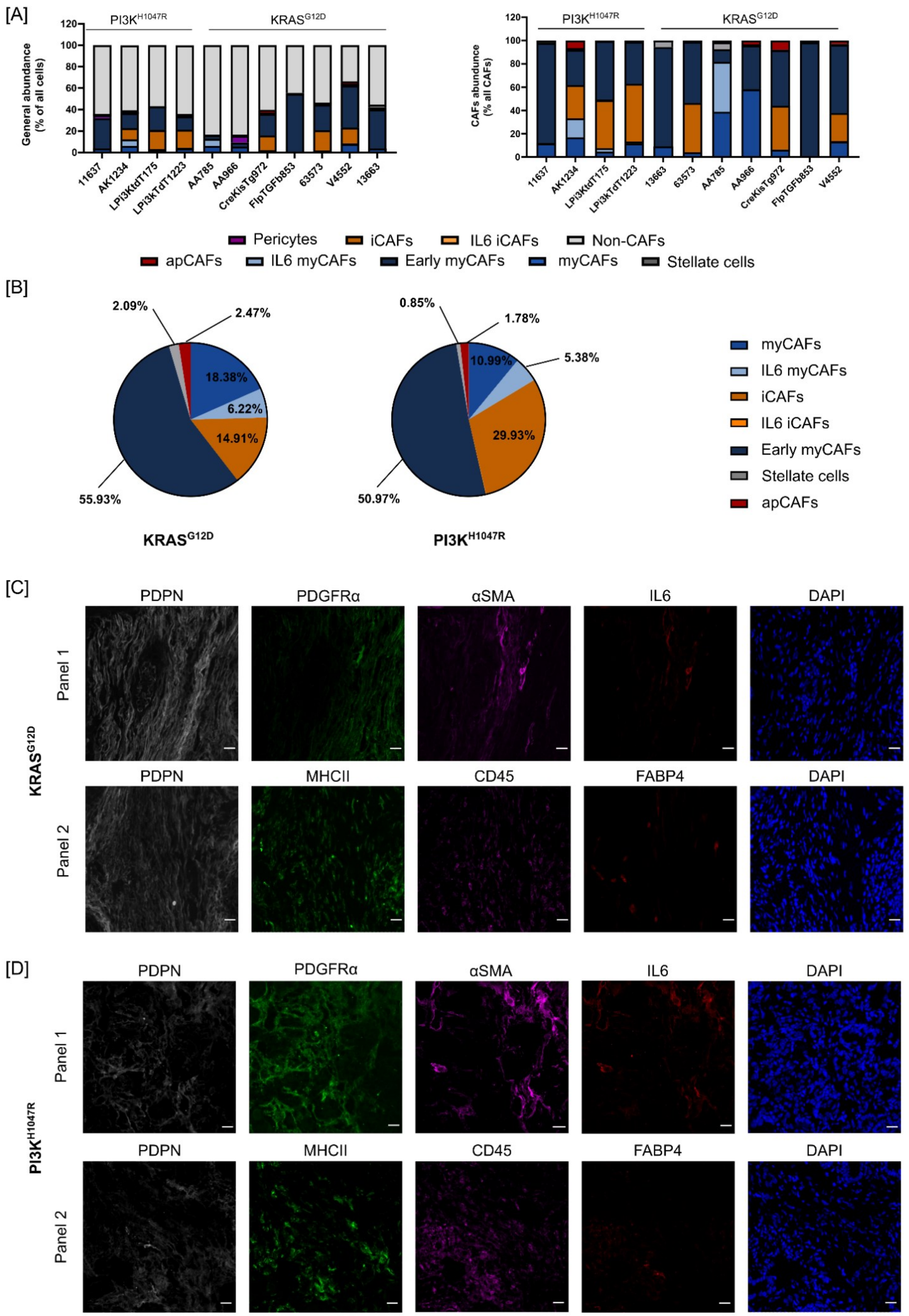

Figure 12 – The PI3K^{H1047R} activation in differentiated PDAC does not impact the stromal microenvironment.

[A] The general CAFs abundance in PI3K and KRAS-driven tumors is shown on the left. The absolute number of each CAFs population was normalized by the total amount of cells – nuclei. In the right panel, the abundance of CAFs populations in PI3K^{H1047R} and KRAS^{G12D} -driven tumors is represented. The absolute number of each CAFs population was normalized by the absolute number of the general CAFs group. The abundance of the populations was determined using the multiplex IF panels followed by the correspondent population segmentation.

[B] Stromal-TME composition of KRAS^{G12D} and PI3K^{H1047R} driven tumors. CAFs mean for both groups is depicted in the pie charts. To evaluate statistical differences in TME remodeling driven by the oncogene, all CAFs populations were compared using an unpaired t-test with Welch correction. No significant alterations were observed between the groups.

[C]-[D] Representative images for the KRAS^{G12D} and PI3K^{H1047R} cohorts. Each channel of the multiplex IF Panel 1, phenotyping early myCAFs, myCAFs, iCAFs, IL6 myCAFs, IL6 iCAFs, and each channel of the multiplex IF Panel 2 that phenotypes stellate cells and apCAFs, is showcased. The scale bar corresponds to 20 µm.

4.1.4.2 PI3K^{H1047R} tumors present different CAFs-tumor cells neighborhood profiles

Although CAFs content was not significantly altered between KRAS and PI3K-driven tumors, the minor differences between CAFs populations may drive an alteration in CAF-tumor cell neighborhood profiles.

The alterations in the neighborhood between CAFs sub-types and tumor cells were assessed using CytoMAP, where the euclidean distances between all CAFs to tumor cells were calculated. The strategy is described in Figure 13-A. First, the images resultant from the samples stained using the multiplex IF panels were segmented, and the spatial information of each segmented cell was retrieved. Then, this information was loaded into CytoMAP, which calculated the distance between each pair of CAFs and tumor cells. The results are depicted in Figure 13-B. Most CAFs-tumor cell interactions derived significant results, except for myCAFs and IL6 iCAFs. On the one hand, IL6 iCAFs abundance in these groups was scarce, not presenting any statistical differences.

On the other hand, myCAFs presented a similar profile between both groups and a similar distribution around tumor cells (Figure 13-C). The median distance of myCAFs to tumor cells was 27.44 and 22.57 µm in the KRAS^{G12D} and PI3K^{H1047R} groups, respectively (p=0.06). Moreover, approximately 50% of myCAFs were located in a 25 µm radius of tumor cells, reinforcing previous thoughts on myCAF and tumor cell close interactions. Even though there was no alteration in the neighborhood pattern between myCAFs and tumor cells, the same pattern was not replicated with other myCAFs-related populations, such as early myCAFs and IL6 myCAFs.

Early myCAFs median distance to tumor cells is similar in both groups. In the KRAS^{G12D} group, early myCAFs sat at 38.73 µm compared with 40.21 µm in PI3K^{H1047R} tumors (p<0.0001). Nevertheless, how these cells were rearranged around tumor cells was quite different. Early myCAFs in PI3K^{H1047R} tumors were most dense around tumor cells, where approximately 12% of early myCAFs were located in a 5 µm radius, compared with only 2% in KRAS^{G12D} tumors.

In PI3K-driven tumors, IL6 myCAFs were closer to tumor cells than in KRAS-driven tumors, with a median distance of 22.04 µm to 37.26 µm, respectively (p<0.0001). This distance was also accompanied by a higher density of this subtype around tumor cells. In the PI3K^{H1047R} tumors, more than 30% of IL6 myCAFs were within 15 µm of tumor cells, with only 5% in the KRAS^{G12D} group.

Another favored neighborhood in the PI3K^{H1047R} group with tumor cells came from apCAFs. apCAFs were located at a median distance of 20.64 µm compared with 37.29 µm in KRAS-driven tumors (p=0.0008). In addition, the bin-centered analysis revealed that approximately 60% of apCAFs were located within 25 µm of tumor cells compared to the 30% in the KRAS-driven group.

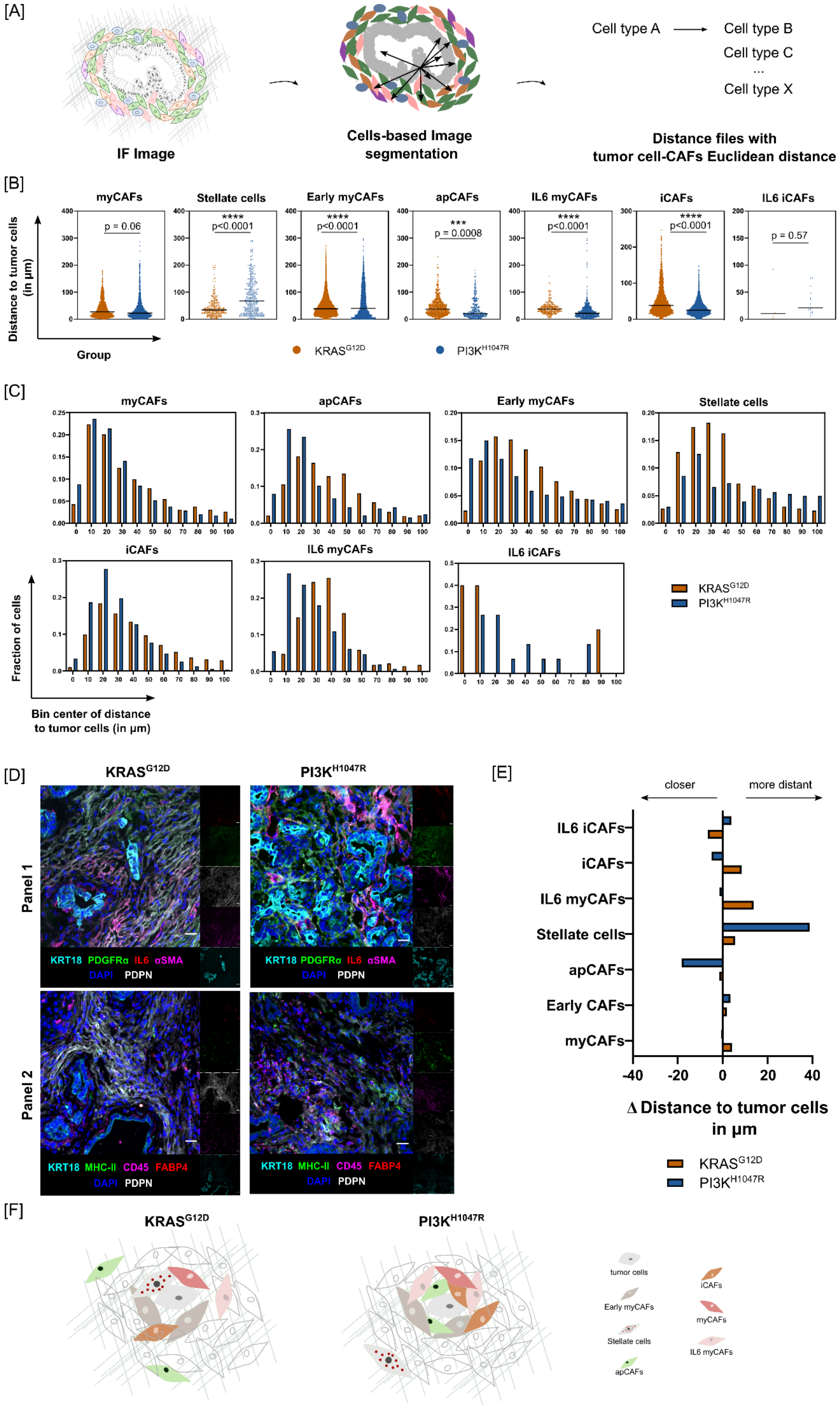

Figure 13 – PI3K-driven tumors exhibit distinct CAFs-tumor cells neighborhood profiles.

[A] Strategy used to determine CAFs-tumor cells communication profiles. First, the multiplex IF images were segmented using the Cell-based algorithm in Imaris. Then, the spatial coordinates information for each cell was extracted, and the shortest distance of CAFs populations to tumor cells was calculated.

[B] Median distance of CAFs populations to tumor cells in KRAS^{G12D} (orange) and PI3K^{H1047R} (blue) cohorts. To understand if the KRAS^{G12D} or the PI3K^{H1047R} derived tumor secretomes would impact the neighborhood of tumor cells with the stromal microenvironment, all correspondent CAFs to tumor cells distances were depicted in the dot plots. Each dot corresponds to one cell. The number of cells analyzed was variable and was dependent on the absolute number of cells segmented for each population. An unpaired t-test with a Welch correction was deployed to evaluate if these alterations were significant. Significant interactions were marked with asterisks (* corresponds to $p < 0.05$, *** corresponds to $p < 0.001$, and corresponds to **** $p < 0.0001$), and the exact p values were showcased.

[C] Frequency distribution of CAFs subpopulations distance to tumor cells. The frequency of the distribution of all CAFs subpopulations is depicted in the bar plot with a 105 µm diameter. The bin size is 10 µm and starts at 0, meaning that for each center, the CAFs are calculated using the intervals [0,5],]5,15,]15, 25],]25, 35],]35, 45],]45, 55],]55, 65],]65, 75],]75, 85],]85, 95],]95, 105]. The KRAS^{G12D} is represented in orange, and PI3K^{H1047R} is represented in blue.

[D] Representative images for the KRAS^{G12D} and PI3K^{H1047R} cohorts. Each channel of the multiplex IF Panel 1 and Panel 2 is represented. The scale bar is 20 µm.

[E] Favorable CAFs interactions with tumor cells. Difference in the median distance of CAFs populations to tumor cells in the KRAS^{G12D} and PI3K^{H1047R} to the reference measurement in Figure 4E. The KRAS^{G12D} is represented in orange, and PI3K^{H1047R} is represented in blue.

[F] Graphic scheme summarizing the findings of Figure 11. In PI3K^{H1047R} tumors, apCAFs, IL6 myCAFs, and iCAFs were closer and denser to tumor cells, whereas stellate cells were located closer to tumor cells in the KRAS^{G12D} group.

Finally, PI3K-driven molecular alterations may also be responsible for increased communication between iCAFs and tumor cells. In this group, iCAFs were at a median distance of 25.06 µm from tumor cells ($p<0.0001$), where 50% of the cells were located within that distance to tumor cells.

In contrast with the favorable interactions in the PI3K^{H1047R} group, stellate cells were located further away from tumor cells. In this group, the median distance to tumor cells was 67.59 µm, while in the KRAS-driven tumors, stellate cells were located at a median of 34.40 µm ($p<0.0001$). As expected, stellate cells density around tumor cells in the KRAS^{G12D} group was higher than in the PI3K^{H1047R}. This difference was evident in Figure 13-E, where the differences in the CAFs' distances to tumor cells, calculated using all 16 tumors as a baseline to highlight context-specific differences in tumor cell neighborhoods, revealed a striking effect of PI3K on stellate cells.

In summary, PI3K^{H1047R} tumors exhibited favorable interactions with tumor cells. CAFs populations such as apCAFs, IL6 myCAFs, and iCAFs were closer and denser to tumor cells, unraveling distinct neighborhood profiles and provoking a different spatial distribution of CAFs compared to the KRAS^{G12D} tumors.

4.1.4.3 Distinct CAFs-tumor cell neighborhoods may contribute to heterogeneous tumor architecture in oncogene-driven PDAC

Tumors driven by KRAS^{G12D} and PI3K^{H1047R} gain-of-function mutations exhibited distinct CAFs-tumor cells neighborhoods profiles, despite the abundance of CAFs, and tumor cells populations remained significantly unaltered. Nevertheless, alterations in cell neighborhood profiles may not translate into functional architectural changes. Cell-centric neighborhoods were therefore calculated to infer changes in tumor architecture. The strategy to determine tumor architecture is depicted in Figure 14-A. Cell neighborhoods were determined using a 20 µm raster scan. Each neighborhood's local cellular density and composition was used as a variable to cluster areas with a similar neighbor profile. The regional neighborhoods in this work were calculated in images resulting from Panel 1. Panel 1 phenotyped more than 95% of CAF, being the most representative of the stromal TME.

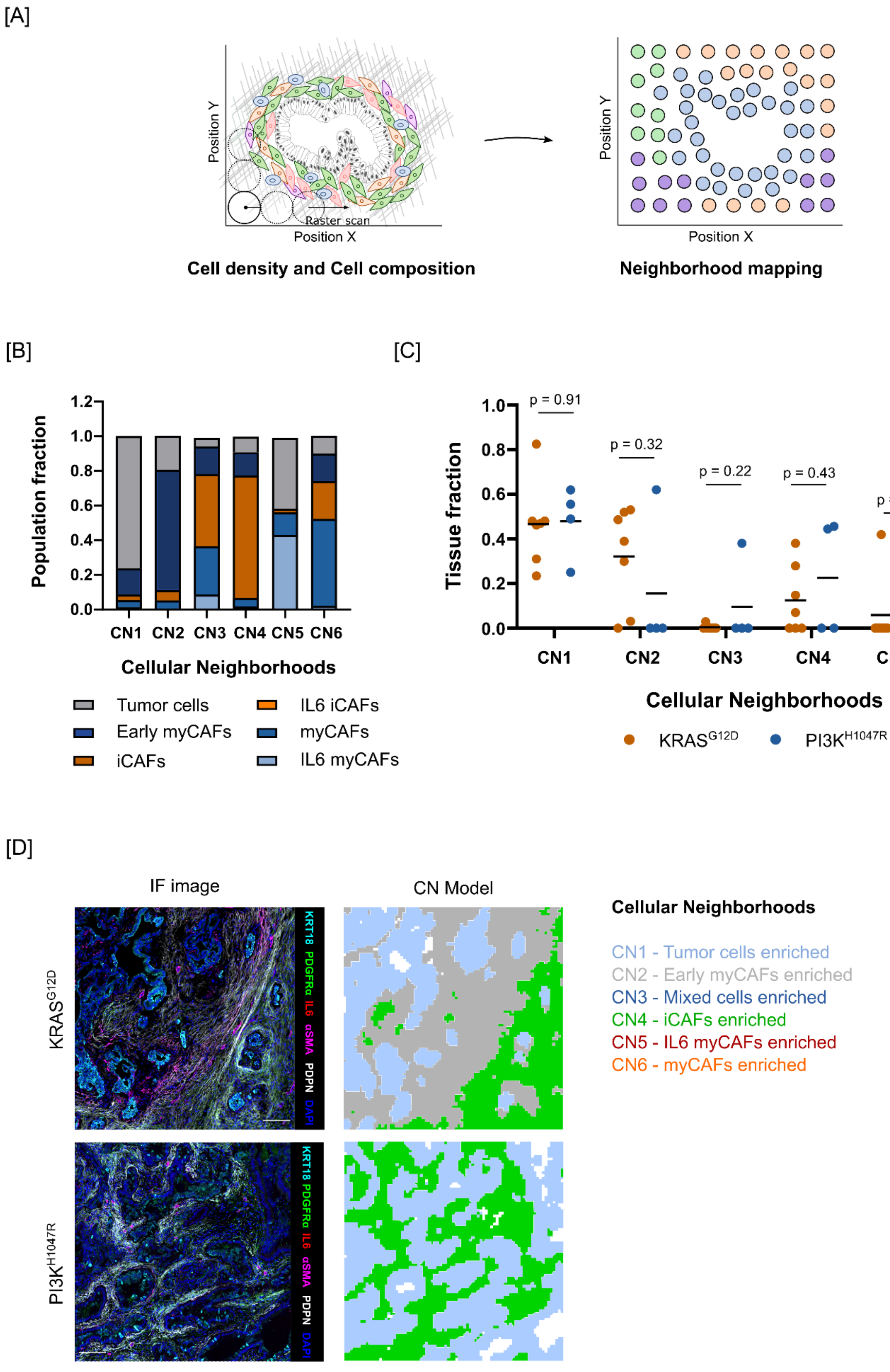

Figure 14 – Stromal TME architectures remain unchanged despite distinct tumor cell - CAFs neighborhoods profiles.

[A] Strategy used to model Cellular Neighborhoods. First, the direct neighbors of every cell were calculated using a 20 µm diameter Raster scan in Cytomap. Then, the individual neighborhoods were clustered based on their cellular composition and density using a Self-Organizing Map algorithm to define a map of regions (CNs) with a similar profile.
[B] Cellular composition of the CNs. Six CNs were identified based on the six populations (Tumor cells, myCAFs, early myCAFs, IL6 myCAFs, iCAFs, and IL6 iCAFs) and their respective frequencies within each CN (pooled data from both groups).
[C] Cellular Neighborhoods distribution in the KRAS^{G12D} (orange) and PI3K^{H1047R} (blue) driven tumors. Data are represented as the mean of the tissue fraction occupied by each CN. Each dot represents an animal. Statistical differences between both groups were assessed using an Unpaired t-test with a Welch correction. No statistical significance was observed, and the exact p-values were depicted.
[D] Graphic representation of the CN model and correspondent IF image. The annotation of each CN was performed based on the most frequent population present on the respective CN. The scale bar corresponds to 100 µm.

This analysis demonstrated that, in this context, PDAC presented 6 types of neighborhoods. Figure 14-B describes the cellular composition of each neighborhood. Most neighborhoods were enriched in one population except for CN3. The CN3 was composed mainly of iCAFs, approximately 40%, and myCAFs (28%), with early myCAFs and IL6 myCAFs making up approximately 20%. The other neighborhoods were enriched by one population, with at least 20% of the cells comprising a mix of other populations, suggesting preferential communication patterns.

The tumor cells-enriched neighborhood – CN1 – was composed of approximately 80% tumor cells, followed by 10 % of early myCAFs and 4% of myCAFs, and 3% iCAFs, showing that tumor cells may communicate closely with those CAFs populations. The tumor cell-enriched neighborhood, however, was not altered between KRAS^{G12D} and PI3K^{H1047R} tumors (p=0.91), which contained approximately 45% of the cells.

KRAS^{G12D} differentiated tumors were composed of neighborhoods CN1, CN2, CN4, CN5, and CN6, as described in Figure 14-C. However, there was not a clear pattern between tumors in the group. The most common neighborhoods cohabitating with CN1 were the early myCAFs-enriched (CN2) and iCAFs-enriched (CN4) neighborhoods. Five animals exhibited a significant portion of the cells in CN2, suggesting that an important communication network between early myCAFs and tumor cells, myCAFs, and iCAFs may occur. Moreover, these tumors also showed an iCAFs-regulated neighborhood – CN4, composed of iCAFs, early myCAFs, myCAFs, and tumor cells. These populations may have intricate communication patterns, relying on each other in different capacities. Of the KRAS^{G12D} animals analyzed, only two showed different neighborhood profiles with the presence of myCAFs and IL6 myCAFs-enriched regions. The tumor sample exhibiting an IL6 myCAFs region relies heavily on tumor cells-driven neighborhood profiles, whereas the tumor with a myCAFs region appears to favor communication networks involving mostly iCAFs and early myCAFs.

PI3K-driven tumors presented a very heterogenous tumor architecture, where there was a shift from the early myCAFs-centered CN2 neighborhoods, with only one tumor displaying CN2 regions. Half of the tumors, however, maintained an iCAFs-driven neighborhood in addition to the tumor cell one. Moreover, one of the tumors showed a mixed neighborhood (CN3), which still relied on iCAFs-centric neighnorhoods, although to a lesser extent.

Although there are significant differences in the tumor cells-CAFs neighborhoods between KRAS^{G12D} and PI3K^{H1047R} tumors, these changes become less pronounced at a regional level. Other cell types not evaluated in this study may contribute to a regional-level organization in PDAC.

4.1.4.4 KRAS^{G12D} and PI3K^{H1047R} tumors present similar transcriptional landscapes

KRAS^{G12D} and PI3K^{H1047R} presented similar stromal TME compositions, similar cellular neighborhood organization but slightly different tumor cell-CAFs neighborhoods. Molecular changes like transcriptional alterations may be responsible for cellular neighborhood reorganization. Therefore, mRNA transcript expression was measured in bulk and tumor samples via RNA sequencing to pinpoint genes that may be responsible for different transcriptional regulations between the groups.

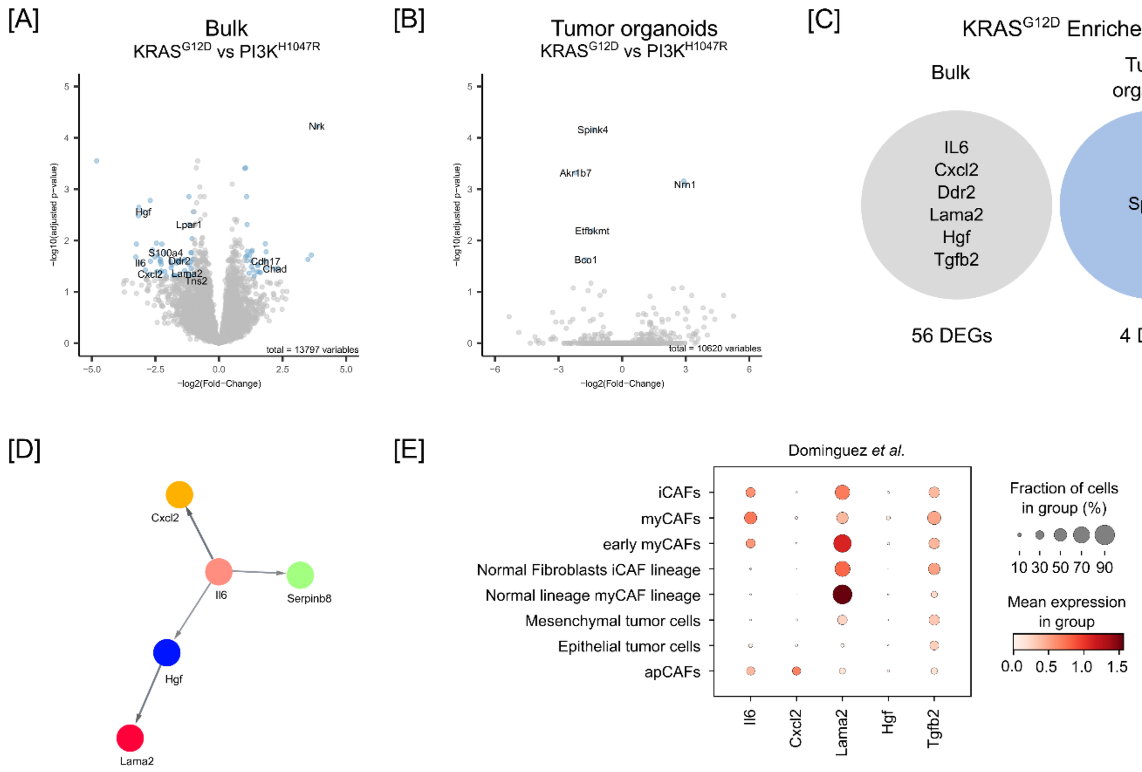

Figure 15 – Tumor cells do not appear to contribute to transcriptional changes between KRAS^{G12D} and PI3K^{H1047R} tumors.

[A] Volcano plot of the differential gene expression analysis of KRAS^{G12D} (n=14) and PI3K^{H1047R} bulk tumors (n=10). The cut-off used for the DEG fold-change was 2 ($\log_2$(Fold-change) < -1 or $\log_2$(Fold-change) < 1), and the cut-off for the adjusted p-value was 0.05 ($\log_{10}$(adjusted p-value) < 1.3). Non-significant DEGs are depicted in grey, and significant DEGs are depicted in blue.

[B] Volcano plot of the differential gene expression analysis of KRAS^{G12D} (n=4) and PI3K^{H1047R} tumor organoids (n=4). The tumor organoids characterized matched the bulk samples performed in [A]. The cut-off used for the DEG fold-change was 2 ($\log_2$(Fold-change) < -1 or $\log_2$(Fold-change) < 1), and the cut-off for the adjusted p-value was 0.05 ($\log_{10}$(adjusted p-value) < 1.3). Non-significant DEGs are depicted in grey, and significant DEGs are depicted in blue.

[C] Venn diagram of the DEGs between the bulk sample and tumor organoids in KRAS-driven tumors. The genes represented in the diagram are an example of DEGs. No intersection between the groups was observed.

[D] String interaction network of selected DEGs of the KRAS^{G12D} bulk sample. The minimum interaction score required to establish an interaction was 0.7.

[E] Expression of the DEGs of the KRAS^{G12D} bulk sample in the CAFs and tumor populations present in the Dominguez *et al.* dataset.

Acknowledgments: All members of AG Saur contributed to the breeding and sacrificing of animals and bulk tumors samples preparation for RNAseq. XiaoXiao Zhang and Fabio Boniolo were responsible for RNAseq reads mapping, quality control, and count matrix generation. Daniele Lucareli analyzed the Dominguez *et al.* scRNAseq dataset.

Fresh-frozen tumor pieces and organoids from KRAS^{G12D} and PI3K^{H1047R} were sequenced, and the mapped transcripts were compared. Bulk RNAseq showed that 86 genes were differentially expressed between KRAS and the PI3K-driven tumor (Figure 15-A). Of those, 56 were differentially expressed in KRAS^{G12D} tumors – Figure 15-C. An overrepresentation analysis did not generate significant results, although genes such as *Il6*, *Tgfb2*, *Ddr2*, *Cxcl2*, *Il6*, *Hgf*, and *Lama2* are generally associated with the fibrotic process (Naba *et al.*, 2016; Tian *et al.*, 2019). Additionally, a high-confidence string analysis of interactions between *Il6*, *Tgfb2*, *Ddr2*, *Cxcl2*, *Hgf*, and *Lama2* did not observe any reported relationships between *Ddr2*, *Tgfb2* (Figure 15-D). Similarly to the KRAS-driven group, PI3K-driven tumors DEGs (30) were not significantly overrepresented in any particular pathway.

To understand if this difference was derived from the tumor compartment, tumor organoids derived from some of the tumor samples analyzed in Figure 15-A were sequenced, and a differential gene expression analysis was performed. Figure 15-B depicts the differential gene expression analysis of tumor organoids derived from KRAS^{G12D} and PI3K^{H1047R} tumors. This analysis revealed that these groups were identical at a transcriptional level, with a mere 6 genes differentially regulated. Among these genes was *Spink4*, which was upregulated in KRAS-driven tumor cells. Nevertheless, this increased expression in tumor cells was not observable in the bulk tumor tissue.

After excluding tumor cell contribution to the differences observed at the transcriptional level, the expression of these transcripts in CAFs was assessed. Figure 15-E shows the CAFs subtypes expression of the selected bulk DEGs shown in Figure 15-C. The Dominguez et al. data set analysis showed that CAFs populations might contribute to the overall expression of *Lama2*, *Tgfb2*, and *Il6*. However, there were no statistical differences in CAFs content between groups, suggesting that CAFs may not be the driver of these transcriptional differences. In addition, *Hgf* and *Cxcl2* expression might originate from compartments other than tumor cells and CAFs since the expression was low in CAFs groups or, in the case of *Ddr2*, not detectable.

Altogether, although the analysis pinpointed genes that may be involved in CAFs biology, one can not exclude that sampling differences may also contribute to these shallow transcriptomic changes. Therefore, further experiments are necessary to understand tumor cell-CAFs neighborhood profiles and whether other cell types might be involved in the interplay between CAFs and tumor cells between KRAS^{G12D} and PI3K^{H1047R} tumors.

4.1.5 Characterization of tumor differentiation status impact on the stromal TME composition and architecture

The TME composition did not statistically change, regardless of whether KRAS^{G12D} or PI3K^{H1047R} drove PDAC tumorigenesis. However, the degree of differentiation of the tumor may induce changes in CAFs activation. Therefore, tumor differentiation status was analyzed to understand the impact of epithelial and mesenchymal regulation on CAFs activation and stromal organization.

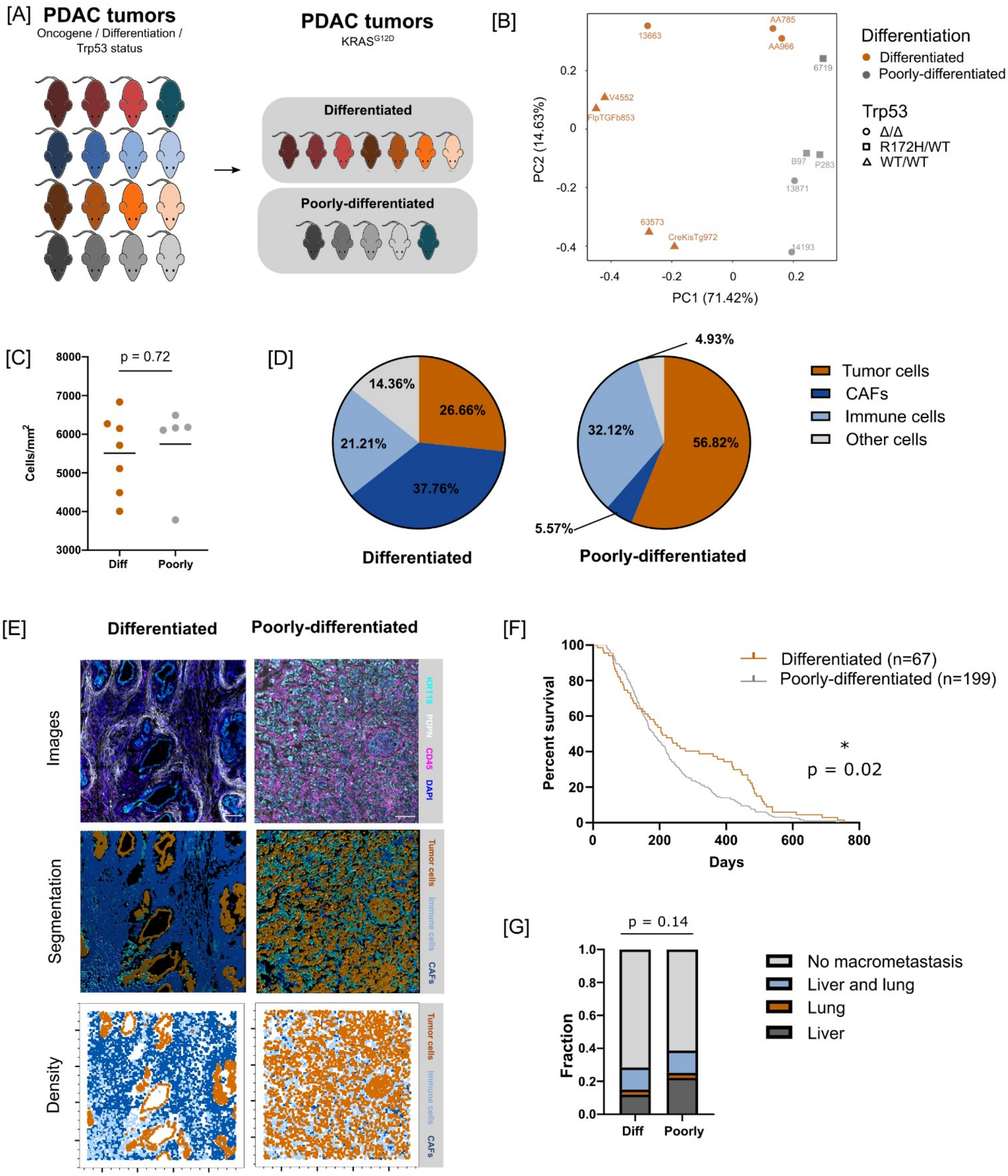

Figure 16 – The differentiation status of the tumors is associated with a remodeling of the TME.

[A] Cohort used for the characterization of PDAC TME depending on its degree of differentiation. The KRAS^{G12D} animals in the initial cohort were allocated to the differentiated group (n=7) or poorly-differentiated (n=5) group, depending on the tumor grade assessed in the histopathological analysis.

[B] Multivariate data analysis of the cohort. The PCA was performed using all cell types in the PDAC stromal TME as variables. PC1 and PC2 were plotted to depict the relationships between the samples. The samples were highlighted in orange (differentiated) or gray (poorly-differentiated), depending on their differentiation status. A further layer of stratification was added to portray the *Trp53* status. Tumor samples were depicted with circles, squares, or triangles depending on if a complete loss of *Trp53* (Trp53$^{\Delta/\Delta}$), just one allele (*Trp53*$^{R172H/WT}$), or if no alterations (*Trp53*$^{WT/WT}$) were introduced from the tumorigenesis.

[C] Cellularity of the tumor samples per group. The cellularity represents the density of nuclei present in the whole area of the images analyzed, and each dot in this analysis represents the mean of the measurements made for each specimen. An Unpaired t-test assessed the statistical differences between both groups with Welch correction.

[D] Composition of the TME in differentiated and poorly-differentiated tumors. The pie charts describe the composition of Tumor cells, CAFs, Immune cells, and other types of cells in the TME. The CAFs populations were subjected to an Unpaired t-test with a Welch correction to understand if there was a significant statistical difference between the TMEs. Post hoc correction for multiple comparisons was not performed. Tumor cell and CAF frequency were increased in differentiated tumors (p=0.003 and p=0.005, respectively). In addition, there was a trend toward an increase in the immune compartment in poorly-differentiated tumors (p=0.11).

[E] Representation of the immunofluorescence images, segmentation, and histocytometry analysis for the differentiated and poorly-differentiated groups. The scale bar is 100 µm.

[F] Survival analysis between groups is depicted in the Kaplan-Meyer curve. Paraffin-embedded tumors were used to perform the histopathological analysis. Differentiated tumors (n=67), in orange, composed of G1 and G2 tumors, were compared to poorly-differentiated tumors (n=199), in gray, which comprised G3 and G4 samples. The Log-rank test was deployed, generating a significant difference between the groups (* corresponds to p = 0.02).

[G] Metastization potential of the cohort analyzed in [F]. The macrometastasis, annotated when the animal was sacrificed, are represented in the bar plot. No significant changes in metastization potential nor the preferred metastization site occurred. Nevertheless, there is a trend toward increased metastasis occurrence in poorly-differentiated tumors. The differences were evaluated using the two-sided Fisher's exact test.

Acknowledgments: The animals used in this study were bred and sacrificed by all the members of AG Saur. The histopathological analysis used in multiplex IF analysis was done together with Tânia Santos. In addition, Chen Zhao and Moritz Jesinghaus performed the histopathological analysis in [F] and [G].

The PDAC cohort was composed of KRAS-driven tumors and was stratified into two groups depending on the tumor grade (Figure 16-A). The differentiated group was composed of 7 tumor samples that retained differentiated features and were classified as G1 and G2 tumors. These specimens could additionally harbor a *Trp53* deletion. Indeed, 3 tumor samples presented a complete deletion of *Trp53*. On the other hand, the poorly-differentiated group lacked mostly differentiated features and was composed of 5 samples, mainly classified as G3, and presented at least one *Trp53* allele with a loss-of-function mutation or a deletion.

The tumors were benchmarked to each other using a multivariate analysis, where the general abundance of all populations was used as variables (Figure 16-B). The PCA plot shows that differentiated tumors are primarily located in the PC1 negative area of the plot, whereas poorly-differentiated tumors were located in the positive part of PC1, suggesting that tumor differentiation status drives differences in the TME.

In the initial comparison of the major cell groups (Figure 16-D), significant changes arose in tumor cells (p=0.003) and CAFs (p=0.005) numbers in differentiated and poorly-differentiated tumors. Tumor cell content in poorly-differentiated tumors was higher, representing approximately 56.82±10.10% of all cells compared with 26.66±15.29% in differentiated tumors. On the other hand, CAFs were negatively correlated with tumor cells, representing 5.57±4.90% of cells in poorly-differentiated tumors and 37.76±19.47% in differentiated tumors. Although immune cell content was not statistically significant between the groups (p= 0.11), there was a trend toward an increase in its content in poorly-differentiated tumors, with 32.12±8.% of cells compared with 21.01±12.01% in differentiated tumors. In addition, the tumors presented approximate cellularity, indicating that changes in the TME composition were not likely to arise from an unequal number of cells analyzed due to changes in cell size, necrotic, and decellularized parts of the tissue included in the analysis – Figure 16-C. As a matter of fact, this can be corroborated by the histocytometry analysis performed and showcased in Figure 16-E.

As expected, differentiated tumors presented a significant survival advantage (Figure 16-F) compared to the poorly-differentiated group (p = 0.02). Additionally, differentiated tumors presented less metastasis than poorly-differentiated tumors (Figure 16-G), exhibiting a negative trend in macrometastasis formation frequency (p=0.14).

Further differences in the stromal compartment, CAFs-tumor cell interactions, and tumor architecture were assessed to understand how the stromal TME could shape survival and metastasis in tumors with different differentiation status.

4.1.5.1 Tumor differentiation status impacts stromal TME composition

To understand the differences in stromal activation between differentiated and poorly-differentiated tumors, CAFs populations abundance within all cells and their proportion within CAFs was calculated.

CAFs ratios in differentiated and poorly-differentiated were disparate. In most differentiated tumors, CAFs content ranged from approximately 11% to 62%, representing in most tumors approximately 40% of the TME – Figure 17-A. In poorly-differentiated tumors, CAFs abundance ranged from approximately 0.5% to 9%, with 3 of the samples presenting 5% CAFs.

The subpopulation frequencies within the CAFs groups are shown in Figure 17-B. Early myCAFs were the most abundant population in differentiated tumors, comprising 55.93±29.21%of all CAFs populations in differentiated tumors and 22.14±27.49% in poorly-differentiated tumors. Since the variance in early myCAFs content was high, only a statistical trend (p=0.07) toward an increased content of early myCAFs was observed.

The most abundant CAFs populations in the poorly-differentiated tumors were IL6 myCAFs, which composed 44.04±28.59% of stromal TME. Although there was a high variance, this population was significantly decreased in differentiated tumors (p=0.01), with a mean abundance of 6.22±16.1% within all CAFs.

Contrary to IL6 myCAFs, most other CAFs remained unaltered between the groups. No statistical differences were observed between the groups in the proportion of myCAFs (p=0.51), iCAFs (p=0.78), IL6-iCAF (p=0.21), and apCAFs (p=0.83) within all CAFs. myCAFs made up 18.38±21.66% of CAFs in differentiated against 10.91±13.36% in poorly-differentiated tumors. In addition, the iCAFs proportion was very similar between both groups, with a mean abundance of 14.91±19.36% in differentiated tumors and 11.60±21.41% in the poorly-differentiated group. Antigen-presenting CAFs mean abundance was low and heterogeneous, representing 2.47±2.61% and 2.02±3.41% of the overall CAF distribution in differentiated and poorly-differentiated tumors. IL6 iCAFs were not detected in differentiated tumors, and, in the poorly-differentiated group, the abundance within CAFs was approximately 5.01±10.19%. Moreover, there was no difference in the content of stellate cells between groups (p=0.20), where poorly differentiated tumors presented a content of 4.32±3.04% compared with 2.094±2.605% in differentiated tumors of all CAFs.

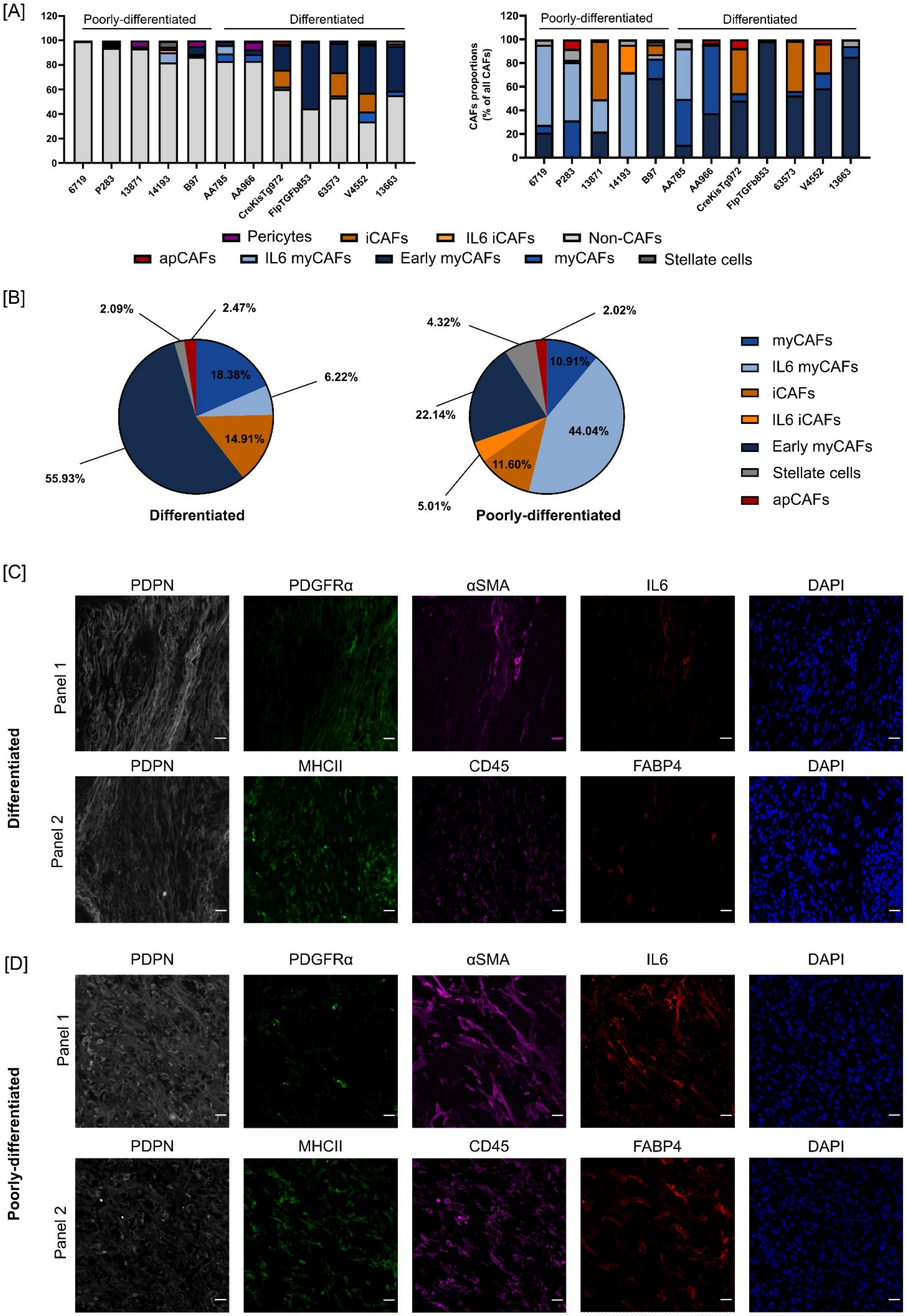

Figure 17 – The differentiation status of the tumors is associated with a distinct stromal TME activation.

[A] General abundance of CAFs populations in differentiated and poorly-differentiated tumors is represented at the left. The absolute number of each CAFs population was normalized by the total number of cells – nuclei. In the right panel is depicted the general abundance of CAFs populations in differentiated and poorly-differentiated tumors. The absolute number of each population of CAFs was normalized by the absolute number of CAFs. The abundance of the populations was determined using the multiplex IF panels followed by the correspondent population segmentation.

[B] Stromal-TME composition of differentiated and poorly-differentiated tumors. The mean of each population is depicted in the pie charts. The CAFs populations of both groups were compared using an unpaired t-test with Welch correction. No multiple correction test was applied. IL6 myCAFs frequency was statistically significant between the groups (p = 0.01). However, the early myCAFs difference between the groups was not statistically significant, with a p-value of 0.07.

[C]-[D] Representative images for both cohorts of each channel of the multiplex IF panel 1, that phenotypes early myCAFs, myCAFs, iCAFs, IL6 myCAFs, IL6 iCAFs, and each channel of the multiplex IF panel 2 that phenotypes stellate cells and apCAFs. The scale bar corresponds to 20 µm.

Although some CAFs populations proportion were not altered between differentiated and poorly-differentiated tumors, it must be stressed that the overall content was changed. For example, the iCAFs proportion within the CAFs group remained unchanged, but its overall content trended toward an increase in the differentiated group (p=0.13). Likewise, myCAFs overall abundance was also significantly increased in differentiated tumors (p=0.04).

All in all, the composition of CAFs between differentiated and poorly-differentiated tumors changed at different levels. CAFs populations such as early myCAFs in differentiated and IL6 myCAFs in poorly-differentiated tumors were more abundant and represented the main difference in activation profiles within all CAFs.

4.1.5.2 Poorly-differentiated tumors display rich stromal interactions

The analysis of the multiplex panels of differentiated and poorly-differentiated tumors showed the remodeling of the stromal TME, where the alteration of specific CAFs population content and proportions was evident. This change in tumor content and intrinsic cellular organization of differentiated and poorly-differentiated tumors likely results in altered CAFs-tumor cell neighborhood profiles.

The alterations in the neighborhood between CAFs sub-types and tumor cells were assessed using CytoMAP, where the Euclidean distances between all CAFs to tumor cells were calculated. The results are depicted in Figure 18-A. Most CAFs-tumor cell interactions derived significant results (p<0.0001), except for IL6-iCAFs, which were rare in these tumors.

MyCAFs-related populations were much closer to tumor cells than other CAFs in poorly-differentiated tumors. Early myCAFs, myCAFs, and IL6 myCAFs were at a median distance of approximately 16.97, 14.94, and 21.63 57 µm, respectively, compared to 27.76, 38.72, 37.26 µm in differentiated tumors. These populations were also more densely located around tumor cells in poorly-differentiated tumors than in differentiated ones. In the poorly-differentiated group, approximately 45% of myCAFs, 50% of early myCAFs, and 35% of IL6 myCAFs were located in a 15 µm radius of tumor cells against 25% of myCAFs, 15% of early myCAFs and 5% of IL6 myCAFs in differentiated tumors (Figure 18-B).

Similarly, apCAFs were much closer to tumor cells in poorly-differentiated tumors at a median distance of 14.91 µm compared with 24.45 µm in differentiated tumors. Moreover, the proximity of apCAFs to tumor cells in poorly-differentiated tumors was also accompanied by a higher density around tumor cells. In these tumors, more than 50% of apCAFs were located at a maximum distance of 25 µm from tumor cells compared with only 25% in differentiated tumors.

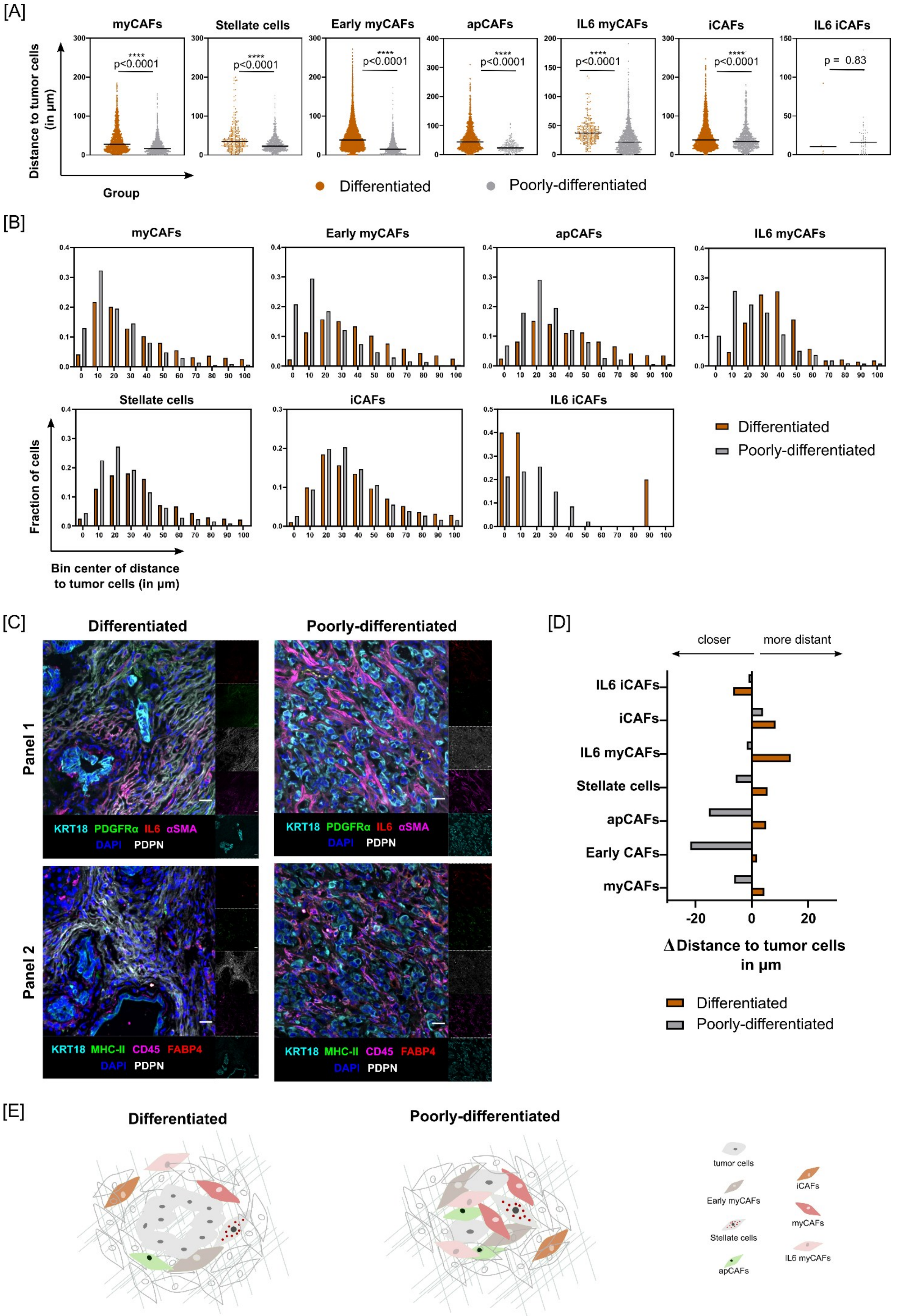

Figure 18 – Loss of the glandular structures and low stromal content impacts CAFs-tumor cell neighborhoods in poorly-differentiated tumors.

[A] Median distance of CAFs populations to tumor cells in the differentiated (orange) and poorly-differentiated (gray) cohorts. All the corresponding CAFs' distances to tumor cells were depicted in the dot plots in which each dot corresponds to one cell. The number of cells analyzed is variable and depends on the absolute number of cells segmented for each population. An unpaired t-test with a Welch correction was deployed to evaluate whether the differences between the groups' neighborhood patterns were significant. Significant interactions were marked with asterisks (**** $p < 0.0001$), or the exact p-value was shown.
[B] Frequency distribution of CAFs populations distances to tumor cells. The frequency of the distribution of all CAFs subpopulations in differentiated and poorly-differentiated tumors is depicted in the bar plot with a 105 µm diameter. The bin size is 10 µm and starts at 0, meaning that for each center, the CAFs frequencies are calculated using the intervals [0,5],]5,15,]15, 25],]25, 35],]35, 45],]45, 55],]55, 65],]65, 75],]75, 85],]85, 95],]95, 105]. Differentiated tumors are represented in orange, and poorly-differentiated tumors are represented in gray.
[C] Representative images for the differentiated and poorly-differentiated cohorts. Each channel of the multiplex IF Panel 1 and Panel 2 is represented. The scale bar is 20 µm.
[D] Difference in the median distance of CAFs populations to tumor cells in both groups to the reference measurement in Figure 4E. Differentiated tumors are represented in orange, and poorly-differentiated tumors are represented in gray.
[E] Graphic scheme summarizing the findings of Figure 16. In poorly-differentiated tumors, most CAFs were closer and denser to tumor cells.

Stellate cells and iCAFs followed the same profile as other CAFs populations, where they were closer to tumor cells in poorly-differentiated tumors than in differentiated tumors. The median distance between tumor cells and stellate cells was approximately 55.91 µm in differentiated tumors and 35.97 µm in the poorly-differentiated group, where approximately 15% in differentiated tumors and 27% in poorly-differentiated tumors were located in a radius of 15 µm to tumor cells. iCAFs presented comparable densities around tumor cells, although the median distance to tumor cells was statistically significant. Indeed, in differentiated tumors, 11% of iCAFs were in a radius of 15 µm to tumor cells compared with 12% in poorly-differentiated tumors. The difference in distance between the groups was only 5 µm, where the median distance between iCAFs and tumor cells in differentiated tumors was 38.42 µm and 33.91 µm in poorly-differentiated tumors

The differences in the CAFs' distances to tumor cells were calculated using all 16 tumors as a baseline to highlight context-specific differences in tumor cell neighborhoods. This score revealed that differentiated and poorly-differentiated tumors presented opposite trends of CAFs populations neighboring tumor cells, namely in early myCAFs, IL6 myCAFs, myCAFs, and apCAFs. These differences are depicted in Figure 18-D, where the neighborhood differences between the groups became more evident.

In summary, poorly-differentiated tumors showcased rich tumor cells-CAFs relationships compared with differentiated tumors, which could be dictated by tumor architecture characteristics such as the presence or absence of glandular structures and stromal abundance. Nonetheless, these tumor cells-CAFs interactions may not redesign tumor niches and cellular neighborhoods.

4.1.5.3 Poorly-differentiated PDAC features mainly tumor cells-centric neighborhoods

Differentiated and poorly-differentiated tumors presented distinct tumor cells-CAFs neighborhood profiles, accompanied by changes in the glandular structure and tumor cell and CAFs ratios. Cell neighborhoods were calculated to assess if alterations in cell neighborhood profiles may translate into architectural changes. As described in 4.1.4.3, cell neighborhoods were determined using a 20 µm raster scan, and the local cellular density and composition were calculated and used as a variable to cluster areas with a similar profile.

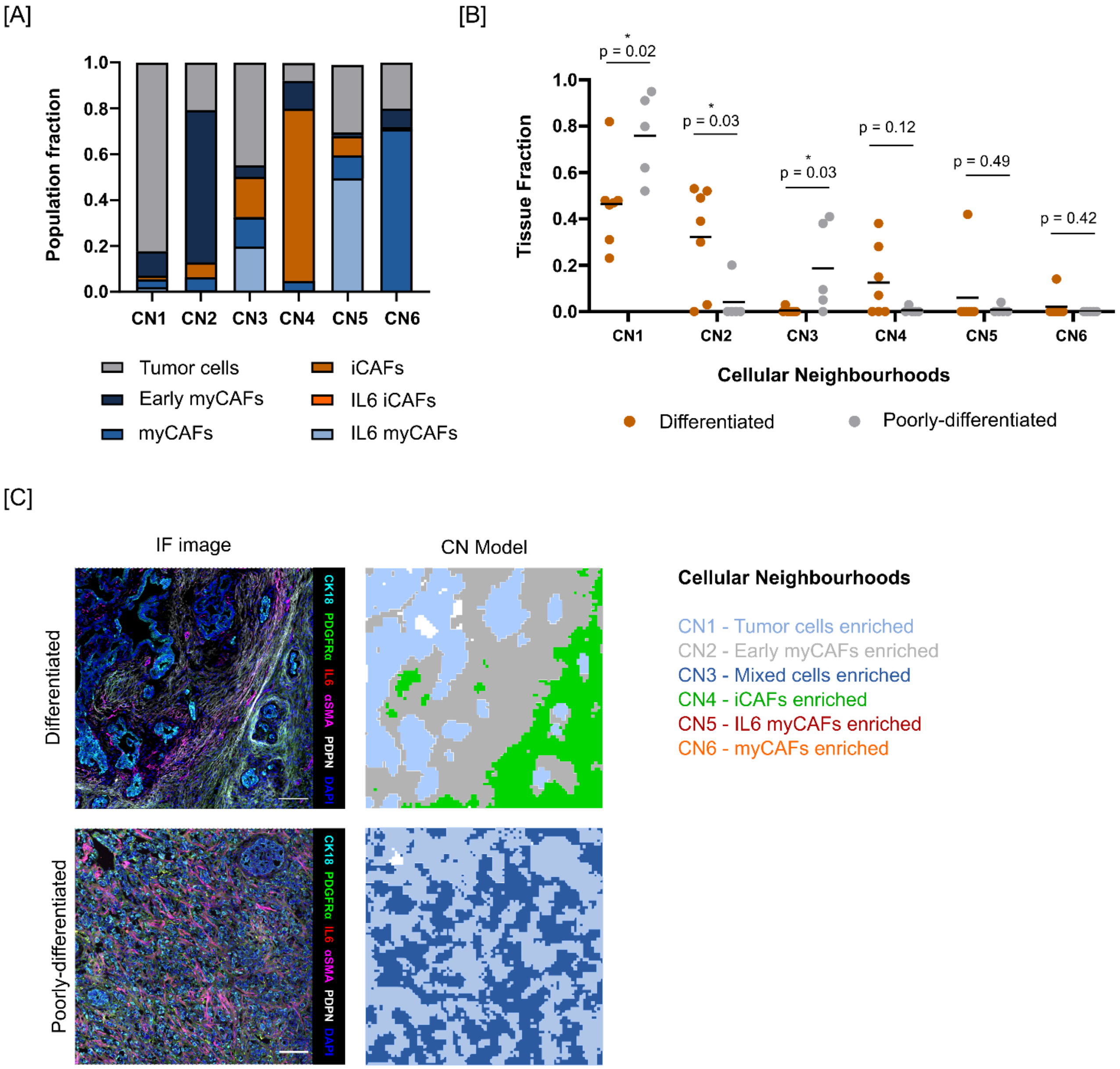

Figure 19 – Loss of well-defined glandular structures and increased tumor cell density on Poorly-differentiated tumors is associated with tumor cell-centric TME niches.

[A] Cellular composition of the CNs. Six CNs were identified based on the seven populations and their respective frequencies within each CN (pooled data from both groups).

[B] Cellular Neighborhoods distribution in the differentiated (orange) and poorly-differentiated tumors (grey). Data are represented as the mean of the tissue fraction occupied by each CN. Each dot represents an animal. Statistical differences between both groups were assessed using an Unpaired t-test with a Welch correction. The statistical significance was marked with asterisks (* corresponds to $p < 0.05$), and the exact p-values were depicted. The scale bar corresponds to 100µm.

[C] Graphic representation of the CN model and correspondent IF image. The annotation of each CN was performed based on the most frequent population present on the respective CN. Scale bar is 100 µm.

Upon clustering, differentiated and poorly-differentiated PDAC presented 6 types of neighborhoods. Their cellular composition is described in Figure 19-A. Most neighborhoods were enriched in one population except for CN3. This CN comprised approximately 45% tumor cells, 20% IL6 myCAFs, 12.6% myCAFs, 5% early myCAFs, and 17.4% iCAFs. The other neighborhoods were enriched by one population, with at least 20% of the cells composed of a mix of other populations, revealing preferential niche patterns.

The tumor cells-enriched neighborhood – CN1 – was composed of mainly tumor cells (Figure 19-B). The CN1 composition was approximately 90% tumor cells, followed by 4% early myCAFs, 3% myCAFs, 2% IL6 myCAFs, and 1.5% iCAFs, suggesting that tumor cells may communicate closely with those CAFs populations. Therefore, this neighborhood composition revealed that in a vast portion of the tumors, tumor cells rely mainly on themselves, and the contribution of CAFs probably may not be so important. Indeed, the CN1 represented 46.40±18.50% of differentiated tumors and 76.00±18.50% in poorly-differentiated tumors (p=0.02), suggesting that probably poorly-differentiated tumors could primarily depend on tumor cell interactions.

Even though the CN1 neighborhood characterizes most cell neighborhoods in poorly-differentiated PDAC, another neighborhood containing tumor cells constituted the remaining ones. The remaining cell niches mainly comprised the CN3 neighborhood (18.70±19.30%), suggesting a secondary dependency on interactions with myCAFs-related populations in poorly-differentiated tumors (p=0.03). This type of niche was generally not represented in differentiated tumors (0.40±1.00%).

Differentiated tumors exhibited more diverse cell neighborhoods. The most frequent neighborhood observed after the tumor cell-enriched CN1 was the Early myCAFs-enriched CN2. This neighborhood, composed of approximately 77% early myCAFs, 9% tumor cells, 7% myCAFs, and 6% iCAFs, made up 32.30±22.50% of niches. In poorly-differentiated tumors, however, the representativity was almost zero (p=0.03). Besides the high content in CN1 neighborhoods, just one animal presented, 4% content in CN2 niches. The CN2 neighborhoods were composed of myCAFs-related populations, such as Early myCAFs and myCAFs, tumors cells, and iCAFs.

Neighborhoods rich in iCAFs, although not statistically significant (p=0.12), were increased in differentiated tumors (12.60±15.30%) and almost inexistent in poorly-differentiated tumors (0.60±1.30%). Similarly, the neighborhoods CN5 and CN6 were only present in one sample of differentiated tumors and did not present any statistical differences.

Overall, differentiated and poorly-differentiated tumors presented different tumor architectures that may be driven by increased tumor cell content concomitant with loss of CAFs content. Allied with this is the loss of glandular structures in the poorly-differentiated samples, contributing to the observed effect and tumor cell-centered niches.

4.1.5.4 Increased Kras gene dosage appears to drive myCAFs-related phenotypes through the regulation of Tgfb1 signaling and ECM-related mechanisms

The tumor's differentiation status showed differences in cell content, cellular organization, and cellular neighborhoods. Poorly-differentiated tumors were characterized by a high content in tumor cells and niches revolving around them. In contrast, differentiated tumors exhibited higher CAFs content and lower content in tumor cell-driven niches. Müller and colleagues characterized the association between phenotypic diversification and Kras increased gene dosage (Kras iGD) (Mueller *et al.*, 2018) (Figure 20-A). Differences in the tumor differentiation status are associated with altered *Kras* dosage, where well-differentiated tumors present heterozygous *Kras*^{G12D} status, and undifferentiated tumors present homozygous *Kras*^{G12D} (Mueller *et al.*, 2018). To understand how *Kras* iGD-induced molecular changes could shift the CAFs phenotype toward a myCAFs-related, mRNA transcript expression was measured in C2a and C1 cluster cell lines via RNA sequencing.

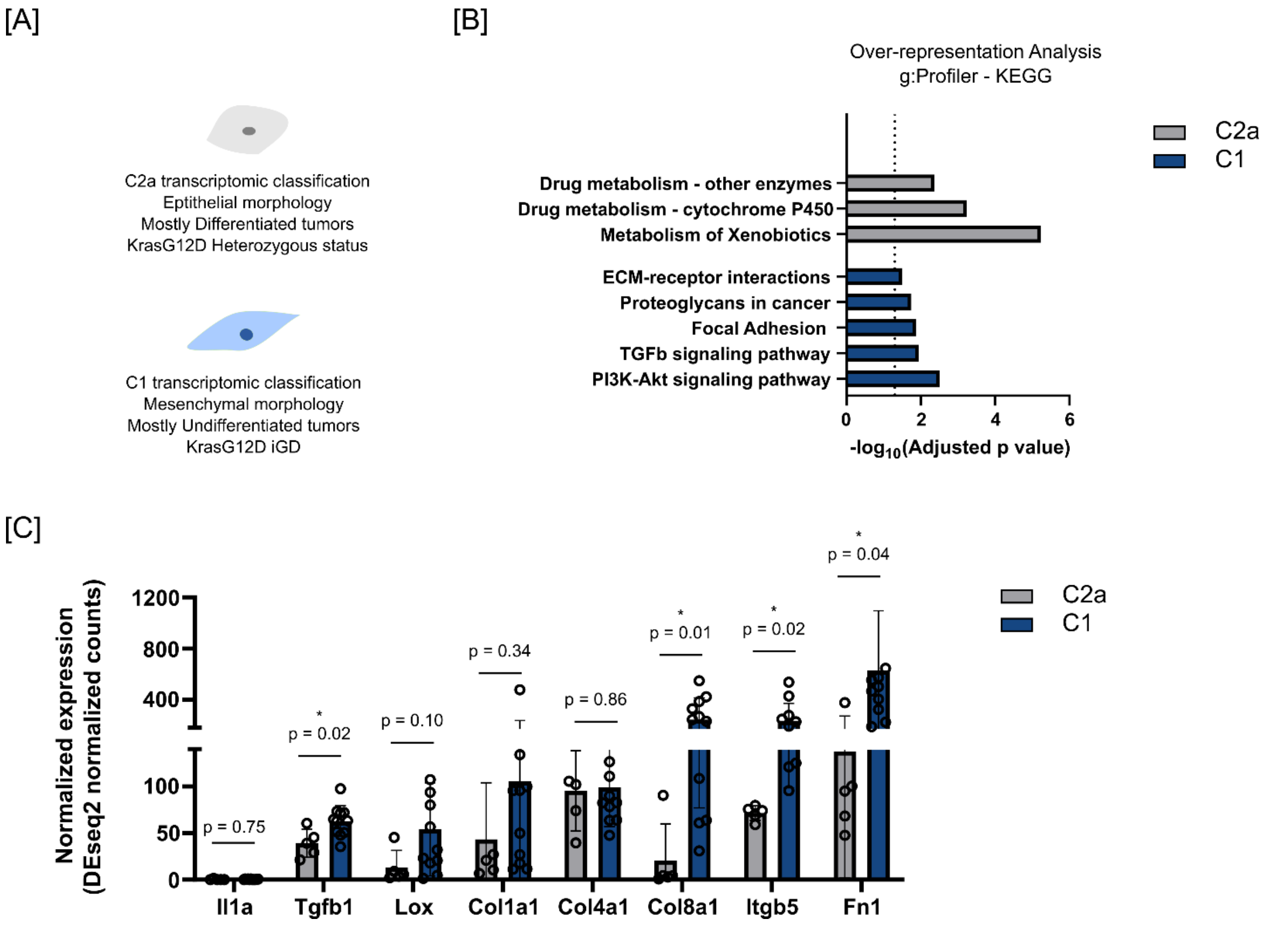

Figure 20 – *Kras* iGD appears responsible for maintaining a myCAFs-related phenotype in poorly-differentiated tumors through increased Tgfb1 and ECM-integrin signaling, although tumor cell-extrinsic cues may be necessary for IL6 myCAFs activation

[A] Summary of the findings described in Müller *et al.*. Increased *Kras*^{G12D} dosage (KrasG12D iGD) defines epithelial and mesenchymal morphology in PDAC. Epithelial cells fell under the C2 cluster, further defined by three sub-groups, which were associated with differentiated tumors that could present different *Kras*^{G12D} statuses and metastization potential. On one side of the spectrum is the C2a cluster, characterized by *Kras*^{G12D} heterozygous status with no associated metastasis. The C1 cluster sits on the opposite side. This group presents poorly-differentiated and undifferentiated histology associated with *Kras*^{G12D} iGD, mesenchymal morphology, and higher metastization potential.

[B] Gene set enrichment analysis of the C2a and C1 cell lines. The RNAseq analysis was performed using the *Kras*^{G12D} heterozygous C2a (n=6) and *Kras*^{G12D} iGD C1 (n=12) cell lines characterized in Müller *et al.*. The DEGs presenting an adjusted p-value inferior to 0.05 and a fold-change above 1 or below -1 were selected. An overrepresentation analysis was performed using g:profiler, and selected KEGG pathways were depicted. The dotted line represents the threshold used for statistical significance (adjusted p-value of 0.05).

[C] Expression levels of selected genes associated with the CAFs phenotypes observed in differentiated and poorly-differentiated tumors and the pathways depicted in [B]. Data are represented as mean ± SD. The statistical significance was tested using an unpaired t-test with a welch correction in which no multiple comparison correction was performed.

The differential gene expression analysis between C2a and C1 lines showed 1031 differentially expressed genes. These genes were input into g:profiler to determine KEGG pathways overrepresented in C2a and C1 cell lines (Figure 20-B). The overrepresentation analysis showed that in C2a lines, the most represented pathways were related to metabolic processes, whether, in C1 lines, pathways related to ECM interactions and TGFβ1 signaling were upregulated.

The upregulation of *Tgfb1* and ECM-related genes are depicted in Figure 20-C. Core matrisome genes such as *Col5a1*, *Col8a1,* and *Fn1* were upregulated, along with matrisome regulators such as *Lox*, *Loxl1*, and *Loxl3*. Moreover, the integrins regulation was changed. The integrin *Itgb5* was upregulated in poorly-differentiated tumors, but *Itga1* and *Itga2* were downregulated. TGFβ signaling pathway enrichment was also a characteristic of C1 tumor cells. The ligand *Tgfb1* was upregulated in addition to its downstream activation targets, such as the *Fn1* and *Lox* family genes.

Nevertheless, IL1a was expressed at very low levels in C2a and C1 tumor cells, suggesting that tumor cell-derived IL1 may not contribute to the activation of IL6 myCAFs in this context.

Altogether, this analysis revealed genes that may be involved in pathways responsible for the changes observed in the stromal TME. However, further experiments are necessary to understand tumor cell-CAFs communication profiles and if other cell types might be involved in the interplay between CAFs and tumor cells.

4.1.6 Influence of tumor cell *Trp53* proficiency in the stromal TME composition and tumor architecture

KRAS-driven PDAC harbors, in approximately 70% of the cases, deletions or missense mutations in *TRP53 (Raphael et al., 2017; Waddell et al., 2015)*. Even though TRP53 has been described as a modulator of immune regulation, how TRP53 signaling remodels the stromal TME and induces CAFs population activation was not described yet. To understand the role of wild-type *Trp53* in the stromal TME content and organization, PDAC tissues containing tumor cells with a *Trp53* wild-type allele (hereafter *Trp53*-proficient) and PDAC tissues in which tumor cells underwent *Trp53* LOH or complete *Trp53* deletion from embryogenesis (hereafter Trp53-deficient) were analyzed using the multiplex immunofluorescent panels, RNAseq, and organoid and fibroblast co-cultures. Since this thesis previously described the differentiation status role in the remodeling of stromal TME composition, the impact of the *Trp53* wild-type allele loss was analyzed in differentiated tumors.

The PDAC cohort was composed of differentiated KRAS-driven tumors and was stratified into two groups depending on *Trp53* status (Figure 21-A). The *Trp53* status in tumor cells was assessed using PCR and co-expression of KRT18 and P21 through imaging. The proficient group comprised 4 tumor samples that retained differentiated features and at least one *Trp53* wild-type allele. The deficient group was composed of three differentiated tumors that lost both *Trp53* wild-type alleles.

The tumors were benchmarked to each other using the general abundance of all populations as variables (Figure 21-B). The PCA analysis showed the *Trp53*-proficient tumors primarily located in the PC1 negative values, whereas *Trp53*-deficient tumors were located in the positive part of PC1, except for 13663, located in the middle of the chart. These differences between the groups suggest that the *Trp53* wild-type signaling in tumor cells may drive differences in the stromal TME.

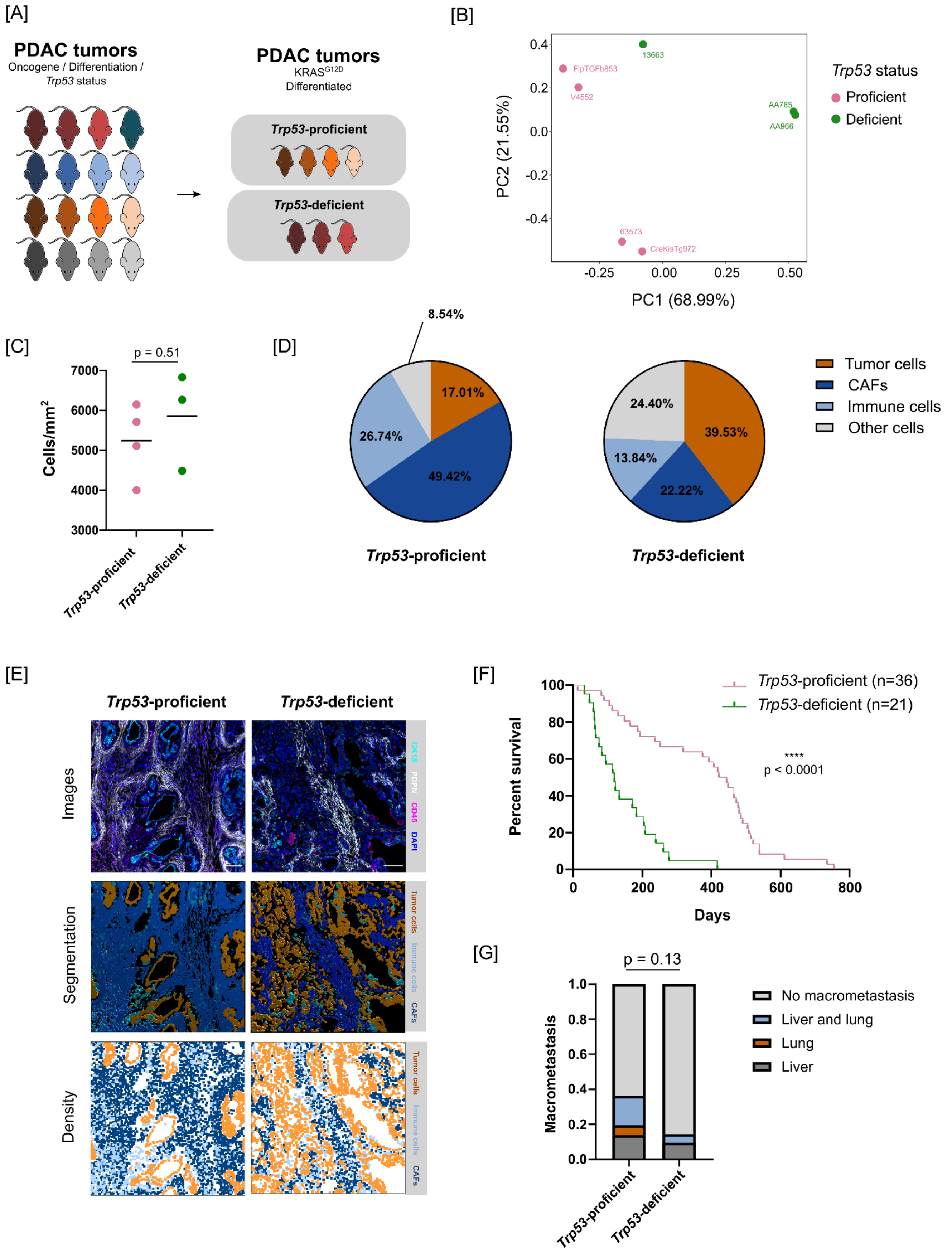

Figure 21 – Loss of the *Trp53* wild-type allele is associated with a remodeling of the PDAC TME.

[A] Cohort used to study tumor cell *Trp53* proficiency effects in PDAC TME. The Differentiated KRAS^{G12D} tumors in the initial cohort were allocated to the *Trp53*-proficient group (n=4) or *Trp53*-deficient group (n=3), depending on whether the *Trp53* allele was present (at least one wild-type allele) or absent in tumor cells.

[B] Multivariate data analysis of the cohort. The PCA was performed using all cell types in the PDAC stromal TME as variables. PC1 and PC2 were plotted to depict the relationships between the samples. Depending on their *Trp53* status, the samples were highlighted in pink (*Trp53*-proficient) or green (*Trp53*-deficient).

[C] Cellularity of the tumor samples per group. The cellularity represents the density of nuclei present in the whole area of the images analyzed, and each dot in this analysis represents the mean of the measurements made for each specimen. An Unpaired t-test assessed the statistical differences between both groups with Welch correction.

[D] Composition of the TME in *Trp53*-proficient and *Trp53*-deficient tumors. The pie charts describe the composition of Tumor cells, CAFs, Immune cells, and other types of cells in the TME. To test for statistical significance between the groups, the CAFs populations were subjected to an Unpaired t-test with a Welch correction. *Post hoc* correction for multiple comparisons was not performed. Tumors that were *Trp53*-proficient presented a significantly higher amount of CAFs (p =0.05) but a lower abundance of tumor cells (p=0.04). Although non-significant, *Trp53*-proficient tumors also tend to display higher immune infiltration (p=0.18).

[E] Representation of the immunofluorescence images, segmentation, and histocytometry analysis for the *Trp53*-proficient and *Trp53*-deficient groups. The scale bar is 100 µm.

[F] Survival analysis between groups is depicted in the Kaplan-Meyer curve. Paraffin-embedded tumors were used to perform the histopathological analysis. Differentiated KRAS^{G12D} tumors in which no *Trp53* deletion/mutation (pink) was introduced from tumorigenesis (n=36) were compared to differentiated KRAS^{G12D} comprising a heterozygous or homozygous deletion/mutation of *Trp53* (n=21) (green). The Log-rank test generated a significant difference between the groups.

[G] Metastization potential of the cohort analyzed in [F]. The macrometastasis, annotated when the animal was sacrificed, are represented in the bar plot. Significant changes were evaluated using the two-sided Fisher's exact test (* corresponding to a p-value inferior to 0.05).

Acknowledgments: The animals used in this study were bred and sacrificed by all the members of AG Saur. The histopathological analysis used in multiplex IF analysis was done together with Tânia Santos. In addition, Chen Zhao and Moritz Jesinghaus performed the histopathological analysis that allowed the analysis in [F] and [G].

The loss of the wild-type *Trp53* allele was associated with an overall remodeling of the TME (Figure 21-D). Tumor cell content was significantly increased in *Trp53*-deficient tumors (p=0.04), where tumor cells accounted for 39.53±14.64% of all cells compared with 17.01±5.92 in *Trp53*-proficient tumors. As expected, increased tumor cell content was accompanied by decreased CAFs numbers (p=0.05). *Trp53*-deficient tumors contained 22.23±17.99% of CAFs, whereas, in *Trp53*-proficient tumors, CAFs accounted for 49.41±10.95% of the tumor. The immune cell abundance was also altered between these groups, but not significantly (p=0.18). *Trp53*-proficient tumors present a higher content of immune cells (26.74±13.66%) compared with *Trp53*-deficient tumors (13.84±3.20%). These alterations did not arise from changes in cellularity but rather an overall remodeling of the TME. In fact, these tumors presented similar cellularity, indicating that changes in cell size, ECM, and other decellularized parts of the tissue were not a confounding factor in the analysis (p=0.40) – Figure 21-C. As a matter of fact, this can be corroborated by the histocytometry analysis performed and showcased in Figure 21-E.

As described in the literature, *TRP53* mutations lead to a worse prognosis in PDAC, exhibiting a worse overall survival (McIntyre *et al.*, 2020; Safi *et al.*, 2022). Mice bearing differentiated KRAS-driven tumors with the introduction of a heterozygous or homozygous deletion or loss-of-function *Trp53* mutation presented a reduced survival rate compared with animals in which *Trp53* was not targeted (p<0.0001). Nonetheless, the metastasis rate was increased in mice in which no *Trp53* alteration was introduced compared with animals with *Trp53* heterozygous or homozygous deletion or loss-of-function mutation (p=0.13).

The stromal compartment, CAFs-tumor cell interactions, and tumor architecture were further studied to understand how the stromal TME could shape survival and metastasis in tumors that lost *Trp53* wild-type signaling.

4.1.6.1 Loss of *Trp53* wild-type allele is associated with iCAFs abrogation and increased content of myCAFs-related populations

To understand the differences in stromal activation between *Trp53*-proficient and -deficient tumors, CAFs populations abundance within all cells and their proportion within CAFs was calculated.

The presence of the *Trp53* WT was associated with higher stromal content. In most *Trp53*-proficient tumors, CAFs content ranged from approximately 39% to 62%, representing in most tumors approximately 50% of the TME – Figure 22-A. In Trp53-deficient tumors, CAFs abundance ranged from approximately 10% to 42%.

The subpopulation frequencies within the CAFs groups are shown in Figure 22-B. Early myCAFs were the most abundant population in both groups, comprising 64.40±23.13% of all CAFs populations in *Trp53*-proficient and 44.64±37.62% in *Trp53*-deficient tumors. Nevertheless, the early myCAFs content was not statistically significant (p=0.43). Despite the fact that early myCAFs content within all CAFs was unchanged, it must be stressed that this population content was increased, among all cells, in *Trp53*-proficient tumors (34.93±15.22%). The content of early myCAFs among all cells in *Trp53*-deficient animals was heterogeneous (14.48±19.02%) and was not statistically different (p=0.17). Other myCAFs-related populations were represented mainly in *Trp53*-deficient tumors, although the abundance was heterogeneous. One example was myCAFs, which were highly abundant among CAFs in two out of three *Trp53*-deficient tumors (p=0.06). In these tumors, myCAFs made up 35.29±24.76% of all CAFs compared with 5.70±5.45% in samples where tumor cells retained at least one WT allele. Another example was IL6 myCAFs, representing only 0.20±0.25% of all CAFs in *Trp53*-proficient tumors and 14.24±24.66% in the *Trp53*-deficient. However, this cell type was present in higher levels on only one *Trp53*-deficient sample (p=0.29).

The most striking difference (p=0.003) between the stromal TMEs was the abrogation of iCAFs content in *Trp53*-deficient tumors (0.04±0.07%), whereas, in *Trp53*-proficient tumors, they were the second most abundant CAF population (34.76±9.53%). This result was also observed not only within the CAFs content but also among all cells. iCAFs represented 12.17±8.34% of cells in *Trp53*-proficient PDAC but were rare in *Trp53*-deficient tumors (0.003±0.006%). IL6 iCAFs were not detected in both groups.

In addition, stellate cells' content was significantly altered in *Trp53*-proficient and -deficient tumors (p=0.04). When tumor cells retained the *Trp53* WT allele, stellate cells represented only 0.49±0.33% of CAFs content, while *Trp53*-deficient samples contained 4.24±2.55%. The global content of stellate cells was also altered, accounting for 1% or less of all cells. *Trp53*-deficient tumors comprised 1.05±1.31% of all cells, while in *Trp53*-proficient samples, stellate cells represented only 0.24±0.20% of all cells.

Antigen-presenting CAFs content, however, remained unaltered in both groups within the CAFs content and overall cell content (p=0.47 and p=0.17, respectively). In *Trp53*-proficient samples, apCAFs represented 3.16±3.25% of all CAFs, but only 1.50±1.26% of all cells. In *Trp53*-deficient samples, apCAFs represented only 1.55±1.26% of all CAFs, dropping to a mere 0.27±0.38% of all cells.

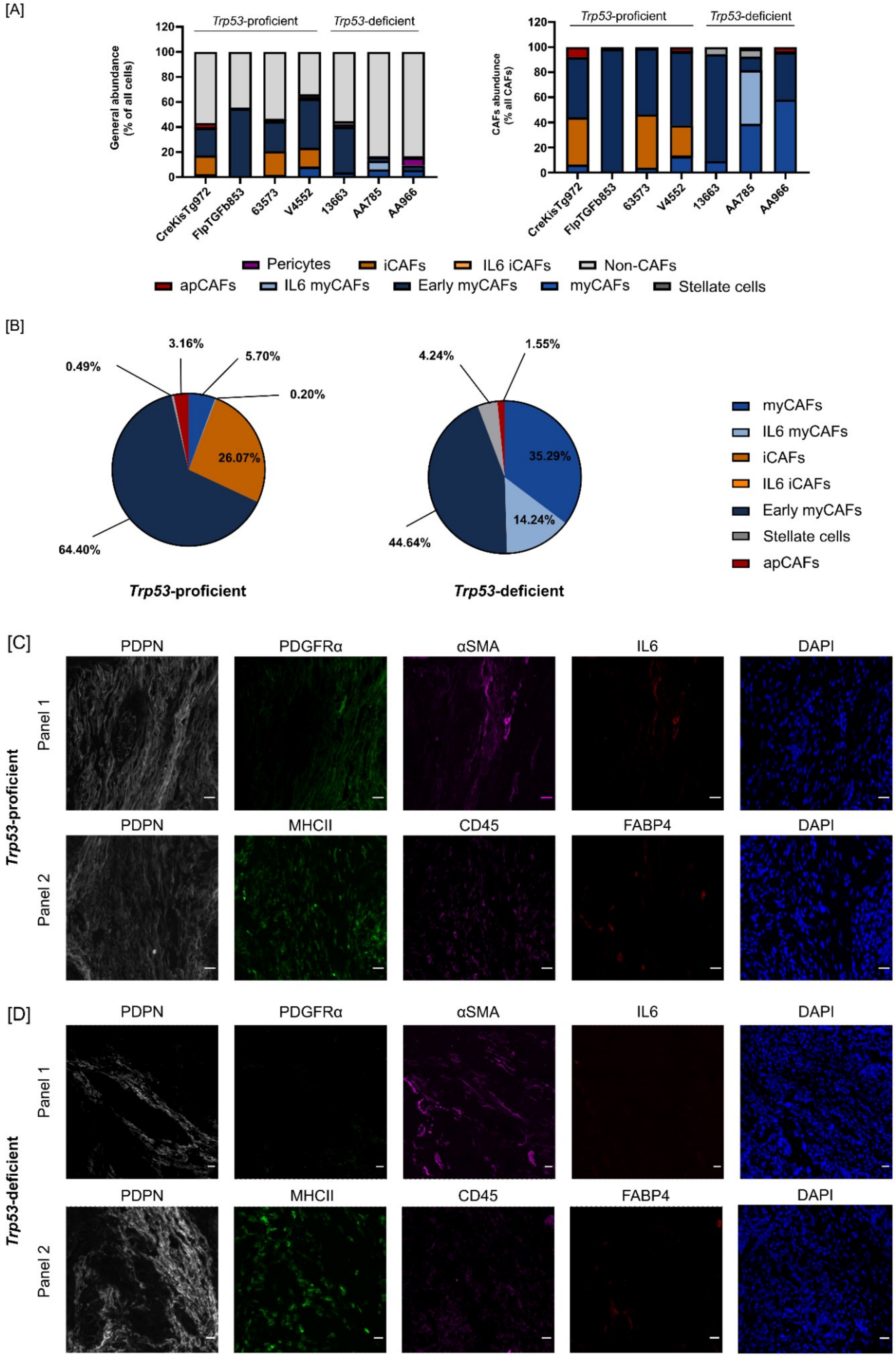

Figure 22 – *Trp53*-deficient tumors present high myCAFs content and abrogation of iCAFs activation in the PDAC TME.

[A] The general abundance of CAFs populations in *Trp53*-proficient and -deficient tumors is represented at the left. The absolute number of each CAFs population was normalized by the total number of cells – nuclei. In the right panel is depicted the general abundance of CAFs populations. The absolute number of each population of CAFs was normalized by the absolute number of CAFs. The abundance of the populations was determined using the multiplex IF panels followed by the correspondent population segmentation.

[B] Mean of CAFs populations in the stromal-TME of *Trp53*-proficient and -deficient tumors. The CAFs populations of both groups were compared using an Unpaired t-test with Welch correction. No multiple correction test was applied. Even though there was a trend toward a significant increase in myCAFs (p=0.062) and a significantly increased content in stellate cells (p=0.04) in *Trp53*-deficient tumors, iCAFs abundance was almost inexistent (p=0.03).

[C]-[D] Representative images for both cohorts of each channel of the multiplex IF panel 1 that phenotypes early myCAFs, myCAFs, iCAFs, IL6 myCAFs, IL6 iCAFs, and each channel of the multiplex IF panel 2 that phenotypes stellate cells and apCAFs. The scale bar corresponds to 20 µm.

In summary, the composition of CAFs between *Trp53*-proficient and -deficient tumors was significantly altered, with iCAFs content characteristic of Trp53-proficient tumors. The data also suggested a dichotomy between the loss of iCAFs and the increased content in myCAFs-related populations.

4.1.6.2 *Trp53* status influences myCAFs-tumor cells interactions

The analysis of the multiplex panels of *Trp53*-proficient and -deficient tumors proved the remodeling of the stromal TME, showing a dichotomy in the activation of iCAFs and myCAFs-related populations. These changes in CAFs populations' content and other cells of the TME may result in altered CAFs-tumor cell neighborhood profiles. To analyze if these differences may exist, the Euclidean distances between CAFs sub-types and tumor cells were calculated using CytoMAP. The results are depicted in Figure 23-A.

Populations within the myCAFs umbrella term (early myCAFs, myCAFs, IL6 myCAFs) presented differences in cell content that did not entirely translate to differences in tumor cell neighborhoods. myCAFs populations were much closer to tumor cells in *Trp53*-deficient tumors (p<0.0001), at a median distance of 21.89 µm compared with *Trp53*-proficient tumors where myCAFs were at approximately 41.28 µm to tumor cells. These differences between groups in the myCAFs population were also observed regarding myCAFs density surrounding tumor cells. In *Trp53*-deficient tumors, about 60% of myCAFs were located within 25 µm of tumor cells, contrarily to *Trp53*-proficient tumors where only 30% of myCAFs were located within that range (Figure 23-B). IL6 myCAFs were also significantly closer to tumor cells in the *Trp53*-deficient group (p<0.0001). In these samples, IL6 myCAFs were at a median distance of 36.92 µm to tumor cells and 63.84 µm in *Trp53*-proficient tumors. Nevertheless, both groups did not present an altered density of IL6 myCAFs surrounding tumor cells. Approximately 25% of IL6 myCAFs in *Trp53*-proficient and 20% in *Trp53*-deficient tumors were located in a 25 µm radius. Early myCAFs, however, presented an opposite profile compared with the other myCAFs-related populations. This population did not present significant differences in the median distance to tumor cells between the groups (p=0.20). In the proficient group, early myCAFs were at a median distance of 35.79 µm, whereas in the Trp53-deficient tumors, early myCAFs were at a median distance to tumor cells of 45.05 µm. This difference was, although, very evident in the density of this population revolving around tumor cells. In samples where tumor cells were proficient in *Trp53*, approximately 34% of the cells were at 25µm of tumor cells compared with 16% in *Trp53*-deficient samples.

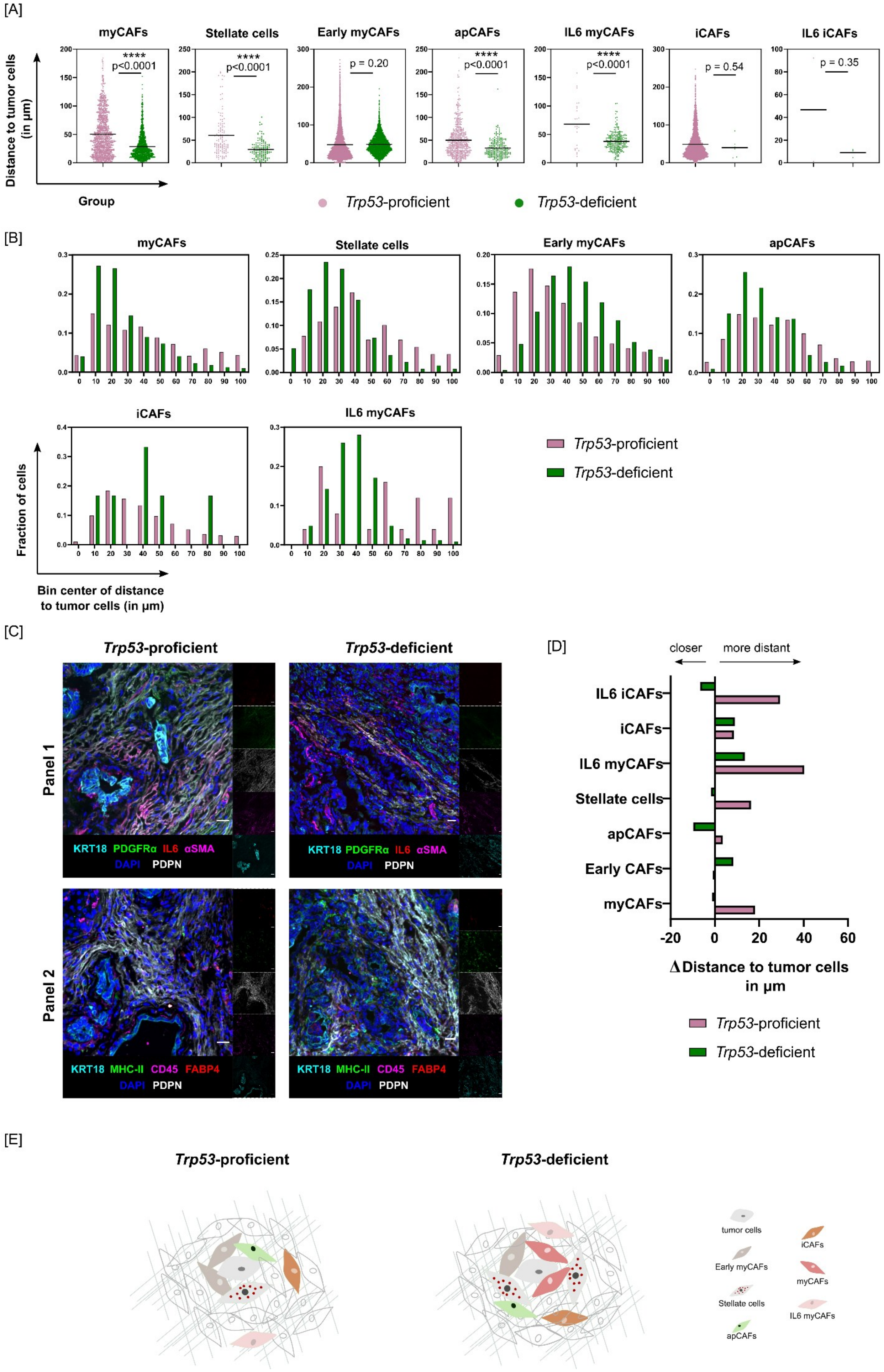

Figure 23 – *Trp53*-deficient tumors present closer interactions between myCAFs and tumor cells.

[A] Median distance of CAFs populations to tumor cells in the *Trp53*-proficient (pink) and *Trp53*-deficient (green) cohorts. All the correspondent CAFs distances to tumor cells were depicted in the dot plots in which each dot corresponds to one cell. The number of cells analyzed is variable and depends on the absolute number of cells segmented for each population. An unpaired t-test with a Welch correction was deployed to evaluate whether the differences between the groups' communication patterns were significant. Significant interactions were marked with asterisks (**** $p < 0.0001$), or the exact p-value was shown.

[B] Frequency distribution of CAFs populations distances to tumor cells. The frequency of the distribution of all CAFs subpopulations is depicted in the bar plot with a 105 µm diameter. The bin size is 10 µm and starts at 0, meaning that for each center, the CAFs are calculated using the intervals [0,5],]5,15,]15, 25],]25, 35],]35, 45],]45, 55],]55, 65],]65, 75],]75, 85],]85, 95],]95, 105]. The *Trp53*-proficient group is depicted in pink, and the -deficient group in green.

[C] Representative images for the *Trp53*-proficient and *Trp53*-deficient groups. Each channel of the multiplex IF Panel 1 and Panel 2 is represented. The scale bar is 20 µm.

[D] Difference in the median distance of CAFs populations to tumor cells in both groups to the reference measurement in Figure 4E. The *Trp53*-proficient group is depicted in pink, and the -deficient group in green.

[E] Graphic scheme summarizing the findings of Figure 21. In *Trp53*-proficient tumors, most CAFs were further located from tumor cells.

Even though there were striking differences in the iCAFs content, there were no differences in the median distance of this CAFs population to tumor cells (p=0.54). iCAFs were, in both *Trp53*-proficient and -deficient, located at approximately 38 µm to tumor cells. Moreover, due to the low abundance of cells in the *Trp53*-deficient, it was difficult to assess if the density profiles of iCAFs surrounding tumor cells changed. IL6 iCAFs were barely present in this analysis, so it was not possible to extract any illations.

The remaining stromal populations, such as stellate cells and apCAFs, were also closer to tumor cells deficient in *Trp53* than to proficient tumor cells. Stellate cells were at a median distance of 45 µm to tumor cells in *Trp53*-proficient samples and 27 µm in *Trp53*-deficient samples. Indeed, this difference was correlated with an increased stellate cells' density around tumor cells in the Trp53-deficient group, where approximately 46% were located in 25 µm of tumor cells. In *Trp53*-proficient samples, only 18% of stellate cells were at a 25 µm radius of tumor cells. Antigen-presenting CAFs were at an approximate median distance of 42 µm in *Trp53*-proficient tumors and 29 µm in -deficient samples. This significant change (p<0.0001) was also linked to a slightly higher density of apCAFs. In *Trp53*-proficient tumors, 26% of apCAFs were located within a radius of 25 µm to tumor cells, wherein the -deficient group, approximately 41% were located within the same distance.

To highlight context-specific differences in tumor cell neighborhoods, the differences in the CAFs' distances to tumor cells were calculated using all 16 tumors as the baseline. Combining this analysis with the CAFs' density information within a specific radius, it became evident that populations such as myCAFs, apCAFs, and stellate cells presented opposite trends when neighboring tumor cells in *Trp53*-deficient tumors. Contrarily, in *Trp53*-proficient tumors, early myCAFs probably exhibit more interactions with tumor cells. These differences are summarized in Figure 23-D and depicted in the graphical summary in Figure 23-E.

In summary, *Trp53*-deficient tumors showcased rich tumor cells-CAFs relationships compared with *Trp53*-proficient, which could be dictated by molecular changes and overall population content. Whether these changes mirror alterations in cell niches and overall architecture need to be determined.

4.1.6.3 Tumors with loss of *Trp53* wild-type allele feature a tumor architecture based on myCAFs-related populations interactions

Trp53-proficient and -deficient tumors presented distinct tumor cells-CAFs neighborhood profiles, accompanied by changes in tumor cell and CAFs ratios. Cell neighborhoods were calculated to assess if alterations in neighborhood profiles may translate into architectural changes. As described in 4.1.4.3, cell neighborhoods were determined using a 20 µm raster scan, and the local cellular density and composition were calculated and used as a variable to cluster areas with a similar profile.

Trp53-proficient and -deficient PDAC presented 5 types of neighborhoods, described in Figure 24-A. The content of the different CNs in this analysis was heterogeneous. However, generally, *Trp53*-deficient tumors presented high content of CNs enriched in tumor cells and myCAFs-related populations and loss of iCAFs niches, albeit these changes were not statistically significant with the sample number analyzed.

As expected, the significant increase in tumor cell content observed between the groups was also translated into a trend toward an increased content of the CN1 neighborhood (p=0.13). The CN1 neighborhood was composed mainly of tumor cells (88%), with approximately 6% early myCAFs, 3.5% myCAFs, 1.5 % IL6 myCAFs, and 1.0% iCAFs. Indeed, in *Trp53*-deficient tumors, 59.00±19.90% of cells were in the CN1 neighborhood compared with 37.00±12.00% in *Trp53*-proficient tumors.

The remaining cells in Trp53-deficient samples were mainly allocated to CNs of myCAFs-related populations, represented by neighborhoods CN2, CN4, and CN5, enriched in early myCAFs, IL6 myCAFs, and myCAFs, respectively. The CN2 neighborhood represented mostly niches between CAFs, containing approximately 73% of early myCAFs, 16% of myCAFs, and 9% of iCAFs. The CN4 and CN5, however, contained approximately 20 and 40% of tumor cells, where IL6 myCAFs and myCAFs could interact with tumor cells. Although there was a general trend toward an increased myCAFs-related neighborhood in *Trp53*-deficient tumors, the three analyzed tumors presented a different CN profile, displaying in each sample either CN2, CN4, or CN5 neighborhoods. Moreover, the presence of CN2 neighborhoods was not exclusive to *Trp53*-deficient tumors. Although only one animal in *Trp53*-deficient tumors exhibited CN2 neighborhoods, all *Trp53*-proficient tumors presented early myCAFs neighborhoods, containing approximately 42.5±10.0% of all cells.

The most striking trend was the loss of iCAFs-enriched neighborhoods due to the observed loss of iCAFs content in *Trp53*-deficient tumors (p=0.16). The CN3 neighborhood exhibited approximately 70% of iCAFs, complemented by 14.5% early myCAFs, 8% tumor cells, and 7% IL6 myCAFs, showing a niche that may rely mainly upon CAFs-to-CAFs interactions. In *Trp53*-proficient tumors, this CN profile accounted for 20.3±16.5% of the cell niches, representing the third most abundant CN in this group in contrast with *Trp53*-deficient tumors where CN3 represented a mere 3.3±5.8% of all niches.

Altogether, *Trp53*-proficient and -deficient tumors presented different tumor architectures. These differences may be driven not only by increased tumor cell content concomitant with loss of CAFs content but also by tumor cell-derived cues, which may drive myCAFs-related neighborhoods in poorly-differentiated tumors.

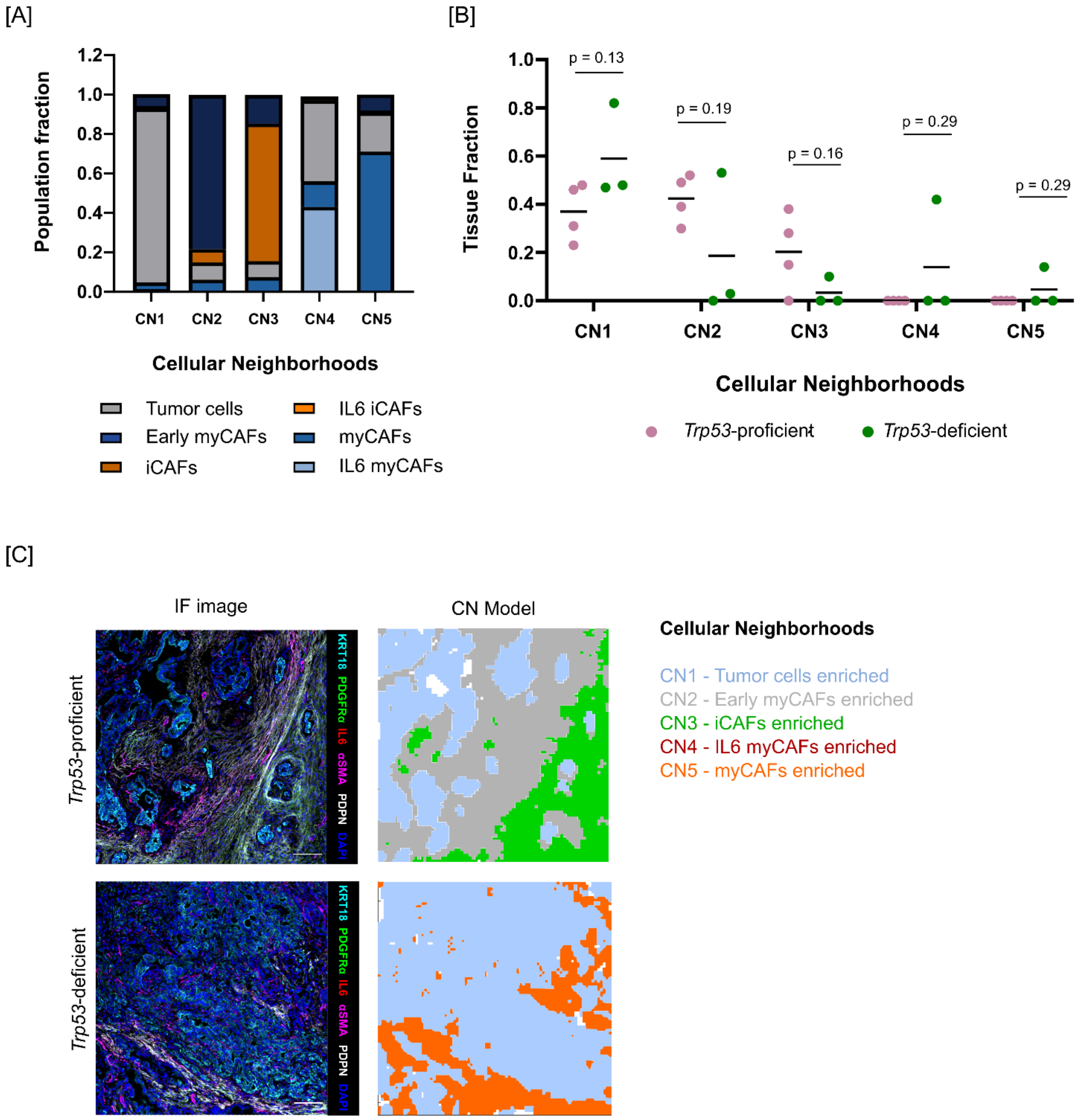

Figure 24 – TME architecture of Trp*53*-deficient tumors is heterogeneous but abundant in tumor cell and myCAFs-related populations interactions.

[A] Cellular composition of the CNs. Five CNs were identified based on the seven populations and their respective frequencies within each CN (pooled data from both groups).
[B] Cellular Neighborhoods distribution in the *Trp53*-proficient (pink) and *Trp53*-deficient (green) tumors. Data are represented as the mean of the tissue fraction occupied by each CN. Each dot represents an animal. Statistical differences between both groups were assessed using an Unpaired t-test with a Welch correction. No statistical significance was observed, and the exact p-values were depicted.
[C] Graphic representation of the CN model and correspondent IF image. The annotation of each CN was performed based on the most frequent population present on the respective CN. Scale bar is 100 µm.

4.1.6.4 Loss of *Trp53* wild-type allele in tumor cells drives the upregulation of ECM genes

Tumors harboring different *Trp53* status showed differences in cell content, cellular organization, and cellular neighborhoods. To understand how tumor cell *Trp53*-driven molecular changes could shift

CAFs activation toward a myCAFs-related phenotype, mRNA transcript expression was measured in *Trp53*-proficient or -deficient organoid lines.

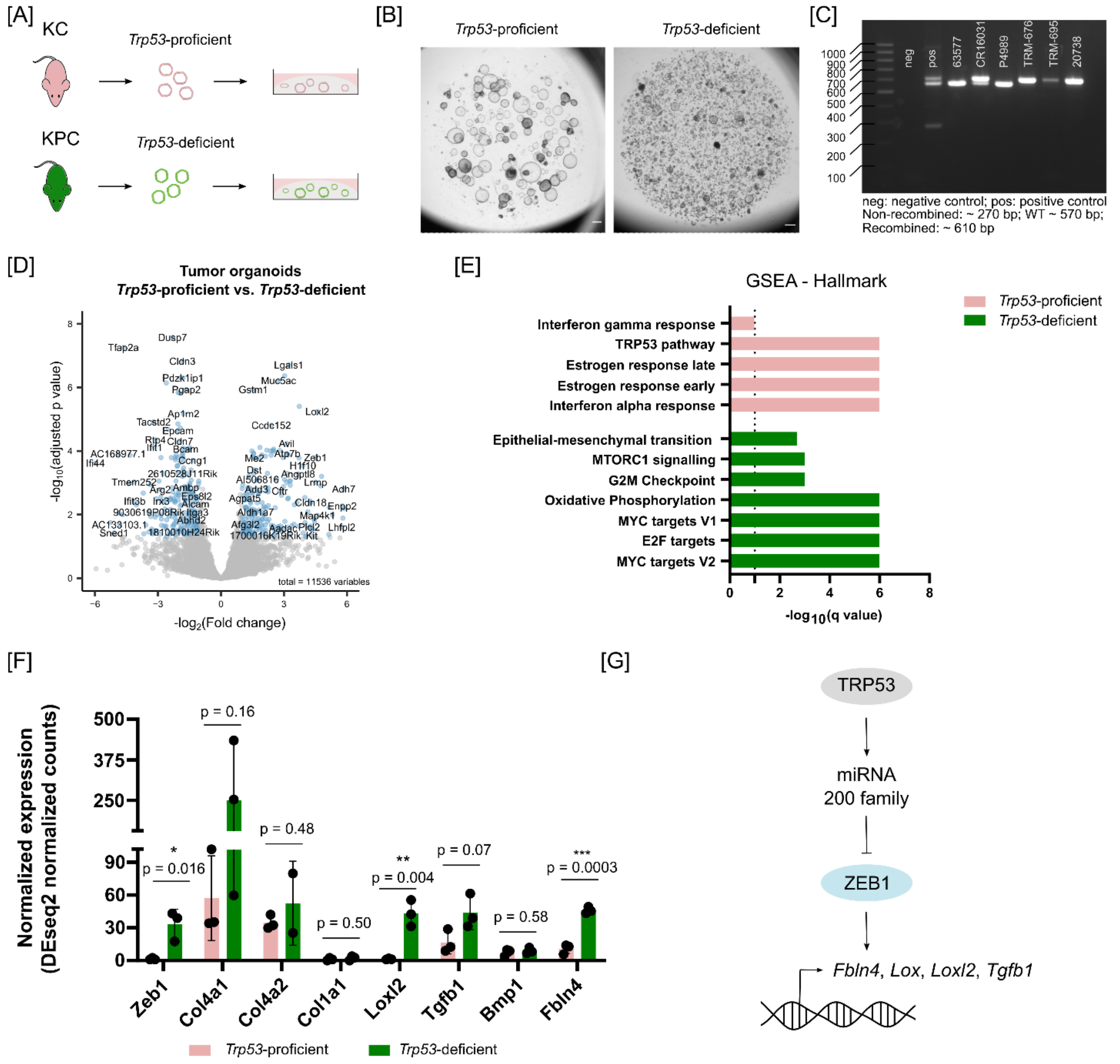

Figure 25 – Loss of *Trp53* wild-type allele may drive *Zeb1* regulation of genes that impact matrix accumulation in the TME.

[A] Experimental design to characterize the tumor-cell intrinsic mechanism of *Trp53*-proficient and -deficient PDAC. Organoids were isolated from KC and KPC tumor-bearing animals and 3D-cultured in matrigel. After seven days of culture, the organoids were collected, *Trp53* status was confirmed, and a transcriptomic characterization was performed.

[B] Representative image of *Trp53*-proficient and *Trp53*-deficient-tumor organoids after seven days of culture in matrigel. The scale bar corresponds to 500 µm.

[C] An end-point PCR was performed to confirm *Trp53* status in the tumor organoids. This PCR originated three bands: a non-recombined band (270 bp), a recombined band (approximately 610 bp), and a band identifying the *Trp53* wild-type allele (570 bp). The controls of this PCR are showcased in the image: a sample to control for random DNA amplification (negative control) and a sample with the desired DNA templates (positive control).

[D] Volcano plot of the differential gene expression analysis of *Trp53*-proficient (n=3) and *Trp53*-deficient (n=3) tumor organoids. The cut-off used for the DEG fold-change was 2 ($\log_2$(Fold-change) < -1 or $\log_2$(Fold-change) < 1), and the cut-off for the adjusted p-value was 0.05 ($\log_{10}$(adjusted p-value) < 1.3). Non-significant DEGs are depicted in grey, and significant DEGs are depicted in blue.

[E] Gene set enrichment analysis of *Trp53*-proficient (pink) and *Trp53*-deficient tumor (green) organoids of well-defined biological hallmarks. The dotted line represents the threshold used for statistical significance (adjusted p-value of 0.05).

[F] Normalized expression levels of genes associated with the *Trp53*-induced regulation of the TME. Data are represented as mean ± SD. The statistical significance was tested using an unpaired t-test with a welch correction in which no multiple comparison correction was performed. The *Trp53*-proficient group is depicted in pink, and the -deficient group in green.
[G] Model of the hypothesis of TRP53-induced tumor cell-intrinsic regulation of the TME. TRP53 regulates the expression of the miRNA 200 family transcriptionally. miRNA200 family can, in its turn, directly inhibit ZEB1-induced transcriptional programs. In the absence of TRP53, downregulation of the miRNA 200 family occurs, leading to ZEB1-regulated transcription of genes like *Fbln4*, *Tgfb1*, and *Loxl2*.

Tumor organoids were isolated from KC and KPC tumor-harboring mice, cultured in matrigel, and their transcriptome was profiled (Figure 25-A and -B). To stratify the organoid lines according to *Trp53* proficiency, the presence of the *Trp53* wild type was confirmed by PCR. Figure 25-C depicts the results of the PCR. All the organoid lines were from the *Pdx1/ p48* lineage, presenting no contamination from cells from the TME, visible by the lack of amplification of the STOP cassette – non-recombined band. The lines 63577, CR16031, and P4989 showed amplification of the wild-type allele of *Trp53*. Conversely, the lines TRM-685, TRM-676, and 20738 showed loss of the wild-type allele due to lack of amplification of the 570 bp band. These lines presented a band occurring at 610 bp, corresponding to the amplification of the *Trp53*^{R172H} mutation.

The RNAseq showed that 470 genes were differentially expressed between *Trp53*-proficient and -deficient tumor cells (Figure 25-D). Of those, 242 genes were differentially expressed in *Trp53*-proficient tumors, mostly belonging to the TRP53 pathway, interferon alpha, gamma, and estrogen responses (Figure 25-E). On the other hand, in the *Trp53*-deficient organoids, epithelial-to-mesenchymal transition genes and MYC target genes were enriched, with 228 genes differentially expressed. The upregulation of EMT- associated genes, such as *Loxl2*, *Fbln4*, *Col4a1*, and *Wnt5a*, is associated with a fibrotic response – Figure 25-F (Naba *et al.*, 2016; Tian *et al.*, 2019). Trp53-deficient organoids presented *Zeb1* upregulation, indicating that there might be a regulation of the upregulated EMT-associated genes by this transcription factor (Figure 25-G). In fact, the deletion of *Trp53* induces the downregulation of the miRNA 200 family, leading to the transcription of *Zeb1*, which may act as a transcriptional activator of *Loxl2*, *Fbln4*, and *Col4a1* (Harmonizome, Zeb1 gene set) (Rouillard *et al.*, 2016). However, *Bmp1* is not differentially between *Trp53*-proficient and -deficient organoids.

In summary, this analysis revealed genes that may be involved in tumor cell regulation of the stromal TME. The upregulation of ECM genes may translate into an increased ECM deposition that can impact CAFs phenotype. Nevertheless, further experiments are necessary to prove the hypothesis of *Trp53*-mediated CAF activation.

4.1.6.5 Tumor cell *Trp53*-driven signaling appears to define CAFs activation state through ECM deposition

Trp53-deficient tumors displayed a higher number of niches in which tumor cells and myCAFs-related populations were in closer contact. Although myCAFs activation is dependent on TGFβ signaling activation, reports state the importance of mechano-transducing mechanisms in the maintenance of the phenotype (Foster *et al.*, 2022; Krishnamurty *et al.*, 2022). Therefore, to assess if CAFs phenotypes were dictated by ECM deposition upregulated by tumor cells, CAFs activation was analyzed in a co-culture setting. *Trp53*-proficient and -deficient organoid lines were co-cultured with a pancreatic pan-fibroblast line in a matrigel dome.

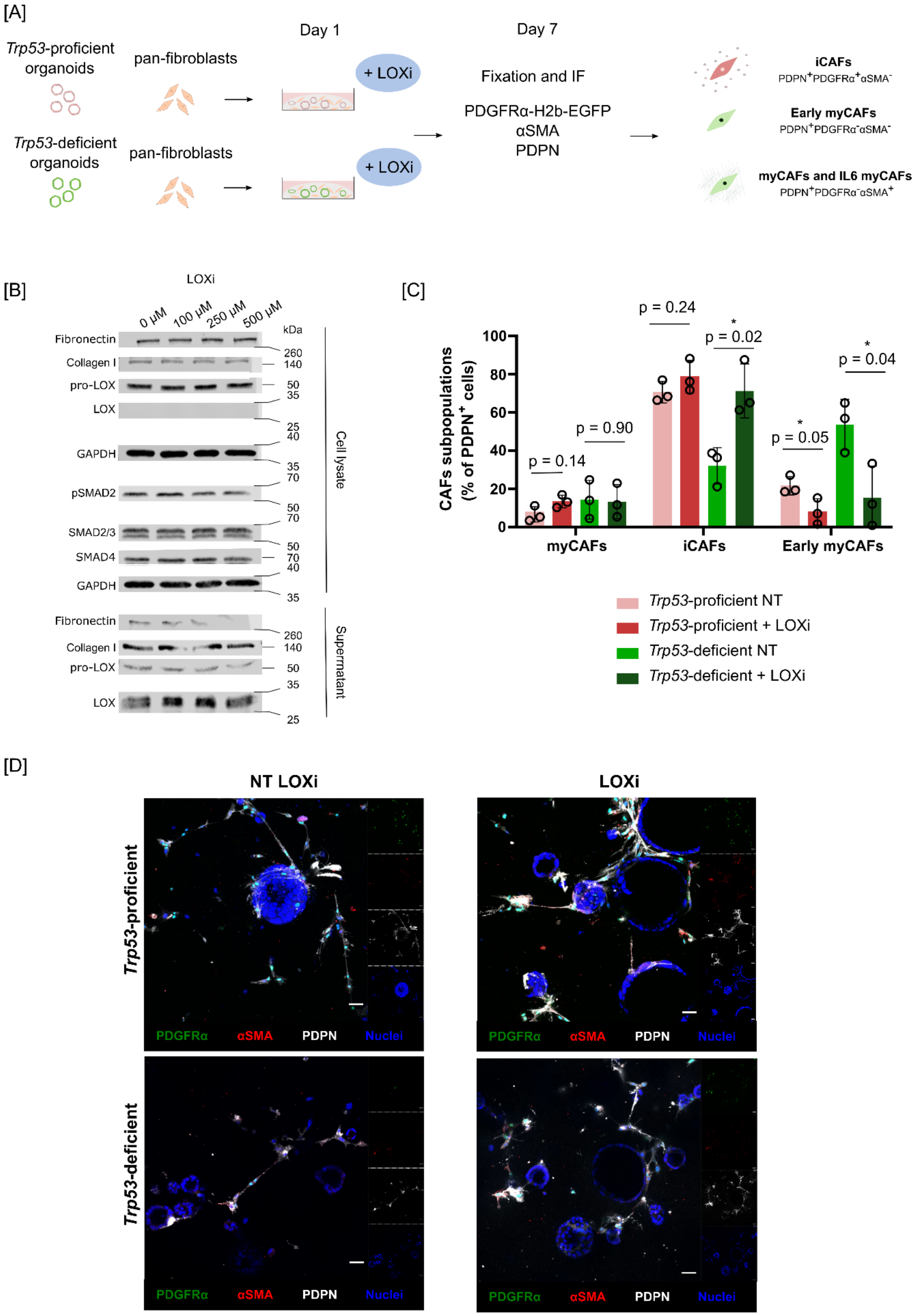

Figure 26 – Inhibition of collagen crosslinking restores iCAF phenotype in *Trp53*-deficient tumor cells co-cultures with pan-fibroblasts.

[A] To evaluate the importance of TRP53 induced-matrix deposition in the determination of CAFs phenotype, *Trp53*-proficient and -deficient tumor organoids were co-cultured with pan-fibroblasts for seven days. On day one of co-culture, Lysy-oxidase inhibitor – BAPN - was added to the culture medium. CAFs activation status was monitored on the seventh day of culture using IF.

[B] Evaluation of the effective dose of LOXi in mPSCs culture on 2D. mPSCs were treated with BAPN, and the cell lysate and cell supernatant were collected. An equal amount of protein was loaded, and proteins related to ECM and the canonical TFGβ1 signaling pathway were blotted. GADPH was used as the endogenous reference protein. The results are resultant of one replicate.

[C] CAFs activation profiles when BAPN inhibits ECM deposition in *Trp53*-proficient (n=3) and *Trp53*-deficient (n=3) organoids and mPSCs co-cultures. NT means non-treated and LOXi means treated with 500 µM of BAPN. The treatment confirmed that ECM deposition drives a shift from iCAFs to early myCAFs activation. The inhibitor exerts only a visible effect on *Trp53*-deficient tumor organoids co-culture setting as a possible consequence of the inhibition of the TRP53-miRNA200-ZEB1 induced ECM deposition. Statistical significance between the *Trp53*-proficient and -deficient treated groups was evaluated using an unpaired t-test with Welch correction. The exact p-values are depicted in the picture, and significant results are marked with an asterisk (* p<0.05 and ** p<0.001). The *Trp53*-proficient NT group is depicted in pink, the *Trp53*-proficient treated group in dark pink, the Trp53-deficient NT group in green, and the -deficient treated group in dark green.

[D] Representative IF images of CAFs phenotyping in the co-culture setting. The scale bar corresponds to 50 µm.

The Lysyl-oxidase inhibitor BAPN (LOXi) is an inhibitor of the Lysyl oxidase family, and it has been shown to reduce collagen deposition and ECM stiffness (Herchenhan *et al.*, 2015; Nicolas-Boluda *et al.*, 2021; Schilter *et al.*, 2019). The LOXi was added from day 1, and the activation state of fibroblasts was analyzed on day 7 by immunofluorescence (Figure 26-A).

Before the co-cultures were treated with LOXi, a pancreatic pan-fibroblast line was treated with increasing concentrations of BAPN to establish the concentration that would inhibit collagen crosslinking (Figure 26-B). The pancreatic pan-fibroblast line was treated with 100, 200, and 500 µM of BAPN, and the latter concentration reduced the amount of fibronectin and collagen I in the supernatant, although the total amount produced by the cells did not change. Moreover, the inhibition of lysyl oxidases using 500 µM BAPN resulted in decreased phosphorylation of SMAD2 and decreased amount of SMAD4.

Trp53-proficient and -deficient organoids, when co-cultured with a pancreatic pan-fibroblast line, originated different CAF activation profiles (Figure 26-C). In *Trp53*-proficient co-cultures, iCAFs comprised approximately 70.57±5.62% of all CAFs, whereas, in *Trp53*-deficient co-cultures, iCAFs made up 32.06±9.58% (p = 0.004). The content of early myCAFs was also changed conversely. *Trp53*-proficient co-cultures presented only 21.61±4.80% of early myCAFs compared with 53.60±13.30% in *Trp53*-deficient co-cultures (p=0.02). Surprisingly, no significant alteration was observed in myCAFs (p=0.36), with *Trp53*-deficient tumor presenting approximately 14.37±10.12% of myCAFs against 7.82±4.06% in -proficient co-cultures. The low myCAFs activation may be due to the time frame used for this study.

When the co-cultures were treated with LOXi, the effects observed were mostly restricted to *Trp53*-deficient co-cultures. CAFs profiles remained mostly significantly unchanged in *Trp53*-proficient co-cultures, presenting only a decrease in early myCAFs levels in LOXi-treated cultures (NT: 21.61±4.80% versus LOXi: 7.94±6.87%, p=0.04). In *Trp53*-deficient co-cultures, the CAFs levels were comparable to the non-treated *Trp53*-proficient model. In fact, iCAFs represented approximately 71.30±14.16% of the CAF compartment of LOXi-treated *Trp53*-deficient co-cultures. The early myCAFs content also decreased to the non-treated *Trp53*-proficient co-culture levels, comprising approximately 15.4±16.49% of all CAFs.

These results corroborated that the loss of the *Trp53* wild-type allele in tumor cells shifts CAFs activation towards a mechano-responsive myCAFs phenotype. Furthermore, tumor cells regulate the activation of CAFs through *Trp53*-induced ECM deposition mechanisms, which may be bypassed using drugs that normalize tumor stiffness.

4.1.6.6 Tumors rich in myCAFs present an upregulation of ECM and inflammatory transcriptional signatures

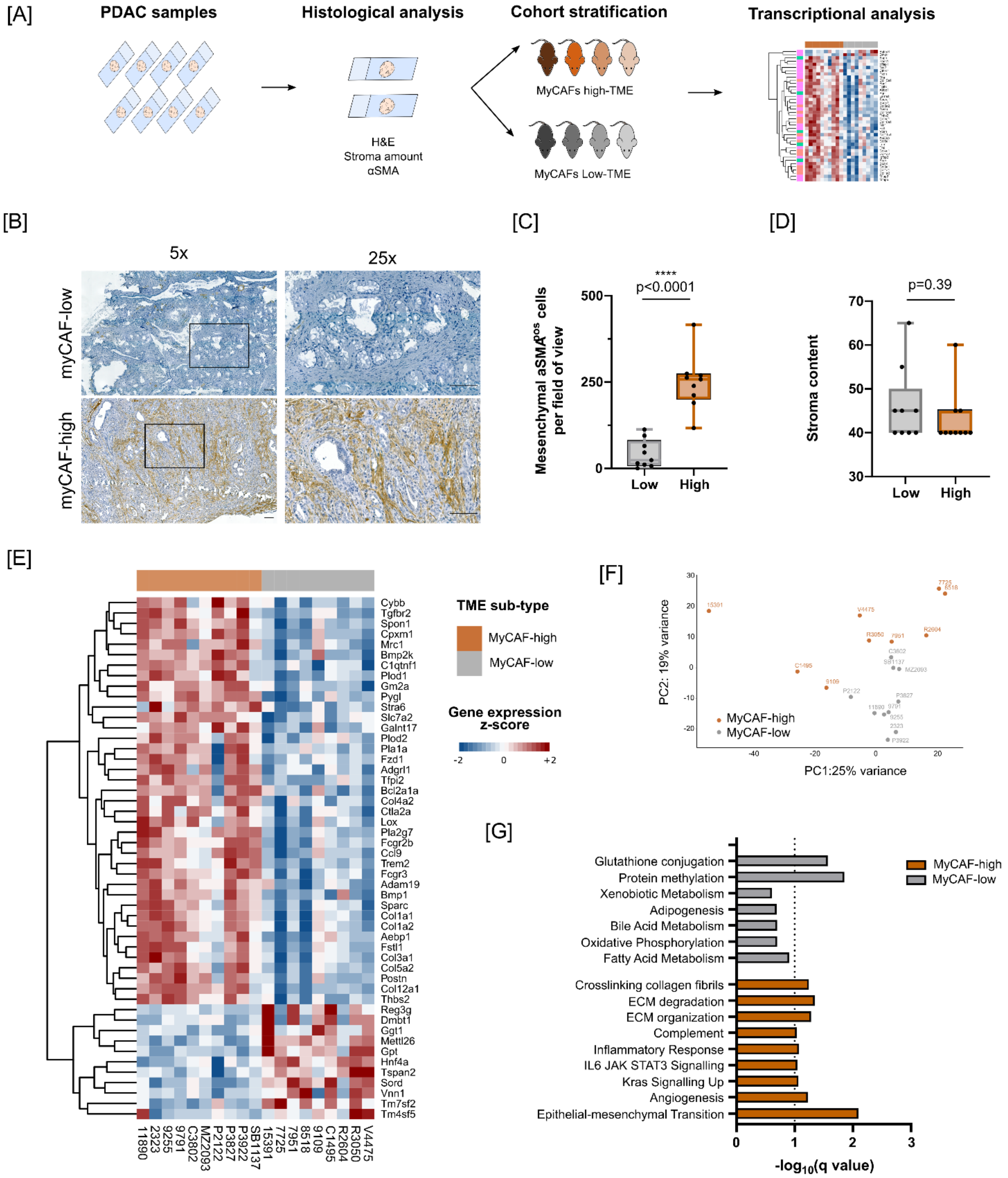

Figure 27 – Molecular signature of myCAFs-high tumors is associated with EMT and ECM remodeling programs.

[A] Workflow of the myCAFs-based stratification of a PDAC cohort. FFPE tumor samples were sectioned, and histopathological analysis was performed. Using the H&E, the tumor grade and stroma amount were annotated. An additional IHC staining was performed to quantify the amount of myCAFs present in the TME. Tumors in which the stroma content made up at least 40% of the TME were segregated into two groups depending on the mesenchymal αSMA expression. The median αSMA expression was used as the cut-off for the allocation to the myCAFs-low group and the myCAFs-high group. Finally, a transcriptomic analysis was performed on bulk tumor samples of both groups to decipher the role of myCAFs in PDAC.
[B] Representative images of the -low and -high groups morphology and αSMA content. The scale bar is 100 µm.
[C] Quantification of the mesenchymal αSMA protein expression in the myCAFs-low (n=9) and myCAFs-high (n=10) TME groups. Each dot corresponds to one animal. Statistical significance was tested using an Unpaired t-test with a Welch correction, and the exact p-value is displayed in the graph.
[D] Stroma amount in the myCAFs-low (n=9) and myCAFs-high (n=10) TME tumors. Each dot corresponds to one animal. Statistical significance was tested using an Unpaired t-test with a Welch correction, and the exact p-value is displayed in the graph.
[E] Representation of the top 50 DEGs between the myCAFs-low (n=9) and myCAFs-high (n=10) groups in a heatmap. A differential gene expression analysis was performed between both groups, and the DEGs with a fold-change bigger than 2 were ordered by the adjusted p-value. The top 50 DEGs were plotted.
[F] Multivariate data analysis of the cohort. The PCA was performed using the top 750 most variable genes. The samples were highlighted in grey (myCAFs-low) or orange (myCAFs- high).
[G] Gene set enrichment analysis of Reactome and Hallmark pathways for the -low and myCAFs-high tumors. The dotted line represents the threshold used for statistical significance (q-value of 0.1).

To understand how myCAFs influence the transcriptional programs in PDAC, tumor samples were stratified based on the myCAFs amount and stroma amount (Figure 27-A).

The mesenchymal αSMA expression was analyzed via immunohistochemistry in KC and KPC tumors that contained at least 40% stroma to avoid a bias in tumor cell/ stroma contribution (Figure 27-D). Tumors were divided into myCAFs-high and myCAFs-low groups using the median as a cut-off (Figure 27-C). Tumor pieces corresponding to both groups were sequenced, and differences in the transcriptional programs were analyzed using differential gene expression and pathway analysis.

Myofibroblasts amount in the TME drives differences in transcriptional landscape, presenting 350 genes that were differentially expressed between myCAFs-high and -low tumors (Figure 27-E and -F). In the myCAFs high-tumors, 248 genes were upregulated, and transcriptional programs such as ECM degradation and organization, collagen fibril crosslinking, and inflammatory pathways were enriched (Figure 27-G). The ECM-related transcriptional programs included the upregulation of ECM genes (*Col1a1*, *Col4a1*, *Fn1*) and ECM regulators (*Mmp2*, *Lox*, and *Bmp1*). Additionally, cytokines and genes associated with inflammation, such as *Mrc1*, *Ccl17*, *Cxcl14*, *Cd40*, and *Cd69,* were also upregulated. On the other hand, myCAFs-low tumors presented 102 DEGs, mostly belonging to metabolic processes, such as glutathione and fatty acid metabolism.

In summary, the amount of myCAFs alters the transcriptional landscape of PDAC, showcasing a substantial upregulation of ECM remodeling and inflammatory response programs.

4.1.6.7 myCAFs-high TMEs showcase a collagen IV-high core-matrisome

myCAFs-high tumors presented enrichment in ECM remodeling and collagen crosslinking pathways, suggesting differences in the matrisome composition between myCAFs-high and myCAFs-low tumors (Figure 28-B). Therefore, to infer changes in the core matrisome of myCAFs-high and -low tumors, tumors were analyzed using transcriptomics and immunohistochemistry.

The matrisome is composed of extracellular matrix proteins divided into proteins of the core matrisome and the associated-matrisome (Naba *et al.*, 2016). The core matrisome can be further subcategorized into collagens, ECM glycoproteins, and proteoglycans (Naba *et al.*, 2016).

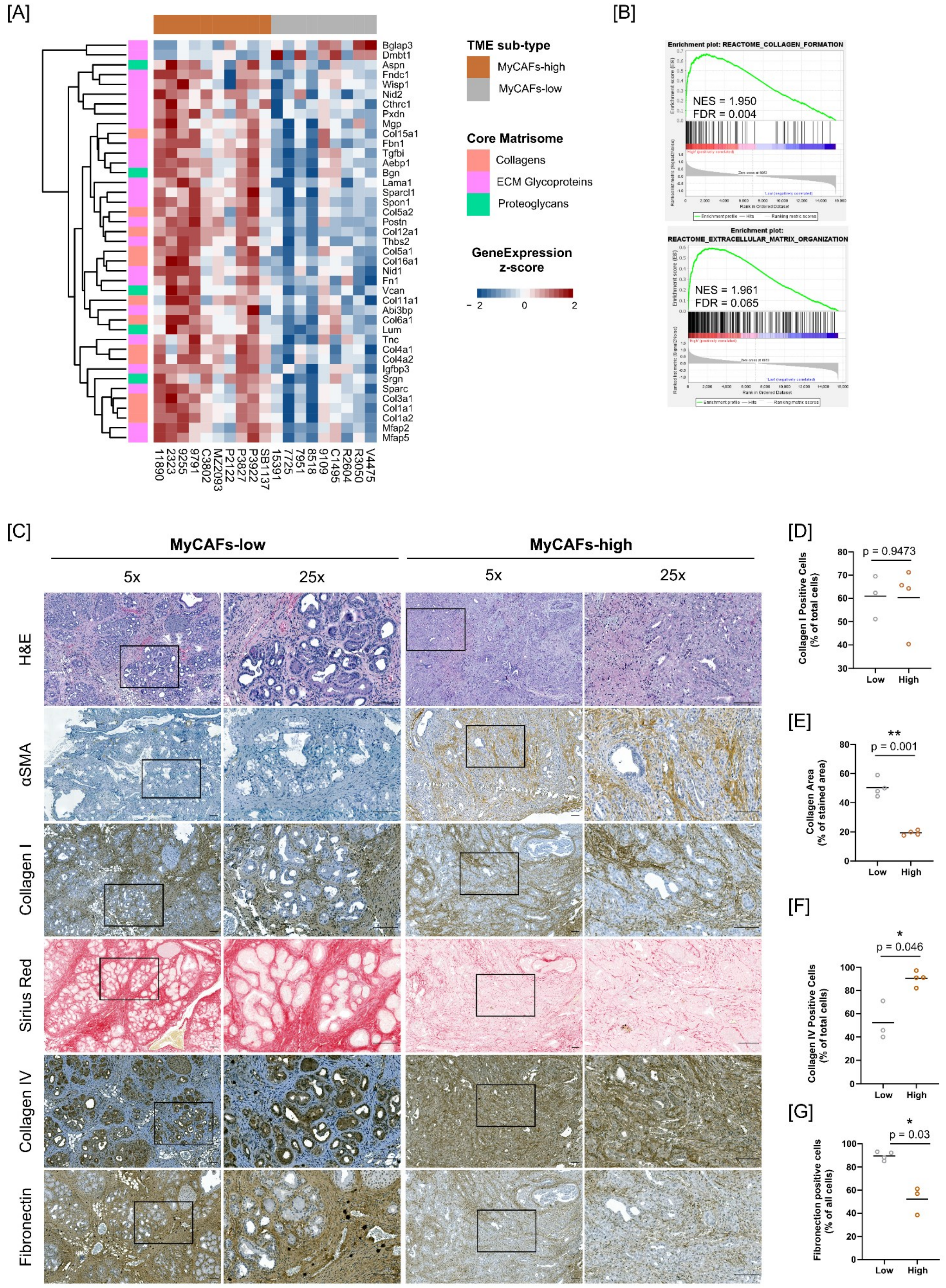

Figure 28 – myCAFs- high tumors core matrisome is high in Collagen IV.

[A] Heatmap representing the differential expressed core matrisome genes between the myCAFs-low (n=9) and myCAFs-high (n=10) groups. A differential gene expression analysis was performed between both groups, and the DEGs with a fold-change bigger than 2-fold and adjusted p-value inferior to 0.05 were selected. Core matrisome DEGs were sub-annotated into collagens, glycoproteins, and proteoglycans encoding genes according to Naba *et al. in silico* determination of the mouse matrisome.
[B] Enrichment plot of ECM anabolic and catabolic-related processes. The normalized enrichment score and the q-value are showcased in the correspondent plot.
[C] Representative images of selected core matrisome proteins altered in the RNAseq analysis for both -low and myCAFs-high groups. The scale bar corresponds to 100 µm.
[D] Collagen I positive cells in myCAFs-low (n=3) and myCAFs-high (n=4) tumors. Each dot corresponds to one animal. Statistical significance was tested using an Unpaired t-test with a Welch correction, and the exact p-value is displayed in the graph.
[E] Collagen area in myCAFs-low (n=3) and myCAFs-high (n=4) tumors. Each dot corresponds to one animal. Statistical significance was tested using an Unpaired t-test with a Welch correction, and the exact p-value is displayed in the graph.
[F] Collagen IV positive cells in myCAFs-low (n=3) and myCAFs-high (n=4) tumors. Each dot corresponds to one animal. Statistical significance was tested using an Unpaired t-test with a Welch correction, and the exact p-value is displayed in the graph.
[G] Fibronectin positive cells in myCAFs-low (n=3) and myCAFs-high (n=3) tumors. Each dot corresponds to one animal. Statistical significance was tested using an Unpaired t-test with a Welch correction, and the exact p-value is displayed in the graph.

To infer differences in the core matrisome, the core matrisome genes that were differentially expressed between myCAFs-high and -low tumors were selected and plotted (Figure 28-A). In total, 41 core matrisome genes were differentially expressed, 39 associated with a myCAFs-high TME and only 2 with myCAFs-low TME. More than half of the core matrisome DEGs in myCAFs-high tumors were glycoproteins, where 22 genes were differentially expressed. The glycoprotein genes upregulated contained *Fbn1*, *Sparc,* and *Postn.* Even though Fibronectin protein expression was in both groups mostly restricted to the TME, its content was significantly higher (p=0.03) in myCAFs-low tumors, with approximately 89.66±3.69% of cells positive compared with 52.15±12.05% in myCAFs-high tumors (Figure 28-C and Figure 28-G). The collagen category presented 12 DEGs, such as *Col4a1*, *Col4a2*, *Col1a1*, *Col1a2,* and *Col3a1*. Even though Col1a1 was upregulated at the mRNA level, the alpha-1 type I collagen content was not altered between groups (myCAFs-low: 60.98±9.24; myCAFs-high: 60.38±13.65, p=0.94) (Figure 28-D). However, collagens I and III were increased in myCAFs-low tumors following Sirius Red staining, representing 50.33±6.24% of the tumor area against 19.30±1.69% in myCAFs-high tumors (Figure 28-C and Figure 28-E). These results, alongside the alpha-1 type I collagen levels, suggest that Collagen III and alpha-2 type I collagen may be upregulated in myCAFs-low tumors. Conversely, Collagen IV was upregulated in myCAFs-high tumors, where 90.31±6.21% of cells positively expressed it, whereas, in myCAFs-low tumors, approximately 52.34±16.51% were positive for collagen IV (p=0.046) (Figure 28-F). Moreover, Collagen IV protein expression was primarily restricted to tumor cells in the myCAFs-low tumors, whereas in myCAFs-high tumors, both tumor cells and the TME compartment appeared to contribute to its deposition (Figure 28-C). Finally, proteoglycans do not seem to be substantially different between the groups, with only 5 genes being upregulated in myCAFs-high tumors.

Altogether, the upregulation of core matrisome genes corroborates the ECM remodeling in myCAFs-high TME. In fact, myCAFs-high tumors presented mainly an increased deposition in collagen IV. However, the upregulation of core matrisome genes did not always translate into increased protein content, with myCAFs-low tumors presenting an increased deposition of fibronectin and collagen I and III, revealing that other layers of ECM regulation may be upregulated.

4.1.6.8 Collagen crosslink regulators are upregulated in myCAFs-high tumors

myCAFs-high tumors exhibited an enhanced core matrisome that translated into increased collagen IV deposition. Alongside the upregulation of core matrisome genes, myCAFs-high tumors presented an upregulation of ECM regulation transcriptional programs (Figure 29-A).

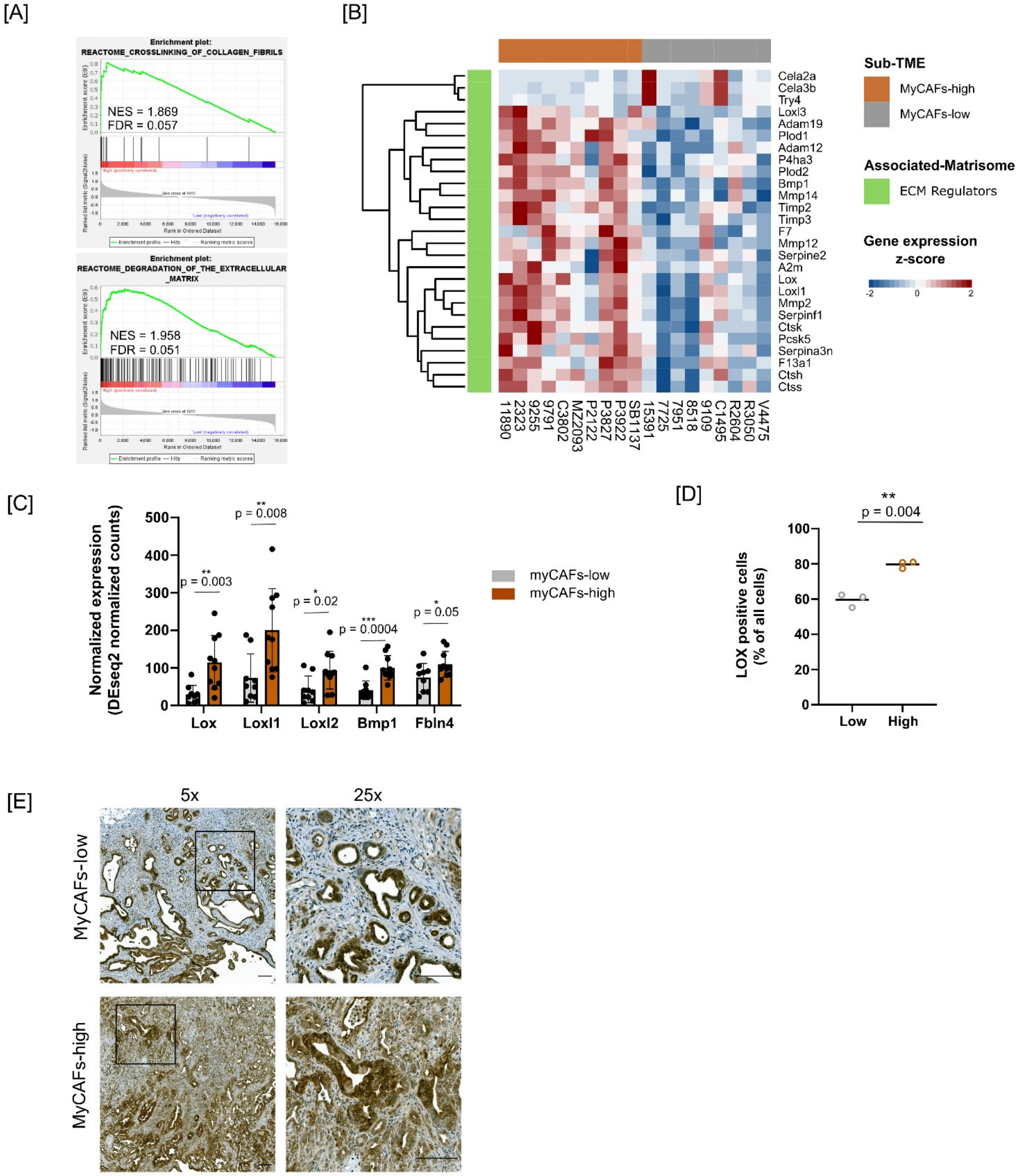

Figure 29 – myCAFs-high tumors present a higher expression of ECM regulators.

[A] Heatmap representing the differential expressed ECM-regulator genes between the myCAFs-low (n=9) and myCAFs-high (n=11) groups. A differential gene expression analysis was performed between both groups, and the DEGs with a fold-change bigger than 2 fold and adjusted p-value inferior to 0.05 were selected. ECM-regulators are a sub-group of the associated-matrisome groups with ECM-affiliated protein and secreted factors, according to Naba *et al. in silico* determination of the mouse matrisome.

[B] Enrichment plot of ECM anabolic and catabolic-related processes. The normalized enrichment score and the q-value are showcased in the correspondent plot.

[C] Normalized expression levels of selected ECM-regulator genes. Data are represented as mean ± SD. The statistical significance was tested using an unpaired t-test with a welch correction in which no multiple comparison correction was performed. The exact p-value is shown on the graph, and the significant changes are marked with asterisks (* $p<0.05$, ** $p<0.01$, and *** $p<0.001$)

[D] Lysyl-oxidase positive cells in myCAFs-low (n=3) and myCAFs-high (n=3) tumors. Each dot corresponds to one animal. Statistical significance was tested using an Unpaired t-test with a Welch correction, and the exact p-value is displayed in the graph.

[E] Representative images of Lysyl-oxidase protein expression in both -low and myCAFs-high groups. The scale bar corresponds to 100 µm.

Therefore, to infer changes in the regulation of the core matrisome in myCAFs-high and -low tumors, tumors were analyzed using transcriptomics and immunohistochemistry.

The associated-matrisome comprises the intracellular and extracellular regulators of matrix proteins (Naba *et al.*, 2016). To analyze the differences in ECM regulation, the involved DEGs between myCAFs-high and -low tumors were selected and plotted (Figure 29-B). In total, 26 ECM regulator genes were differentially expressed, 23 associated with a myCAFs-high TME and only 3 with myCAFs-low TME. Many of these genes were involved in collagen synthesis (*P4ha3*, *Plod1*, *Plod2*) and post-translational collagen modification (*Lox*, *Loxl1*, *Loxl2*). Moreover, genes encoding enzymes regulating the ECM turnover were upregulated, namely metalloproteinases and disintegrins such as *Mmp2*, *Mmp12*, *Mmp14*, *Adam12*, and *Adam19*, but also their inhibitors *Timp2*, *Timp3*, *Serpinf1*, *Serpina3n*, *Serpin2*. Interestingly, the genes encoding the activators of LOX enzymes were upregulated (Figure 29-C). *Bmp1* and *Fbln4* are genes that encode proteins responsible for the proteolytic activation of LOX enzymes, suggesting that collagen production is tightly regulated in myCAFs-high tumors.

ECM accumulation regulated by LOX enzymes was determinant in the activation of CAFs subtypes. Therefore, to understand if the upregulation of collagen crosslinking genes was translated into an increased content of the enzyme, LOX protein expression was analyzed by IHC. Indeed, LOX content was increased in myCAFs-high tumors, where approximately 79.73±2.02% of cells presented positive expression compared with 59.59±3.83% in myCAFs-low tumors (Figure 29-D). Moreover, the secretion of LOX appeared to be more general in myCAFs-high tumors, with more cell types contributing to its secretion, whereas, in myCAFs-low tumors, tumor cells appeared to be the major contributor (Figure 29-E).

In summary, myCAFs-high tumors present an upregulation in ECM regulation transcriptional programs, governing processes from collagen production to collagen crosslinking and turnover. The collagen crosslinking enzyme LOX is increased in myCAFs-high tumors, alongside its regulators BMP1 and FBLN4, facilitating matrix deposition. Nonetheless, further analysis on ECM regulators is needed.

4.1.6.9 myCAFs may communicate with tumor associated-macrophages through secretion of CXCL14

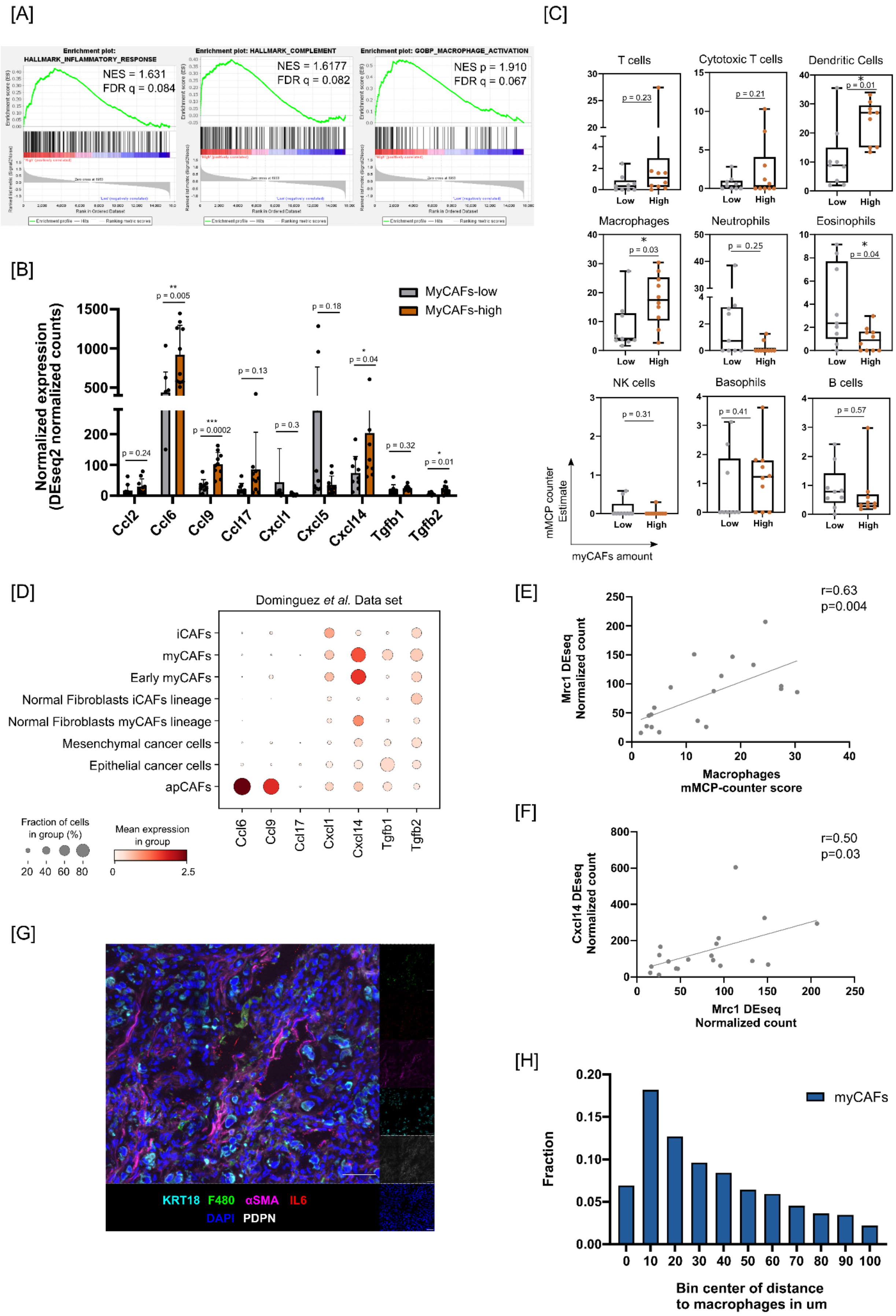

Figure 30 – myCAFs correlate with increased content of tumor-associated macrophages and *Cxcl14*.

[A] Enrichment plot of inflammatory response and complement hallmarks and gene ontology macrophage activation. The normalized enrichment score and the q-value are showcased in the correspondent plot.

[B] Normalized expression levels of selected cytokines involved in the recruitment/activation of different immune cells. Data are represented as mean ± SD. The statistical significance was tested using an unpaired t-test with a welch correction in which no multiple comparison correction was performed. The exact p-value is shown on the graph, and the significant changes are marked with asterisks (* $p<0.05$, ** $p< 0.01$, and *** $p<0.001$)

[C] Immune cell mMCP counter estimate score in myCAFs-high and myCAFs-low tumors. The relative deconvolution was derived from bulk transcriptomic data of myCAFs-low and -high tumors using mMCP counter signatures with the addition of a dendritic cell signature. An unpaired t-test with a welch correction was deployed to assess if the differences between the groups were statistically significant. No multiple comparison correction was performed. P values lower than 0.05 were marked with an asterisk, and the exact value was shown.

[D] Dot plot displaying different expression levels of the selected cytokines among the CAFs subpopulations and tumor cells. The dot size represents the percentage of cells from that population expressing the gene, and the color represents the intensity of expression.

[E] Pearson correlation between macrophages mMCP-counter score and *Mrc1* gene expression. The correlation score (r) and the p-value are depicted in the image.

[F] Pearson correlation *Mrc1* and *Cxcl14* gene expression. The correlation score (r) and the p-value are depicted in the image.

[G] Representative images of myCAFs and macrophages in the TME. The scale bar corresponds to 20 µm.

[H] Frequency distribution of myCAFs distance to macrophages. The frequency of the distribution of all CAFs subpopulations is depicted in the bar plot with a 105 µm diameter. The bin size is 10 µm and starts at 0, meaning that for each center, the frequency is calculated using the intervals [0,5],]5,15,]15, 25],]25, 35],]35, 45],]45, 55],]55, 65],]65, 75],]75, 85],]85, 95],]95, 105].

Acknowledgments: Fabio Boniolo modified the mMCP counter script to allow signatures not contemplated in the original paper. Tatiana Martins curated the additional signatures. In addition, Daniele Lucareli performed the scRNAseq analysis of the CAFs dataset from Dominguez *et al.*

Alongside the upregulation in ECM-related transcriptional programs, the inflammatory response and immune cell activation programs were altered in the TME with different content of myCAFs. Changes in cytokine gene profiles, complement activation, and macrophage activation-related genes were enriched in myCAFs-high tumors (Figure 30-A).

To infer if the inflammatory response was accompanied by different content of immune infiltrate, the immune cell types were quantified using the MCPcounter. MCPcounter is a deconvolution tool that attributes a relative intersample score (Petitprez *et al.*, 2020). The scores attributed are a proxy for the immune cell type content in each tumor sample. Therefore, myCAFs-high and myCAFs-low tumor samples were deconvoluted using the cell type signatures from Petitprez *et al.* and an additional dendritic cell signature, described by Zilionis and colleagues (Figure 30-C). There was no statistical significance between myCAFs-low and -high tumors in adaptive immune cell content, where for most tumors, the score for T cells, $CD8^+$ T cells, and B cells was very low. Only macrophages, dendritic cells, and eosinophils in the innate immune system presented a differential content between groups. myCAFs-high tumors were enriched in macrophages ($p=0.03$) and dendritic cells ($p=0.01$), while myCAFs-low tumors presented a higher content in eosinophils ($p=0.04$). Additionally, the expression of *Mrc1* positively correlated with the macrophage signature and with *Cxcl14*, suggesting a possible communication between myCAFs and macrophages (Figure 30-E and -F). This idea was corroborated by the presence of approximately 40% of myCAFs in a 25 µm radius of macrophages (Figure 30-H).

Several cytokines were differentially expressed between myCAFs-high and myCAFs-low tumors (Figure 30-B). The cytokines *Ccl17*, *Ccl6*, *Ccl9*, and *Cxcl14* were significantly upregulated in myCAFs-high tumors. Nevertheless, *Cxcl14* appeared to be secreted mainly by early myCAFs and myCAFs, whereas Ccl6 and Ccl9 appeared to be secreted by apCAFs (Figure 30-D). Even though contributions besides tumor cells and CAFs could not be assessed with this dataset, other populations could likely contribute to the overall expression.

Altogether, myCAFs-high TME appeared to induce changes in the innate compartment, presenting a higher abundance score for macrophages. The macrophage content was associated with *Mrc1* and *Cxcl14* expression, suggesting a communication between myCAFs and macrophages through cytokines, such as *Cxcl14*.

4.1.6.10 myCAFs content impact macrometastasis in a context-specific manner

Myofibroblast content in tumors induces transcriptional programs related to ECM remodeling and inflammatory response. Therefore, to understand if changes in the transcriptional programs could impact disease progression, macrometastasis frequency was evaluated in myCAFs-high and -low tumors. Since tumors harboring *TRP53* loss-of-function mutations or wild-type allele loss present increased metastasis potential (Kim *et al.*, 2021; Morton *et al.*, 2010; Nakayama *et al.*, 2020), the influence of myCAFs in macrometastasis formation was evaluated in a KC animal cohort.

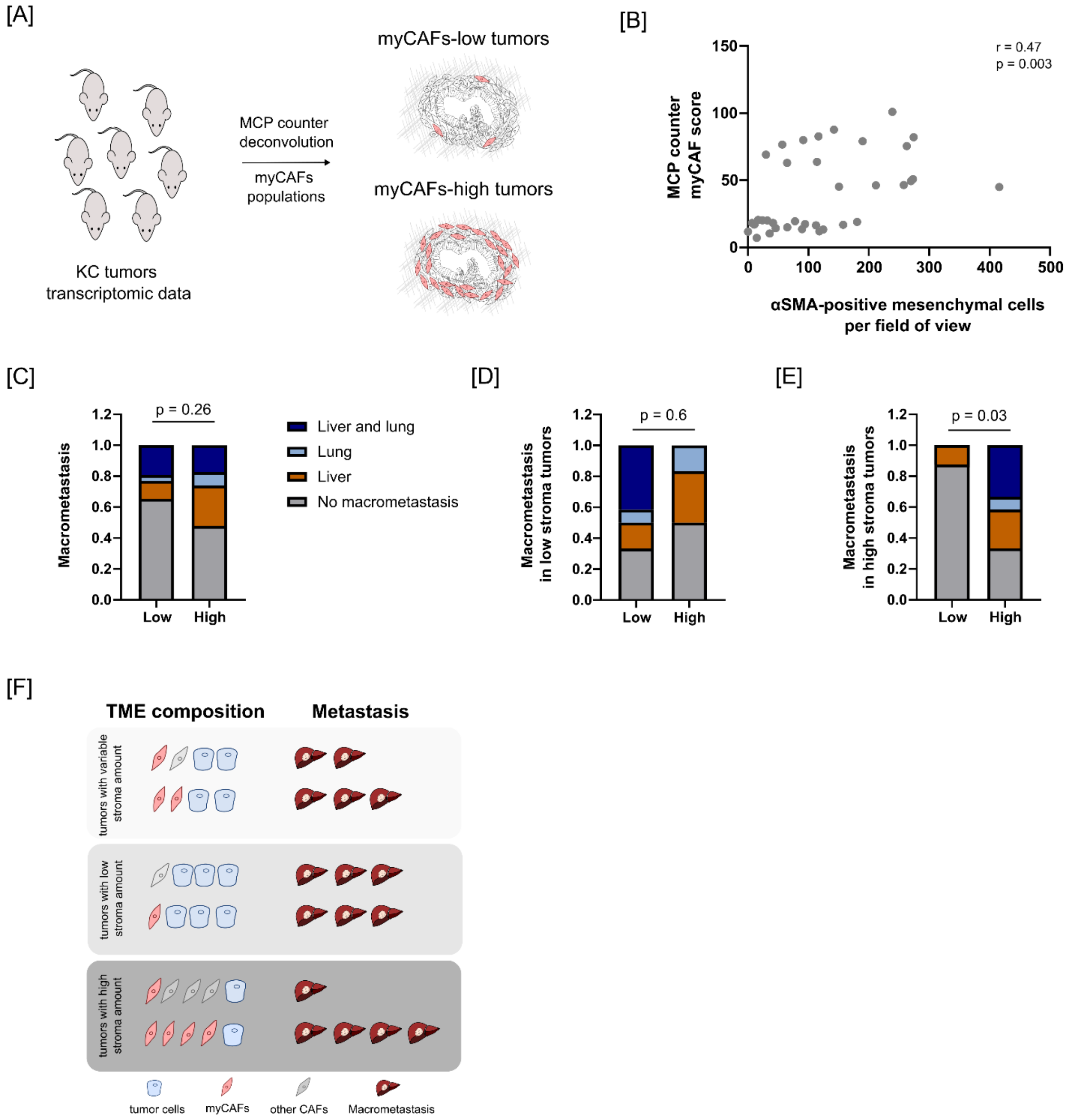

Figure 31 – Analysis of a KC validation cohort reveals increased macrometastasis frequency in myCAFs high-tumors.

[A] Workflow of the myCAFs-based stratification of a PDAC cohort. Transcriptomic data of bulk KC tumors were deconvoluted using a myCAFs signature. The deconvolution generated a score as a proxy of myCAFs content in the tumors. The scores median was used as the cut-off for allocating the tumors to the myCAFs-low and myCAFs-high groups.

[B] Validation of the signature as a measure of myCAFs content in PDAC. In the y-axis is plotted a score indicative of myCAFs content. This score was generated by MCPcounter using a modified signature derived from Dominguez *et al.* containing the genes *Mmp11*, *Col11a1*, *C1qtnf3*, *Cthrc1*, *Col12a1*, *Col10a1*, *Lrrc15*, and *Itga11*. In the x-axis is plotted the mesenchymal αSMA protein expression content. The Spearman correlation was calculated with a r of 0.47 and a p-value of 0.003.

[C] Metastization potential in myCAFs-low (n=26) and myCAFs-high (n=23) tumors. The macrometastasis, annotated when the animal was sacrificed, are represented in the bar plot. Significant changes were evaluated using the two-sided Fisher's exact test, originating a p-value of 0.26.

[D] Metastization potential in myCAFs-low (n=12) and myCAFs-high (n=6) tumors with a low-stroma amount. Tumors in which the stroma content made up less than 40% of the TME were segregated into two groups depending on myCAFs signature score. The macrometastasis, annotated when the animal was sacrificed, are represented in the bar plot. Significant changes were evaluated using the two-sided Fisher's exact test, originating a p-value of 0.6.

[E] Metastization potential in myCAFs-low (n=8) and myCAFs-high (n=12) tumors with a high-stroma amount. Tumors in which the stroma content made up at least 40% of the TME were segregated into two groups depending on myCAFs signature score. The macrometastasis, annotated when the animal was sacrificed, are represented in the bar plot. Significant changes were evaluated using the two-sided Fisher's exact test, originating a p-value of 0.03.

[F] Graphical representation summarizing the results. MyCAFs' impact on macrometastasis is affected by both stromal content and composition. Regardless of presenting a high or a low composition in myCAFs, tumors with low stromal content presented the same macrometastasis frequency. However, tumors with high stromal content and high myCAFs score present an increased frequency of macrometastasis.

Acknowledgments: The animals used in this study were bred and sacrificed by all the members of AG Saur. The histopathological analysis that quantified the stromal content in the tumors was performed by Chen Zhao and Moritz Jesinghaus.

The KC cohort transcriptomic data were deconvoluted using a published myCAFs gene signature to infer the myCAFs content in tumor samples (Figure 31-A). The myCAFs signature used was modified from Dominguez *et al.*, excluding the gene *Thbs2*, which showed promiscuous expression in C1 mesenchymal tumor cells. The signature was validated using paired deconvoluted myCAFs scores (y-axis) and αSMA mesenchymal protein expression (x-axis), resulting in a positive correlation (r=0.47, p=0.003) (Figure 31-B). Therefore, the derived score was used as a proxy of myCAFs content in tumors.

Macrometastasis frequency was evaluated in myCAFs-low and myCAFs-high tumors. The tumors were divided into high and low groups using the score median as the cut-off, resulting in 26 tumors allocated to the myCAFs-low group and 23 tumor samples to the myCAFs-high tumors. The macrometastasis formation in the lungs and liver was annotated at the time of the sacrifice of the animals. Myofibroblasts content in PDAC does not appear to impact macrometastasis formation, with a frequency of macrometastasis of 34.69% in myCAFs-low tumors and 52.2% in myCAFs-high tumors (Figure 31-C). There was also no preferential metastization site.

Nevertheless, these results do not consider the tumor-to-stroma ratio in the samples. Therefore, the tumor samples were stratified regarding their stroma composition. After a histopathological evaluation of the stromal contribution in each sample, tumors with at least 40% stroma amount were allocated to a stroma-high group, with the remaining being allocated to a stroma-low group. Indeed, the amount of stroma played a role in macrometastasis formation. In the stroma-low cohort, independently of myCAFs content in the tumor, there was no difference in macrometastasis formation (Figure 31-D) or preferential metastization site. However, myCAFs were an indicator of macrometastasis in tumors with high stromal content (Figure 31-E). myCAFs-high tumors presented a macrometastasis frequency of 66.6% compared with 12.5% in myCAFs-low tumors (p=0.03).

Altogether, myCAFs were associated with increased macrometastasis in a context-specific manner, suggesting that stroma amount and its composition impact disease progression (Figure 31-F).

4.2 Characterization of *in vitro* and *in vivo* models to study Pancreatic Adenocarcinoma stromal tumor microenvironment

Divergent reports have been published about CAFs' tumor-promoting or restraining functions. Most of these reports were performed in mouse models, endogenous or implanted, not accounting for model suitability to only target CAFs, CAFs representativity, and additional contributions from other populations. Additionally, CAFs are highly plastic cells, skewing their phenotype once cultured in 2D, highlighting the importance of finding good *in vitro* models to study CAFs' function. Considering that, initial insights on *in* vitro models to mimic CAFs phenotypes and an overview of the dual-recombinase system (DRS) as resources to study CAFs are described in this thesis.

4.2.1 *In vitro* modeling of CAFs populations

Cell lines provide a straightforward approach to studying populations' cell-autonomous and non-cell-autonomous mechanisms. However, due to the high plasticity of CAFs populations, 2D and 3D cultures result in skewed phenotypes without adding specific cues (Biffi *et al.*, 2019; Elyada *et al.*, 2019). Therefore, to understand if CAFs phenotypic diversification could be modeled *in vitro*, cell lines derived from normal pancreatic fibroblasts (pan-fibroblasts) were manipulated with the addition of specific cues to measure the transcriptional activation into myCAFs and iCAFs.

To model the myCAF phenotype, pan-fibroblast lines were isolated and expanded from a GEMM harboring full-body inducible *Tgfb1* knock-in (Figure 32-A). These lines were treated for 14 days with 4-hydroxy-tamoxifen (TAM) or with the vehicle (EtOH), originating paired cell lines with and without *Tgfb1* overexpression (Figure 32-B). The overexpression of *Tgfb1* was achieved in most of the fibroblasts, originating spindle-shaped fibroblasts with increased wound-healing properties, confirming the activation of TGFβ1 downstream signaling (Figure 32-C to G).

It was reported that the culture of fibroblasts in 2D skews the phenotype toward a contractile myCAF phenotype (Elyada *et al.*, 2019). To characterize the dynamic activation of pan-fibroblasts, the EtOH and TAM cell lines were embedded in matrigel and treated with IL1α (Figure 32-H). On day 5, the whole content of the well was collected and analyzed by qPCR (Figure 32-I). As expected, the cell line overexpressing *Tgfb1* presented an increase of approximately 2-fold in *Acta2* mRNA (p=0.02). However, no differences in *Acta2* levels were observed when both EtOH and TAM pan-fibroblast lines when treated with IL1α. Similarly, *Ctgf* and *Col1a1* were increased in the TAM-treated fibroblast line *versus* EtOH control, suggesting that TGFβ1 signaling is active in this group (p=0.04, p=0.02, respectively). Additionally, TAM pan-fibroblast lines treated with IL1α did express *Il6* ($p<0.0001$), indicating that NfκB signaling might be active. Even though TAM pan-fibroblasts treated with IL1α did not present an increase in *Acta*2, *Ctgf,* and *Col1a1* mRNA, they did present an increase in *Tgfb1* compared with the EtOH non-treated line (p=0.02). This data may indicate that Tgfb1 signaling is differently regulated when IL1α is present. No alterations were observed in *Pdgfra* mRNA levels, independently of the treatment.

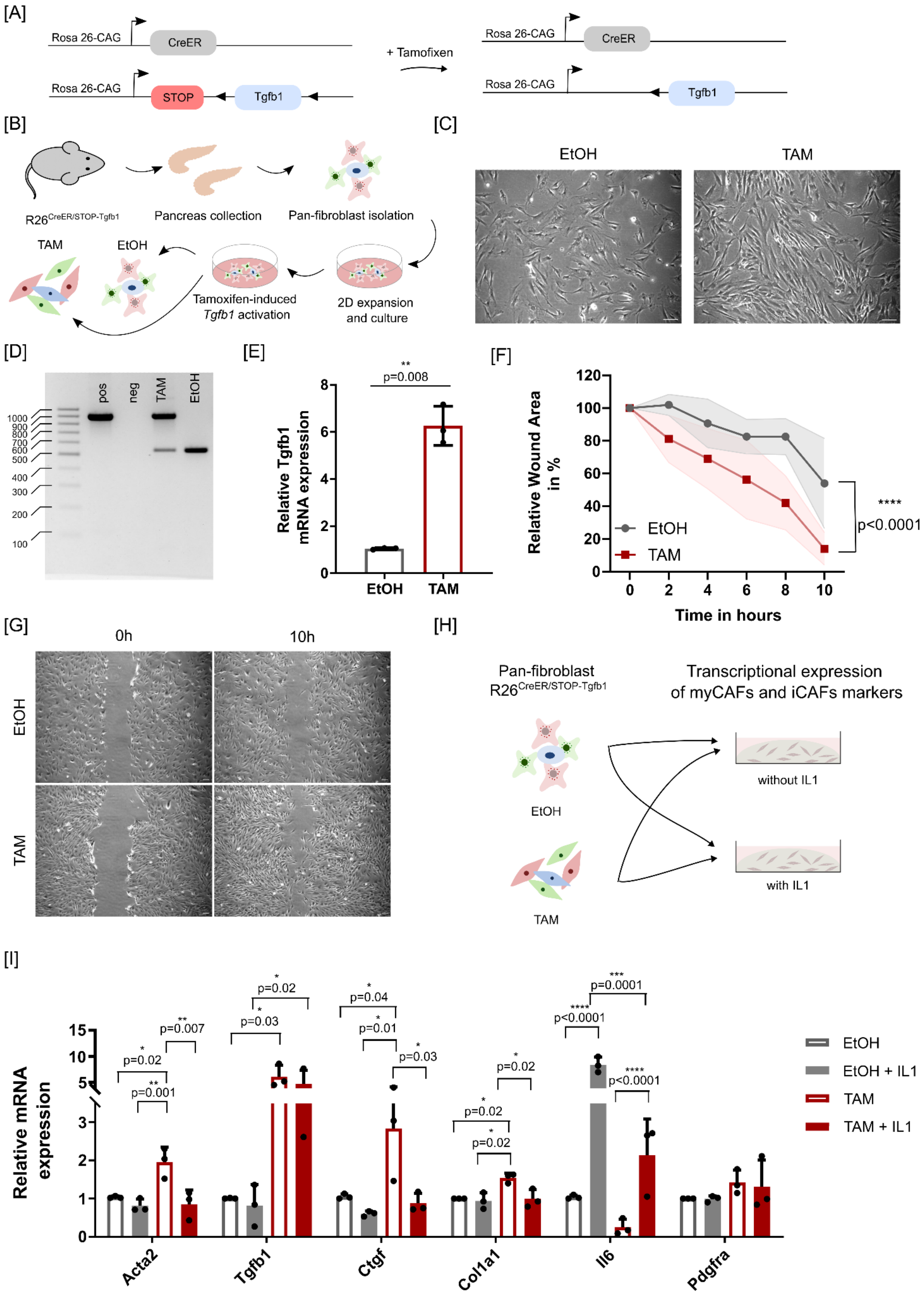

Figure 32 – CAFs phenotypes can be modeled *in vitro*.

[A] PDAC GEMM with a whole-body inducible *Tgfb1* overexpression. Inducible Cre recombinase was expressed under the control of the CAG promotor in the *Rosa 26* locus. Likewise, *Tgfb1* expression was controlled by a CAG promotor in the *Rosa 26* locus, with a floxed STOP cassette preceding the *Tgfb1* construct. After tamoxifen treatment, Cre activation leads to the excision of the STOP cassette and the expression of the Tgfb1 construct.
[B] Experimental workflow used to study CAFs *in vitro* models. Mice containing the LSL-TGFb1 and R26-CAG-CreER alleles were intercrossed, and whole pancreas were collected and subjected to enzymatic and mechanical digestion. The fibroblasts were separated from immune, acinar, and ductal cells by differential centrifugation due to decrease density conferred by the presence of pancreatic fibroblasts lipid vesicles. The cells were expanded and cultured in 2D. After cell line establishment, the pan-fibroblasts were treated with ethanol (EtOH) or 4-hydroxy-tamoxifen (TAM) for 14 days to activate Cre and excised the stop cassette preventing the overexpression of *Tgfb1*.
[C] Morphology of the pancreatic pan-fibroblast line after *Tgfb1* induction. Scale bar is 100 µm.
[D] Validation of the recombination of a representative cell line after tamoxifen induction. The pan-fibroblast lines treated after 14 days with EtOH or TAM were collected, and the presence of the recombined Tgfb1 allele (500 bp) and the presence of the stop cassette (500 bp) were analyzed. Pos stands for positive control, and neg stands for negative control.
[E] Relative expression of *Tgfb1* mRNA in EtOH (n=3) and TAM (n=3) treated lines. The relative expression of *Tgfb1* mRNA was determined by the $2^{-\Delta\Delta Ct}$ method. In addition, statistical differences between the groups were evaluated using an unpaired t-test with a welch correction. The data corresponds to 3 technical replicates and is depicted in mean±SD.
[F] Relative wound area in % a long time, evaluation migration potential between EtOH and TAM treated lines. A two-way ANOVA was used to evaluate statistical differences between treatments. Statistical differences were detected between the groups relative to the area of the wound closed. The data corresponds to 6 technical replicates and is depicted as the mean and the 95% confidence interval.
[G] Representation of the wound area at the initial (0h) and final (10h) time points. Scale bar represents 100 µm.
[H] Experimental workflow to model CAFs population *in vitro*. EtOH and TAM treated-fibroblast lines were cultured in matrigel for 5 days and treated with IL1 at day 1. The entire content of the well was collected, and RNA was isolated and converted to cDNA for transcriptional analysis of myCAFs (*Tgfb1*, *Ctgf*, *Col1a1, Acta2*) and iCAFs (*Il6*, *Pdgfra*) markers by qPCR.
[I] Relative expression of *Acta2*, *Tgfb1*, *Ctgf*, *Col1a1*, *Il6*, and *Pdgfra* mRNA in EtOH and TAM treated lines. The relative expression was determined by the $2^{-\Delta\Delta Ct}$ method. In addition, statistical differences between the groups were evaluated using a one-way ANOVA with Tukey *post hoc* correction for multiple comparisons. The adjusted p values of the significant comparisons are depicted in the figure. The data corresponds to 3 technical replicates and is depicted in mean±SD.

In conclusion, pan-fibroblast lines can be manipulated to model CAFs phenotypes *in vitro*. However, further manipulations must be performed to lock the phenotype and avoid the characteristic phenotypic diversification upon the presence of TGFβ1 and IL1α.

4.2.2 Dual Recombinase System to study CAFs in endogenous PDAC

The dual-recombinase system (DRS) is an elegant way to target multiple genes in different TME compartments (Schonhuber *et al.*, 2014). The primary genetic modifications generally result in tumor formation, where the Flp-mediated activation of the silenced oncogenic *Kras*^{G12D} occurs through the excision of the preceding frt flanked stop cassette and the deletion of *Trp53* with the excision of most of its exons (Lee *et al.*, 2012; Schonhuber *et al.*, 2014). The secondary genetic modifications are introduced via Cre recombinase and present a high degree of versatility (Schonhuber *et al.*, 2014). In this work, Cre-mediated genetic modifications label the stroma compartment, using stromal promotors to activate Cre and mediate the excision of the loxP-flanked td-tomato allele, signaling recombination through EGFP expression (Muzumdar *et al.*, 2007; Schonhuber *et al.*, 2014). The Cre recombinase in this work was expressed using *Col6a1*, *Fsp1*, *Pdgfra*, *Gfap*, *Tagln*, *Myh11*, *Cspg4*, and *Nes* as promotors. Therefore, from herein, these Cre lines will be addressed as stromal-Cre driver lines. The stromal Cre-driver can monitor cell lineages from embryogenesis – non-inducible stromal Cre-driver lines, or cell populations from specific-time frames – inducible stromal-Cre driver lines. Tumors harboring the inducible stromal Cre-driver lines, such as *Pdgfra*-CreER, *Myh11*-CreER, *Cspg4*-CreER, and *Nestin*-CreER were treated at 2-3 months with chow containing tamoxifen to label stromal populations. When the animals reached the end-point, the tumors were collected, fixed, and cryopreserved for further analysis. To determine the cell types targeted by each stromal-Cre driver line, tumor samples were sectioned and stained with antibodies targeting tumor, immune, and CAFs epitopes. The cell types targeted by the stromal-Cre driver lines were identified by the colocalization of the protein marker and the recombined cells (double-positive cells). The experimental design used to characterize the stromal-Cre driver lines is depicted in Figure 33.

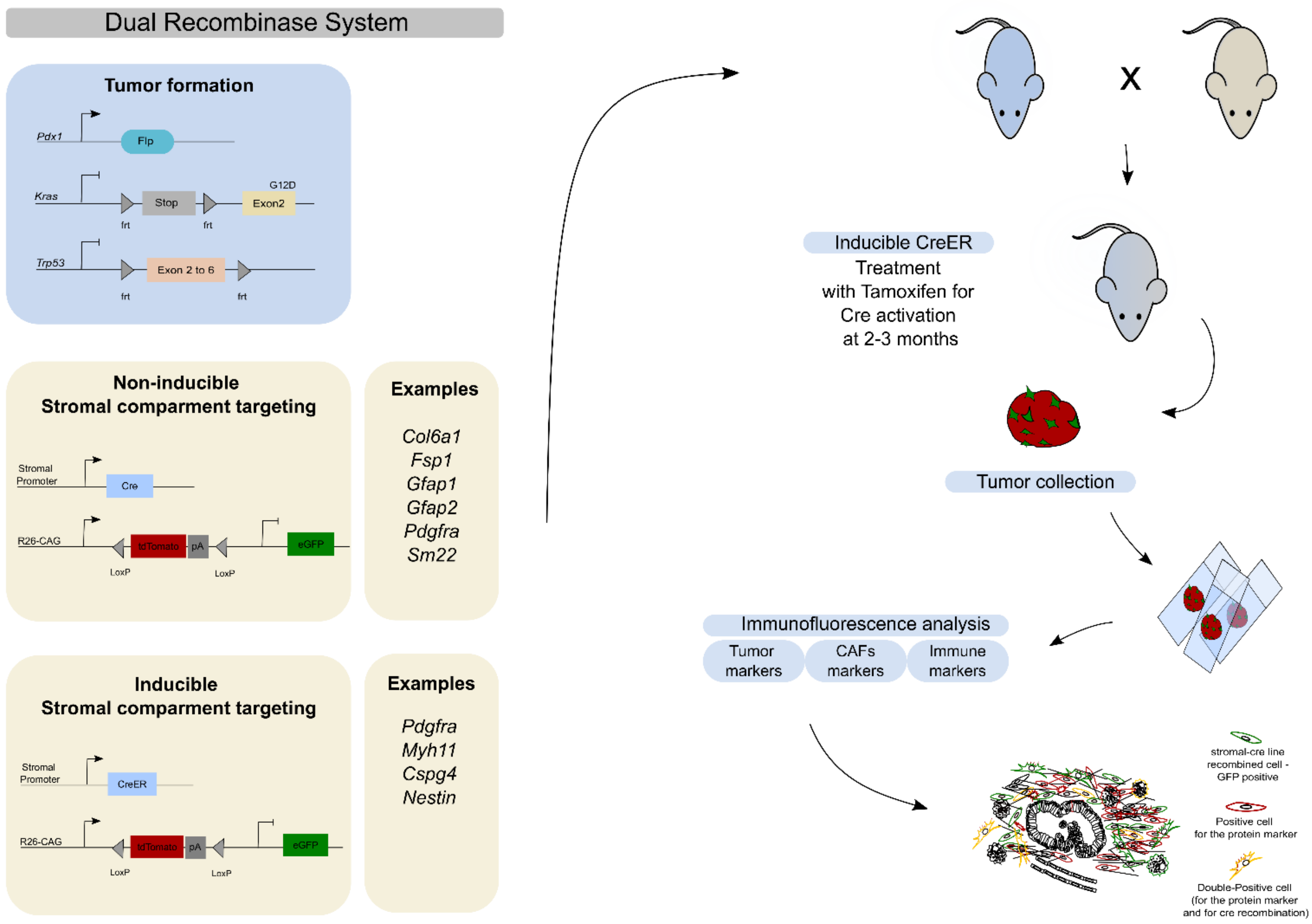

Figure 33 – Experimental design of Stromal-cre driver lines characterization.

Schematic representation of the DRS as a resource to study CAFs. PDAC tumors were induced by *Pdx1*-mediated activation of Flp, and consequent activation of an oncogenic *Kras*^{G12D} allele through excision of frt flanked stop cassette. To target the stromal compartment, non-inducible and inducible Cre recombinase were introduced in the breeding scheme with the additional R26-mTmG reporter to monitor cell recombination. Each tumor could additionally harbor a *Trp53* Flp-mediated deletion of exons 2 to 6, which were flanked by frt sites. The Cre recombinase was transcribed following the activation of stromal promoters and mediated the excision of the loxP-flanked tomato cassette. Therefore, cells in which the stromal promoter was activated, even momentarily, would lose td-Tomato expression and gain EGFP expression. The non-inducible stromal Cre driver lines comprised the *Col6a1*-cre, *Fsp1*-cre, *Gfap1*-cre, *Gfap2*-cre, *Pdgfra*-cre, and *Sm22*-Cre lines and targeted cells from embryogenesis. The inducible stromal Cre driver lines comprised the *Pdgfra*-CreER, *Myh11*-CreER, *Cspg4*-creER, and *Nestin*-CreER lines, targeting cells from the moment the animals were treated with tamoxifen (2-3 months old). Tumors were collected when the animal reached the end of the experiment, fixed, embedded in OCT, and cryopreserved. Finally, the tumors were sectioned and stained with tumor, immune, and CAFs markers and analyzed via confocal microscopy. Non-recombined (red) and recombined cells, positive (yellow) or negative (green) for the markers tested, were quantified.

Previously, this thesis described the role of differentiation and *Trp53* status in CAFs activation. Therefore, it is likely that the populations targeted by the stromal-Cre driver lines would differ according to the differentiation and *Trp53* status of the tumors. The frequency of *Trp53* alterations introduced from embryogenesis in the tumors analyzed, as well as the frequency of differentiated, poorly-differentiated, and undifferentiated tumors are represented in Figure 34.

The majority of the tumors, independently of the stromal promotor in which Cre is activated, presented at least one *Trp53* allele lost (Figure 34-A). The stromal-Cre driver lines *Cspg4*-CreER, *Col6a1*-Cre, *Nest*-CreER, *Gfap1*-Cre, and *Gfap*-CreER presented a heterozygous *Trp53* deletion in all tumor samples. Nevertheless, LOH likely occurred during tumor progression, resulting in the complete loss of *Trp53* (Hingorani *et al.*, 2005). Moreover, all *Fsp1*-Cre tumors analyzed presented complete deletion of the *Trp53* wild-type allele. The representation of the CAFs populations targeted by the stromal-Cre driver lines in *Trp53*-proficient TME was low, with only 4 tumors distributed along the *Sm22*-Cre, *Myh11*-CreER, *Gfap2*-Cre, and *Pdgfra*-CreER not being subjected to the introduction of *Trp53* deletion.

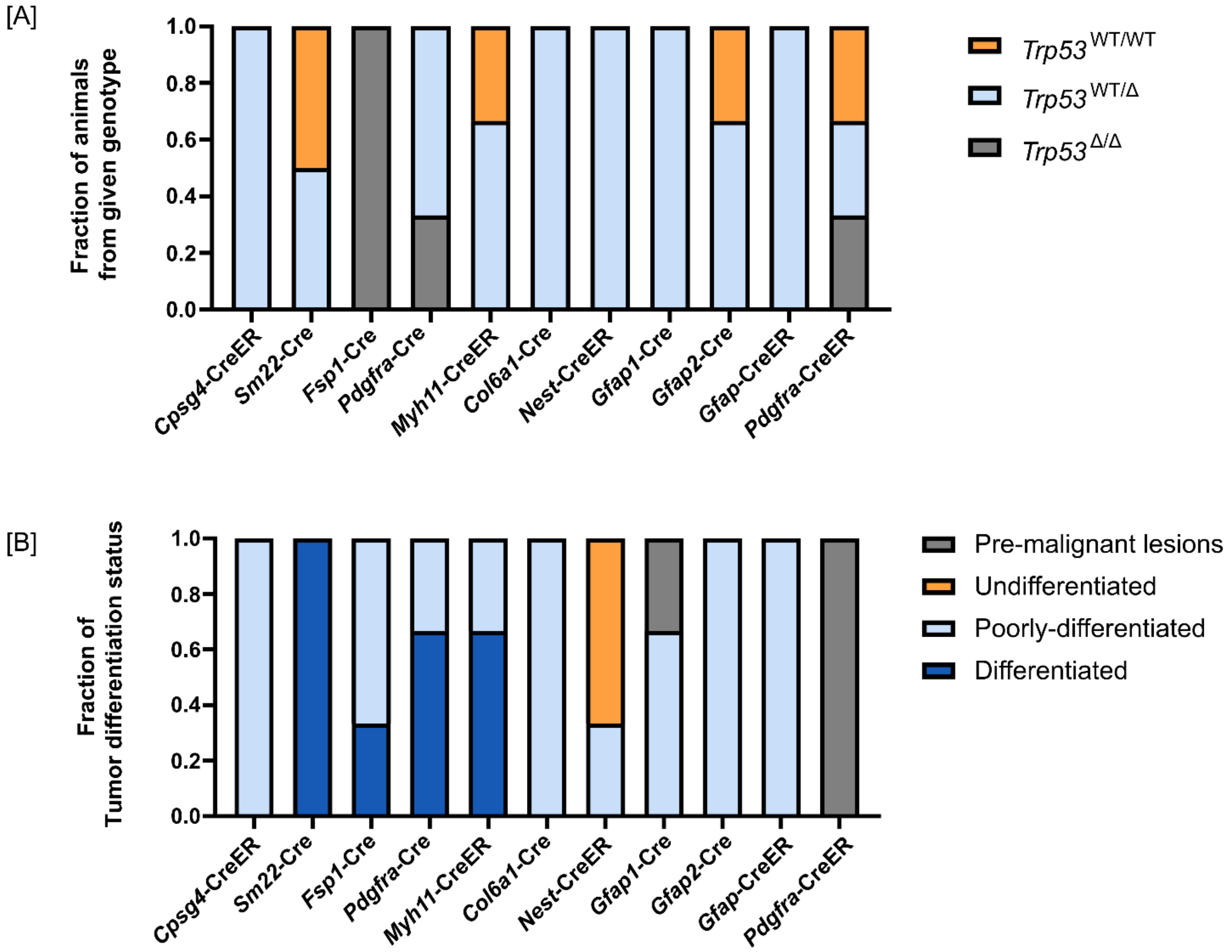

Figure 34 – Cohort description of the samples used to characterize the stromal-Cre driver lines.

[A] *Trp53* alterations introduced from embryogenesis in the tumors within each stromal-Cre driver line. Besides the expression of oncogenic *Kras*$^{\mathrm{G12D}}$, a *Trp53* deletion might have been introduced via the excision of most exons 2-6. The frequency of homozygous wild-type (*Trp53*$^{\mathrm{WT/WT}}$, in orange), heterozygous deletion (*Trp53*$^{\mathrm{WT/\Delta}}$, in blue), or homozygous deletion (*Trp53*$^{\Delta/\Delta}$, in grey) is depicted for each stromal-Cre driver line. For each stromal-Cre driver line, the following tumor samples were analyzed: *Cspg4*-CreER n=2; *Sm22*-Cre n=2, *Fsp1*-Cre n=3, *Pdgfra*-Cre n=3, *Myh11*-CreER n=3, *Col6a1*-Cre n=1, *Nest*-Cre n=3, *Gfap1*-Cre n=3, *Gfap2*-Cre n=1, *Gfap*-CreER n=2, *Pdgfra*-CreER n=3.

[B] Differentiation status of the tumors within each stroma-Cre driver line. The histopathological analysis was performed using H&E stainings, and the tumors were annotated accordingly to the differentiation status of the glandular compartment; pre-malignant (in grey), differentiated (dark blue), poorly-differentiated (light blue), and undifferentiated (orange). For each stromal-

Cre driver line, the following tumor samples were analyzed: *Cspg4*-CreER n=2; *Sm22*-Cre n=2, *Fsp1*-Cre n=3, *Pdgfra*-Cre n=3, *Myh11*-CreER n=3, *Col6a1*-Cre n=1, *Nest*-Cre n=3, *Gfap1*-Cre n=3, *Gfap2*-Cre n=1, *Gfap*-CreER n=2, *Pdgfra*-CreERT2 n=3.

Acknowledgments: The animals used in this study were bred and sacrificed by all the members of AG Saur. Tatiana Martins and Elizaveta Gorbunova performed the histopathological analysis of the tumors.

Poorly-differentiated tumors were the most represented differentiation state across all samples, namely in *Cspg4*-CreER, *Col6a1*-Cre, *Gfap2*-Cre, and *Gfap*-CreER (Figure 34-B). The *Nest*-CreER line samples showcase one tumor with undifferentiated morphology besides the ones displaying poorly-differentiated features. Conversely, the *Sm22*-Cre cohort comprised only differentiated tumors, which, although present, were less represented in *Fsp1*-Cre, *Pdgfra*-Cre, and *Myh11*-CreER tumor samples. The presence of pre-malignant tissue was only detected in the *Pdgfra*-CreER sample cohort. The analysis of the groups *Cspg4*-CreER, *Sm22*-Cre, and *Gfap*-CreER was only performed in two tumor samples and *Col6a1*-Cre and *Gfap2*-Cre in one tumor sample because there were no additional samples available.

In summary, diverse stromal-Cre driver lines were characterized in this thesis, comprising non-inducible lines that trace cell lineage from embryogenesis and inducible models which can be activated in a time-specific fashion. In addition, most of the tumor samples analyzed showcase alterations in wild-type *Trp53* from embryogenesis and poorly-differentiated morphology, variables that could impact the diversity of CAFs populations labeled.

4.2.2.1 Stromal-Cre driver lines exhibit a heterogeneous pattern of recombination in PDAC tumor samples

The ability of the stromal-Cre driver lines to target cells in PDAC tumors depends not only on the moment Cre is activated but also on how many cells are expressing Cre. When the promotor is active, Cre is transcribed and translated into CRE protein, migrating from the cytoplasm to the nucleus. CRE recognizes the loxP sites, anchoring to the DNA sequence, resulting in the excision of the tdTomato cassette and the transcription of GFP. The tumors in which Cre is active will consequently lose tdTomato and gain GFP expression, whereas tumors without promotor and Cre activation will retain the tdTomato expression (Figure 35-A). Therefore, to characterize the recombination efficiency, each stroma-Cre driver line was stained with an antibody against the protein encoded by the promoter (protein marker). The double-positive cells, exhibiting colocalization between GFP recombined cells and cells positive for the protein marker, were stained in a paired manner. For example, stromal-Cre driver lines harboring a *Gfap* promotor were stained with an antibody against GFAP protein, the *Cspg4* promotor was stained with an antibody against CSPG4 protein, and so on (Figure 35-B).

The stromal-Cre driver lines presented a divergent recombination profile (Figure 35-C). Depending on the promotor under which Cre is activated, the recombined cells can range from 0.00±0.00% in *Pdgfra*-CreER to 71.21±3.08% in *Cspg4*-CreER. Similarly to the *Pdgfra*-CreER, *Gfap*-CreER did not show any recombination. The *Gfap1*-Cre, *Gfap2*-Cre, and *Nest*-CreER showed shallow recombination levels, with 0.93±1.43%, 1.93%, and 1.90±0.88% of GFP^+ cells, respectively.

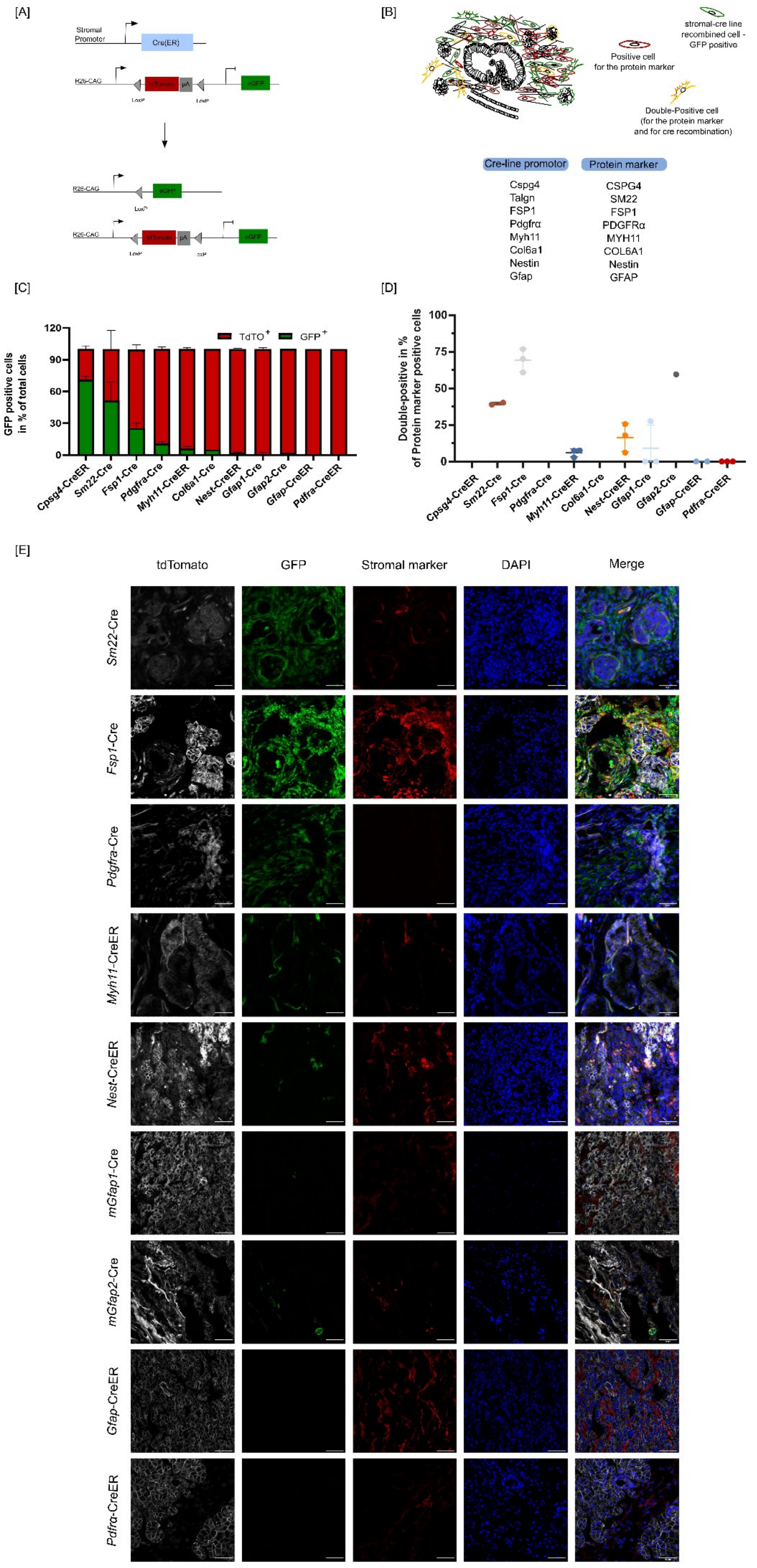

Figure 35 – Stromal-cre driver lines recombine heterogeneously.

[A] Schematic representation of stromal cell labeling using the Cre system. When the promotor is active, Cre is transcribed and translated into Cre protein, migrating from the cytoplasm to the nucleus. Cre recognizes the loxP sites, anchoring to the DNA sequence, resulting in the excision of the tdTomato cassette and the transcription of GFP. The tumors in which Cre is active will consequently lose tdTomato and gain GFP expression, whereas tumors without promotor and Cre activation will retain the tdTomato expression. In the stromal-cre driver lines with CreER expression instead of Cre, the activation is mediated by tamoxifen-induced stimulation of the modified estrogen receptor and the migration of Cre to the nucleus, which would not be otherwise possible.

[B] Schematic representation of the recombination profile analysis of stromal-Cre driver lines. Tumor samples belonging to *Cspg4*-CreER, *Sm22*-Cre, *Fsp1*-Cre, *Pdgfra*-Cre, *Myh11*-CreER, *Col6a1*-Cre, *Nest*-Cre, *Gfap1*-Cre, *Gfap2*-Cre, *Gfap*-CreER, *Pdgfra*-CreER were stained with a protein marker corresponding to the promotor in the stromal-cre driver lines and analyzed by confocal microscopy. Then, recombined cells positive and negative for the protein markers were quantified. For each stromal-Cre driver line, the following tumor samples were analyzed: *Cspg4*-CreER n=2; *Sm22*-Cre n=2, *Fsp1*-Cre n=3, *Pdgfra*-Cre n=3, *Myh11*-CreER n=3, *Col6a1*-Cre n=1, *Nest*-Cre n=3, *Gfap1*-Cre n=3, *Gfap2*-Cre n=1, *Gfap*-CreER n=2, *Pdgfra*-CreER n=3.

[C] Recombination profile of the stromal-Cre lines *Cspg4*-CreER, *Sm22*-Cre, *Fsp1*-Cre, *Pdgfra*-Cre, *Myh11*-CreER, *Col6a1*-Cre, *Nest*-Cre, *Gfap1*-Cre, *Gfap2*-Cre, *Gfap*-CreER, and *Pdgfra*-CreER. The bar plot depicts the fraction of recombined cells (GFP+) and non-recombined cells (td-Tomato$^+$) among all cells (DAPI$^+$). Data is represented as mean±SD.

[D] Recombination efficacy of the stromal-Cre lines *Cspg4*-CreER, *Sm22*-Cre, *Fsp1*-Cre, *Pdgfra*-Cre, *Myh11*-CreER, *Col6a1*-Cre, *Nest*-Cre, *Gfap1*-Cre, *Gfap2*-Cre, *Gfap*-CreER, and *Pdgfra*-CreER. The bar plot depicts the faction of recombined cells positive for the protein marker – double-positive cells – among all protein marker-positive cells. Data is represented as mean±SD. The recombination efficiency values for the lines *Cspg4*-CreER and *Col6a1*-Cre are not present because the tumor samples analyzed showed no fluorescence signal. Moreover, in the *Pdgfra*-Cre, PDGFRα expression was not detected, and due to the mathematical impossibility of null division, no recombination efficiency was assessed in these lines.

[E] Representative images of the channels td-tomato, GFP, Protein marker, and DAPI indicate non-recombined cells, recombined cells, Protein marker positive cells, and the total number of cells in the stromal lines *Cspg4*-CreER, *Sm22*-Cre, *Fsp1*-Cre, *Pdgfra*-Cre, *Myh11*-CreER, *Col6a1*-Cre, *Nest*-Cre, *Gfap1*-Cre, *Gfap2*-Cre, *Gfap*-CreER, and *Pdgfra*-CreER. The scale bar is 50 µm.

Acknowledgments: The animals used in this study were bred and sacrificed by all the members of AG Saur. Tatiana Martins and Elizaveta Gorbunova performed the immunofluorescence confocal acquisition of the tumor samples.

On the other hand, the stromal lines *Sm22*-Cre, *Fsp1*-Cre, *Pdgfra*-Cre, *Myh11*-CreER, and *Col6a1*-Cre presented higher recombination levels. *Col6a1*-Cre and *Myh11*-CreER were located in the lower half of all lines, with mean recombination levels of 6.21±1.64% and 5.13% of GFP$^+$ cells. The remaining, *Sm22*-Cre, *Fsp1*-Cre, *Pdgfra*-Cre presented recombination levels higher than 10%, with a mean 51.33±17.78%, 25.44±4.84% and 10.77±2.01%, respectively.

The recombination efficiency indicates if Cre was active in a given cell (Figure 35-D). Therefore, the double-positive cells were quantified and benchmarked against the total amount of the protein marker. The highest recombination efficiency belonged to the *Fsp1*-Cre, with 69.22±8.01% of FSP1$^+$ cells recombined. The Sm22-Cre line also presented high recombination efficiency with approximately 39.60±0.86%. On the other hand, *Gfap2*-Cre recombined approximately 60% of GFAP$^+$ cells, but the recombination level of this line was very low, with only 16 cells GFP$^+$ positive. However, the *Gfap1*-Cre line presented a much lower recombination efficiency, with approximately 9.17±15.88% of GFAP$^+$ cells recombined.

The inducible lines presented low levels of recombination efficiency, with most of them presenting efficiency below 20%. From these lines, *Nest*-CreER presented a recombination efficiency of 16.56±9.83%, and *Myh11*-CreER exhibited only 5.94±2.72% of MYH11$^+$ cells recombined. No signal following the staining of GFAP and PDGFRα was detected with *Gfap*-CreER and *Pdgfra*-CreER presenting recombination efficiency of 0.0±0.0%.

The lines *Cspg4*-CreER and *Col6a1*-Cre did not show any fluorescence signal for the protein marker. However, this may be related to the lack of reactivity of the antibody clone tested. Moreover, in the

Pdgfra-Cre, PDGFRα expression was not detected, most likely due to the *Trp53* status of the tumor analyzed. Therefore, due to the mathematical impossibility of null division, there was no assessment of the recombination efficiency in these lines.

Altogether, The stromal-Cre driver lines present divergent recombination levels and different recombination efficiency. In addition, the inducible recombination lines exhibited lower efficiency than the non-inducible models, which is likely related to the ability to activate Cre. Therefore, the recombination levels vary with the method of Cre induction and the moment of treatment, and each line needs an independent recombination profile analysis and optimization of Cre activation.

4.2.2.2 Stromal-Cre driver lines present a promiscuous recombination profile

To determine if the stromal-Cre driver lines could target other cell types than CAFs, each tumor sample was stained with antibodies against KRT18, CD45, and PDPN, identifying tumor cells, immune cells, and CAFs, respectively. The recombined cells positive for these markers (double-positive cells) revealed the pervasive profile of each line (Figure 36-A).

The stromal-Cre driver lines presented different levels of pervasiveness (Figure 36-B). *Pdgfra*-Cre recombined cells comprised approximately 54.69±28.27% of PDPN^{+} cells. In this model, tumor and immune cells were labeled to a lower extent, presenting approximately 5.73±7.14% and 5.96±5.41% of the recombined cells, respectively. Nonetheless, it also targeted cell types other than tumor cells and immune cells substantially (33.63±20.33%).

The stromal lines *Fsp1*-Cre and *Myh11*-CreER targeted CAFs similarly, comprising approximately 19.55±8.17% and 18.82±17.33% of recombined cells positive for PDPN. However, the number of recombined cells targeting tumor and immune cells differed. The *Fsp1*-Cre model targeted mainly immune cells, with approximately half of the recombined cells (53.14±8.54%) positive for the immune cell marker CD45. Conversely, 9.99±6.35% of the recombined *Myh11* line cells targeted immune cells. The content of double-positive cells for tumor markers was low, representing only 3.25±1.16% of the recombined cells in *Fsp1*-Cre and 6.97±10.52% in *Myh11*-CreER.

The stromal-Cre driver lines analyzed that targeted the most tumor cells were *Cspg4*-CreER and *Sm22*-Cre, with approximately 51.69±20.75% and 21.01±29.03% double-positive cells, respectively. However, the content of recombined cells positive for PDPN and CD45 was low. The content of PDPN double-positive cells was 12.27±15.49% in the *Cspg4*-CreER line and 7.64±8.35% in *Sm22*-Cre. Similarly, the content of CD45^{+} cells recombined in the *Cspg4*-CreER and *Sm22*-Cre lines was 25.68±7.18% and 10.10±13.47%.

It was difficult to depict an accurate recombination profile in the *Col6a1*-Cre line since only one tumor sample was available to perform the marker analysis. Nevertheless, in this sample, *Col6a1*-Cre targeted CAFs (12.61%), tumor cells (4.31%), and immune cells (4.42%). However, most recombined cells (78.66%) were not positive for PDPN, KRT18, and CD45.

The *Nest*-CreER line did not primarily target CAFs, tumor cells, and immune cells. There was no co-localization between EGFP and KRT18, and PDPN markers. Additionally, the number of recombined cells positive for CD45 was also shallow (5.56±9.62%).

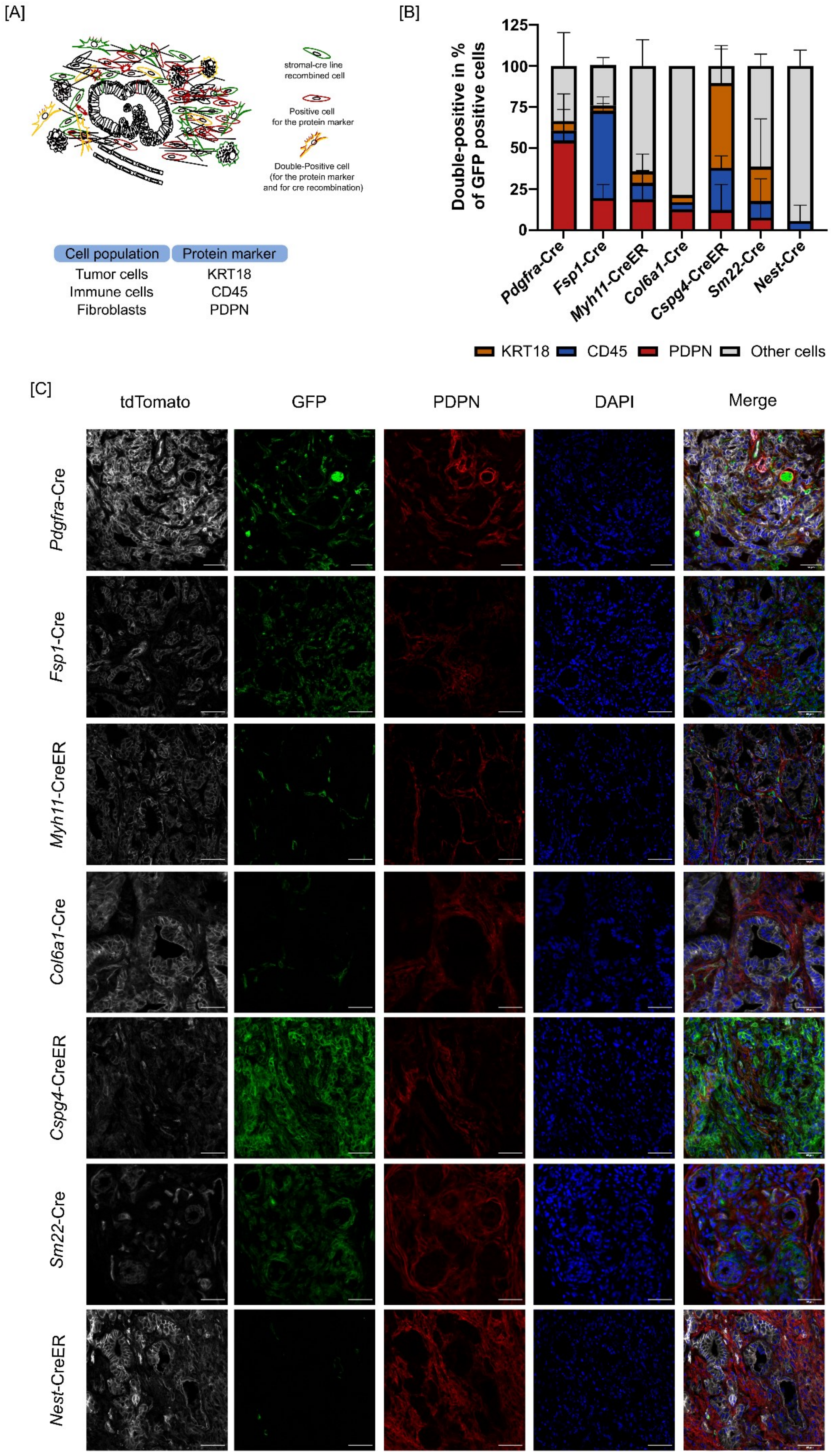

Figure 36 – Stromal-Cre driver lines extensively target populations other than CAFs.

[A] Schematic representation of the recombination profile analysis of stromal-Cre driver lines. Tumor samples belonging to *Pdfgra*-Cre, *Fsp1*-Cre, *Myh11*-CreER, *Col6a1*-Cre, *Cspg4*-CreER, *Sm22*-Cre, and *Nest*-CreER were stained with a CAFs marker (PDPN), a tumor cell marker (KRT18), and an immune marker (CD45) and analyzed by confocal microscopy. Then, recombined cells positive and negative for the protein markers were quantified. For each stromal-Cre driver line, the following tumor samples were analyzed: *Cspg4*-CreER n=2; *Sm22*-Cre n=2, *Fsp1*-Cre n=3, *Pdgfra*-Cre n=3, *Myh11*-CreERT2 n=3, *Col6a1*-Cre n=1, and *Nest*-Cre n=3

[B] Recombination profile of the stromal-Cre lines *Pdfgra*-Cre, *Fsp1*-Cre, *Myh11*-CreER, *Col6a1*-Cre, *Cspg4*-CreER, *Sm22*-Cre, and *Nest*-Cre. The bar plot depicts the faction of recombined cells positive for CAFs marker (PDPN, red), tumor cell marker (KRT18, orange), and immune cell marker (CD45, blue) – double-positive cells – among all recombined cells. Recombined cells negative for PDPN, KRT18, and CD45 were identified as other cells (grey). Data is represented as mean±SD of the fraction of double-positive cells by recombined cells.

[C] Representative images of the channels td-tomato, GFP, PDPN, and DAPI indicate non-recombined cells, recombined cells, CAFs, and the total number of cells in the stromal lines *Pdfgra*-Cre, *Fsp1*-Cre, *Myh11*-CreER, *Col6a1*-Cre, *Cspg4*-CreER, *Sm22*-Cre, and *Nest*-CreER. The scale bar is 50 µm.

Acknowledgments: The animals used in this study were bred and sacrificed by all the members of AG Saur. Tatiana Martins and Elizaveta Gorbunova performed the immunofluorescence confocal acquisition of the tumor samples.

The lines *Gfap1*-Cre, *Gfap2*-Cre, *Gfap*-CreER, and *Pdgfra*-CreER presented none to low recombination efficiency alongside very low recombination levels and were no longer considered for further analysis.

Altogether, the results showed that the ability to target CAFs is limited in most lines, with *Pdgfra*-Cre presenting the highest potential. In addition, the stromal-Cre driver lines analyzed presented a promiscuous recombination profile, targeting multiple cell types.

4.2.2.3 Stromal-Cre driver lines target tumor cell populations with mesenchymal features

To measure tumor cell populations targeted by the stromal-Cre driver lines, each tumor sample was stained with antibodies against KRT18, and EpCAM, identifying the overall tumor cell content and the epithelial tumor cell content, respectively (Figure 37-A). The stromal-Cre driver lines' ability to capture dynamic EMT states was determined by quantifying the recombined cells positive for KRT18, measuring tumor cells with mesenchymal features, and quantifying EpCAM double-positive cells, measuring tumor cell populations undergoing EMT.

The stromal-Cre driver lines presented different capacities to label tumor cells, including populations that underwent epithelial-to-mesenchymal transition or were transitioning at that moment (Figure 37-B). The *Cspg4*-CreER line targeted all tumor cells (100±0%) but did not target cells expressing EpCAM, suggesting that expression of *Cspg4* might be associated with a fully developed mesenchymal program. Moreover, *Sm22*-Cre targeted approximately 32.94±42.96% of all tumor cells, comprising approximately 10.15±14.35% of EpCAM$^+$ populations among recombined cells. However, as previously described, the stromal lines *Fsp1*-Cre, *Myh11*-CreER, *Pdgfra*-Cre, and *Col6a1*-Cre targeted a low amount of tumor cells, labeling 3.68±0.91%, 1.85±1.81%, 3.40±5.11%, and 1.23% of tumor cells respectively (Figure 37-C). Additionally, these lines targeted tumor cells undergoing EMT with a mean expression of EpCAM double-positive cells of 4.77±1.68%, 8.80 ±2.54%, 3.62±6.28% and 2.56% among all recombined cells in the lines *Fsp1*-Cre, *Myh11*-CreER, *Pdgfra*-Cre, and *Col6a1*-Cre, respectively. The *Nest*-Cre stromal line was not evaluated since data from 4.2.2.1 showed no recombination of tumor cell populations.

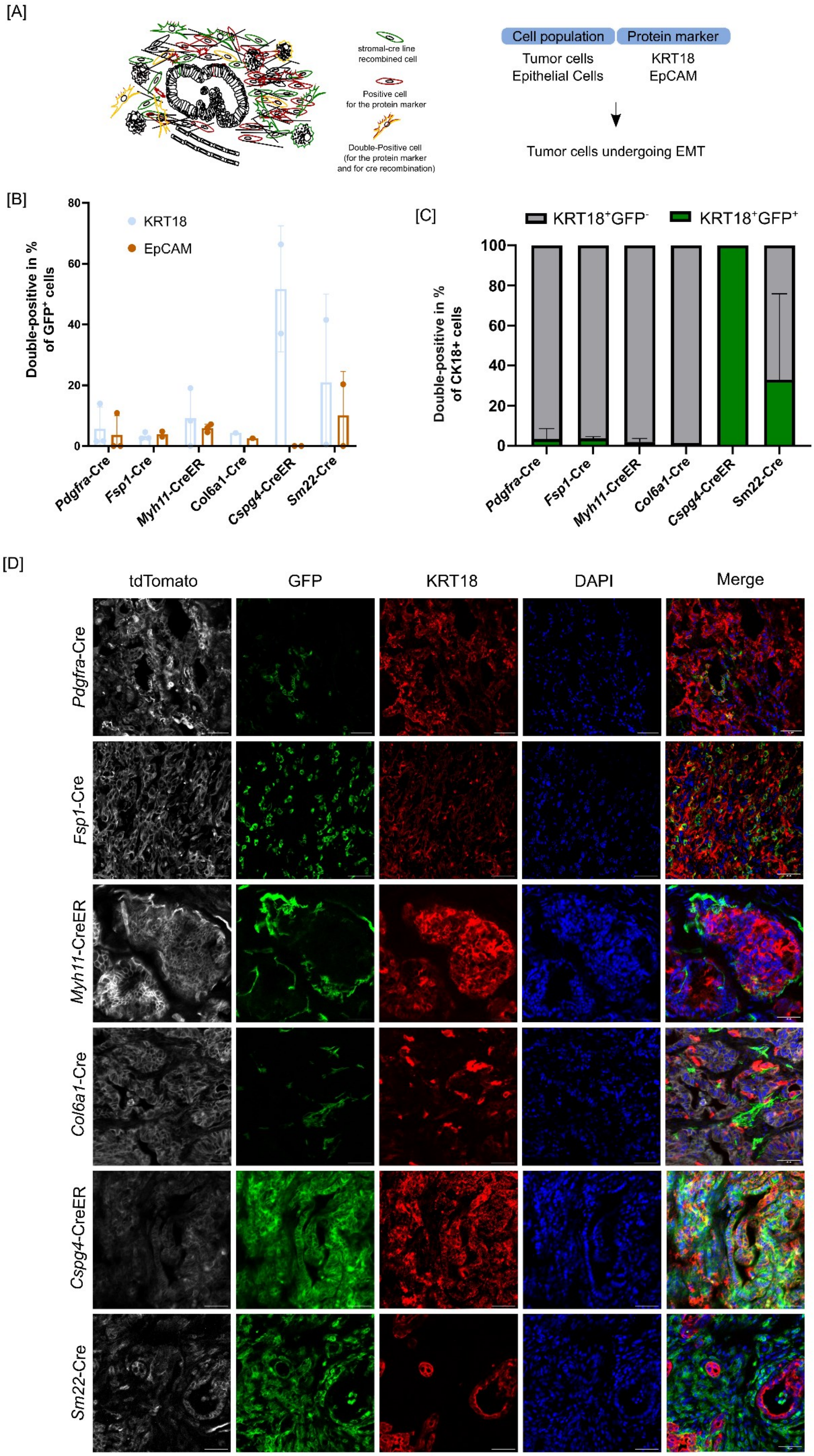

Figure 37 – Stromal-Cre driver lines target cells undergoing epithelial to mesenchymal transition.

[A] Schematic representation of the recombination profile analysis of stromal-Cre driver lines. Tumor samples belonging to *Pdfgra*-Cre, *Fsp1*-Cre, *Myh11*-CreER, *Col6a1*-Cre, *Cspg4*-CreER, *Sm22*-Cre, and *Nest*-CreER were stained with a tumor cell marker (KRT18), and an epithelial tumor cell marker (EpCAM) and analyzed by confocal microscopy. Then, recombined cells positive and negative for the protein markers were quantified to quantify tumor cells undergoing EMT. For each stromal-Cre driver line, the following tumor samples were analyzed: *Cspg4*-CreER n=2; *Sm22*-Cre n=2, *Fsp1*-Cre n=3, *Pdgfra*-Cre n=3, *Myh11*-CreER n=3, and *Col6a1*-Cre n=1.

[B] Frequency of recombination of tumor cells and epithelial tumor cells in the stromal-Cre lines *Pdfgra*-Cre, *Fsp1*-Cre, *Myh11*-CreER, *Col6a1*-Cre, *Cspg4*-CreER, *Sm22*-Cre. The bar plot depicts the percentage of KRT18 (blue) or EpCAM (orange) double-positive cells among all recombined cells. Data is represented as mean±SD.

[C] Recombination of tumors cells by the stromal-Cre lines *Pdfgra*-Cre, *Fsp1*-Cre, *Myh11*-CreER, *Col6a1*-Cre, *Cspg4*-CreER, *Sm22*-Cre. The bar plot depicts the fraction of recombined and non-recombined cells positive for the KRT18 marker among all tumor cells. KRT18 double-positive cells were depicted in green, and KRT18$^+$ non-recombined cells were shown in grey. Data is represented as mean±SD of the fraction of double-positive cells by KRT18$^+$ cells.

[D] Representative images of the channels td-tomato, GFP, KRT18, and DAPI indicate non-recombined cells, recombined cells, tumor cells, and the total number of cells in the stromal lines *Pdfgra*-Cre, *Fsp1*-Cre, *Myh11*-CreER, *Col6a1*-Cre, *Cspg4*-CreER, and *Sm22*-Cre. The scale bar is 50 µm.

Acknowledgments: The animals used in this study were bred and sacrificed by all the members of AG Saur. Tatiana Martins and Elizaveta Gorbunova performed the immunofluorescence confocal acquisition of the tumor samples.

Overall, these results showed the possibility of using the stromal-Cre driver lines as EMT tracing models, offering different mesenchymal promotors that could be exploited to study convergent pathways leading to EMT activation.

4.2.2.4 Stromal-Cre driver lines exhibit divergent CAFs recombination profiles

The most abundant CAFs populations in the TME are myCAFs-related populations and iCAFs. Therefore, to determine if these CAFs subpopulations could be targeted by the stromal-Cre driver lines analyzed, each tumor sample was stained with antibodies against a wide range of mesenchymal markers that phenotype stellate cells, such as GFAP and desmin, and CAFs, such as PDPN, PDGFRα, FSP1, Vimentin, and αSMA. The recombined cells positive for these markers (double-positive cells) revealed the CAFs targeting profile of each line (Figure 38-A).

CAFs populations, defined by the expression of PDPN, were targeted differently depending on the promotor under which Cre was expressed (Figure 38-B). These lines presented a PDPN double-recombined cells percentage ranging from approximately 3% to 51%. The lines that recombined the least amount of CAFs were *Myh11*-CreER and *Col6a1*-Cre, with a CAFs recombination rate of approximately 6.06±4.75% and 3.76%, respectively. In the *Myh11*-CreER, approximately 33.21±6.61% of the recombined cells were positive for αSMA, suggesting that myCAFs could be targeted with this line (Figure 38-C and Figure 38-D). Additionally, Desmin was also expressed in 29.62±14.64% of the recombined cells. When this data was compared against the transcript expression in the scRNAseq data published by Dominguez and colleagues, it could be denoted that *Des* was moderately expressed in Early myCAFs and myCAFs, reinforcing the idea that *Myh11*-CreER could target myCAFs populations. However, GFAP was not expressed in recombined cells to the same extent as Desmin (4.97±2.24% against 29.62±14.64%). Additionally, no recombined cells exhibited PDGFRα expression. In the *Col6a1*-Cre line, the double-positive cells predominantly expressed general CAFs and mesenchymal cell markers such as Vimentin, PDPN, GFAP, and the myCAF marker αSMA, which labeled approximately 14.22% of the recombined cells.

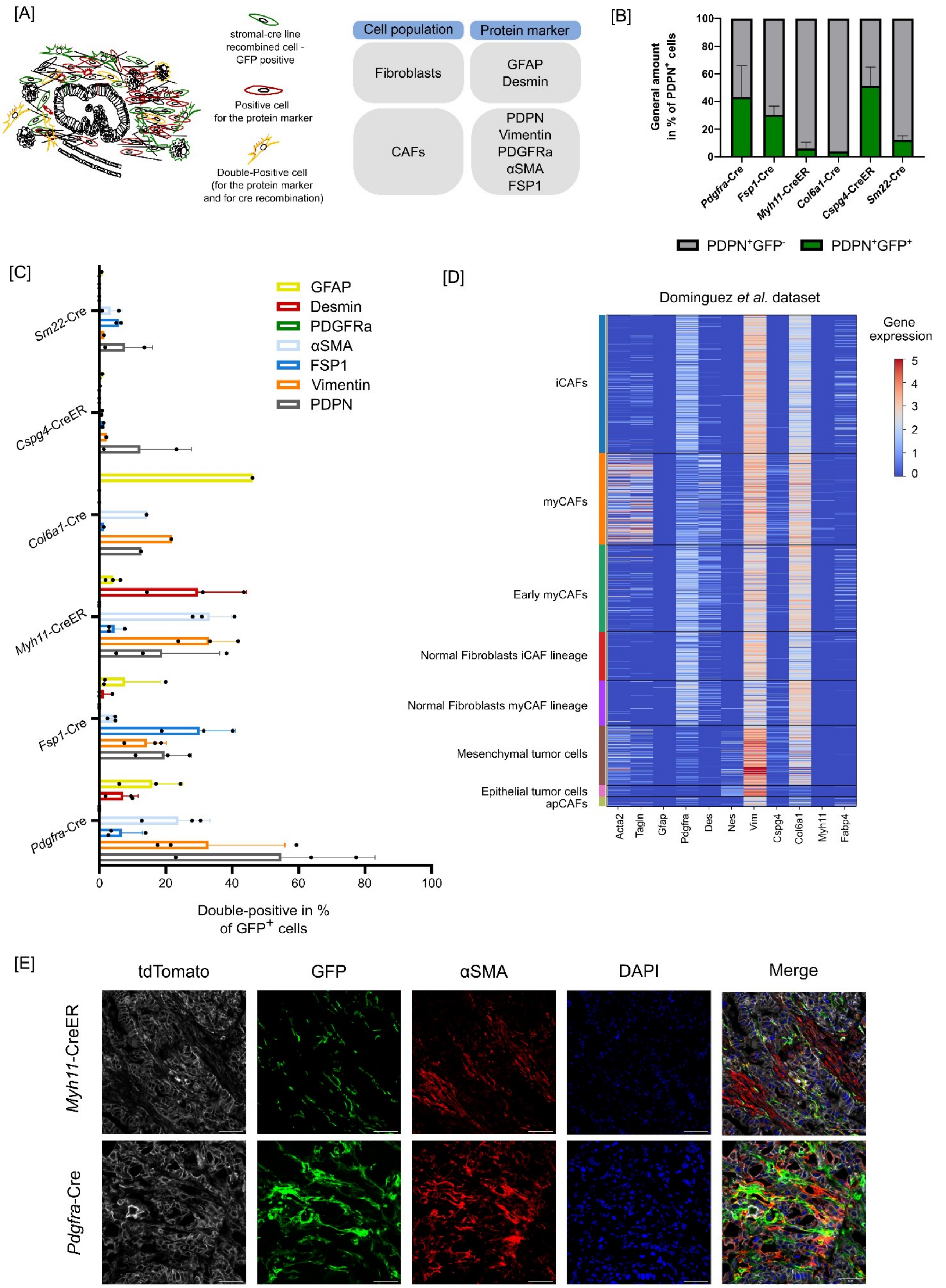

Figure 38 – Stromal-Cre driver lines target CAFs populations with different efficiency.

[A] Schematic representation of the recombination profile analysis of stromal-Cre driver lines. Tumor samples belonging to *Pdfgra*-Cre, *Fsp1*-Cre, *Myh11*-CreER, *Col6a1*-Cre, *Cspg4*-CreER, *Sm22*-Cre, and *Nest*-CreER were stained with fibroblasts, such as Desmin and GFAP, and CAFs markers, such as PDPN, Vimentin, PDGFRα, αSMA, and analyzed by confocal microscopy. Then, recombined cells positive and negative for the protein markers were quantified. For each stromal-Cre driver line, the following tumor samples were analyzed: *Cspg4*-CreER n=2; *Sm22*-Cre n=2, *Fsp1*-Cre n=3, *Pdgfra*-Cre n=3, *Myh11*-CreER n=3, and *Col6a1*-Cre n=1.

[B] Recombination of CAFs by the stromal-Cre lines *Pdfgra*-Cre, *Fsp1*-Cre, *Myh11*-CreER, *Col6a1*-Cre, *Cspg4*-CreER, *Sm22*-Cre. The bar plot depicts the fraction of recombined and non-recombined cells positive for the PDPN marker among all PDPN$^+$ cells. PDPN double-positive cells were depicted in green, and PDPN$^+$ non-recombined cells were shown in grey. Data is represented as mean±SD of the fraction of double-positive cells by PDPN$^+$ cells.

[C] Frequency of recombination of fibroblasts and CAFs in the stromal-Cre lines *Pdfgra*-Cre, *Fsp1*-Cre, *Myh11*-CreER, *Col6a1*-Cre, *Cspg4*-CreER, *Sm22*-Cre. The bar plot depicts the percentage of GFAP (yellow), Desmin (red), PDGFRα (green), αSMA (light blue), FSP1 (dark blue), Vimentin (orange), and PDPN (grey) double-positive cells among all recombined cells. Data is represented as mean±SD.

[D] Stromal promotor expression across the CAFs populations and tumor cell populations in the Dominguez *et al.* dataset.

[E] Representative images of the channels td-tomato, GFP, KRT18, and DAPI indicate non-recombined cells, recombined cells, αSMA, and the total number of cells in the stromal lines *Pdfgra*-Cre, *Fsp1*-Cre, *Myh11*-CreER, *Col6a1*-Cre, *Cspg4*-CreER, and *Sm22*-Cre. The scale bar is 50 µm.

Acknowledgments: The animals used in this study were bred and sacrificed by all the members of AG Saur. Tatiana Martins and Elizaveta Gorbunova performed the immunofluorescence confocal acquisition of the tumor samples.

The Fsp1-Cre presented approximately 30.37±6.43% of PDPN double-positive cells. However, the recombined cells presented low expression for CAFs-related markers such as PDGFRα (0±0%), αSMA (3.96±1.31%), GFAP (7.66±10.64%), and Desmin (1.31±2.26%), appearing that this stromal-Cre driver line does not target CAFs populations effectively.

Comparably, the stromal lines *Sm22*-Cre and *Cspg4*-CreER also presented a low expression of CAFs-related markers. Although *Cspg4*-CreER and *Sm22*-Cre lines targeted approximately 51.25±13.54% and 12.18±2.95% of all CAFs, respectively, the expression of fibroblasts markers such as Desmin, GFAP, αSMA, and PDGFRα in recombined cells was low. In fact, the content of αSMA double-positive cells in the *Cspg4*-CreER line was approximately 0.75±0.19% of the recombined cells, along with a low gene expression across all mesenchymal populations. In addition, although *Tagln* was a highly expressed gene in fully differentiated myCAFs, the *Sm22*-Cre line did not present a high content of αSMA double-positive cells (3.32±3.58%).

The line that best targeted CAFs was the *Pdgfra*-Cre line, labeling from approximately 18% to 63% of all CAFs. The analysis of several mesenchymal markers colocalizing with GFP expression in the recombined cells revealed that besides the classical mesenchymal marker expression, such as PDPN and Vimentin, the *Pfgfra*-Cre labeled a considerable amount of αSMA positive cells (23.69±9.55%), revealing the potential to target not only iCAFs but fibroblasts that undergo iCAF-to-myCAF transition. However, no PDGFRα expression was detected in the tumors. This was likely due to the loss of *Trp53* in the tumor analyzed. In addition, this line was able to target GFAP and desmin double-positive cells (7.11±4.56% and 15.82±9.29%, respectively).

In summary, the stromal-Cre driver lines target the stroma to a different extent, with the different CAFs populations being targeted. From the lines analyzed, although presenting some pervasiveness, *Pdgfra*-Cre, and *Myh11*-CreER are the most capable of targeting myCAFs.

5 Discussion and outlook

5.1 Stromal tumor microenvironment in PDAC

PDAC is one of the deadliest cancers, with an overall 5-year survival rate of 10% (American Cancer Society, 2022; Park *et al.*, 2021; Rahib *et al.*, 2021). Pancreatic adenocarcinoma is generally diagnosed at the late stages, with only 20% of the patients presenting localized resectable disease and an associated 5-year survival rate of 42% (American Cancer Society, 2022; Park *et al.*, 2021). The standard of care therapy in PDAC is defined by tumor stage and performance status. Independently of the performance status, the therapy is based on DNA-interfering agents, such as gemcitabine, FOLFORINOX, nab-paclitaxel, 5-fluorouracil, platin-based, or a combination of those agents (Neoptolemos *et al.*, 2018). Nevertheless, patients showed different responses to therapy, with studies showing that stroma interferes with its response (Deng *et al.*, 2020; Heger *et al.*, 2022; Olive *et al.*, 2009; Raghavan *et al.*, 2021). In fact, patients harboring tumors with a higher stromal content exhibit a longer overall survival (Jiang *et al.*, 2020; Knudsen *et al.*, 2017).

The stromal TME is a diverse and dynamic ecosystem composed of several CAFs in a rich ECM. CAFs compose most of the tumor area, showcasing a continuum of phenotypes. On the one hand, CAFs populations mediate therapy resistance through senescence-associated secretory phenotype, stiffness-induced DSB repair, maintenance of cancer stem cell niche, facilitating the activation of cancer-driving pathways, and inducing immunosuppressive environments (Deng *et al.*, 2020; Krishnamurty *et al.*, 2022; Nicolas *et al.*, 2022; Su *et al.*, 2018). On the other hand, stroma restrains tumor progression (Chen *et al.*, 2021; Jiang *et al.*, 2020)

Until today it is not entirely understood how the stromal TME is shaped in different oncogenic backgrounds and phenotypically divergent tumors and how the context-specific stromal TME composition impacts disease progression. Therefore, to evaluate the stromal TME in PDAC, multiplex immunofluorescence, transcriptomic and organoid models were used to characterize GEMMs of PDAC.

5.1.1 Immunofluorescence workflow to measure CAFs activation and spatial distribution in PDAC

PDAC presents a developed stromal response comprising most of the tumor area (Whatcott *et al.*, 2015). The stratification of tumors according to the stromal microenvironment highlighted CAFs as populations with prognostic value (Grunwald *et al.*, 2021; Heger *et al.*, 2022; Hu *et al.*, 2022; Peng *et al.*, 2022). CAFs populations are phenotypically diverse and assume tumor-promoting and tumor-restraining roles in the TME (Chen *et al.*, 2021; Huang *et al.*, 2022; Jiang *et al.*, 2020; Nicolas *et al.*, 2022; Rhim *et al.*, 2014). However, CAFs TME composition has not been associated with tumor mutational landscape or tumor grade. Therefore, to understand how tumor-specific features affect the activation of CAFs and the organization of stromal architecture, a workflow relying on immunofluorescence detection of stromal markers was optimized.

Previous methods have characterized the stromal microenvironment in PDAC. These studies used high-dimensional dissociative single-cell techniques, identifying new populations, lineages, and their content (Dominguez *et al.*, 2020; Elyada *et al.*, 2019; Foster *et al.*, 2022; Friedman *et al.*, 2020; Hutton *et al.*, 2021). Nevertheless, even though CAFs make up most of the TME, the dissociation significantly decreases CAFs numbers, representing less than 15% of all cells (Dominguez *et al.*, 2020; Elyada *et al.*, 2019; Hutton *et al.*, 2021). To overcome this limitation, many studies used enrichment to increase CAFs numbers, but that does not address the potential susceptibilities of CAFs populations to digestion, which can induce skewed CAFs proportions. In addition, single-cell dissociative techniques do not preserve tissue architecture, providing a shallow representation of cell-cell communications.

Multiplex immunofluorescence techniques allow the use of multiple phenotypic markers while maintaining tissue architecture (Schurch *et al.*, 2020; Stoltzfus *et al.*, 2020). The informational content extracted from multiplex images quantifies not only the content of cell populations but also cellular neighborhoods, highlighting cell populations that are likely communicating and are recurrent across the sample (Bodenmiller, 2016; Schurch *et al.*, 2020; Stoltzfus *et al.*, 2020). This thesis describes the first multiplex immunofluorescence workflow that focuses on stromal TME characterization, determining CAFs populations' content, neighborhoods, and density in the tissue architecture.

One of the initial challenges in establishing multiplex immunofluorescence panels is biomarker selection. CAFs are phenotypically diverse, assuming intermediate phenotypes between the three established CAFs populations – iCAFs, myCAFs, and apCAFs (Dominguez *et al.*, 2020; Elyada *et al.*, 2019; Friedman *et al.*, 2020; Huang *et al.*, 2022). Therefore, the biomarkers selected aimed to perform the identification of CAFs populations based on markers in existing literature, where PDPN, IL6, αSMA, PDGFRα, and MHCII would cover the CAFs spectrum. The selection of the markers allowed the phenotyping iCAFs, myCAFs, and apCAFs but also intermediate populations such as early myCAFs, IL6 myCAFs, IL6 iCAFs, and stellate cells. In addition, markers such as KRT18 and CD45 were used as support to identify tumor cells and immune populations. This strategy offered low discovery potential of new populations but offered the possibility to structure panels with high characterization potential of populations already described. In fact, this workflow revealed the heterogenous composition of PDAC stromal TME, although stratification for variables such as histological grade, oncogenic drivers, and *Trp53* mutations suggested more cohesive stromal TMEs. Further analysis showed populations with a high probability of co-occurring together, such as apCAFs and APC immune cells, likely due to interferon-gamma signaling (Kaur *et al.*, 2008), IL6 iCAFs and IL6 myCAFs, due to NFκb signaling (Biffi *et al.*, 2019), and the negative co-occurrence of iCAFs and tumor cells, due to non-autonomous tumor cell signaling (Ohlund *et al.*, 2017).

This workflow presented some challenges at the experimental and downstream analysis levels. At the experimental level, tissue quality highly impacts the staining quality. Tissue quality depends on the tissue of origin, tissue preservation, and fixation. Basal autofluorescence is linked to the tissue of origin. However, poor fixation and preservation lead to an increased autofluorescence, lowering the signal-tonoise ratio and originating misleading staining patterns. The quality of the imaging is crucial for downstream analysis. Proper acquisition requires optimization since spectral overlap was possible using a confocal system with the number of markers used, extending panel development time. At the downstream level, segmentation was performed in a supervised manner, meaning that *a priori* cell populations had a pre-defined set of markers. This strategy requires a previous biomarker plan and knowledge of the cell populations of interest. Additionally, the neighborhood analysis was contingent on the neighborhoods that could be identified in the original data, limiting the power of discovery. Using two phenotyping panels did not allow the integration of apCAFs in the CNs defined by the cell types phenotyped with Panel 1. Moreover, the identification of the CNs was performed by empiric determination of the neighborhood diameter, with a further manual merge of clusters with similar cell composition.

In conclusion, the workflow allows for a comprehensive characterization of the stromal TME, defining CAFs population content and determining cellular neighborhoods. In addition, this work opens the opportunity for further integration of these panels in highly multiplex immunofluorescence workflows that incorporate immune cell and ECM markers.

5.1.2 Oncogene-driven CAFs activation

KRAS gain-of-function mutations are the most common genetic alteration in PDAC, and approximately 43% of *KRAS* mutations present a G12D substitution (Philip *et al.*, 2022; Raphael *et al.*, 2017; Witkiewicz *et al.*, 2015). Nevertheless, approximately 10% of tumors present other mutations, including *BRAF*, *PI3KCA*, and *BRCA2* (Philip et al., 2022; Witkiewicz et al., 2015). Curiously, *PI3KCA* activating mutations represent 4-6% of tumors, and their occurrence is mostly concomitant with KRAS mutations (Aung et al., 2018; Witkiewicz et al., 2015). Conversely, *BRAF* mutations occurred alongside *TRP53* but were mutually exclusive of *KRAS* (data from QCMG study, cBioPortal)(Witkiewicz *et al.*, 2015). These differences in the genetic landscape of tumors translate into different clinical outcomes. In fact, patients harboring *KRAS*^{WT} tumors had better overall survival than those with *KRAS* mutations (Philip *et al.*, 2022; Windon *et al.*, 2018).

The mutation and transcriptional landscape are closely connected, with genetic alterations governing tumor cell states (Mercatelli *et al.*, 2019; Neftel *et al.*, 2019). PDAC tumors present a multitude of tumor cell states likely arising from clonal diversity (Bailey *et al.*, 2016; Barkley *et al.*, 2022; Raphael *et al.*, 2017). In turn, the extrinsic mechanisms induced by tumor cell states may influence the activation of stromal populations (Barkley *et al.*, 2022). Studies have shown that *BRCA2* mutated tumors showcase proliferative epithelial tumor cell states that can shape the TME, activating a pro-inflammatory immune response, the activation of MHCII^{+} bone-marrow CAFs but lower stromal-to-tumor ratio (Friedman *et al.*, 2020; Launonen *et al.*, 2022). Moreover, other tumor cell states correlated with specific stromal populations, suggesting a bidirectional interplay between tumor and stromal cells (Barkley *et al.*, 2022; Raghavan *et al.*, 2021; Tape *et al.*, 2016). However, the influence of oncogenic drivers and CAFs activations remain largely unknown, as well as the mechanisms shaping the stromal TME.

To determine the influence of oncogenic drivers in stromal TME activation, tumors harboring either KRAS^{G12D} mutations or PI3K^{H1047R} were analyzed using the multiplex immunofluorescence workflow established. The PI3K^{H1047R} tumors presented more frequently differentiated features than their KRAS^{G12D} counterparts. Tumor morphology is associated with increased *Kras* gene dosage, and it would be expected that mesenchymal tumor cell states would make up the majority of the tumor cell populations in poorly-differentiated and undifferentiated tumors (Mueller *et al.*, 2018). Although tumors with *Kras* iGD exhibit upregulated PI3K-AKT transcriptional programs, it is unknown if increased *Pi3kca* gene levels induce the same changes (Mueller *et al.*, 2018). Therefore, the sub-cohort analyzed was restricted to tumors presenting differentiated morphology.

PI3K is an arm of the KRAS signaling pathway that flows through PDK1 to activate AKT and mTOR, regulating cell proliferation, survival, and metabolism (Hoxhaj and Manning, 2020). KRAS can also signal through the BRAF arm, activating MEK and ERK kinases to regulate cell proliferation, survival, and migration (Samatar and Poulikakos, 2014). The G12D mutation locks KRAS in its GTP-bound state, sustaining persistent downstream activation (Scheffzek *et al.*, 1997). In fact, KRAS^{G12D} regulates tumor cell-autonomous mechanisms through the phosphorylation of ERK, in opposition to KRAS^{WT}, where phosphorylated AKT regulates tumor cell processes (Tape *et al.*, 2016). Since the secretome of tumor cells regulates stromal cell mechanisms, it would be expected that KRAS^{G12D} and KRAS^{WT} tumors would present different stromal phenotypes. Surprisingly, no alterations in the TME were observed between KRAS-driven and PI3K-driven tumors, presenting equivalent compositions of tumor cells, CAFs, and immune cells. The same effect was observed when the stromal TME was evaluated in more detail. Tumors harboring KRAS^{G12D} and PI3K^{H1047R} mutations did not show differential activation of CAFs populations. The resemblance in the TME between both groups suggests that the PI3K signaling arm may maintain the stromal phenotype in differentiated KRAS-driven tumors.

The communication of KRAS^{G12D} tumor cells with stromal cells is bi-directional, involving tumor cell-extrinsic and reciprocal signaling (Tape *et al.*, 2016). The secretome is part of the heterocellular oncogene signaling, encoding an intricate communication profile. Tumor cells' secretome shapes stromal signaling, and stroma, in turn, reciprocates signal to tumor cells, inducing the activation of AKT and controlling multiple pathways and phenotypes in tumor cells (Barkley *et al.*, 2022; Raghavan *et al.*, 2021; Tape *et al.*, 2016). Therefore, the heterocellular oncogene signaling would depend on tumor cell neighborhoods. In this study, KRAS and PI3K-driven cellular neighborhoods remained unaltered. Tumors from both groups present the same density of tumor cell-centric neighborhoods, and no preferential enrichment was observed in the different tumor cell-CAFs regional neighborhoods. Even though it was not possible to evaluate the contribution of apCAFs in the cellular neighborhoods analysis performed, apCAFs were located further apart from KRAS^{G12D} tumor cells. Increased signal flowing through the PI3K signaling arm in PI3K^{H1047R} tumors activates interferon-gamma responses that may sustain apCAFs phenotype closer to tumor cells (Kaur *et al.*, 2008). Nevertheless, the number of apCAFs did not change between groups, likely due to the induction of active PI3K signaling in KRAS^{G12D} tumor cells by the stromal compartment or the PI3K axis regulation by tumor cells in KRAS^{G12D} PDAC. Similarly, IL6 myCAFs and iCAFs levels were not altered, but these cells were closer to PI3K^{H1047R}

tumor cells without significant changes in tumor architecture, likely due to PI3K-induced NF-κB signaling (Kane *et al.*, 1999).

It can not be excluded that in TRP53^{WT} PI3K and KRAS-driven tumors, the influence of reciprocal pAKT activation in tumor cells may be redundant, with tumor cell PI3K^{H1047R} and KRAS^{G12D} upregulating the same signaling arm (Eser *et al.*, 2013). In fact, there was no transcriptional difference between the groups in a RNAseq analysis of PI3K^{H1047R} and KRAS^{G12D} organoids in mice in which TRP53 was not targeted from embryogenesis. Moreover, bulk tumor analysis showed minimal differences between groups, with a few TME-related genes upregulated in the KRAS^{G12D} group. These differences may arise from sampling heterogeneity, maximizing differences that may not exist.

In conclusion, PI3K-driven and Kras-driven differentiated tumors present similar CAFs activation and TME organization, likely maintained by PI3K via reciprocal signaling. These changes happen in a context-specific environment where stromal cells outnumber tumor cells. Nonetheless, in contexts with low stromal abundance or poor tumor cell differentiation, PIK3 and KRAS-driven tumors may present divergent stromal TME.

5.1.3 PDAC phenotypes and CAFs activation

The prognosis of patients with PDAC is closely linked with tumor stage, where patients with resectable disease and absence of metastasis showcase longer 5-year survival rates (Hartwig *et al.*, 2011; Neoptolemos *et al.*, 2018). The criteria defining tumor stage are based on tumor size, amount of lymph node metastasis, and presence of distant metastasis (van Roessel *et al.*, 2018). However, even though patients in earlier stages do not showcase lymph node metastasis (stages I and IIA), their survival does not always correlate with tumor size (Shin *et al.*, 2019; van Roessel *et al.*, 2018; Yin *et al.*, 2020). Therefore, this classification system should accommodate new variables, such as tumor grade and TME composition, to stratify patients with PDAC more efficiently.

Tumor grade is a three-tiered system based on the gradual loss of differentiation features (Haeberle and Esposito, 2019; Kalimuthu *et al.*, 2020). These morphological alterations are indicative of patient survival, with patients harboring well-differentiated (G1) and moderately-differentiated tumors (G2) exhibiting a longer overall survival rate than poorly-differentiated tumors (G3) (Hartwig *et al.*, 2011; Kalimuthu *et al.*, 2020; Yin *et al.*, 2020). However, even though tumor grade is reflective of survival prognosis, the use of these features for therapeutic purposes is not linear. Tumors are heterogeneous and comprise several cellular tumor cell states. Transcriptomic characterization of PDAC tumor samples showed that tumor cells comprise a continuum of cell states co-existing in the same TME (Barkley *et al.*, 2022; Chan-Seng-Yue *et al.*, 2020; Raghavan *et al.*, 2021). The diverse classical and basal tumor cell states make up the tumor compartment in different ratios, with KRAS-imbalanced basal tumor cells associated with advanced disease (Chan-Seng-Yue *et al.*, 2020). In fact, pure-classical phenotypes were associated with differentiated glandular PDAC, while pure-basal correlated with poorly-differentiated and undifferentiated tumors (Kalimuthu *et al.*, 2020; Puleo *et al.*, 2018). Müller and colleagues also observed similar findings, where the extreme epithelial C2a and mesenchymal C1 clusters were associated with differentiated and undifferentiated PDAC, respectively (Mueller *et al.*, 2018).

Transcriptomic classifications of PDAC combined tumor cell and TME states, revealing the potential of stromal populations shaping tumor prognosis (Moffitt *et al.*, 2015; Puleo *et al.*, 2018). Stroma has a crucial role in the TME, defining tumor cell states, therapy resistance, and overall survival (Barkley *et al.*, 2022; Moffitt *et al.*, 2015; Puleo *et al.*, 2018; Raghavan *et al.*, 2021). Therefore, to understand how differentiated and poorly-differentiated TMEs are composed and organized, KRAS^{G12D} tumor samples belonging to both groups were processed and analyzed with the multiplex-immunofluorescence workflow established. The tumor differentiation state induced significant remodeling of the TME, where differentiated PDAC presented a well-developed stromal response, comprising most of the tumor mass, and decreased tumor cell content. Conversely, in poorly-differentiated tumors, most of the tumor mass was composed of tumor cells with an undeveloped stromal response. This dichotomy between differentiated and poorly-differentiated tumors is not surprising since the loss of a stromal response is associated with increased tumor grade (Haeberle and Esposito, 2019). Upon further dissection of the stromal TME, differentiated and poorly-differentiated tumors exhibited different CAFs activation profiles, with differentiated tumors presenting a higher content of early myCAFs and poorly-differentiated tumors a higher content of IL6 myCAFs and different tumor organization.

The tumor organization is influenced by cellular composition and cellular neighborhoods. Poorly-differentiated PDAC exhibited a tumor cell-centric TME, with most tumors enriched in tumor cell-rich neighborhoods. This feature of poorly-differentiated tumors is likely due to the lack of glandular structure, and the increased tumor cell content observed, facilitating tumor cells and CAFs' proximity and suggesting a privileged communication profile between the cell types. Therefore, it is likely that tumor cells influenced CAFs phenotypes in poorly-differentiated tumors. Myofibroblasts-related populations composed of early myCAFs, myCAFs, and IL6 myCAFs, are activated via TGFβ-induced mechanisms (Biffi *et al.*, 2019; Krishnamurty *et al.*, 2022). The mesenchymal C1 cluster presents an increased *Kras* gene dosage and is enriched in poorly-differentiated and undifferentiated tumors (Mueller *et al.*, 2018). When the transcriptional landscape of C2a and C1 tumor cells were compared, C1 mesenchymal cells upregulated TGFβ1 and ECM interactions transcriptional programs, with the enrichment of collagen genes, *Tgfb1*, and *Fn*. Increased KRAS signaling upregulates these pathways that likely differentiate CAFs into myCAFs phenotypes by the stimulation of TGFBR2 and by mechanosensing mechanisms (Biffi *et al.*, 2019; Discher *et al.*, 2005; Huang *et al.*, 2012; Krishnamurty *et al.*, 2022; Laklai *et al.*, 2016) In fact, poorly-differentiated tumors were described to accumulate thicker collagen fibers that are associated with increased actomyosin tension (Laklai *et al.*, 2016). In addition, the expression of IL6 in CAFs is induced by cell-extrinsic stimulation of the IL1 receptor by IL1α (Biffi *et al.*, 2019). However, C1 mesenchymal tumor cells did not present increased *Il1a* expression, and the activation of IL6 myCAFs phenotype likely results from the interactions with other TME cells. Poorly-differentiated tumors presented a trend toward a higher infiltration of immune cells than in differentiated tumors, which may contribute to the activation of this CAFs phenotype.

In conclusion, the differentiation degree of PDAC tumors influences the TME, with poorly-differentiated tumors presenting a tumor cell-centric architecture associated with a shallow stromal response. These results bring new insights into TME regulation in poorly-differentiated tumors, where the stromal compartment may act as a bystander agent. Therefore, studies addressing drugs targeting this PDAC subtype should consider the regulation of tumor architecture, focusing on tumor cell-intrinsic mechanisms and their impact on immune regulation.

5.1.4 *Trp53* status in CAFs activation

TRP53 mutations are recurrent in PDAC, occurring in approximately 70% of *KRAS*-mutated tumors (Raphael *et al.*, 2017; Waddell *et al.*, 2015). Most mutations lead to partial-to-total loss of the protein function, perturbing the complex network of processes regulated by *TRP53* (Kastenhuber and Lowe, 2017; Raphael *et al.*, 2017; Waddell *et al.*, 2015). Molecular alterations in *TRP53* are associated with a poor prognosis, presenting an enrichment in basal-like phenotypes, increased metastasis, resistance to therapy, and shorter overall survival (Chan-Seng-Yue *et al.*, 2020; Kastenhuber and Lowe, 2017; McIntyre *et al.*, 2020; Safi *et al.*, 2022). Furthermore, the loss of TRP53 function is an important event during PDAC progression, in which loss of heterozygosity (LOH) of *TRP53* leads to its biallelic inactivation, resulting in increased genomic instability and the accumulation of copy number alterations (Baslan *et al.*, 2022). However, even though cell-autonomous consequences of *TRP53* mutations have been studied extensively, the role of TRP53 cell-extrinsic mechanisms in regulating stromal activation is not well understood.

Therefore, to understand the role of the *TRP53* wild-type allele in regulating stromal activation and tumor architecture, differentiated KRAS^{G12D} tumor samples belonging to both groups were processed and analyzed with the multiplex-immunofluorescence workflow established. The loss of the *Trp53* wild-type allele induced a change in TME composition, in which *Trp53*-proficient tumors presented a lower tumor cell content and an increased content in CAFs compared with *Trp53*-deficient tumors. Furthermore, when the CAFs compartment was analyzed in more detail, revealing a preferential activation of myCAFs-related populations in *Trp53*-deficient tumors and iCAFs in *Trp53*-proficient tumors. The TME in Trp53-proficient tumors was composed mainly of early myCAFs and iCAFs and iCAFs organized in tumor cell-centric, early myCAFs, and iCAFs neighborhoods. Conversely, *Trp53*-deficient tumors were governed by tumor cell-centric and myCAFs-related neighborhoods. However, the organization of the *Trp53*-deficient tumor was heterogeneous, composed of early myCAFs, myCAFs, and IL6 myCAFs neighborhoods. It is possible that the IL6 myCAFs population could arise from tumor cell-derived NFκB signaling with the secretion of IL1α associated with *Trp53*^{R172H} gain of function mutation (Kastenhuber and Lowe, 2017). Nevertheless, one homogenous variable was the lack of any iCAFs content in *Trp53*-deficient tumors, suggesting that the TRP53 may regulate cancer-specific mechanisms responsible for CAFs composition in the TME.

CAFs populations content in the TME occurs in a dichotomous fashion, where myCAFs content is inverse to iCAFs (Biffi *et al.*, 2019; Hutton *et al.*, 2021). Therefore, to identify the tumor cell-driven mechanisms involved in activating myCAFs populations in PDAC, the transcriptional landscapes between Trp53-proficient and -deficient tumor cells were evaluated. *Myc* target genes and EMT-related genes were enriched in tumor cells that lost the *Trp53* allele. This transcriptional upregulation of *Myc* targets genes is not particularly unexpected since TRP53 regulates MYC overexpression, and *Myc* amplification occurs following *Trp53* LOH (Baslan *et al.*, 2022; Sachdevaa *et al.*, 2009). It was also worth noticing that several ECM-related genes, constituting the EMT hallmark signature, were enriched in tumor cells, namely *Col4a1*, *Loxl2*, and *Fbln4*. Therefore, since myCAFs populations are associated with *Trp53*-deficient tumors that, in turn, present an upregulation of ECM-related genes, it would be expected that tumor cells-specific ECM would be involved in myCAFs activation.

Myofibroblast phenotype depends on TFGβ1-induced SMAD activation (Biffi *et al.*, 2019). However, a desmoplastic ECM in the TME can activate myCAFs through integrin-dependent FAK activity (Discher *et al.*, 2005; Foster *et al.*, 2022; Franco-Barraza *et al.*, 2017). Therefore, a combination of mechanisms may be responsible for the trans-differentiation of iCAFs into myCAFs-related phenotypes: i) secretion of cancer-specific ECM and cross-linking enzymes, increasing tumor stiffness and consequent activation of mechanosensing mechanisms through FAK-dependent integrins; ii) the entrapment of TGFβ1 in the ECM, leading to the differentiation through the classical TGFβ1-TGFBR2-SMAD axis. On the one hand, the desmoplastic ECM is mainly composed of collagen molecules secreted by CAFs, crosslinked into fibrils by LOX enzymes (Tian *et al.*, 2019; Yamauchi and Sricholpech, 2012). The upregulation of *Loxl2*, *Col4a1*, and *Fbln4* in *Trp53*-deficient tumor cells suggests the participation of tumor cells in the ECM remodeling process. The histopathological stratification of PDAC tumors according to myCAFs content showed that the ECM remodeling was a hallmark of the myCAFs-high tumors phenotype, presenting a high deposition of Collagen IV and the collagen crossling enzyme LOX. The increased collagen IV and LOX expression were not solely compartmentalized to the tumor compartment but also expressed in the stroma. Moreover, *Fbln4* may be responsible for activating a highly active form of LOX enzymes, mediating the fibrillogenesis and accumulation of collagen IV, further activating FAK-dependent integrins, and initiating the myCAFs activation process (Grau-Bove *et al.*, 2015; Noda *et al.*, 2020; Wang *et al.*, 2020). In fact, the inhibition of LOX-induced collagen deposition in PDAC organoids co-cultures with naïve pan-fibroblasts showed that tumor cell-derived ECM deposition modulates CAFs activation, mainly in *Trp53*-deficient tumors. On the other hand, *Trp53*-deficient tumor cells presented a trend toward *Tgfb1* upregulation. Tumor cells and iCAFs ECM secretion may entrap TGFβ1, leading to the activation of myCAFs via TGFBR2 and the expression of a matrix remodeling phenotype (Biffi *et al.*, 2019; Dominguez *et al.*, 2020; Franco-Barraza *et al.*, 2017). The activation of matrix remodeling myCAFs phenotype may lead to an exacerbation of the ECM deposition and may increase the signaling pressure on FAK.

The regulation of ECM appears to be an essential regulatory node of tumor progression. The upregulation of ECM-related mechanisms engages mechanosensing signaling pathways associated with FAK-dependent integrins and YAP, which lead to EMT, invasion, and metastasis (Cox *et al.*, 2013; Laklai *et al.*, 2016; Ungewiss *et al.*, 2016; Wei *et al.*, 2015; Zaghdoudi *et al.*, 2020). Collagen deposition, namely collagen IV, is described to stimulate integrin β1, initiating the FAK signaling axis involved in tumor cell invasion and metastasis (Ungewiss *et al.*, 2016; Wang *et al.*, 2020; Zaghdoudi *et al.*, 2020).

LOX enzymes are also associated with a pro-metastatic environment (Alonso-Nocelo *et al.*, 2022; Cox *et al.*, 2013; Peng *et al.*, 2017). The association between ECM deposition and metastasis is likely orchestrated by MYC. *Myc* overexpression is common in metastatic PDAC and is a hallmark of the loss of TRP53 function (Baslan *et al.*, 2022; Maddipati *et al.*, 2022; Sachdevaa *et al.*, 2009; Santoro *et al.*, 2019). MYC negative regulation of the miRNA200 family leads to the upregulation of *Zeb1* in *Trp53*-deficient tumor cells, which likely regulates the transcription of *Loxl2*, *Col4a1,* and *Fbln4* (*ZEB1* transcriptional targets, Encode) (Schaub *et al.*, 2018; Ungewiss *et al.*, 2016). MYC non-cell autonomous mechanisms have been shown to modulate the immune TME, activating mechanisms that recruit tumor-associated macrophages (Maddipati *et al.*, 2022; Sodir *et al.*, 2020). Similarly to what was described by Maddipaati and colleagues and Sodir and colleagues, myCAFs-high TME presented a high score of macrophages that positively correlated with *Mrc1* and high expression of *Cxcl14*, suggesting that myCAFs in the TME may communicate with tumor-associated macrophages involved in the metastatic cascade.

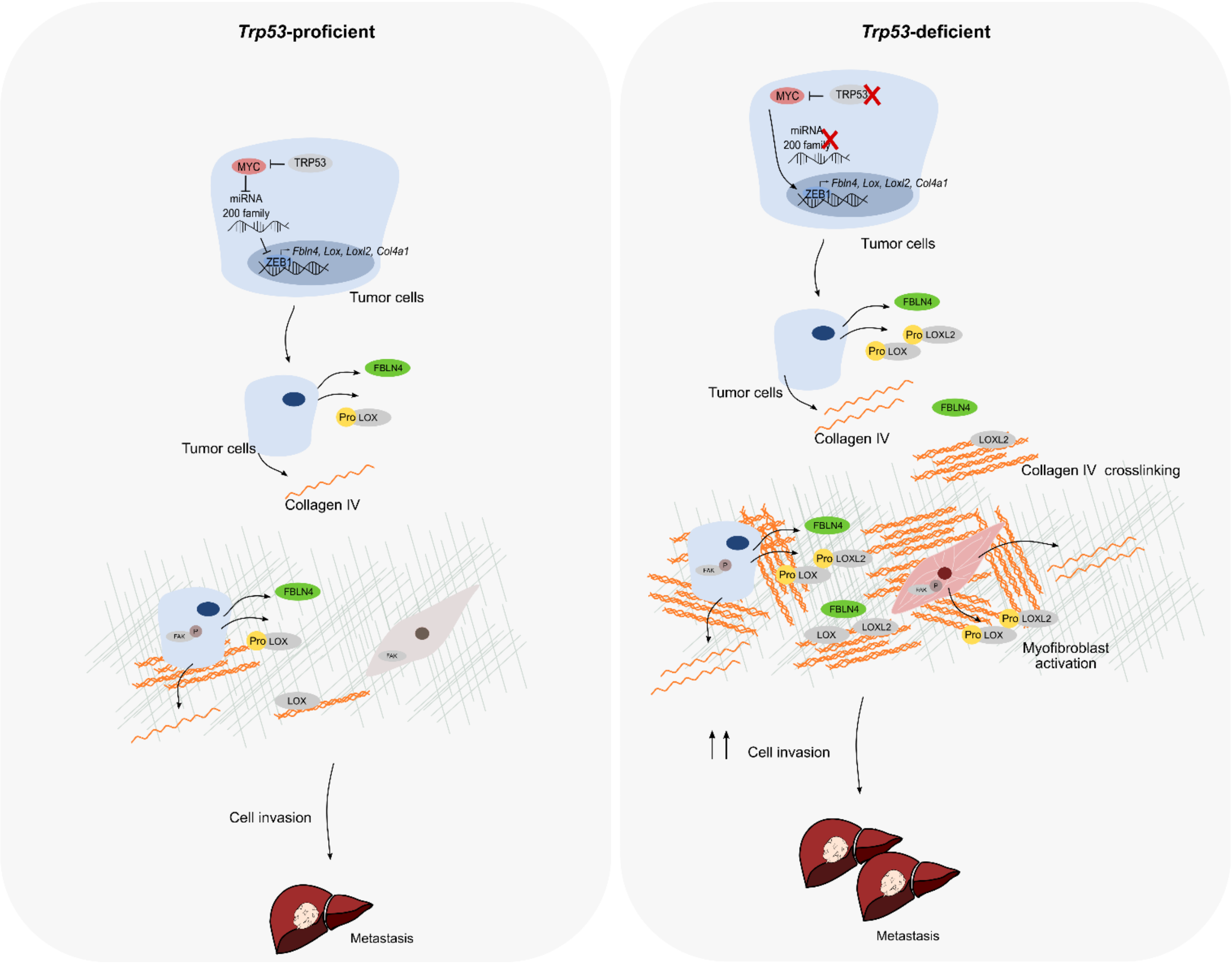

Figure 39 – Hypothesis for the mechanism of Trp53-deficient driven alterations in PDAC TME and their influence on metastasis.

Model of the hypothesis of TRP53-induced tumor cell-intrinsic regulation of the TME. TRP53 negatively regulates the expression MYC, which negatively regulates the miRNA 200 family transcriptionally. miRNA200 family can directly inhibit ZEB1-induced transcriptional programs, inducing lower accumulation of collagens, lower FAK signaling activation, and lower metastasis formation. Conversely, in the absence of TRP53, MYC gets overactivated, downregulating the miRNA 200 family, leading to ZEB1-regulated transcription of genes like *Fbln4*, *Tgfb1*, and *Loxl2*. FBLN4 activates LOXL2 crosslinking collagen IV, increasing collagen deposition and matrix stiffness. CAFs sense the increased stiffness and activate mechanosensing mechanisms that lead to myCAFs activation. myCAFs exacerbate collagen deposition, leading to sustained activation of FAK, increased cell invasion, and increased metastasis.

Non-tumor cell populations, alongside the metastatic potential of ECM, promote tumor metastasis. Tumor-associated macrophages educated by tumor cells secrete proteins, such as LOXL2, that potentiate the metastatic cascade (Alonso-Nocelo *et al.*, 2022; Maddipati *et al.*, 2022). Although myCAFs-high TME presented a high expression of LOX and collagen IV in this study, it was not associated with an increased metastization potential. Metastasis formation was, in fact, influenced by both tumor stromal ratios and stromal composition. Regardless of the myCAFs content, tumors with a low stromal abundance did not present a myCAFs-dependent metastatic potential, suggesting that tumor cell-induced mechanisms appear sufficient for metastasis formation. Conversely, myCAFs-high tumors were associated with increased metastasis potential in tumors with high stromal content, suggesting that myCAFs likely collaborate with Trp53-deficient cells to induce metastasis in this context. In fact, abundant stromal reaction associated with increased FAK activity in the stromal compartment correlates with a poor prognosis and increased tumor metastasis (Zaghdoudi *et al.*, 2020).

In conclusion, Trp53 impacts the stromal TME, shifting CAFs activation toward the myCAFs-related phenotypes. Trp53 LOH appears to induce a cascade of events that upregulate ECM deposition and tumor cell-induced mechanosensing activation of myCAFs populations, which, in turn, appear to exacerbate ECM deposition. In contexts of higher stromal abundance, myCAFs may cooperate with tumor cells to induce metastasis formation. Even though the hypothesis presented for myCAFs activation requires additional experiments, these results suggest myCAFs as a potential biomarker of metastasis formation in well-differentiated tumors.

5.1.5 Models to study CAFs function

CAFs population can assume tumor-promoting and tumor-restraining functions (Huang *et al.*, 2022; Ozdemir *et al.*, 2014; Peng *et al.*, 2022; Rhim *et al.*, 2014). Most functional studies reporting CAFs functions were performed in GEMM, with endogenous tumor formation or tumor cell implantation, or CAFs cell lines isolated from tumors or normal pancreas (Elyada *et al.*, 2019; Huang *et al.*, 2022; Krishnamurty *et al.*, 2022; Ozdemir *et al.*, 2014). However, the models available until now present some challenges.

On the one hand, modeling CAFs using naïve pan-fibroblasts allowed the determination of the mechanisms responsible for the dichotomous relationship between iCAFs and myCAFs (Biffi *et al.*, 2019). Adding specific cues to fibroblasts cultured in 3D matrigel domes differentiated cells toward a myCAF or an iCAFs phenotype (Biffi *et al.*, 2019). However, the 2D *in vitro* culture of naïve pan-fibroblasts and CAFs phenotypes isolated from tumors did not maintain the initial phenotypic profile, suggesting that the control of specific cues is necessary to avoid the shift toward a myCAF activation (Elyada *et al.*, 2019). Although work has been published on what drives CAFs activation in PDAC tumors, there are no good models to study CAFs function *in vitro*, and there is no published work on

CAFs phenotype locking *in vitro*. To determine which factor needs to be addressed to model the continuum of phenotypes seen in endogenous PDAC, a pan-fibroblasts cell line containing an inducible *Tgfb1* overexpression construct was generated. The cell lines were treated with 4-hydroxy-tamoxifen and its vehicle, ethanol, to originate paired lines with basal *Tgfb1* expression and overexpression of *Tgfb1*. The treatment with IL1α in pan-fibroblast lines with basal *Tgfb1* expression and overexpression of *Tgfb1* corroborated the data from Biffi *et al.*, with TAM pan-fibroblasts lines presenting an increase in myCAFs markers (*Tgfb1*, *Ctgf*, and *Col1a1*). Additionally, the treatment of EtOH pan-fibroblast lines presented an increase in *Il6*. Surprisingly, treating TAM pan-fibroblast lines with IL1α increased *Il6* and *Tgfb1* mRNA levels without increasing *Acta2* and *Ctgf*, suggesting the co-stimulation of IL1α and Tgfb1 may induce a different regulation of Tgfb1 downstream signaling.

To establish *in vitro* models that can model CAFs phenotypes, it is essential to model matrix stiffness and composition to induce CAFs phenotypes. Therefore, to generate locked phenotypes, it is necessary to engineer key pathways genetically. An iCAFs-locked phenotype would need to harbor TGFBRII and FAK knock-out alongside JAK gain-of-function mutation. Moreover, the establishment of iCAFs should be performed in CD105$^-$ pan-fibroblasts. To model myCAFs, besides the overexpression of *Tgfb1*, the additional deletion of IL1R would be necessary. Otherwise, upon the stimulation with IL1α, IL6 myCAFs phenotype will probably occur. To fully develop an IL6 myCAFs phenotype, not only the introduction of Tgfb1 overexpression and a JAK gain-of-function mutation is necessary, but also a stiffer ECM than matrigel should be considered for cell embedding.

Experts in the field view the DRS as an elegant model for CAFs functional studies (Sahai *et al.*, 2020). This sophisticated resource allows the induction of the tumor and further targeting of a stromal CAF promotor (Schonhuber *et al.*, 2014). However, the CAFs targeting efficiency is directly linked with the specificity of the promotor used to express Cre and Cre induction by tamoxifen. Furthermore, other factors, such as additional targeting of other populations or CAFs' representativity, are presented as confounding factors in *in vivo* CAFs functional studies. Few efforts have been made to systematically characterize stromal-cre driver lines and understand the potential biases that *in vivo* strategies might originate. To understand how the DRS system could be used to study CAFs function, multiple stromal-cre driver lines were characterized by immunofluorescence using CAFs, tumor cells, and immune markers. Even though most of the stromal-cre driver lines showcased cross-population targeting in the cohort of lines analyzed, Pdgfra-Cre and Myh11-creER presented the highest potential to target CAFs, namely myCAFs. Nevertheless, future studies using stromal-cre driver lines should investigate CAFs populations' specific markers to unravel promotors or genes that can accurately target CAFs. An example is a strategy by Krishnamurty and colleagues, where they studied TGFBRII importance on myCAF differentiation using a *Dpt*-creER line (Krishnamurty *et al.*, 2022). A cross-tissue characterization of fibroblasts unraveled the potential of using Dpt as a universal fibroblast marker (Buechler *et al.*, 2021). This characterization of the *Dpt*-creER line showed that Cre expression under the Dpt promotor primarily targets fibroblasts with only a vestigial amount of cells expressing EpCAM (Buechler *et al.*, 2021). Similarly, targeted strategies should be adopted to deplete CAFs in *in vivo* models. The Turley laboratory described additionally, after extensive scRNAseq and immunohistochemical characterization, LRRC15 as a specific myCAFs marker, allowing restricted depletion of myCAFs without compromising the additional stromal content (Krishnamurty *et al.*, 2022).

In conclusion, studying the function of CAFs in *in vivo* and *in vitro* requires the establishment of new models. Specific markers need to be discovered to perform depletion or to ablate gene expression in CAFs subpopulations and provide a better Cre-based platform for CAFs *in vivo* manipulation. Even though specific promotor expression is required for restricted CAF genetic targeting, stromal-cre driver lines are valuable in lineage tracing studies. Moreover, *in vitro* models provide a simpler assessment of CAFs functions, possible by the straightforward genetic manipulation of pan-fibroblast lines.

Acknowledgments

I would like to thank Prof. Dr. med. Dieter Saur for accepting me in his laboratory and allowing me to perform my doctoral work. In addition, I would like to thank Dr. Jan Böttcher and Prof. Dr. med. Maximilian Reichert, for the insightful contributions and support.

I would like to acknowledge all the people connected to this work, especially Tânia Santos and Elizabeta Gorbunova.

Additionally, I would like to thank all people that were not directly linked to this work, but contributed with suggestions and support.

Finalmente, gostaria de agradecer à minha familia pelo seu apoio incondicional. E ao Danilo, por tudo.

References

Akhurst RJ and Hata A (2012) Targeting the TGFbeta signalling pathway in disease. *Nat Rev Drug Discov* **11**:790-811.

Alonso-Nocelo M, Ruiz-Canas L, Sancho P, Gorgulu K, Alcala S, Pedrero C, Vallespinos M, Lopez-Gil JC, Ochando M, Garcia-Garcia E, David Trabulo SM, Martinelli P, Sanchez-Tomero P, Sanchez-Palomo C, Gonzalez-Santamaria P, Yuste L, Wormann SM, Kabacaoglu D, Earl J, Martin A, Salvador F, Valle S, Martin-Hijano L, Carrato A, Erkan M, Garcia-Bermejo L, Hermann PC, Algul H, Moreno-Bueno G, Heeschen C, Portillo F, Cano A and Sainz B, Jr. (2022) Macrophages direct cancer cells through a LOXL2-mediated metastatic cascade in pancreatic ductal adenocarcinoma. *Gut*.

American Cancer Society (2022) Cancer Facts & Figures 2022.

Apte MV, Park S, Phillips PAS, N. Goldstein, D., Kumar RK, Ramm GA, Buchler M, Friess H, McCarroll JAK, G., Merrett N, Pirola R and Wilson JS (2004) Desmoplastic reaction in pancreatic cancer: role of pancreatic stellate cells. *Pancreas* **29**:179-187.

Arensman MD, Kovochich AN, Kulikauskas RM, Lay AR, Yang PT, Li X, Donahue T, Major MB, Moon RT, Chien AJ and Dawson DW (2014) WNT7B mediates autocrine Wnt/beta-catenin signaling and anchorage-independent growth in pancreatic adenocarcinoma. *Oncogene* **33**:899-908.

Aung KL, Fischer SE, Denroche RE, Jang GH, Dodd A, Creighton S, Southwood B, Liang SB, Chadwick D, Zhang A, O'Kane GM, Albaba H, Moura S, Grant RC, Miller JK, Mbabaali F, Pasternack D, Lungu IM, Bartlett JMS, Ghai S, Lemire M, Holter S, Connor AA, Moffitt RA, Yeh JJ, Timms L, Krzyzanowski PM, Dhani N, Hedley D, Notta F, Wilson JM, Moore MJ, Gallinger S and Knox JJ (2018) Genomics-Driven Precision Medicine for Advanced Pancreatic Cancer: Early Results from the COMPASS Trial. *Clin Cancer Res* **24**:1344-1354.

Avgustinova A, Iravani M, Robertson D, Fearns A, Gao Q, Klingbeil P, Hanby AM, Speirs V, Sahai E, Calvo F and Isacke CM (2016) Tumour cell-derived Wnt7a recruits and activates fibroblasts to promote tumour aggressiveness. *Nat Commun* **7**:10305.

Awad MM, Liu S, Rybkin, II, Arbour KC, Dilly J, Zhu VW, Johnson ML, Heist RS, Patil T, Riely GJ, Jacobson JO, Yang X, Persky NS, Root DE, Lowder KE, Feng H, Zhang SS, Haigis KM, Hung YP, Sholl LM, Wolpin BM, Wiese J, Christiansen J, Lee J, Schrock AB, Lim LP, Garg K, Li M, Engstrom LD, Waters L, Lawson JD, Olson P, Lito P, Ou SI, Christensen JG, Janne PA and

Aguirre AJ (2021) Acquired Resistance to KRAS(G12C) Inhibition in Cancer. *N Engl J Med* **384**:2382-2393.

Bailey P, Chang DK, Nones K, Johns AL, Patch AM, Gingras MC, Miller DK, Christ AN, Bruxner TJ, Quinn MC, Nourse C, Murtaugh LC, Harliwong I, Idrisoglu S, Manning S, Nourbakhsh E, Wani S, Fink L, Holmes O, Chin V, Anderson MJ, Kazakoff S, Leonard C, Newell F, Waddell N, Wood S, Xu Q, Wilson PJ, Cloonan N, Kassahn KS, Taylor D, Quek K, Robertson A, Pantano L, Mincarelli L, Sanchez LN, Evers L, Wu J, Pinese M, Cowley MJ, Jones MD, Colvin EK, Nagrial AM, Humphrey ES, Chantrill LA, Mawson A, Humphris J, Chou A, Pajic M, Scarlett CJ, Pinho AV, Giry-Laterriere M, Rooman I, Samra JS, Kench JG, Lovell JA, Merrett ND, Toon CW, Epari K, Nguyen NQ, Barbour A, Zeps N, Moran-Jones K, Jamieson NB, Graham JS, Duthie F, Oien K, Hair J, Grutzmann R, Maitra A, Iacobuzio-Donahue CA, Wolfgang CL, Morgan RA, Lawlor RT, Corbo V, Bassi C, Rusev B, Capelli P, Salvia R, Tortora G, Mukhopadhyay D, Petersen GM, Australian Pancreatic Cancer Genome I, Munzy DM, Fisher WE, Karim SA, Eshleman JR, Hruban RH, Pilarsky C, Morton JP, Sansom OJ, Scarpa A, Musgrove EA, Bailey UM, Hofmann O, Sutherland RL, Wheeler DA, Gill AJ, Gibbs RA, Pearson JV, Waddell N, Biankin AV and Grimmond SM (2016) Genomic analyses identify molecular subtypes of pancreatic cancer. *Nature* **531**:47-52.

Bankhead P, Loughrey MB, Fernandez JA, Dombrowski Y, McArt DG, Dunne PD, McQuaid S, Gray RT, Murray LJ, Coleman HG, James JA, Salto-Tellez M and Hamilton PW (2017) QuPath: Open source software for digital pathology image analysis. *Sci Rep* **7**:16878.

Barkley D, Moncada R, Pour M, Liberman DA, Dryg I, Werba G, Wang W, Baron M, Rao A, Xia B, Franca GS, Weil A, Delair DF, Hajdu C, Lund AW, Osman I and Yanai I (2022) Cancer cell states recur across tumor types and form specific interactions with the tumor microenvironment. *Nat Genet* **54**:1192-1201.

Baslan T, Morris JPt, Zhao Z, Reyes J, Ho YJ, Tsanov KM, Bermeo J, Tian S, Zhang S, Askan G, Yavas A, Lecomte N, Erakky A, Varghese AM, Zhang A, Kendall J, Ghiban E, Chorbadjiev L, Wu J, Dimitrova N, Chadalavada K, Nanjangud GJ, Bandlamudi C, Gong Y, Donoghue MTA, Socci ND, Krasnitz A, Notta F, Leach SD, Iacobuzio-Donahue CA and Lowe SW (2022) Ordered and deterministic cancer genome evolution after p53 loss. *Nature* **608**:795-802.

Biffi G, Oni TE, Spielman B, Hao Y, Elyada E, Park Y, Preall J and Tuveson DA (2019) IL1-Induced JAK/STAT Signaling Is Antagonized by TGFbeta to Shape CAF Heterogeneity in Pancreatic Ductal Adenocarcinoma. *Cancer Discov* **9**:282-301.

Black S, Phillips D, Hickey JW, Kennedy-Darling J, Venkataraaman VG, Samusik N, Goltsev Y, Schurch CM and Nolan GP (2021) CODEX multiplexed tissue imaging with DNA-conjugated antibodies. *Nat Protoc* **16**:3802-3835.

Bodenmiller B (2016) Multiplexed Epitope-Based Tissue Imaging for Discovery and Healthcare Applications. *Cell Syst* **2**:225-238.

Bradford MM (1976) A rapid and sensitive method for the quantification of microgram quantities of protein utilizing the principle of protein-dye binding. *Analytical biochemistry*:248-254.

Buechler MB, Pradhan RN, Krishnamurty AT, Cox C, Calviello AK, Wang AW, Yang YA, Tam L, Caothien R, Roose-Girma M, Modrusan Z, Arron JR, Bourgon R, Muller S and Turley SJ (2021) Cross-tissue organization of the fibroblast lineage. *Nature* **593**:575-579.

Candido JB, Morton JP, Bailey P, Campbell AD, Karim SA, Jamieson T, Lapienyte L, Gopinathan A, Clark W, McGhee EJ, Wang J, Escorcio-Correia M, Zollinger R, Roshani R, Drew L, Rishi L, Arkell R, Evans TRJ, Nixon C, Jodrell DI, Wilkinson RW, Biankin AV, Barry ST, Balkwill FR and Sansom OJ (2018) CSF1R(+) Macrophages Sustain Pancreatic Tumor Growth through T Cell Suppression and Maintenance of Key Gene Programs that Define the Squamous Subtype. *Cell Rep* **23**:1448-1460.

Chakravarthy A, Khan L, Bensler NP, Bose P and De Carvalho DD (2018) TGF-beta-associated extracellular matrix genes link cancer-associated fibroblasts to immune evasion and immunotherapy failure. *Nat Commun* **9**:4692.

Chan-Seng-Yue M, Kim JC, Wilson GW, Ng K, Figueroa EF, O'Kane GM, Connor AA, Denroche RE, Grant RC, McLeod J, Wilson JM, Jang GH, Zhang A, Dodd A, Liang SB, Borgida A, Chadwick D, Kalimuthu S, Lungu I, Bartlett JMS, Krzyzanowski PM, Sandhu V, Tiriac H, Froeling FEM, Karasinska JM, Topham JT, Renouf DJ, Schaeffer DF, Jones SJM, Marra MA, Laskin J, Chetty R, Stein LD, Zogopoulos G, Haibe-Kains B, Campbell PJ, Tuveson DA, Knox JJ, Fischer SE, Gallinger S and Notta F (2020) Transcription phenotypes of pancreatic cancer are driven by genomic events during tumor evolution. *Nat Genet* **52**:231-240.

Chang DK, Grimmond SM, Evans TRJ and Biankin AV (2014) Mining the genomes of exceptional responders. *Nature Reviews Cancer* **14**:291-292.

Chao T, Furth EE and Vonderheide RH (2016) CXCR2-Dependent Accumulation of Tumor-Associated Neutrophils Regulates T-cell Immunity in Pancreatic Ductal Adenocarcinoma. *Cancer Immunol Res* **4**:968-982.

Chen Y, Kim J, Yang S, Wang H, Wu CJ, Sugimoto H, LeBleu VS and Kalluri R (2021) Type I collagen deletion in alphaSMA(+) myofibroblasts augments immune suppression and accelerates progression of pancreatic cancer. *Cancer Cell* **39**:548-565 e546.

Clark CE, Hingorani SR, Mick R, Combs C, Tuveson DA and Vonderheide RH (2007) Dynamics of the immune reaction to pancreatic cancer from inception to invasion. *Cancer Res* **67**:9518-9527.

Colle R, Radzik A, Cohen R, Pellat A, Lopez-Tabada D, Cachanado M, Duval A, Svrcek M, Menu Y and Andre T (2021) Pseudoprogression in patients treated with immune checkpoint inhibitors for microsatellite instability-high/mismatch repair-deficient metastatic colorectal cancer. *Eur J Cancer* **144**:9-16.

Collisson EA, Bailey P, Chang DK and Biankin AV (2019) Molecular subtypes of pancreatic cancer. *Nat Rev Gastroenterol Hepatol* **16**:207-220.

Collisson EA, Sadanandam A, Olson P, Gibb WJ, Truitt M, Gu S, Cooc J, Weinkle J, Kim GE, Jakkula L, Feiler HS, Ko AH, Olshen AB, Danenberg KL, Tempero MA, Spellman PT, Hanahan D and Gray JW (2011) Subtypes of pancreatic ductal adenocarcinoma and their differing responses to therapy. *Nat Med* **17**:500-503.

Connor AA, Denroche RE, Jang GH, Timms L, Kalimuthu SN, Selander I, McPherson T, Wilson GW, Chan-Seng-Yue MA, Borozan I, Ferretti V, Grant RC, Lungu IM, Costello E, Greenhalf W, Palmer D, Ghaneh P, Neoptolemos JP, Buchler M, Petersen G, Thayer S, Hollingsworth MA, Sherker A, Durocher D, Dhani N, Hedley D, Serra S, Pollett A, Roehrl MHA, Bavi P, Bartlett JMS, Cleary S, Wilson JM, Alexandrov LB, Moore M, Wouters BG, McPherson JD, Notta F, Stein LD and Gallinger S (2017) Association of Distinct Mutational Signatures With Correlates of Increased Immune Activity in Pancreatic Ductal Adenocarcinoma. *JAMA Oncol* **3**:774-783.

Connor AA and Gallinger S (2022) Pancreatic cancer evolution and heterogeneity: integrating omics and clinical data. *Nat Rev Cancer* **22**:131-142.

Cox TR, Bird D, Baker AM, Barker HE, Ho MW, Lang G and Erler JT (2013) LOX-mediated collagen crosslinking is responsible for fibrosis-enhanced metastasis. *Cancer Res* **73**:1721-1732.

Dal Molin M, Zhang M, de Wilde RF, Ottenhof NA, Rezaee N, Wolfgang CL, Blackford A, Vogelstein B, Kinzler KW, Papadopoulos N, Hruban RH, Maitra A and Wood LD (2015) Very Long-term Survival Following Resection for Pancreatic Cancer Is Not Explained by Commonly Mutated Genes: Results of Whole-Exome Sequencing Analysis. *Clin Cancer Res* **21**:1944-1950.

Danilova L, Ho WJ, Zhu Q, Vithayathil T, De Jesus-Acosta A, Azad NS, Laheru DA, Fertig EJ, Anders R, Jaffee EM and Yarchoan M (2019) Programmed Cell Death Ligand-1 (PD-L1) and CD8 Expression Profiling Identify an Immunologic Subtype of Pancreatic Ductal Adenocarcinomas with Favorable Survival. *Cancer Immunol Res* **7**:886-895.

Deng M, Lin J, Nowsheen S, Liu TZ, Yingchun , Villalta PWS, Delphine Tschumperlin, Daniel J. , Lee S, Kim J and Lou Z (2020) Extracellular matrix stiffness determines DNA repair efficiency and cellular sensitivity to genotoxic agents. *Science Advances* **6**.

Desmoulière A, Geinoz A, Gabbiani F and Gabbiani G (1993) Transforming growth factor-beta 1 induces alpha-smooth muscle actin expression in granulation tissue myofibroblasts and in quiescent and growing cultured fibroblasts *J Cell Biol* **122**:103-111.

Discher DE, Janmey P and Wang Y-I (2005) Tissue Cells Feel and Respond to the Stiffness of Their Substrate. *Science* **310**:1139-1143.

Dominguez CX, Muller S, Keerthivasan S, Koeppen H, Hung J, Gierke S, Breart B, Foreman O, Bainbridge TW, Castiglioni A, Senbabaoglu Y, Modrusan Z, Liang Y, Junttila MR, Klijn C, Bourgon R and Turley SJ (2020) Single-Cell RNA Sequencing Reveals Stromal Evolution into LRRC15(+) Myofibroblasts as a Determinant of Patient Response to Cancer Immunotherapy. *Cancer Discov* **10**:232-253.

Ducreux M, Cuhna AS, Caramella C, Hollebecque A, Burtin P, Goere D, Seufferlein T, Haustermans K, Van Laethem JL, Conroy T, Arnold D and Committee EG (2015) Cancer of the pancreas: ESMO Clinical Practice Guidelines for diagnosis, treatment and follow-up. *Ann Oncol* **26 Suppl 5**:v56-68.

Elyada E, Bolisetty M, Laise P, Flynn WF, Courtois ET, Burkhart RA, Teinor JA, Belleau P, Biffi G, Lucito MS, Sivajothi S, Armstrong TD, Engle DD, Yu KH, Hao Y, Wolfgang CL, Park Y, Preall J, Jaffee EM, Califano A, Robson P and Tuveson DA (2019) Cross-Species Single-Cell Analysis of Pancreatic Ductal Adenocarcinoma Reveals Antigen-Presenting Cancer-Associated Fibroblasts. *Cancer Discov* **9**:1102-1123.

Eser S, Reiff N, Messer M, Seidler B, Gottschalk K, Dobler M, Hieber M, Arbeiter A, Klein S, Kong B, Michalski CW, Schlitter AM, Esposito I, Kind AJ, Rad L, Schnieke AE, Baccarini M, Alessi DR, Rad R, Schmid RM, Schneider G and Saur D (2013) Selective requirement of PI3K/PDK1 signaling for Kras oncogene-driven pancreatic cell plasticity and cancer. *Cancer Cell* **23**:406-420.

Feldmann K, Maurer C, Peschke K, Teller S, Schuck K, Steiger K, Engleitner T, Ollinger R, Nomura A, Wirges N, Papargyriou A, Jahan Sarker RS, Ranjan RA, Dantes Z, Weichert W, Rustgi AK, Schmid RM, Rad R, Schneider G, Saur D and Reichert M (2021) Mesenchymal Plasticity Regulated by Prrx1 Drives Aggressive Pancreatic Cancer Biology. *Gastroenterology* **160**:346-361 e324.

Ferlay J EM, Lam F, Colombet M, Mery L, Piñeros M, Znaor A, Soerjomataram I, Bray F (2020a) Global Cancer Observatory: Cancer Today, International Agency for Research on Cancer, Lyon, France.

Ferlay J LM, Ervik M, Lam F, Colombet M, Mery L, Piñeros M, Znaor A, Soerjomataram I, Bray F (2020b) Global Cancer Observatory: Cancer Tomorrow, International Agency for Research on Cancer, Lyon, France.

Foster DS, Januszyk M, Delitto D, Yost KE, Griffin M, Guo J, Guardino N, Delitto AE, Chinta M, Burcham AR, Nguyen AT, Bauer-Rowe KE, Titan AL, Salhotra A, Jones RE, da Silva O, Lindsay HG, Berry CE, Chen K, Henn D, Mascharak S, Talbott HE, Kim A, Nosrati F, Sivaraj D, Ransom RC, Matthews M, Khan A, Wagh D, Coller J, Gurtner GC, Wan DC, Wapnir IL, Chang HY, Norton JA and Longaker MT (2022) Multiomic analysis reveals conservation of cancer-associated fibroblast phenotypes across species and tissue of origin. *Cancer Cell*.

Franco-Barraza J, Francescone R, Luong T, Shah N, Madhani R, Cukierman G, Dulaimi E, Devarajan K, Egleston BL, Nicolas E, Katherine Alpaugh R, Malik R, Uzzo RG, Hoffman JP, Golemis EA and Cukierman E (2017) Matrix-regulated integrin alpha(v)beta(5) maintains alpha(5)beta(1)-dependent desmoplastic traits prognostic of neoplastic recurrence. *Elife* **6**.

Friedman G, Levi-Galibov O, David E, Bornstein C, Giladi A, Dadiani M, Mayo A, Halperin C, Pevsner-Fischer M, Lavon H, Mayer S, Nevo R, Stein Y, Balint-Lahat N, Barshack I, Ali HR, Caldas C, Nili-Gal-Yam E, Alon U, Amit I and Scherz-Shouval R (2020) Cancer-associated fibroblast compositions change with breast cancer progression linking the ratio of S100A4(+) and PDPN(+) CAFs to clinical outcome. *Nat Cancer* **1**:692-708.

Gabbiani G, Hirschel BJ, Ryan GB, Statkov PR and Majno G (1972) Granulation tissue as a contractile organ. A study of structure and function. *J Exp Med* **135**:719-734.

Geller LT, Barzily-Rokni M, Danino T, Jonas OH, Shental N, Nejman D, Gavert N, Zwang Y, Cooper ZA, Shee K, Thaiss CA, Reuben A, Livny J, Avraham R, Frederick DL, M., Chatman KJ, S.E. Mosher, C.M. Brandis, A., Fuks G, Gurbatri CG, V. Kim, M., Hurd MW, Katz M, Fleming J, Maitra A, Smith DA, Skalak M, Bu J, Michaud MT, S.A. Barshack, I., Golan T, Sandbank JF, K.T. Mandinova, A. Garrett, W.S., Thayer SP, Ferrone CRH, C. Bhatia, S.N., Gevers D, Wargo JA and Golub TRS, R. (2017) Potential role of intratumor bacteria in mediating tumor resistance to the chemotherapeutic drug gemcitabine. *Science* **357**:1156-1160.

Grau-Bove X, Ruiz-Trillo I and Rodriguez-Pascual F (2015) Origin and evolution of lysyl oxidases. *Sci Rep* **5**:10568.

Grauel AL, Nguyen B, Ruddy D, Laszewski T, Schwartz S, Chang J, Chen J, Piquet M, Pelletier M, Yan Z, Kirkpatrick ND, Wu J, deWeck A, Riester M, Hims M, Geyer FC, Wagner J, MacIsaac K, Deeds J, Diwanji R, Jayaraman P, Yu Y, Simmons Q, Weng S, Raza A, Minie B, Dostalek M, Chikkegowda P, Ruda V, Iartchouk O, Chen N, Thierry R, Zhou J, Pruteanu-Malinici I, Fabre C, Engelman JA, Dranoff G and Cremasco V (2020) TGFbeta-blockade uncovers stromal plasticity in tumors by revealing the existence of a subset of interferon-licensed fibroblasts. *Nat Commun* **11**:6315.

Grunwald BT, Devisme A, Andrieux G, Vyas F, Aliar K, McCloskey CW, Macklin A, Jang GH, Denroche R, Romero JM, Bavi P, Bronsert P, Notta F, O'Kane G, Wilson J, Knox J, Tamblyn L, Udaskin M, Radulovich N, Fischer SE, Boerries M, Gallinger S, Kislinger T and Khokha R (2021) Spatially confined sub-tumor microenvironments in pancreatic cancer. *Cell* **184**:5577-5592 e5518.

Haeberle L and Esposito I (2019) Pathology of pancreatic cancer. *Transl Gastroenterol Hepatol* **4**:50.

Hallin J, Bowcut V, Calinisan A, Briere DM, Hargis L, Engstrom LD, Laguer J, Medwid J, Vanderpool D, Lifset E, Trinh D, Hoffman N, Wang X, David Lawson J, Gunn RJ, Smith CR, Thomas NC, Martinson M, Bergstrom A, Sullivan F, Bouhana K, Winski S, He L, Fernandez-Banet J, Pavlicek A, Haling JR, Rahbaek L, Marx MA, Olson P and Christensen JG (2022) Anti-tumor efficacy of a potent and selective non-covalent KRAS(G12D) inhibitor. *Nat Med* **28**:2171-2182.

Hartwig W, Hackert T, Hinz U, Gluth A, Bergmann F, Strobel O, Buchler MW and Werner J (2011) Pancreatic cancer surgery in the new millennium: better prediction of outcome. *Ann Surg* **254**:311-319.

Hegde S, Krisnawan VE, Herzog BH, Zuo C, Breden MA, Knolhoff BL, Hogg GD, Tang JP, Baer JM, Mpoy C, Lee KB, Alexander KA, Rogers BE, Murphy KM, Hawkins WG, Fields RC, DeSelm CJ, Schwarz JK and DeNardo DG (2020) Dendritic Cell Paucity Leads to Dysfunctional Immune Surveillance in Pancreatic Cancer. *Cancer Cell* **37**:289-307 e289.

Heger U, Martens A, Schillings L, Walter B, Hartmann D, Hinz U, Pausch T, Giese N, Michalski CW and Hackert T (2022) Myofibroblastic CAF Density, Not Activated Stroma Index, Indicates Prognosis after Neoadjuvant Therapy of Pancreatic Carcinoma. *Cancers (Basel)* **14**.

Herchenhan A, Uhlenbrock F, Eliasson P, Weis M, Eyre D, Kadler KE, Magnusson SP and Kjaer M (2015) Lysyl Oxidase Activity Is Required for Ordered Collagen Fibrillogenesis by Tendon Cells. *J Biol Chem* **290**:16440-16450.

Hingorani SR, Wang L, Multani AS, Combs C, Deramaudt TB, Hruban RH, Rustgi AK, Chang S and Tuveson DA (2005) Trp53R172H and KrasG12D cooperate to promote chromosomal instability and widely metastatic pancreatic ductal adenocarcinoma in mice. *Cancer Cell* **7**:469-483.

Hong DS, Fakih MG, Strickler JH, Desai J, Durm GA, Shapiro GI, Falchook GS, Price TJ, Sacher A, Denlinger CS, Bang YJ, Dy GK, Krauss JC, Kuboki Y, Kuo JC, Coveler AL, Park K, Kim TW, Barlesi F, Munster PN, Ramalingam SS, Burns TF, Meric-Bernstam F, Henary H, Ngang J, Ngarmchamnanrith G, Kim J, Houk BE, Canon J, Lipford JR, Friberg G, Lito P, Govindan R and

Li BT (2020) KRAS(G12C) Inhibition with Sotorasib in Advanced Solid Tumors. *N Engl J Med* **383**:1207-1217.

Hoxhaj G and Manning BD (2020) The PI3K-AKT network at the interface of oncogenic signalling and cancer metabolism. *Nat Rev Cancer* **20**:74-88.

Hu B, Wu C, Mao H, Gu H, Dong H, Yan J, Qi Z, Yuan L, Dong Q and Long J (2022) Subpopulations of cancer-associated fibroblasts link the prognosis and metabolic features of pancreatic ductal adenocarcinoma. *Ann Transl Med* **10**:262.

Huang H, Wang Z, Zhang Y, Pradhan RN, Ganguly D, Chandra R, Murimwa G, Wright S, Gu X, Maddipati R, Muller S, Turley SJ and Brekken RA (2022) Mesothelial cell-derived antigen-presenting cancer-associated fibroblasts induce expansion of regulatory T cells in pancreatic cancer. *Cancer Cell* **40**:656-673 e657.

Huang X, Yang N, Fiore VF, Barker TH, Sun Y, Morris SW, Ding Q, Thannickal VJ and Zhou Y (2012) Matrix stiffness-induced myofibroblast differentiation is mediated by intrinsic mechanotransduction. *Am J Respir Cell Mol Biol* **47**:340-348.

Hutton C, Heider F, Blanco-Gomez A, Banyard A, Kononov A, Zhang X, Karim S, Paulus-Hock V, Watt D, Steele N, Kemp S, Hogg EKJ, Kelly J, Jackstadt RF, Lopes F, Menotti M, Chisholm L, Lamarca A, Valle J, Sansom OJ, Springer C, Malliri A, Marais R, Pasca di Magliano M, Zelenay S, Morton JP and Jorgensen C (2021) Single-cell analysis defines a pancreatic fibroblast lineage that supports anti-tumor immunity. *Cancer Cell* **39**:1227-1244 e1220.

Ino Y, Yamazaki-Itoh R, Shimada K, Iwasaki M, Kosuge T, Kanai Y and Hiraoka N (2013) Immune cell infiltration as an indicator of the immune microenvironment of pancreatic cancer. *Br J Cancer* **108**:914-923.

Jiang H, Torphy RJ, Steiger K, Hongo H, Ritchie AJ, Kriegsmann M, Horst D, Umetsu SE, Joseph NM, McGregor K, Pishvaian MJ, Blais EM, Lu B, Li M, Hollingsworth M, Stashko C, Volmar K, Yeh JJ, Weaver VM, Wang ZJ, Tempero MA, Weichert W and Collisson EA (2020) Pancreatic ductal adenocarcinoma progression is restrained by stromal matrix. *J Clin Invest* **130**:4704-4709.

Jiang X, Hao HX, Growney JD, Woolfenden S, Bottiglio C, Ng N, Lu B, Hsieh MH, Bagdasarian L, Meyer R, Smith TR, Avello M, Charlat O, Xie Y, Porter JA, Pan S, Liu J, McLaughlin ME and Cong F (2013) Inactivating mutations of RNF43 confer Wnt dependency in pancreatic ductal adenocarcinoma. *Proc Natl Acad Sci U S A* **110**:12649-12654.

Kalimuthu SN, Wilson GW, Grant RC, Seto M, O'Kane G, Vajpeyi R, Notta F, Gallinger S and Chetty R (2020) Morphological classification of pancreatic ductal adenocarcinoma that predicts molecular subtypes and correlates with clinical outcome. *Gut* **69**:317-328.

Kane LP, Shapiro VS, Stokoe D and Weiss A (1999) Induction of NF-κB by the Akt/PKB kinase. *Current biology* **9**.

Kastenhuber ER and Lowe SW (2017) Putting p53 in Context. *Cell* **170**:1062-1078.

Kaur S, Sassano A, Joseph AMM-K, B., Eklund EA, Verma AB, S.M., Fish EN and Platanias LC (2008) Dual regulatory roles of phosphatidylinositol 3-kinase in IFN signaling. *J Immunol* **181**:7316-7323.

Kieffer Y, Hocine HR, Gentric G, Pelon F, Bernard C, Bourachot B, Lameiras S, Albergante L, Bonneau C, Guyard A, Tarte K, Zinovyev A, Baulande S, Zalcman G, Vincent-Salomon A and Mechta-Grigoriou F (2020) Single-Cell Analysis Reveals Fibroblast Clusters Linked to Immunotherapy Resistance in Cancer. *Cancer Discov* **10**:1330-1351.

Kim MP, Li X, Deng J, Zhang Y, Dai B, Allton KL, Hughes TG, Siangco C, Augustine JJ, Kang Y, McDaniel JM, Xiong S, Koay EJ, McAllister F, Bristow CA, Heffernan TP, Maitra A, Liu B, Barton MC, Wasylishen AR, Fleming JB and Lozano G (2021) Oncogenic KRAS Recruits an Expansive Transcriptional Network through Mutant p53 to Drive Pancreatic Cancer Metastasis. *Cancer Discov* **11**:2094-2111.

Klein AP (2021) Pancreatic cancer epidemiology: understanding the role of lifestyle and inherited risk factors. *Nature Reviews Gastroenterology & Hepatology* **18**:493-502.

Knudsen ES, Vail P, Balaji U, Ngo H, Botros IW, Makarov V, Riaz N, Balachandran V, Leach S, Thompson DM, Chan TA and Witkiewicz AK (2017) Stratification of Pancreatic Ductal Adenocarcinoma: Combinatorial Genetic, Stromal, and Immunologic Markers. *Clin Cancer Res* **23**:4429-4440.

Krishnamurty AT, Shyer JA, Thai M, Gandham V, Buechler MB, Yang YA, Pradhan RN, Wang AW, Sanchez PL, Qu Y, Breart B, Chalouni C, Dunlap D, Ziai J, Elstrott J, Zacharias N, Mao W, Rowntree RK, Sadowsky J, Lewis GD, Pillow TH, Nabet BY, Banchereau R, Tam L, Caothien R, Bacarro N, Roose-Girma M, Modrusan Z, Mariathasan S, Muller S and Turley SJ (2022) LRRC15(+) myofibroblasts dictate the stromal setpoint to suppress tumour immunity. *Nature*.

Kwan AK, Piazza GA, Keeton AB and Leite CA (2022) The path to the clinic: a comprehensive review on direct KRAS(G12C) inhibitors. *J Exp Clin Cancer Res* **41**:27.

Laemmli U (1970) Cleavage of Structural Proteins during the Assembly of the Head of Bacteriophage T4. *Nature*:680-685.

Laklai H, Miroshnikova YA, Pickup MW, Collisson EA, Kim GE, Barrett AS, Hill RC, Lakins JN, Schlaepfer DD, Mouw JK, LeBleu VS, Roy N, Novitskiy SV, Johansen JS, Poli V, Kalluri R, Iacobuzio-Donahue CA, Wood LD, Hebrok M, Hansen K, Moses HL and Weaver VM (2016)

Genotype tunes pancreatic ductal adenocarcinoma tissue tension to induce matricellular fibrosis and tumor progression. *Nat Med* **22**:497-505.

Launonen IM, Lyytikainen N, Casado J, Anttila EA, Szabo A, Haltia UM, Jacobson CA, Lin JR, Maliga Z, Howitt BE, Strickland KC, Santagata S, Elias K, D'Andrea AD, Konstantinopoulos PA, Sorger PK and Farkkila A (2022) Single-cell tumor-immune microenvironment of BRCA1/2 mutated high-grade serous ovarian cancer. *Nat Commun* **13**:835.

Lee CL, Moding EJ, Huang X, Li Y, Woodlief LZ, Rodrigues RC, Ma Y and Kirsch DG (2012) Generation of primary tumors with Flp recombinase in FRT-flanked p53 mice. *Dis Model Mech* **5**:397-402.

Livak KJ and Schmittgen TD (2001) Analysis of relative gene expression data using real-time quantitative PCR and the 2(-Delta Delta C(T)) Method. *Methods* **25**:402-408.

Love MI, Huber W and Anders S (2014) Moderated estimation of fold change and dispersion for RNA-seq data with DESeq2. *Genome Biol* **15**:550.

Luchini C, Brosens LAA, Wood LD, Chatterjee D, Shin JI, Sciammarella C, Fiadone G, Malleo G, Salvia R, Kryklyva V, Piredda ML, Cheng L, Lawlor RT, Adsay V and Scarpa A (2021) Comprehensive characterisation of pancreatic ductal adenocarcinoma with microsatellite instability: histology, molecular pathology and clinical implications. *Gut* **70**:148-156.

Lun AT, Bach K and Marioni JC (2016) Pooling across cells to normalize single-cell RNA sequencing data with many zero counts. *Genome Biol* **17**:75.

Maddipati R, Norgard RJ, Baslan T, Rathi KS, Zhang A, Saeid A, Higashihara T, Wu F, Kumar A, Annamalai V, Bhattacharya S, Raman P, Adkisson CA, Pitarresi JR, Wengyn MD, Yamazoe T, Li J, Balli D, LaRiviere MJ, Ngo TC, Folkert IW, Millstein ID, Bermeo J, Carpenter EL, McAuliffe JC, Oktay MH, Brekken RA, Lowe SW, Iacobuzio-Donahue CA, Notta F and Stanger BZ (2022) MYC Levels Regulate Metastatic Heterogeneity in Pancreatic Adenocarcinoma. *Cancer Discov* **12**:542-561.

Majno G and Gabbiani GH, B.J. Statkov, P.R. (1971) Contraction of Granulation Tissue in vitro: Similarity to Smooth Muscle. *Science* **173**:548-550.

McIntyre CA, Lawrence SA, Richards AL, Chou JF, Wong W, Capanu M, Berger MF, Donoghue MTA, Yu KH, Varghese AM, Kelsen DP, Park W, Balachandran VP, Kingham TP, D'Angelica MI, Drebin JA, Jarnagin WR, Iacobuzio-Donahue CA, Allen PJ and O'Reilly EM (2020) Alterations in driver genes are predictive of survival in patients with resected pancreatic ductal adenocarcinoma. *Cancer* **126**:3939-3949.

Mercatelli D, Ray F and Giorgi FM (2019) Pan-Cancer and Single-Cell Modeling of Genomic Alterations Through Gene Expression. *Front Genet* **10**:671.

Moffitt RA, Marayati R, Flate EL, Volmar KE, Loeza SG, Hoadley KA, Rashid NU, Williams LA, Eaton SC, Chung AH, Smyla JK, Anderson JM, Kim HJ, Bentrem DJ, Talamonti MS, Iacobuzio-Donahue CA, Hollingsworth MA and Yeh JJ (2015) Virtual microdissection identifies distinct tumor- and stroma-specific subtypes of pancreatic ductal adenocarcinoma. *Nat Genet* **47**:1168-1178.

Mootha V, Lindgren C, Eriksson K and al. e (2003) PGC-1α-responsive genes involved in oxidative phosphorylation are coordinately downregulated in human diabetes. *Nature genetics*.

Morton JP, Timpson P, Karim SA, Ridgway RA, Athineos D, Doyle B, Jamieson NB, Oien KA, Lowy AM, Brunton VG, Frame MC, Evans TR and Sansom OJ (2010) Mutant p53 drives metastasis and overcomes growth arrest/senescence in pancreatic cancer. *Proc Natl Acad Sci U S A* **107**:246-251.

Mosa MH, Michels BE, Menche C, Nicolas AM, Darvishi T, Greten FR and Farin HF (2020) A Wnt-Induced Phenotypic Switch in Cancer-Associated Fibroblasts Inhibits EMT in Colorectal Cancer. *Cancer Res* **80**:5569-5582.

Mueller S, Engleitner T, Maresch R, Zukowska M, Lange S, Kaltenbacher T, Konukiewitz B, Ollinger R, Zwiebel M, Strong A, Yen HY, Banerjee R, Louzada S, Fu B, Seidler B, Gotzfried J, Schuck K, Hassan Z, Arbeiter A, Schonhuber N, Klein S, Veltkamp C, Friedrich M, Rad L, Barenboim M, Ziegenhain C, Hess J, Dovey OM, Eser S, Parekh S, Constantino-Casas F, de la Rosa J, Sierra MI, Fraga M, Mayerle J, Kloppel G, Cadinanos J, Liu P, Vassiliou G, Weichert W, Steiger K, Enard W, Schmid RM, Yang F, Unger K, Schneider G, Varela I, Bradley A, Saur D and Rad R (2018) Evolutionary routes and KRAS dosage define pancreatic cancer phenotypes. *Nature* **554**:62-68.

Muzumdar MD, Tasic B, Miyamichi K, Li L and Luo L (2007) A global double-fluorescent Cre reporter mouse. *Genesis* **45**:593-605.

Naba A, Clauser KR, Ding H, Whittaker CA, Carr SA and Hynes RO (2016) The extracellular matrix: Tools and insights for the "omics" era. *Matrix Biol* **49**:10-24.

Nakayama M, Hong CP, Oshima H, Sakai E, Kim SJ and Oshima M (2020) Loss of wild-type p53 promotes mutant p53-driven metastasis through acquisition of survival and tumor-initiating properties. *Nat Commun* **11**:2333.

Neftel C, Laffy J, Filbin MG, Hara T, Shore ME, Rahme GJ, Richman AR, Silverbush D, Shaw ML, Hebert CM, Dewitt J, Gritsch S, Perez EM, Gonzalez Castro LN, Lan X, Druck N, Rodman C, Dionne D, Kaplan A, Bertalan MS, Small J, Pelton K, Becker S, Bonal D, Nguyen QD, Servis RL, Fung JM, Mylvaganam R, Mayr L, Gojo J, Haberler C, Geyeregger R, Czech T, Slavc I, Nahed BV, Curry WT, Carter BS, Wakimoto H, Brastianos PK, Batchelor TT, Stemmer-

Rachamimov A, Martinez-Lage M, Frosch MP, Stamenkovic I, Riggi N, Rheinbay E, Monje M, Rozenblatt-Rosen O, Cahill DP, Patel AP, Hunter T, Verma IM, Ligon KL, Louis DN, Regev A, Bernstein BE, Tirosh I and Suva ML (2019) An Integrative Model of Cellular States, Plasticity, and Genetics for Glioblastoma. *Cell* **178**:835-849 e821.

Neoptolemos JP, Kleeff J, Michl P, Costello E, Greenhalf W and Palmer DH (2018) Therapeutic developments in pancreatic cancer: current and future perspectives. *Nat Rev Gastroenterol Hepatol* **15**:333-348.

Nicolas-Boluda A, Vaquero J, Vimeux L, Guilbert T, Barrin S, Kantari-Mimoun C, Ponzo M, Renault G, Deptula P, Pogoda K, Bucki R, Cascone I, Courty J, Fouassier L, Gazeau F and Donnadieu E (2021) Tumor stiffening reversion through collagen crosslinking inhibition improves T cell migration and anti-PD-1 treatment. *Elife* **10**.

Nicolas AM, Pesic M, Engel E, Ziegler PK, Diefenhardt M, Kennel KB, Buettner F, Conche C, Petrocelli V, Elwakeel E, Weigert A, Zinoveva A, Fleischmann M, Haupl B, Karakutuk C, Bohnenberger H, Mosa MH, Kaderali L, Gaedcke J, Ghadimi M, Rodel F, Arkan MC, Oellerich T, Rodel C, Fokas E and Greten FR (2022) Inflammatory fibroblasts mediate resistance to neoadjuvant therapy in rectal cancer. *Cancer Cell* **40**:168-184 e113.

Nielsen SR, Strobech JE, Horton ER, Jackstadt R, Laitala A, Bravo MC, Maltese G, Jensen ARD, Reuten R, Rafaeva M, Karim SA, Hwang CI, Arnes L, Tuveson DA, Sansom OJ, Morton JP and Erler JT (2021) Suppression of tumor-associated neutrophils by lorlatinib attenuates pancreatic cancer growth and improves treatment with immune checkpoint blockade. *Nat Commun* **12**:3414.

Noda K, Kitagawa K, Miki T, Horiguchi M, Akama TO, Taniguchi T, Taniguchi H, Takahashi K, Ogra Y, Mecham RP, Terajima M, Yamauchi M and Nakamura T (2020) A matricellular protein fibulin-4 is essential for the activation of lysyl oxidase. *Science Advances* **6**.

Notta F, Hahn SA and Real FX (2017) A genetic roadmap of pancreatic cancer: still evolving. *Gut* **66**:2170-2178.

Ohlund D, Handly-Santana A, Biffi G, Elyada E, Almeida AS, Ponz-Sarvise M, Corbo V, Oni TE, Hearn SA, Lee EJ, Chio, II, Hwang CI, Tiriac H, Baker LA, Engle DD, Feig C, Kultti A, Egeblad M, Fearon DT, Crawford JM, Clevers H, Park Y and Tuveson DA (2017) Distinct populations of inflammatory fibroblasts and myofibroblasts in pancreatic cancer. *J Exp Med* **214**:579-596.

Olive KP, Jacobetz MAD, C.J. Gopinathan, A. McIntyre, D., Honess D, Madhu BG, M.A., Caldwell ME, Allard D, Frese KK, Denicola G, Feig C, Combs C, Winter SP, Ireland-Zecchini H, Reichelt S, Howat WJ, Chang A, Dhara M, Wang L, Rückert F, Grützmann R, Pilarsky C, Izeradjene K, Hingorani SR, Huang P, Davies SE, Plunkett W, Egorin M, Hruban RH, Whitebread N, McGovern K, Adams J, Iacobuzio-Donahue C, Griffiths J and Tuveson DA (2009) Inhibition of Hedgehog signaling enhances delivery of chemotherapy in a mouse model of pancreatic cancer. *Science* **324**:1457-1461.

Ostrem JM, Peters U, Sos ML, Wells JA and Shokat KM (2013) K-Ras(G12C) inhibitors allosterically control GTP affinity and effector interactions. *Nature* **503**:548-551.

Ozdemir BC, Pentcheva-Hoang T, Carstens JL, Zheng X, Wu CC, Simpson TR, Laklai H, Sugimoto H, Kahlert C, Novitskiy SV, De Jesus-Acosta A, Sharma P, Heidari P, Mahmood U, Chin L, Moses HL, Weaver VM, Maitra A, Allison JP, LeBleu VS and Kalluri R (2014) Depletion of carcinoma-associated fibroblasts and fibrosis induces immunosuppression and accelerates pancreas cancer with reduced survival. *Cancer Cell* **25**:719-734.

Park W, Chawla A and O'Reilly EM (2021) Pancreatic Cancer: A Review. *JAMA* **326**:851-862.

Peng DH, Ungewiss C, Tong P, Byers LA, Wang J, Canales JR, Villalobos PA, Uraoka N, Mino B, Behrens C, Wistuba, II, Han RI, Wanna CA, Fahrenholtz M, Grande-Allen KJ, Creighton CJ and Gibbons DL (2017) ZEB1 induces LOXL2-mediated collagen stabilization and deposition in the extracellular matrix to drive lung cancer invasion and metastasis. *Oncogene* **36**:1925-1938.

Peng Z, Ye M, Ding H, Feng Z and Hu K (2022) Spatial transcriptomics atlas reveals the crosstalk between cancer-associated fibroblasts and tumor microenvironment components in colorectal cancer. *J Transl Med* **20**:302.

Petitprez F, Levy S, Sun CM, Meylan M, Linhard C, Becht E, Elarouci N, Tavel D, Roumenina LT, Ayadi M, Sautes-Fridman C, Fridman WH and de Reynies A (2020) The murine Microenvironment Cell Population counter method to estimate abundance of tissue-infiltrating immune and stromal cell populations in murine samples using gene expression. *Genome Med* **12**:86.

Philip PA, Azar I, Xiu J, Hall MJ, Hendifar AE, Lou E, Hwang JJ, Gong J, Feldman R, Ellis M, Stafford P, Spetzler D, Khushman MM, Sohal D, Lockhart AC, Weinberg BA, El-Deiry WS, Marshall J, Shields AF and Korn WM (2022) Molecular Characterization of KRAS Wild-type Tumors in Patients with Pancreatic Adenocarcinoma. *Clin Cancer Res* **28**:2704-2714.

Puleo F, Nicolle R, Blum Y, Cros J, Marisa L, Demetter P, Quertinmont E, Svrcek M, Elarouci N, Iovanna J, Franchimont D, Verset L, Galdon MG, Deviere J, de Reynies A, Laurent-Puig P, Van Laethem JL, Bachet JB and Marechal R (2018) Stratification of Pancreatic Ductal Adenocarcinomas Based on Tumor and Microenvironment Features. *Gastroenterology* **155**:1999-2013 e1993.

Pushalkar S, Hundeyin M, Daley D, Zambirinis CP, Kurz E, Mishra A, Mohan N, Aykut B, Usyk M, Torres LE, Werba G, Zhang K, Guo Y, Li Q, Akkad N, Lall S, Wadowski B, Gutierrez J, Kochen Rossi JA, Herzog JW, Diskin B, Torres-Hernandez A, Leinwand J, Wang W, Taunk PS, Savadkar S, Janal M, Saxena A, Li X, Cohen D, Sartor RB, Saxena D and Miller G (2018) The Pancreatic Cancer Microbiome Promotes Oncogenesis by Induction of Innate and Adaptive Immune Suppression. *Cancer Discov* **8**:403-416.

Pylayeva-Gupta Y, Lee KE, Hajdu CH, Miller G and Bar-Sagi D (2012) Oncogenic Kras-induced GM-CSF production promotes the development of pancreatic neoplasia. *Cancer Cell* **21**:836-847.

Raghavan S, Winter PS, Navia AW, Williams HL, DenAdel A, Lowder KE, Galvez-Reyes J, Kalekar RL, Mulugeta N, Kapner KS, Raghavan MS, Borah AA, Liu N, Vayrynen SA, Costa AD, Ng RWS, Wang J, Hill EK, Ragon DY, Brais LK, Jaeger AM, Spurr LF, Li YY, Cherniack AD, Booker MA, Cohen EF, Tolstorukov MY, Wakiro I, Rotem A, Johnson BE, McFarland JM, Sicinska ET, Jacks TE, Sullivan RJ, Shapiro GI, Clancy TE, Perez K, Rubinson DA, Ng K, Cleary JM, Crawford L, Manalis SR, Nowak JA, Wolpin BM, Hahn WC, Aguirre AJ and Shalek AK (2021) Microenvironment drives cell state, plasticity, and drug response in pancreatic cancer. *Cell* **184**:6119-6137 e6126.

Rahib L, Wehner MR, Matrisian LM and Nead KT (2021) Estimated Projection of US Cancer Incidence and Death to 2040. *JAMA Netw Open* **4**:e214708.

Raphael, Aguirre and Network CGAR (2017) Integrated Genomic Characterization of Pancreatic Ductal Adenocarcinoma. *Cancer Cell* **32**:185-203 e113.

Reimand J, Kull M, Peterson H, Hansen J and Vilo J (2007) g:Profiler--a web-based toolset for functional profiling of gene lists from large-scale experiments. *Nucleic Acids Res* **35**:W193-200.

Rhim AD, Oberstein PE, Thomas DH, Mirek ET, Palermo CF, Sastra SA, Dekleva EN, Saunders T, Becerra CP, Tattersall IW, Westphalen CB, Kitajewski J, Fernandez-Barrena MG, Fernandez-Zapico ME, Iacobuzio-Donahue C, Olive KP and Stanger BZ (2014) Stromal elements act to restrain, rather than support, pancreatic ductal adenocarcinoma. *Cancer Cell* **25**:735-747.

Riquelme E, Zhang Y, Zhang L, Montiel M, Zoltan M, Dong W, Quesada P, Sahin I, Chandra V, San Lucas A, Scheet P, Xu H, Hanash SM, Feng L, Burks JK, Do KA, Peterson CB, Nejman D, Tzeng CD, Kim MP, Sears CL, Ajami N, Petrosino J, Wood LD, Maitra A, Straussman R, Katz M, White JR, Jenq R, Wargo J and McAllister F (2019) Tumor Microbiome Diversity and Composition Influence Pancreatic Cancer Outcomes. *Cell* **178**:795-806 e712.

Rouillard AD, Gundersen GW, Fernandez NF, Wang Z, Monteiro CD, McDermott MG and Ma'ayan A (2016) The harmonizome: a collection of processed datasets gathered to serve and mine knowledge about genes and proteins. *Database (Oxford)* **2016**.

Sachdevaa MZ, Shoumin, Wua F, Wua H, Waliab V, Kumarb S, Elbleb R, Watabea K and Moa Y-Y (2009) p53 represses c-Myc through induction of the tumor suppressor miR-145. *PNAS* **106**.

Safi SA, Haeberle L, Goering W, Keitel V, Fluegen G, Stoecklein N, Rehders A, Knoefel WT and Esposito I (2022) Genetic Alterations Predict Long-Term Survival in Ductal Adenocarcinoma of the Pancreatic Head. *Cancers (Basel)* **14**.

Sahai E, Astsaturov I, Cukierman E, DeNardo DG, Egeblad M, Evans RM, Fearon D, Greten FR, Hingorani SR, Hunter T, Hynes RO, Jain RK, Janowitz T, Jorgensen C, Kimmelman AC, Kolonin MG, Maki RG, Powers RS, Pure E, Ramirez DC, Scherz-Shouval R, Sherman MH, Stewart S, Tlsty TD, Tuveson DA, Watt FM, Weaver V, Weeraratna AT and Werb Z (2020) A framework for advancing our understanding of cancer-associated fibroblasts. *Nat Rev Cancer* **20**:174-186.

Salmon H, Franciszkiewicz K, Damotte D, Dieu-Nosjean MC, Validire P, Trautmann A, Mami-Chouaib F and Donnadieu E (2012) Matrix architecture defines the preferential localization and migration of T cells into the stroma of human lung tumors. *J Clin Invest* **122**:899-910.

Samatar AA and Poulikakos PI (2014) Targeting RAS-ERK signalling in cancer: promises and challenges. *Nat Rev Drug Discov* **13**:928-942.

Santoro A, Vlachou T, Luzi L, Melloni G, Mazzarella L, D'Elia E, Aobuli X, Pasi CE, Reavie L, Bonetti P, Punzi S, Casoli L, Sabo A, Moroni MC, Dellino GI, Amati B, Nicassio F, Lanfrancone L and Pelicci PG (2019) p53 Loss in Breast Cancer Leads to Myc Activation, Increased Cell Plasticity, and Expression of a Mitotic Signature with Prognostic Value. *Cell Rep* **26**:624-638 e628.

Schaub FX, Dhankani V, Berger AC, Trivedi M, Richardson AB, Shaw R, Zhao W, Zhang X, Ventura A, Liu Y, Ayer DE, Hurlin PJ, Cherniack AD, Eisenman RN, Bernard B, Grandori C and Cancer Genome Atlas N (2018) Pan-cancer Alterations of the MYC Oncogene and Its Proximal Network across the Cancer Genome Atlas. *Cell Syst* **6**:282-300 e282.

Scheffzek K, Ahmadian MR, Kabsch W, Wiesmüller L, Lautwein A, Schmitz F and Wittinghofer A (1997) The Ras-RasGAP Complex: Structural Basis for GTPase Activation and Its Loss in Oncogenic Ras Mutants. *Science* **277**:333-339.

Schilter H, Findlay AD, Perryman L, Yow TT, Moses J, Zahoor A, Turner CI, Deodhar M, Foot JS, Zhou W, Greco A, Joshi A, Rayner B, Townsend S, Buson A and Jarolimek W (2019) The lysyl oxidase like 2/3 enzymatic inhibitor, PXS-5153A, reduces crosslinks and ameliorates fibrosis. *J Cell Mol Med* **23**:1759-1770.

Schonhuber N, Seidler B, Schuck K, Veltkamp C, Schachtler C, Zukowska M, Eser S, Feyerabend TB, Paul MC, Eser P, Klein S, Lowy AM, Banerjee R, Yang F, Lee CL, Moding EJ, Kirsch DG, Scheideler A, Alessi DR, Varela I, Bradley A, Kind A, Schnieke AE, Rodewald HR, Rad R, Schmid RM, Schneider G and Saur D (2014) A next-generation dual-recombinase system for time- and host-specific targeting of pancreatic cancer. *Nat Med* **20**:1340-1347.

Schurch CM, Bhate SS, Barlow GL, Phillips DJ, Noti L, Zlobec I, Chu P, Black S, Demeter J, McIlwain DR, Kinoshita S, Samusik N, Goltsev Y and Nolan GP (2020) Coordinated Cellular Neighborhoods Orchestrate Antitumoral Immunity at the Colorectal Cancer Invasive Front. *Cell* **182**:1341-1359 e1319.

Shin DW, Lee JC, Kim J, Woo SM, Lee WJ, Han SS, Park SJ, Choi KS, Cha HS, Yoon YS, Han HS, Hong EK and Hwang JH (2019) Validation of the American Joint Committee on Cancer 8th edition staging system for the pancreatic ductal adenocarcinoma. *Eur J Surg Oncol* **45**:2159-2165.

Siolas D, Vucic E, Kurz E, Hajdu C and Bar-Sagi D (2021) Gain-of-function p53(R172H) mutation drives accumulation of neutrophils in pancreatic tumors, promoting resistance to immunotherapy. *Cell Rep* **36**:109578.

Siret C, Collignon A, Silvy F, Robert S, Cheyrol T, Andre P, Rigot V, Iovanna J, van de Pavert S, Lombardo D, Mas E and Martirosyan A (2019) Deciphering the Crosstalk Between Myeloid-Derived Suppressor Cells and Regulatory T Cells in Pancreatic Ductal Adenocarcinoma. *Front Immunol* **10**:3070.

Sodir NM, Kortlever RM, Barthet VJA, Campos T, Pellegrinet L, Kupczak S, Anastasiou P, Swigart LB, Soucek L, Arends MJ, Littlewood TD and Evan GI (2020) MYC Instructs and Maintains Pancreatic Adenocarcinoma Phenotype. *Cancer Discov* **10**:588-607.

Steele NG, Biffi G, Kemp SB, Zhang Y, Drouillard D, Syu L, Hao Y, Oni TE, Brosnan E, Elyada E, Doshi A, Hansma C, Espinoza C, Abbas A, The S, Irizarry-Negron V, Halbrook CJ, Franks NE, Hoffman MT, Brown K, Carpenter ES, Nwosu ZC, Johnson C, Lima F, Anderson MA, Park Y, Crawford HC, Lyssiotis CA, Frankel TL, Rao A, Bednar F, Dlugosz AA, Preall JB, Tuveson DA, Allen BL and Pasca di Magliano M (2021) Inhibition of Hedgehog Signaling Alters Fibroblast Composition in Pancreatic Cancer. *Clin Cancer Res* **27**:2023-2037.

Stoltzfus CR, Filipek J, Gern BH, Olin BE, Leal JM, Wu Y, Lyons-Cohen MR, Huang JY, Paz-Stoltzfus CL, Plumlee CR, Poschinger T, Urdahl KB, Perro M and Gerner MY (2020) CytoMAP: A Spatial Analysis Toolbox Reveals Features of Myeloid Cell Organization in Lymphoid Tissues. *Cell Rep* **31**:107523.

Storz P (2017) Acinar cell plasticity and development of pancreatic ductal adenocarcinoma. *Nat Rev Gastroenterol Hepatol* **14**:296-304.

Su S, Chen J, Yao H, Liu J, Yu S, Lao L, Wang M, Luo M, Xing Y, Chen F, Huang D, Zhao J, Yang L, Liao D, Su F, Li M, Liu Q and Song E (2018) CD10+GPR77+ Cancer-Associated Fibroblasts Promote Cancer Formation and Chemoresistance by Sustaining Cancer Stemness. *Cell* **172**:841-856.e816.

Suarez-Arnedo A, Torres Figueroa F, Clavijo C, Arbelaez P, Cruz JC and Munoz-Camargo C (2020) An image J plugin for the high throughput image analysis of in vitro scratch wound healing assays. *PLoS One* **15**:e0232565.

Subramanian A, Tamayo P, Mootha VK, Mukherjee S, Ebert BL, Gillette MA, Paulovich A, Pomeroy SL, Golub TR, Lander ES and Mesirov JP (2005) Gene set enrichment analysis: A knowledge-based approach for interpreting genome-wideexpression profiles. *PNAS* **102**.

Tape CJ, Ling S, Dimitriadi M, McMahon KM, Worboys JD, Leong HS, Norrie IC, Miller CJ, Poulogiannis G, Lauffenburger DA and Jorgensen C (2016) Oncogenic KRAS Regulates Tumor Cell Signaling via Stromal Reciprocation. *Cell* **165**:910-920.

Tian C, Clauser KR, Ohlund D, Rickelt S, Huang Y, Gupta M, Mani DR, Carr SA, Tuveson DA and Hynes RO (2019) Proteomic analyses of ECM during pancreatic ductal adenocarcinoma progression reveal different contributions by tumor and stromal cells. *Proc Natl Acad Sci U S A* **116**:19609-19618.

Togashi Y, Shitara K and Nishikawa H (2019) Regulatory T cells in cancer immunosuppression - implications for anticancer therapy. *Nat Rev Clin Oncol* **16**:356-371.

Torphy RJ, Wang Z, True-Yasaki A, Volmar KE, Rashid N, Yeh B, Anderson JM, Hollingsworth MA, Yeh JJ and Collisson EA (2018) Stromal Content Is Correlated With Tissue Site, Contrast Retention, and Survival in Pancreatic Adenocarcinoma. *JCO Precis Oncol*.

Ungewiss C, Rizvi ZH, Roybal JD, Peng DH, Gold KA, Shin DH, Creighton CJ and Gibbons DL (2016) The microRNA-200/Zeb1 axis regulates ECM-dependent beta1-integrin/FAK signaling, cancer cell invasion and metastasis through CRKL. *Sci Rep* **6**:18652.

van Roessel S, Kasumova GG, Verheij J, Najarian RM, Maggino L, de Pastena M, Malleo G, Marchegiani G, Salvia R, Ng SC, de Geus SW, Lof S, Giovinazzo F, van Dam JL, Kent TS, Busch OR, van Eijck CH, Koerkamp BG, Abu Hilal M, Bassi C, Tseng JF and Besselink MG (2018) International Validation of the Eighth Edition of the American Joint Committee on Cancer (AJCC) TNM Staging System in Patients With Resected Pancreatic Cancer. *JAMA Surg* **153**:e183617.

Verrecchia F, Chu M-L and Mauviel A (2001) Identification of Novel TGF-β/Smad Gene Targets in Dermal Fibroblasts using a Combined cDNA Microarray/Promoter Transactivation Approach. *Journal of Biological Chemistry* **276**:17058-17062.

Waddell N, Pajic M, Patch AM, Chang DK, Kassahn KS, Bailey P, Johns AL, Miller D, Nones K, Quek K, Quinn MC, Robertson AJ, Fadlullah MZ, Bruxner TJ, Christ AN, Harliwong I, Idrisoglu S, Manning S, Nourse C, Nourbakhsh E, Wani S, Wilson PJ, Markham E, Cloonan N, Anderson

MJ, Fink JL, Holmes O, Kazakoff SH, Leonard C, Newell F, Poudel B, Song S, Taylor D, Waddell N, Wood S, Xu Q, Wu J, Pinese M, Cowley MJ, Lee HC, Jones MD, Nagrial AM, Humphris J, Chantrill LA, Chin V, Steinmann AM, Mawson A, Humphrey ES, Colvin EK, Chou A, Scarlett CJ, Pinho AV, Giry-Laterriere M, Rooman I, Samra JS, Kench JG, Pettitt JA, Merrett ND, Toon C, Epari K, Nguyen NQ, Barbour A, Zeps N, Jamieson NB, Graham JS, Niclou SP, Bjerkvig R, Grutzmann R, Aust D, Hruban RH, Maitra A, Iacobuzio-Donahue CA, Wolfgang CL, Morgan RA, Lawlor RT, Corbo V, Bassi C, Falconi M, Zamboni G, Tortora G, Tempero MA, Australian Pancreatic Cancer Genome I, Gill AJ, Eshleman JR, Pilarsky C, Scarpa A, Musgrove EA, Pearson JV, Biankin AV and Grimmond SM (2015) Whole genomes redefine the mutational landscape of pancreatic cancer. *Nature* **518**:495-501.

Wang T, Jin H, Hu J, Li X, Ruan H, Xu H, Wei L, Dong W, Teng F, Gu J, Qin W, Luo X and Hao Y (2020) COL4A1 promotes the growth and metastasis of hepatocellular carcinoma cells by activating FAK-Src signaling. *J Exp Clin Cancer Res* **39**:148.

Wei SC, Fattet L, Tsai JH, Guo Y, Pai VH, Majeski HE, Chen AC, Sah RL, Taylor SS, Engler AJ and Yang J (2015) Matrix stiffness drives epithelial-mesenchymal transition and tumour metastasis through a TWIST1-G3BP2 mechanotransduction pathway. *Nat Cell Biol* **17**:678-688.

Whatcott CJ, Diep CH, Jiang P, Watanabe A, LoBello J, Sima C, Hostetter G, Shepard HM, Von Hoff DD and Han H (2015) Desmoplasia in Primary Tumors and Metastatic Lesions of Pancreatic Cancer. *Clin Cancer Res* **21**:3561-3568.

Windon AL, Loaiza-Bonilla A, Jensen CE, Randall M, Morrissette JJD and Shroff SG (2018) A KRAS wild type mutational status confers a survival advantage in pancreatic ductal adenocarcinoma. *J Gastrointest Oncol* **9**:1-10.

Witkiewicz AK, McMillan EA, Balaji U, Baek G, Lin WC, Mansour J, Mollaee M, Wagner KU, Koduru P, Yopp A, Choti MA, Yeo CJ, McCue P, White MA and Knudsen ES (2015) Whole-exome sequencing of pancreatic cancer defines genetic diversity and therapeutic targets. *Nat Commun* **6**:6744.

Wolf FA, Angerer P and Theis FJ (2018) SCANPY: large-scale single-cell gene expression data analysis. *Genome Biol* **19**:15.

Yamamoto K, Venida A, Yano J, Biancur DE, Kakiuchi M, Gupta S, Sohn ASW, Mukhopadhyay S, Lin EY, Parker SJ, Banh RS, Paulo JA, Wen KW, Debnath J, Kim GE, Mancias JD, Fearon DT, Perera RM and Kimmelman AC (2020) Autophagy promotes immune evasion of pancreatic cancer by degrading MHC-I. *Nature* **581**:100-105.

Yamauchi M and Sricholpech M (2012) Lysine post-translational modifications of collagen. *Essays Biochem* **52**:113-133.

Yin F, Saad M, Xie H, Lin J, Jackson CR, Ren B, Lawson C, Karamchandani DM, Bernabeu BQ, Jiang W, Dhir T, Zheng R, Schultz CW, Zhang D, Thomas CL, Zhang X, Lai J, Schild M, Zhang X and Liu X (2020) Validation of American Joint Committee on Cancer 8(th) edition of TNM staging in resected distal pancreatic cancer. *World J Gastrointest Pharmacol Ther* **11**:25-39.

Ying H, Dey P, Yao W, Kimmelman AC, Draetta GF, Maitra A and DePinho RA (2016) Genetics and biology of pancreatic ductal adenocarcinoma. *Genes Dev* **30**:355-385.

Zaghdoudi S, Decaup E, Belhabib I, Samain R, Cassant-Sourdy S, Rochotte J, Brunel A, Schlaepfer D, Cros J, Neuzillet C, Strehaiano M, Alard A, Tomasini R, Rajeeve V, Perraud A, Mathonnet M, Pearce OM, Martineau Y, Pyronnet S, Bousquet C and Jean C (2020) FAK activity in cancer-associated fibroblasts is a prognostic marker and a druggable key metastatic player in pancreatic cancer. *EMBO Mol Med* **12**:e12010.

Zhang D, Li L, Jiang H, Li Q, Wang-Gillam A, Yu J, Head R, Liu J, Ruzinova MB and Lim KH (2018) Tumor-Stroma IL1beta-IRAK4 Feedforward Circuitry Drives Tumor Fibrosis, Chemoresistance, and Poor Prognosis in Pancreatic Cancer. *Cancer Res* **78**:1700-1712.

Zhao F, Obermann S, von Wasielewski R, Haile L, Manns MP, Korangy F and Greten TF (2009) Increase in frequency of myeloid-derived suppressor cells in mice with spontaneous pancreatic carcinoma. *Immunology* **128**:141-149.

Zilionis R, Engblom C, Pfirschke C, Savova V, Zemmour D, Saatcioglu HD, Krishnan I, Maroni G, Meyerovitz CV, Kerwin CM, Choi S, Richards WG, De Rienzo A, Tenen DG, Bueno R, Levantini E, Pittet MJ and Klein AM (2019) Single-Cell Transcriptomics of Human and Mouse Lung Cancers Reveals Conserved Myeloid Populations across Individuals and Species. *Immunity* **50**:1317-1334 e1310.